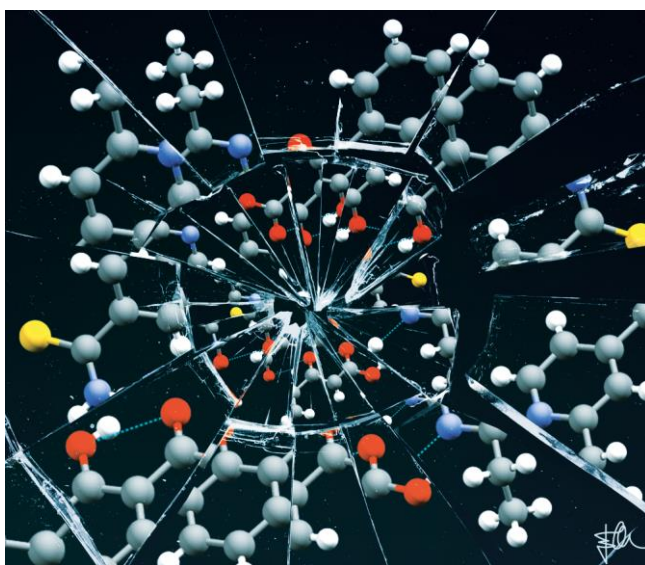**Università degli Studi di Torino**

Doctoral School of the University of Torino

PhD Programme in Chemical and Materials Sciences XXXIV Cycle

Breaking and harnessing crystal engineering rules for achieving functional pharmaceutical crystal forms

Simone Bordignon

Supervisor:
Prof. Michele R. Chierotti

Università degli Studi di Torino

Doctoral School of the University of Torino

PhD Programme in Chemical and Materials Sciences XXXIV cycle

Breaking and harnessing crystal engineering rules for achieving functional pharmaceutical crystal forms

Candidate: **Simone Bordignon**

Supervisor: Prof. **Michele Chierotti**

Jury Members: Prof. **Roberto Gobetto**
Università degli Studi di Torino
Dipartimento di Chimica

Prof. **Marco Geppi**
Università di Pisa
Dipartimento di Chimica e Chimica Industriale

Dr. **Matteo Lusi**
University of Limerick
Department of Chemical Sciences & Bernal Institute

Head of the Doctoral School: Prof. Alberto Rizzuti
PhD Programme Coordinator: Prof. Bartolomeo Civalleri

Torino, 08/07/2022

«Ma non ti rendi conto di quant'è bello?
Che non ti porti il peso del mondo sulle spalle,
che sei soltanto un filo d'erba in un prato?
Non ti senti più leggero?»

«Le persone so' complesse: hanno lati che non conosci, hanno
comportamenti mossi da ragioni intime e insondabili dall'esterno.
Noi vediamo solo un pezzetto piccolissimo di quello che c'hanno
dentro e fuori.
E da soli non spostiamo quasi niente.
Siamo fili d'erba,
ti ricordi?»

Zerocalcare

Table of contents

Preface

Since the very beginning of humanity, the understanding of how materials could be made available and how they worked played a pivotal role in the scientific and technological development of society. With the discovery of X-rays in 1895 and the subsequent advent of crystallography in 1912, crystalline materials could be thoroughly investigated for the first time. This provided the ultimate evidence of the intrinsic long-range order of such substances. Soon, achieving insight into the structure of a crystalline material of interest, i.e., understanding the identity, connectivity and periodicity of its components, became extremely important to fully describe it. Beside the structural characterization of crystalline solids, the investigation of their physicochemical properties rapidly emerged as a fundamental need for their practical employment. Indeed, understanding the "bigger picture" in terms of structure and properties of ordered materials can lead to their application in countless fields of technology: from architecture to biomedicals; from agriculture to energy materials; from pharmaceuticals and food ingredients to the dyes/pigments industry.

It is in this framework that crystal engineering gained tremendous interest and became central in the achievement of functional crystalline materials. Crystal engineering is a branch of supramolecular chemistry based on the understanding of intermolecular interactions in the context of crystal packing and its application in designing novel crystal forms with desired physicochemical properties, such as chemical and photochemical reactivity, hygroscopicity, spectroscopic and optical properties, tabletability, dissolution rate, and melting point.

The application of rational design of crystal architectures to the field of pharmaceutically active molecules proves of particular interest. This is especially true when drugs characterized by unsatisfactory aqueous

dissolution rates, that are commonly administered orally in solid form, are considered. Indeed, the achievement of enhanced crystal forms of such active ingredients allows providing patients with better care and even introducing poorly performing drugs back into the market.

This doctoral project deals with the exploration and employment of crystal engineering to obtain new crystal forms of pharmaceutically active molecules. The main focus was to consider, investigate, and ultimately employ some principles of crystal engineering with the final aim of enhancing the dissolution behavior of active ingredients.

The present thesis work is organized in 6 chapters.

Chapter 1 acts as a brief introduction of crystal engineering and its main aspects, featured and exploited during the work that was carried out in the 3 years of the PhD project. Emphasis was placed on defining hydrogen bonds and supramolecular synthons as essential tools of the design step, as well as introducing the primary types of multicomponent crystal forms investigated in the work. The employment of crystal engineering in the pharmaceutical field is stressed, with a concise summary of the most common synthetic techniques for preparing new crystal forms.

In **Chapter 2**, the pseudopolymorphism of the methyl gallate-L-proline system is explored, and the repercussions of stoichiometry and hydration state of L-proline on the final outcome of the supramolecular synthesis analyzed (**S. Bordignon**, P. Cerreia Vioglio, C. Bertoncini, E. Priola, R. Gobetto, M. R. Chierotti, *Cryst. Growth Des.* **2021**, *21*, 6776–6785).

Chapter 3 is centered around anti-tubercular drug ethionamide. The drug was combined with simple dicarboxylic acids to improve its dissolution rate, affording three new crystal forms, including a rare kryptoracemate, with the desired enhancement (**S. Bordignon**, P. Cerreia Vioglio, E. Amadio, F. Rossi, E. Priola, D. Voinovich, R. Gobetto, M. R. Chierotti, *Pharmaceutics* **2020**, 12, 818–835).

2

As for **Chapter 4**, it works as a conceptual bridge between the previous and the next chapters: indeed, ethionamide was coupled with salicylic acid to rationally manipulate the synthetic conditions into observing salt/cocrystal polymorphism in the intermediate range of ΔpK_a values in which the prediction of the final ionization state of the adduct fails (D. Bernasconi, **S. Bordignon**, F. Rossi, E. Priola, C. Nervi, R. Gobetto, D. Voinovich, D. Hasa, N. T. Duong, Y. Nishiyama, M. R. Chierotti, *Cryst. Growth Des.* **2020**, *20*, 906–915).

Continuing the work about salt/cocrystal polymorphism, **Chapter 5** deals with another such case, that of the ketoprofen-lysine system, which has been marketed as a molecular salt for decades. The work that was carried out revealed that it is, in fact, much more likely to be a cocrystal, while an actual molecular salt of ketoprofen-lysine was obtained with the same stoichiometry (A. Aramini, G. Bianchini, S. Lillini, **S. Bordignon**, M. Tomassetti, R. Novelli, S. Mattioli, L. Lvova, R. Paolesse, M. R. Chierotti, M. Allegretti, *Pharmaceuticals*, **2021**, *14*, 555–572).

Chapter 6 reports a study performed in collaboration with Dr. Lusi's group at the Bernal Institute of the University of Limerick (Ireland) regarding the successful obtainment of solid solutions between drug hydrocortisone and prodrug cortisone, all characterized by higher dissolution rates for hydrocortisone with respect to the pure drug. Interestingly, the achievement of these adducts breaks Hume-Rothery's rules, which prescribe solid solubility only between components with very similar crystal structures (V. Verma, **S. Bordignon**, M. R. Chierotti, M. Lestari, K. Lyons, L. Padrela, K. Ryan, M. Lusi, *IUCrJ*, **2020**, *7*, 1124–1130).

Finally, conclusive remarks about the importance and growing interest around the field of crystal engineering applied to pharmaceutical compounds are given.

Chapter 1

Crystal engineering and its employment in the pharmaceutical field

1.1 Introduction

Crystalline supramolecular systems (i.e., ordered solid adducts containing molecules linked by weak interactions) represent the cornerstones of crystal engineering. The main challenge that field experts devote themselves to overcome, still far from being fully met, is predicting how molecules of a given substance are going to be arranged in three-dimensional space and, in turn, which properties the achieved crystal form would exhibit. Indeed, it is well known that the macroscopic performances of a crystalline material are intimately connected to its structural features.[1–3] Different crystal forms of the very same compound can thus display even dramatically different behaviors, in terms of physicochemical properties, such as solubility,[4] thermal stability[5] or hygroscopicity.[6]

Among the many classes of existent crystalline materials, molecular ones are of particular interest since they dominate the vast world of organic and organometallic compounds. Their crystal structure is characterized by molecules bound together by weak interactions, such as hydrogen bonds (HBs), halogen bonds, and dispersion forces, like π-stacking.[7,8] HBs, in particular, are arguably the most studied intermolecular bonds when it comes to designing new crystal forms, since they are characterized by strong directionality and they are rather robust and selective.[9] It stands to reason, then, that HBs are central in the formation of what are called *supramolecular synthons*. Based on Corey's definition of *synthon* related to organic synthesis,[10] G. R. Desiraju defined supramolecular synthons as structural

units in molecular crystals that are achievable through known or plausible synthetic pathways involving weak interactions.[11] The idea behind the exploitation of supramolecular synthons as building blocks in crystal engineering is that of increasing the level of predictability of the crystal structures that one aims to obtain.

1.2 The hydrogen bond: a fundamental tool of the crystal engineer

When one thinks of a crystal, they are intuitively led to think of it as a stable and robust entity, which apparently clashes with the concept of weak interactions keeping it together. This is actually explained by the so-called "Gulliver effect": a large number of non-covalent bonds are able to direct crystal packing as efficiently as few strong bonds would, or even more so.[12] Most of all, weak anisotropic interactions are particularly interesting and useful to crystal engineers in the pursuit of specific crystal architectures. As explained by Desiraju,[13] they are mainly responsible for the observed deviations from the close-packing theory proposed by Kitajgorodskij,[14] and can in turn be properly employed to engineer the desired structure. Among anisotropic weak bonds, the most significant and common one is the HB.

In the context of weak interactions, the uniqueness of HBs consists in their peculiar strength, selectivity, and directionality. Indeed, considering the strongest observed HBs, due to their significant electrostatic component, one can find that they are characterized by bond energies that are comparable to those of weak covalent bonds;[12] moreover, their precise recognition mechanisms stand as the foundation of life as we know it. Suffice to say, HBs are what allows for nucleobases to correctly pair up in the double helixes of RNA and DNA; they are responsible for the achievement of secondary structures in proteins; they determine the lower density of ice with respect

to liquid water, which in turn allowed for life to thrive on the planet in the early stages of its history.[15]

As for crystal engineering, the peculiar directionality of HBs is appreciated as their most valuable feature, since it drives the assembly of HB-based supramolecular synthons to be used as building blocks in the design of new crystal architectures.

HBs (schematically represented in Figure 1.1) arise when hydrogens covalently bound to electronegative atoms (HB donors, such as F, O or N) experience attractive forces towards a different electronegative atom (HB acceptor, in the same molecule or in another one).
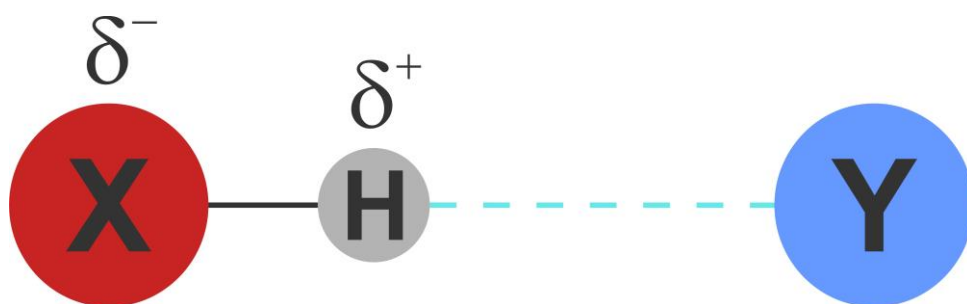
Figure 1.1 Schematic representation of a typical hydrogen bond (dashed cyan line), between a donor electronegative atom (labeled X) and an electronegative acceptor (labeled Y).

As the IUPAC defined in 2011,[16] the strength of the resulting HB is correlated to factors such as the entity of the X-H bond polarization and the linearity of the X-H$\cdots$Y interaction (X being the HB donor and Y being the acceptor). According to Steiner and Desiraju,[15] it is in this regard that HBs can be tentatively classified based on their strength into weak, strong and very strong. Weak HBs (e.g., C-H$\cdots$O or O-H$\cdots$ π) feature energies lower than 4 kcal/mol and a significant dispersive character, that diminishes their directionality; strong HBs, such as O-H$\cdots$O or N-H$\cdots$O, are indicatively

6

included in the 4-15 kcal/mol range and are those more feasibly exploited to drive the crystal assembly, given their higher electrostatic component, that provides them with better directionality. The same applies for very strong HBs, that present energies up to 40 kcal/mol, to which charge transfer phenomena contribute greatly.[15]

The presence and strength of HBs in supramolecular adducts can be inquired by means of a handful of solid-state techniques: whenever a properly sized single crystal is available, X-ray crystallography is the elective one, providing information about the position and relative distances of heteroatoms such as N or O, consequently providing insight about HBs.[17] Complementary to diffraction analyses are vibrational (Fourier Transform Infrared, or FTIR) spectroscopy and solid-state nuclear magnetic resonance (SSNMR): for the former, when HBs are established, signals associated to the X-H stretching band decrease their infrared absorption wavelength proportionally to the strength of the HB;[18] similarly, the NMR frequency of the involved hydrogen atom increases with the energy of the HB in ^{1}H SSNMR spectra, while ^{13}C and ^{15}N SSNMR chemical shifts of moieties participating in the interaction are influenced as well.[19,20]
Finally, a loyal partner to experimental techniques is found in computational chemistry, which is able to provide energetic and geometric features of the HB pattern in the investigated systems.[21]

1.3 Supramolecular synthons

As previously established, supramolecular synthons act as building blocks for crystal engineers to use for driving crystallization towards the achievement of a desired crystal packing. As it appears, the concept of supramolecular synthon is of a probabilistic nature: given specific chemical moieties (e.g., carboxylic groups or pyridinic rings), the chance of attaining

the desired structural motif is much higher the more frequent the same motif is observed in known structures. This is where the Cambridge Structural Database (or CSD) comes into play: it collects all crystal structures reported in the literature for organic and organometallic compounds. Statistical surveys on the CSD reveal that the most frequent (and, thus, more robust) supramolecular synthons are carboxylic or amidic homodimers, as well as acid-amide and carboxyl-pyridine heterosynthons (represented in Figure 1.2).[22] This last term refers to motifs made up of two different functional groups, and usually considered more stable than the homosynthon counterparts.[12,22]
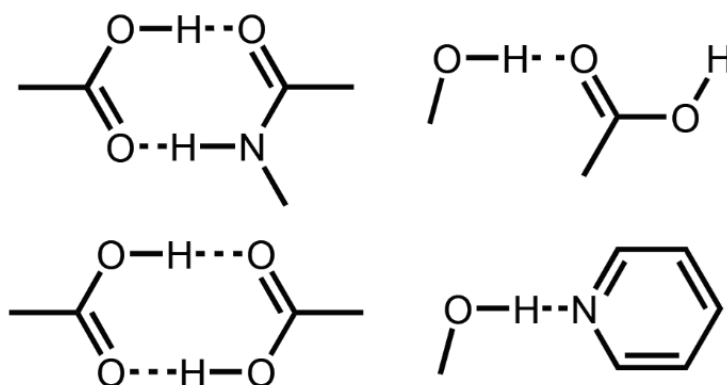
Figure 1.2 Graphic example of some of the most common HB-based supramolecular synthons, namely acid-amide heterosynthon (top left); acid-acid homodimer (bottom left); hydroxyl-carboxyl synthon (top right); hydroxyl-pyridine synthon (bottom right).

Nonetheless, as Mukherjee warns,[23] the final outcome of the designing process in terms of supramolecular synthons also depends on the presence of other functional groups in the considered molecular compounds, that may hinder the arrangement of the intended structural motif. This is, in fact, a matter of transferability of the synthons of interest from structures observed

8

in the CSD to the ultimate architecture of the sought adduct. Insulating functional groups on the molecule of interest (i.e., selecting molecules with useful moieties for the design that are far enough to not interfere with each other) may definitely help in successfully transferring robust synthons from one structure to another, but the lack of a proper predictability of the crystal engineering approach still remains, to this day, the biggest challenge in the field.

It is no coincidence that, in the last 2 decades, great effort was put into what is known as crystal structure prediction (CSP).[24,25] Basically, computational methods are employed to probe the lattice energies of the possible crystal packings of a given molecule, so to find the candidates coinciding with minima on a potential energy surface.[26,27] After geometry optimization and possibly the combination of experimental data coming, for instance, from powder diffraction or solid-state NMR data,[21,28,29] a ranked list of predicted structures is originated. The candidate with the lowest lattice energy and with the best agreement with the experimental information is predicted as the structure which is most likely to be observed.

The CSP approach was found to be particularly fit to explore the polymorph landscape of organic molecules (especially APIs). In this sense, combining calculation efforts with the experimental screening feature of crystal engineering is proved to lead to overwhelming results. One example of the strength of such a combination is represented by antipsychotic olanzapine: a recent review by Reutzel-Edens and Bhardwaj reveals how the prediction of stable crystal structures, different from those already known for this API, drove the screening towards the isolation of a novel anhydrous polymorph, 4 different hydrate phases and several solvates of olanzapine.[30,31] In general, the advancement in the power of the computational tools and the growing interest from the academic and industrial sectors has allowed for CSP to provide more and more reliable results in the recent years.[32,33] Although,

despite the more and more rewarding work in the field, a great challenge remains not fully met: that of consistently and reliably model dispersion forces, which are often predominant in determining the crystal packing of an ordered material.[15]

1.4 The main types of multicomponent crystal forms

A quite straightforward way in which molecular crystals are classified relates to the number of different species that are included in their unit cell. If only molecules of the same compound are present, then the material is regarded as monocomponent; on the contrary, multicomponent crystals are those that exhibit multiple molecular species in their asymmetric unit. A given molecule can present itself in different crystal forms, belonging to either of these two classes, which are characterized by different physicochemical properties. This acts as the driving force for crystal engineers to focus on the obtainment and in-depth description of novel molecular materials.

In the field of crystal forms, great interest has always been reserved to the exploration of the polymorph landscape of molecular compounds.[34–41] Polymorphism is a phenomenon that consists in the ability of many substances of crystallizing in crystal forms that do not differ in chemical composition and stoichiometry, but only in their crystal structure.[42] Since they feature dissimilar crystal packings, polymorphs of the very same molecule exhibit different and peculiar physicochemical properties with respect to each other. As McCrone notoriously stated in 1965, "every compound has different polymorphic forms…, the number of forms known for a given compound is proportional to the time and money spent on research on that compound".[43] Moreover, most couples of polymorphs for the same substance only differ for less than about 7 kJ/mol in their lattice energies,[44] which has the effect of complicating the ranking step of the computational procedure for the

10

prediction of crystal structures. It does not surprise, then, that many resources still get invested to this day in the never-ending search for new crystal forms.

If polymorphs are indeed quite capable of piquing the interest of crystal engineers, in the last few decades multicomponent crystal forms have elicited a strong enthusiasm among those who deal with their design, preparation and characterization.[45–56] These mainly include solvates, molecular salts and cocrystals, and all fall under the definition of solid crystalline adducts consisting of a single homogeneous phase and composed of at least two different molecular species in definite a stoichiometric ratio, linked by weak interactions (see Figure 1.3 for a schematic depiction of the most common crystal forms).[57]
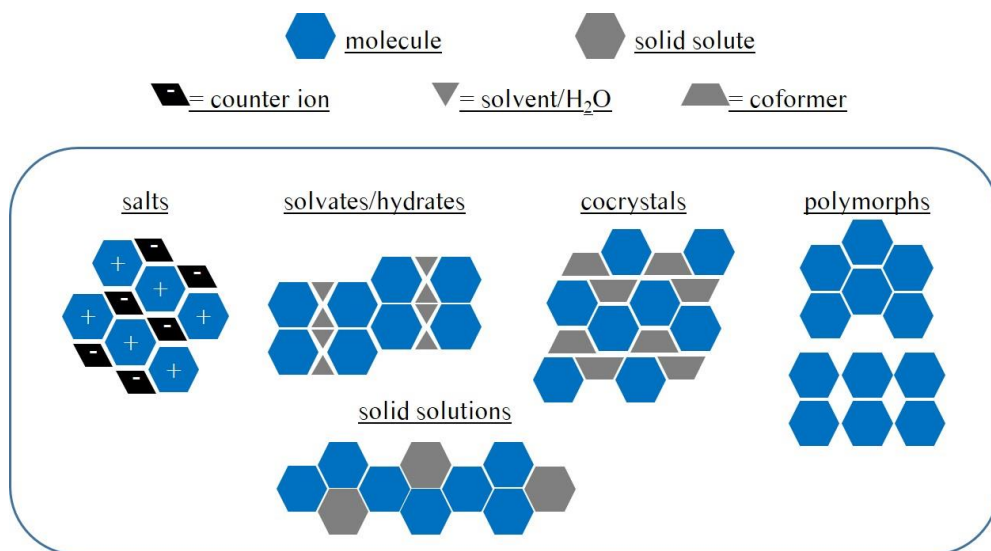
Figure 1.3 Illustrative examples of typical crystal forms, both mono- and multicomponent.

In the simplest of cases, the unit cell of solvates hosts a molecular compound weakly bonded to molecules of a solvent, which is found in the liquid state at

room temperature; molecular salts can be distinguished by the presence of charged acid-base couples (i.e., a complete protonic transfer has occurred usually along a HB) in the same asymmetric unit; finally, cocrystals exhibit unit cells inhabited by neutral molecules interacting *via* neutral weak interactions (i.e., usually HBs where no acid proton is transferred to basic sites). Although in principle these different classes of multicomponent molecular crystals are thus easily discriminated based on the content of their unit cell, a unanimous and unambiguous definition is still nowadays an object of controversy among experts and many adducts that place themselves at the threshold between the three described classes can be found in the literature.[58–60] What is now quite clear to crystal engineers is that the obtainment of multicomponent forms is almost always thermodynamically favored, with respect to their monocomponent counterparts: Taylor and Day demonstrated how the crystal structures of a statistical pool of cocrystals were averagely 8 kJ/mol more stable than polymorphs of their main constituent.[61]

1.5 Crystal forms applied to APIs

The crystal engineering approach has been adopted in the latest years in several fields of material sciences.[62–65] It proves a valid tool to yield improved novel crystal forms of a molecular compound, with properly tailored performances to meet specific requirements. Specifically, the pharmaceutical industry got more and more interested in achieving new multicomponent forms of drugs, with the aim of fine-tuning for instance their solubility, their thermal stability, flowability[66] and tabletability,[67] as well as organoleptic properties.[68] Many active pharmaceutical ingredients (APIs), in particular, suffer from poor aqueous dissolution rates, which hinders their bioavailability.

The design and preparation of new crystal forms of APIs involve three fundamental needs of pharmaceutical industries: first, they offer the chance of improving the scientific community's comprehension of the mechanisms behind molecular recognition, crystallization and structure-property relationship of multicomponent phases; they then respond to the ethical obligation of improving drug performances while preserving the patients' health at the same time; finally, they grant the possibility of producing new patentable and financially rewarding forms of APIs.

Some of the most pursued crystal forms of drugs are represented by pharmaceutical salts and cocrystals, and, more recently, by solid solutions.

In the first two cases, the molecule to be crystallized together with the pharmaceutical compound is usually selected among substances generally recognized as safe (GRAS) by the U.S. Food and Drug Administration (FDA), i.e., harmless for patients in the employed dosages.[69] They include many α-aminoacids (e.g., L-lysine, glycine, DL-methionine…), simple organic acids (e.g., propionic acid, succinic acid, fumaric acid, …), or even common cations/anions (e.g., Na^+, K^+, Cl^-, PO_4^{3-}, …).

Salification of APIs has been employed for years as a viable strategy for enhancing the dissolution rate of poorly soluble drugs.[70] Pharmaceutical compounds that bear ionizable moieties (i.e., acid or basic functional groups) are crystallized together with potential counterions in order to induce a protonic transfer. In that case, charge-assisted HBs are formed between the two components.

Some of the many examples of molecular salts with improved solubility and dissolution properties are represented by (*S*)-ketoprofen-trometamol;[71] a series of salts of sildenafil with dicarboxylic acids;[72] molecular salts of trimethoprim with L-aspartic and L-glutamic acid;[73] four different salt forms of meclofenamic acid with piperazine.[74]

A phenomenon similar to salification leads to the formation of pharmaceutical cocrystals: in this case, even non-ionizable molecules[75] can combine in the same adduct if HBs are able to form between the donor and acceptor groups of the API and its so-called *coformer*.

When considering poorly soluble drugs, the aim is still that of improving their dissolution rate and/or solubility, and, in this context, cocrystals have already proved their worth: such is the case for the meloxicam adducts with dicarboxylic acids,[76] as well as with aspirin;[77] the same can be said for the cocrystal series of ketoconazole, itraconazole and posaconazole with 4-aminobenzoic acid,[78] as well as for indomethacin·saccharin[79] and naringenin cocrystals with isonicotinamide, picolinic acid and betaine.[80]

As it appears, salts and cocrystals lie on the two extremes of a continuum of supramolecular entities for which the protonic transfer is more or less effective.[81–83] To try and predict the outcome of protonic transfer in the preparation of multicomponent crystals of acid-base couples, a good rule of thumb is represented by the pK_a rule: when the difference between the pK_a values is greater than 3, protonic transfer is more likely to occur, whereas for differences lower than 0, cocrystals are expected with higher probability.[84,85] A plethora of papers in the literature show how it reliably leads to the predicted outcome in most cases, despite the rule being an approximation: indeed, it considers dissociation constants of equilibria in aqueous solutions at specific temperatures.[86–89] Although, a whole region of intermediate ΔpK_a values ($0 < \Delta pK_a < 3$) exists, in which it proves quite challenging to get an *a priori* idea of the result in terms of protonic transfer.[85,90]

Regarding molecular substitutional solid solutions, they can be defined as crystalline monophasic systems in which a minority molecular component (the solute) statistically replaces the majority one (the solvent) in its crystal lattice, in a variable but controllable amount within a range of compositions, up to the solubility limit of the specific system.[91] William Hume-Rothery,

14

considered one of the most renowned experts in the field of solid solutions, prescribed that solubility in the solid state was possible only if the size, the shape and the crystal structure of the two (or more) components of the solid solution were similar.[92] This is why the preparation of solid solutions is seen by many crystal engineers as a very tough challenge to address, leading most of them to give up much early in the process. Nonetheless, solid solutions, especially in the pharmaceutical world, afford the benefit of being homogeneous crystal forms promptly adjustable in terms of stoichiometric ratios between the components.[93–97] This juxtaposes them to salts and cocrystals, in which the stoichiometry is fixed. As it appears, this specific property of solid solutions offers the chance of combining the right dosages of different drugs, usually co-administered, in novel, enhanced and patentable crystal forms.

1.6 The most common techniques for preparing supramolecular adducts

Preparing new crystal forms falls under the definition of supramolecular synthesis. Indeed, bonds, even if they are of a weak and intermolecular nature, are formed among molecules combined in the solid state. The most conventional methods for screening new crystal forms belong to two classes: mechanochemical and solution techniques.

The former group are intrinsically greener:[98,99] they consist in grinding the reagents together in agate mortars or ball mills, with no employment of solvents, if not in catalytic amounts (also said *kneading*), yielding microcrystalline powders. Indeed, mechanochemistry is not compatible with crystal growth, since it is designed to decrease particle size. The employment of solvents is then always needed to afford crystals suitable for obtaining crystal structures (see Figure 1.4).

Figure 1.4 Graphical depiction of the complementarity of solution and mechanochemical techniques in the screening for crystal forms.

Common alternatives to crystallization from mother liquor are the slow evaporation of a solution of the reagents[58] or the slurry technique, in which the starting powders are stirred together in the presence of few drops of a solvent.[100] In this last case, interesting comparative studies with solvent-drop grinding applications reveal how the slurry technique is statistically more efficient than mechanochemical methods in affording new crystalline products; besides, the adducts obtained through slurrying result purer than those derived from kneading applications.[101]

If these techniques are all quite simple to carry out, the final outcome is very much dependent on several experimental factors: the nature and the amount of the employed solvent,[102] as well as the operative temperature,[103–105] pressure[104,105] and humidity conditions,[106,107] may have drastic influence on

the success of the preparation, on its yield, and on the identity of the obtained crystal form.

This is why, for screening new crystal forms, solution and mechanochemical methods are often attempted on the same system, and several trials, in which different variables are altered, might be needed to get to the desired result.

When both of these routine screening methods fail, other more unusual approaches can be adopted. Some of these include procedures involving the co-melting of the reagents,[108] which is often incompatible with organic molecules such as APIs; the cosublimation of the starting materials onto a cold finger apparatus;[109] the diffusion of antisolvent vapors to induce precipitation;[110] rapid evaporation of mother liquors, especially used to entrap kinetic phases;[111] spray drying.[112]

Of course, from a sustainability point-of-view, the mechanochemical approach is preferable; although its scale-up still proves quite challenging and, despite a growing number of studies in the field, it remains to this day strongly affected by a trial-and-error character, which needs to be addressed by researchers in the near future.[113]

References

1   D. Braga; F. Grepioni; L. Maini; M. Polito, *Struct. Bonding* **2009**, *132*, 25–50.

2   S. Datta; D. J. W. Grant, *Nat. Rev. Drug Discovery* **2004**, *3*, 42–57.

3   K. Gholivand; A. A. E. Valmoozi; M. R. Dashtaki; F. Mohamadpanah; M. Dusek; V. Eigner; M. Pooyan; M. Bonsaii; M. Sharifi; M. Ghadamyari, *ChemistrySelect*, **2017**, *2*, 8828–8840.

4   S. Bordignon; P. Cerreia Vioglio; E. Priola; D. Voinovich; R. Gobetto; Y. Nishiyama; M. R. Chierotti, *Cryst. Growth Des.* **2017**, *17*, 5744–5752.

5   J. Lu; S. Rohani, *Org. Process Res. Dev.* **2009**, *13*, 1269–1275.

6   L. Wang; S. Liu; Z. Gao, *Pharmazie* **2020**, *75*, 483–487.

7   D. Braga; L. Maini; G. de Sanctis; K. Rubini; F. Grepioni; M. R. Chierotti; R. Gobetto, *Chem. Eur. J.* **2003**, *9*, 5538–5548.

8   M. Baldrighi; G. Cavallo; M. R. Chierotti; R. Gobetto; P. Metrangolo; T. Pilati; G. Resnati; G. Terraneo, *Mol. Pharmaceutics* **2013**, *10*, 1760–1772.

9   A. Shahi; E. Arunan, *J. Chem. Sci.* **2016**, *128*, 1571–1577.

10 E. J. Corey, *Pure Appl. Chem.* **1967**, *14*, 19–38.

11 G. R. Desiraju, *Angew. Chem. Int. Ed.* **1995**, *34*, 2311–2327.

12 G. R. Desiraju; J. J. Vittal; A. Ramanan, *Crystal Engineering: A Textbook*, World Scientific, Singapore, **2011**.

13 G. R. Desiraju, *J. Am. Chem. Soc.* **2013**, *135*, 9952–9967.

14 A. I. Kitajgorodskij, *Acta Cryst.* **1965**, *18*, 585–590.

15 G. R. Desiraju; T. Steiner, *The Weak Hydrogen Bond*, Oxford University Press, New York, **1999**.

16 E. Arunan; G. R. Desiraju; R. A. Klein; J. Sadlej; S. Scheiner; I. Alkorta; D. C. Clary; R. H. Crabtree; J. J. Dannenberg; P. Hobza; H. G. Kjaergaard; A. C. Legon; B. Mennucci; D. J. Nesbitt, *Pure Appl. Chem.* **2011**, *83*, 1637–1641.

17 M. Woińska; S. Grabowsky; P. M. Dominiak; K. Woźniak; D. Jayatilaka, *Sci. Adv.* **2016**, *2*, e1600192

18 T. Fornaro; D. Burini; M. Biczysko; V. Barone, *J. Phys. Chem. A* **2015**, *119*, 4224–4236.

19 R. Gobetto; C. Nervi; M. R. Chierotti; D. Braga; L. Maini; F. Grepioni; R. K. Harris; P. Hodgkinson, *Chem. Eur. J.* **2005**, *11*, 7461–7471.

20 P. Cerreia Vioglio; M. R. Chierotti; R. Gobetto, *Adv. Drug Delivery Rev.* **2017**, *117*, 86–110.

21 F. Bravetti; S. Bordignon; E. Alig; D. Eisenbeil; L. Fink; C. Nervi; R. Gobetto; M. U. Schmidt; M. R. Chierotti, *Chem. Eur. J.* **2022**, *28*, e202103589

22   N. Qiao; M. Li; W. Schlindwein, N. Malek; A. Davies; G. Trappitt, *Int. J. Pharm.* **2011**, *419*, 1–11.

23   A. Mukherjee, *Cryst. Growth Des.* **2015**, *15*, 3076–3085.

24   T. Beyer; T. Lewis; S. L. Price, *CrystEngComm* **2001**, *44*, 1–35.

25   S. L. Price, *Adv. Drug Delivery Rev.* **2004**, *56*, 301–319.

26   D. H. Bowskill; I. J. Sugden; S. Kostantinopoulos; C. S. Adjiman; C. C. Pantelides, *Annu. Rev. Chem. Biomol. Eng.* **2021**, *12*, 593–623.

27   G. M. Day, *Crystallogr. Rev.* **2011**, *17*, 3–52.

28   T. Pawlak; I. Sudgen; G. Bujacz; D. Iuga; S. P. Brown; M. J. Potrzebowski, *Cryst. Growth Des.* **2021**, *21*, 3328–3343.

29   R. Mathew; K. A. Uchman; L. Gkoura; C. J. Pickard; M. Baias, *Magn. Reson. Chem.* **2020**, *58*, 1018–1025.

30   R. M. Bhardwaj; L. S. Price; S. L. Price; S. M. Reutzel-Edens; G. J. Miller; I. D. H. Oswald; B. F. Johnston; A. J. Florence, *Cryst. Growth Des.* **2013**, *13*, 1602–1617.

31   S. M. Reutzel-Edens; R. M. Bhardwaj, *IUCrJ* **2020**, *7*, 955–964.

32   A. F. Shunnar; B. Dhokale; D. P. Karothu; D. H. Bowskill; I. J. Sugden; H. H. Hernandez; P. Naumov; S. Mohamed, *Chem. Eur. J.* **2020**, *26*, 4752 –4765.

33   M. Kaltenegger; L. Delaive; S. M. Gali; P. Brocorens; O. Werzer; H. Riegler; Y. H. Geerts; R. Lazzaroni; R. Resel; J. Liu, *Cryst. Growth Des.* **2022**, *22*, 1548–1553.

34   E. H. Lee, *Asian J. Pharm. Sci.* **2014**, *9*, 163–175.

35   P. Lang; V. Kiss; R. Ambrus; G. Farkas; P. Szabó-Révész; Z. Aigner; E. Várkonyi, *J. Pharm. Biomed. Anal.* **2013**, *84*, 177–183.

36   M. Otsuka; T. Ofusa; Y. Matsuda, *Drug Dev. Ind. Pharm.* **1999**, *25*, 197–203.

37   C. Gu; V. Young Jr.; D. J. W. Grant, *J. Pharm. Sci.* **2001**, *90*, 1878–1890.

38   S. Mohamed; S. A. Barnett; D. A. Tocher; S. L. Price; K. Shankland; C. K. Leech, *CrystEngComm* **2008**, *10*, 399–404.

39   N. Madusanka; M. D. Eddleston; M. Arhangelskis; W. Jones, *Acta Cryst.* **2014**, *B70*, 72–80.

40   M. Karashima; K. Kimoto; T. Kojima; Y. Ikeda, *J. Cryst. Growth* **2014**, *390*, 30–37.

41   H. H. Shi; F. Li; X. Huang; T. Wang; Y. Bao; Q. X. Yin; C. Xie; H. X. Hao, *Ind. Eng. Chem. Res.* **2020**, *59*, 6102–6111.

42   F. D. Chattaway, *Sci. Prog.* **1917**, *11*, 545–559.

43   W. C. McCrone; A. Weissberger; M. M. Labes; D. Fox, *Physics and Chemistry of the Organic Solid State,* Wiley, New York, **1965**.

44   J. Nyman; G. M. Day, *CrystEngComm* **2015**, *17*, 5154–5165.

45 S. L. Childs; L. J. Chyall; J. T. Dunlap; V. N. Smolenskaya; B. C. Stahly; G. P. Stahly, *J. Am. Chem. Soc.* **2004**, *126*, 13335–13342.

46 F. T. Martins; N. Paparidis; A. C. Doriguetto; J. Ellena, *Cryst. Growth Des.* **2009**, *9*, 5283–5292.

47 A. J. Cruz-Cabeza; S. Karki; L. Fabian; T. Friscic; G. M. Day; W. Jones, *Chem. Commun.* **2010**, *46*, 2224–2226.

48 S. Jin; J. Guo; L. Liu; D. Wang, *J. Mol. Struct.* **2011**, *1004*, 227–236.

49 H. D. Clarke; M. B. Hickey; B. Moulton; J. A. Perman; M. L. Peterson; L. Wojtas; O. Almarsson; M. J. Zaworotko, *Cryst. Growth Des.* **2012**, *12*, 4194–4201.

50 F. Grifasi; M. R. Chierotti; K. Gaglioti; R. Gobetto; L. Maini; D. Braga; E. Dichiarante; M. Curzi, *Cryst. Growth Des.* **2015**, *15*, 1939–1948.

51 S. Domingos; A. Fernandes; M. T. Duarte; M. F. M. Piedade, *Cryst. Growth Des.* **2016**, *16*, 1879–1892.

52 A. Czapik; M. Jelecki; M. Kwit, *Int. J. Mol. Sci.* **2019**, *20*, 5004–5019

53 B. Bhattacharya; S. Das; G. Lal; S. R. Soni; A. Ghosh; C. M. Reddy; S. Ghosh, *J. Mol. Struct.* **2020**, *1199*, 127028.

54 D. Wu; B. Zhang; Q. Yao; B. Hou; L. Zhou; C. Xie; J. Gong; H. X. Hao; W. Chen, *Cryst. Growth Des.* **2021**, *21*, 4531–4546.

55 J. Wang; Q. Yu; W. Dai; X. Mei, *Chem. Commun.* **2016**, *52*, 3572–3575.

56 F. Rossi; P. Cerreia Vioglio; S. Bordignon; V. Giorgio; C. Nervi; E. Priola; R. Gobetto; K. Yazawa; M. R. Chierotti, *Cryst. Growth Des.* **2018**, *18*, 2225–2233.

57 O. D. Putra; H. Uekusa, *Advances in Organic Crystal Chemistry – Comprehensive Reviews 2020,* Springer Nature, Singapore, **2020**.

58 S. Aitipamula; R. Banerjee; A. K. Bansal; K. Biradha; M. L. Cheney; A. R. Choudhury; G. R. Desiraju; A. G. Dikundwar; R. Dubey; N. Duggirala *et al., Cryst. Growth Des.* **2012**, *12*, 2147–2152.

59 E. Grothe; H. Meekes; E. Vlieg; J. H. ter Horst; R. de Gelder, *Cryst. Growth Des.* **2016**, *16*, 3237–3243.

60 M. Gryl; M. Koziel; K. M. Stadnicka, *Acta Cryst.* **2019**, *B75*, 53–58.

61 C. R. Taylor; G. M. Day, *Cryst. Growth Des.* **2018**, *18*, 892–904.

62 E. Nauha; E. Kolehmainen; M. Nissinen, *CrystEngComm* **2011**, *13*, 6531–6537.

63 K. B. Landenberger; O. Bolton; A. J. Matzger, *Angew. Chem. Int. Ed.* **2013**, *52*, 6468–6471.

64 S. K. Park; S. Varghes; J. H. Kim; S. Yoon; O. K. Kwon; B. An; J. Gierschner; S. Y. Park, *J. Am. Chem. Soc.* **2013**, *135*, 4757–4764.

65 W. Yu; X. Wang; J. Li; Z. Li; Y. Yan; W. Wang; J. Pei, *Chem. Commun.* **2013**, *49*, 54–56.

66 C. Chen; S. Ghosh; C. Malla Reddy; M. J. Buehler, *Phys. Chem. Chem. Phys.* **2014**, *16*, 13165–13171.

67 M. K. C. Mannava; A. Gunnam; A. Lodagekar; N. R. Shastri; A. K. Nangia; K. A. Solomon, *CrystEngComm* **2021**, *23*, 227–237.

68 S. Liu; C. Wang; H. Chen; C. C. Sun, *Cryst. Growth Des.* **2021**, *21*, 1077–1085.

69 A. Roberts; L. A. Haighton, *Regul. Toxicol. Pharmacol.* **2016**, *79*, S124–S128.

70 A. T. M. Serajuddin, *Adv. Drug Delivery Rev.* **2007**, *59*, 603–616.

71 J. S. Walczak, *Pain Manage.* **2011**, *1*, 409–416.

72 P. Sanphui; S. Tothadi; S. Ganguly; G. R. Desiraju, *Mol. Pharmaceutics* **2013**, *10*, 46874697.

73 A. ElShaer; P. Hanson; T. Worthington; P. Lambert; A. R. Mohammed, *Pharmaceutics* **2012**, *4*, 179–196.

74 P. Sanphui; G. Bolla; A. Nangia, *Cryst. Growth Des.* **2012**, *12*, 2023–2036.

75 S.G. Fleischman; S. S. Kuduva; J. A. McMahon; B. Moulton; R. D. B. Walsh; N. Rodriguez-Hornedo; M. J. Zaworotko, *Cryst. Growth Des.* **2003**, 3, 909–919.

76 M. L. Cheney; D. R. Weyna; N. Shan; M. Hanna; L. Wojtas; M. J. Zaworotko, *Cryst. Growth Des.* **2010**, *10*, 4401–4413.

77 M. L. Cheney; D. R. Weyna; N. Shan; M. Hanna; L. Wojtas; M. J. Zaworotko, *J. Pharm. Sci.* **2011**, *6*, 2172–2181.

78 M. Kataoka; K. Minami; T. Takagi; G. E. Amidon; S. Yamashita, *Mol. Pharmaceutics* **2021**, *18*, 4122–4130.

79 S. Basavoju; D. Bostrom; S. P. Velaga, *Pharm. Res.* **2008**, *25*, 530–541.

80 C. Luo; W. Liang; X. Chen; J. Wang; Z. Deng; H. Zhang, *CrystEngComm* **2018**, *20*, 3025–3033.

81 V. R. Hathwar; R. Pal; T. N. Guru Row, *Cryst. Growth Des.* **2010**, *10*, 3306–3310.

82 C. L. Jones; J. M. Skelton; S. C. Parker; P. R. Raithby; A. Walsh; C. C. Wilson; L. H. Thomas, *CrystEngComm* **2019**, *21*, 1626–1634.

83 S. L. Childs; G. P. Stahly; A. Park, *Mol. Pharmaceutics* **2007**, *4*, 323–338.

84 M. K. Corpinot; D. K. Bucar, *Cryst. Growth Des.* **2019**, *19*, 1426–1453.

85 A. J. Cruz-Cabeza, *CrystEngComm* **2012**, *14*, 6362–6365.

86 L. F. Diniz; M. S. Souza; P. S. Carvalho Jr.; C. C. P. da Silva; R. F. D'Vries; J. Ellena, *J. Mol. Struct.* **2018**, *1153*, 58–68.

87 P. Gilli; L. Pretto; V. Bertolasi; G. Gilli, *Acc. Chem. Res.* **2009**, *42*, 33–44.

88   J. D. Loya; S. J. Li; D. K. Unruh; K. M. Hutchins, *Supramol. Chem.* **2019**, *31*, 558–564.

89   G. L. Denisov; Y. V. Nelyubina, *Crystals* **2022**, *12*, 497–515.

90   A. J. Cruz-Cabeza; M. Lusi; H. P. Wheatcroft; A. D. Bond, *Faraday Discuss.* **2022** *Advance Article.*

91   K. S. Sharma; J. Sahoo; S. Agrawal; A. Kumari, *J. Anal. Pharm. Res* **2019**, *8*, 127–133.

92   W. Hume-Rothery, *The Structure of Metals and Alloys*, Institute of Metals, London, **1936**.

93   J. de Castro Fonseca; J. C. T. Clavijo; N. Alvarez; J. Ellena; A. P. Ayala, *Cryst. Growth Des.* **2018**, *18*, 3441–3448.

94   S. Cherukuvada; A. Nangia, *Chem. Commun.* **2014**, *50*, 906–923.

95   A. Delori; P. Maclure; R. M. Bhardwaj; A. Johnston; A. J. Florence; O. B. Sutcliffe; I. D. H. Oswald, *CrystEngComm.* **2014**, *16*, 5827–5831.

96   E. Schur; E. Nauha; M. Lusi; J. Bernstein, *Chem. Eur. J.* **2015**, *21*, 1735–1742.

97   M. Lestari; M. Lusi, *Chem. Commun.* **2019**, *55*, 2297–2300.

98   S. L. James; C. J. Adams; C. Bolm, D. Braga; P. Collier; T. Friscic; F. Grepioni *et al.*, *Chem. Soc. Rev.* **2012**, *41*, 413–447.

99   D. R. Weyna; T. Shattock; P. Vishweshwar; M. J. Zaworotko, *Cryst. Growth Des.* **2009**, *9*, 1106–1123.

100   D. K. Bučar; R. F. Henry; X. Lou; R. W. Duerst; L. R. MacGillivray; G. G. Z. Zhang, *Cryst. Growth Des.* **2009**, *9*, 1932–1943.

101   M. M. Haskins; M. J. Zaworotko, *Cryst. Growth Des.* **2021**, *21*, 4141–4150.

102   M. Arhangelskis; D. K. Bučar; S. Bordignon; M. R. Chierotti; S. A. Stratford; D. Voinovich; W. Jones; D. Hasa, *Chem Sci* **2021**, *12*, 3264–3269.

103   L. A. Stevens; K. P. Goetz; A. Fonari; Y. Shu; R. M. Williamson; J. L. Brédas; V. Coropceanu; O. D. Jurchescu; G. E. Collis, *Chem. Mater.* **2015**, *27*, 112–118.

104   L. E. Budd; R. M. Ibberson; W. G. Marshall; S. Parsons, *Chem. Cent. J.* **2015**, *9*, 18.

105   R. Chinnasamy; B. Munjal; R. Suryanarayanan; A. M. P. Peedikakkal; M. K. Mishra; S. Ghosh, *Cryst. Growth Des.* **2022**, *22*, 615–624.

106   D. J. Lee; S. Lee; I. W. Kim, *Int. J. Mol. Sci.* **2012**, *13*, 10296–10304.

107   R. V. Manek; W. M. Kolling, *AAPS PharmSciTech* **2004**, *5*, 14.

108   Y. Yan; J. Chen; T. Lu, *CrystEngComm* **2015**, *17*, 612–620.

109   M. D. Eddleston; S. Sivachelvam; W. Jones, *CrystEngComm* **2013**, *15*, 175–181.

110   C. B. Aakeröy; A. B. Grommet; J. Desper, *Pharmaceutics* **2011**, *3*, 601–614.

22

111   A. U. Chowdhury; C. M. Dettmar; S. Z. Sullivan; S. Zhang; K. T. Jacobs; D. J. Kissick; T. Maltais; H. G. Hedderich; P. A. Bishop; G. J. Simpson, *J. Am. Chem. Soc.* **2014**, *136*, 2404–2412.

112   V. Sladkova; J. Cibulkova; V. Eigner; A. Sturc; B. Kratochvil; J. Rohlicek, *Cryst. Growth Des.* **2014**, *14*, 2931–2936.

113   C. B. Aakeröy, *Acta Cryst.* **2015**, *B71*, 387–391.

Chapter 2

The role of the hydration state and stoichiometry of starting materials for the methyl gallate/L-proline system

2.1 Introduction

When it comes to crystal engineering,[1] a well-established definition is the understanding of intermolecular interactions in the context of crystal packing and the exploitation of such a comprehension in the rational design of novel crystalline materials, characterized by desired physicochemical properties, such as hygroscopicity,[2] optical properties,[3] tabletability,[4] dissolution rate,[5–7] or melting point.[8] Among the many possible strategies, cocrystallization represents a valid approach to pursue the aims of crystal engineering.[9] Cocrystals are defined as homogenous crystalline phases described by asymmetric units containing at least two different chemical entities, usually ones that are solid at room temperature.[10] The components are linked by means of weak interactions, like hydrogen bonds (HBs), halogen bonds, and π-stacking forces.[11,12]

Especially in the case of APIs (Active Pharmaceutical Ingredients), the selection step of the coformers (molecules that cocrystallize with the main component), is pivotal in the designing process of cocrystals. Indeed, these need to be harmless to patients and capable of forming stable supramolecular synthons with the API. GRAS molecules (generally recognized as safe by the U.S. FDA) are thus usually employed as coformers. Among these, α-amino acids have been extensively exploited to produce molecular salts of APIs, as well as some cocrystals.[18] This is mainly due to their non-toxicity, ready availability, affordability and to their zwitterionic nature at a physiological pH, which provides salt-like dissolution properties to cocrystals. GRAS substances

are already included in a variety of developed and marketed pharmaceutical salts.[19] The efforts to obtain new crystal forms are justified by several implications on many aspects. For example, cocrystallization allows for a better understanding of molecular recognition mechanisms and weak interactions,[13,14] besides structure-property relations;[11] it can lead to the improvement of drug performances with the advantage of minor side effects;[15,16] it implies the chance of patenting the new crystal forms.[17] Though salification has long been adopted as a strategy to improve the dissolution properties of poorly soluble drugs, cocrystallization serves as a valid alternative. Moreover, it can be applied to APIs that do not display any ionizable site, and it offers a wider range of coformers with respect to the available counterions for salts. L-proline (Pro) (Scheme 2.1, left), in particular, represents an ideal candidate for cocrystallization: it is characterized by a high water solubility and it exhibits a rigid five-membered ring in its molecular structure, which can aid the intermolecular assembly from an entropic point of view. A survey performed on the CSD (Cambridge Structural Database) gives 117 hits for crystal structures containing Pro. In each of them, Pro exhibits a zwitterionic character. Out of the 117 structures, less than 20 are pharmaceutical cocrystals involving Pro. Some examples are represented by cocrystals between Pro and celecoxib,[20] niflumic acid, clonixin and diclofenac,[21] and naproxen.[22]

The supramolecular synthons that are most frequently established by Pro consist in charge-assisted HBs between the carboxylate and the ammonium moieties of Pro, or between either of them and a carboxylic group of a different molecule (e.g., naproxen,[14] fumaric acid[23]). Both moieties tend to form interactions with OH groups from alcohols (e.g., dapagliflozin)[24] or phenols (e.g., ezetimibe,[25] quercetin[26]), while the COO^- group is prone to engage in dimeric interactions with molecules exhibiting two proximal NH (e.g., ureas)[27] or OH (e.g., boronic acids)[27] groups.
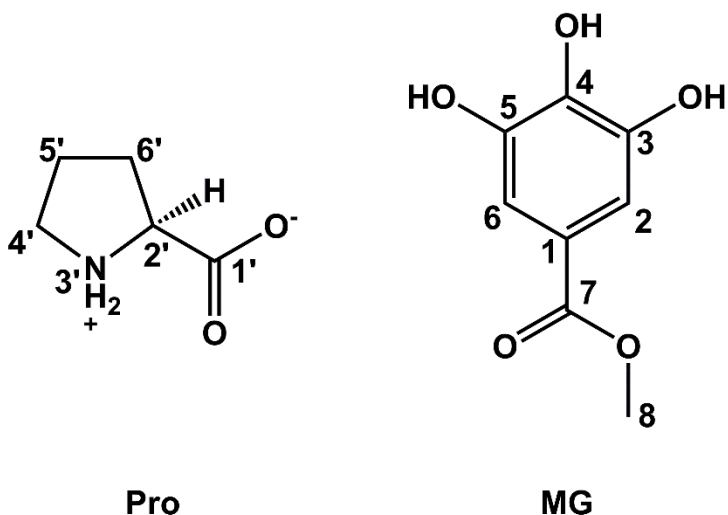
Scheme 2.1 Chemical structures of Pro (left) and MG (right), with atom numbering.

In this chapter, methyl gallate (MG, Scheme 2.1, right) was made the focal point. MG naturally exists in several plants, such as *Toona sinensis*, *Sapium sabiferum*, *Acer barbinerve*; it is commonly employed in traditional oriental medicine for the treatment of pathogenic bacteria.[28] MG shows fairly good antibacterial and anti-inflammatory activity,[28] and it is currently under study as a promising anti-tumor agent.[29,30] Although, since it is not included in either the European or the US Pharmacopoeias, MG cannot be officially considered as an API. Nonetheless, MG was chosen as a model molecule, due to it displaying several HB donors and acceptors which are promising in the establishment of supramolecular synthons with Pro. An extensive search in crystal structure databases and in literature indicates that a single polymorph of MG is known as of today, with a monoclinic lattice and $P2_1/n$ space group.[31]

The main objective of the work presented in this chapter was to explore the possibility of selectively driving the cocrystallization of MG and Pro towards phases with different hydration states, solely by changing that

of starting material Pro. Indeed, an anhydrous (MG·Pro$_2$) and a hemihydrate (MG$_2$·Pro$_2$·H$_2$O) cocrystal of MG were successfully achieved by employing Pro as a coformer in its anhydrous and monohydrated (Pro·H$_2$O) forms, respectively. Interestingly enough, MG·Pro$_2$ was obtained only when starting from anhydrous Pro, even if water is present during the synthesis. On the contrary, the hemihydrate could be obtained either starting with Pro·H$_2$O or with anhydrous Pro, but in this last case this was possible only when the correct stoichiometry was matched.

The novel cocrystals (MG·Pro$_2$ and MG$_2$·Pro$_2$·H$_2$O) were achieved by means of mechanochemical methods; they were thoroughly characterized by single crystal X-ray diffraction (SCXRD), powder X-ray diffraction (PXRD), solid-state Nuclear Magnetic Resonance (SSNMR), Hirshfeld surface analysis and infrared spectroscopy. Complementary to structural data, calorimetric analyses, namely differential scanning calorimetry (DSC) and thermogravimetric analysis (TGA), were carried out to elucidate the change in the performances of the cocrystals. Lastly, further evidence from energy framework analysis allowed rationalizing the peculiar behavior of the investigated system concerning the water uptake.

2.2 Materials and methods

Pro, MG and 99% ethanol were purchased from Sigma-Aldrich and used without further purification. Pro·H$_2$O was obtained by slurrying Pro in distilled water for about six hours.

2.2.1 Synthesis procedures of cocrystals

MG$_2$·Pro$_2$·H$_2$O: A white microcrystalline powder was obtained by manually grinding MG (200 mg; 1.1 mmol) with Pro·H$_2$O (145 mg; 1.1 mmol) for 30 min in equimolar stoichiometry. The hydrate form was also obtained

by kneading MG (200 mg; 1.1 mmol) with Pro (125 mg; 1.1 mmol) in water for 30 min or by kneading MG·Pro$_2$ (228 mg; 0.55 mmol) with MG (100 mg; 0.55 mmol) in water for 30 min. Crystals suitable for SCXRD were obtained by slow evaporation of a (1:1) solution of MG and Pro·H$_2$O in 99% ethanol.

MG·Pro$_2$: A white microcrystalline powder was obtained by manually grinding MG (200 mg; 1.1 mmol) with Pro (250 mg; 2.2 mmol) for 60 min. The anhydrous form was also obtained by kneading MG (200 mg; 1.1 mmol) with Pro (250 mg; 2.2 mmol) in water for 30 min. Crystals suitable for SCXRD were obtained by seeding of the cocrystal in 99% ethanol.

2.2.2 Single crystal and powder X-ray diffraction

The single-crystal data were collected with a Gemini R Ultra diffractometer with graphite-monochromated Mo Kα radiation ($\lambda = 0.71073$ Å) by the ω-scan method. The cell parameters were retrieved with the CrysAlisPro software, and the same program was used to perform data reduction with corrections for Lorenz and polarizing effects. Scaling and absorption corrections were applied through the CrysAlisPro[32] multiscan technique. The structures of MG$_2$·Pro$_2$·H$_2$O and MG·Pro$_2$ were solved with direct methods by using SHELXS-97[33] and refined with full-matrix least-squares techniques on F^2 with SHELXL-97. All non-hydrogen atoms were refined anisotropically. Hydrogen atoms were calculated, riding on the corresponding bonded atoms. Crystal data and refinement results can be found in Table 2.1. Bond lengths, angles and HB distances are reported in Tables A1.1-A1.4 together with the X-ray atom numeration (Figures A1.1 and A1.2) in Appendix I. The underlying net derived by simplification from the crystal structure was analyzed and represented with ToposPro, Version 5.1.0.9[34] by considering the HBs between different fragments as the defining interactions.[35] The graphics of the crystal structure were generated using Mercury 3.9.[36] A check with the Platoon algorithm[37] and the PSEUDO

program[38] in the Bilbao Crystallographic Database for pseudosymmetry confirmed the exactness of the $P1$ space group for $MG_2 \cdot Pro_2 \cdot H_2O$ with the absence of hidden symmetry elements and defects in the resulting structure, often present for this specific space group.[39] Both $MG \cdot Pro_2$ and $MG_2 \cdot Pro_2 \cdot H_2O$ present a high number of molecular entities in the asymmetric unit (3 and 5, respectively), although Z' equals 1 for both the crystal structures. By looking at this peculiarity of our cocrystals, the Z' distribution of the reported Pro cocrystals in the CSD was analyzed. The Z' parameter was focused on because it correlates with the number of molecules in the asymmetric unit and is automatically calculated and reported in the database. High Z' structures are in general quite uncommon ($< \sim 10\%$),[40] although the tendency of non-centrosymmetric space groups to show high Z' is more pronounced.[41] From the analysis of the 117 purely organic Pro-containing crystals present in the CSD, it is possible to observe a propension for Z' $\geq$ 2 ($\sim 20\%$) (Figure A1.3 in Appendix I). CCDC CODES 2085041 and 2085042 contain the supplementary crystallographic data for $MG_2 \cdot Pro_2 \cdot H_2O$ and $MG \cdot Pro_2$, respectively. These data can be obtained free of charge *via* http://www.ccdc.cam.ac.uk/conts/retrieving.html, or from the Cambridge Crystallographic Data Centre, 12 Union Road, Cambridge CB2 1EZ, UK; fax: (+44) 1223-336-033; or e-mail: deposit@ccdc.cam.ac.uk.

Powder diffractograms were obtained on a Philips X'Pert PW3020 Bragg-Brentano instrument, equipped with a Cu Kα X-ray source (λ = 1.54506 Å), operating at 40 kV and 20 mA. Measurements were carried out in $\theta/2\theta$ mode, with a scanning range of 3–50° for 2θ.

Table 2.1 Crystallographic data of MG$_2$·Pro$_2$·H$_2$O and MG·Pro$_2$.

	MG$_2$·Pro$_2$·H$_2$O	MG·Pro$_2$
Chemical formula	2(C$_8$H$_8$O$_5$)·2(C$_5$H$_9$NO$_2$)·H$_2$O	C$_8$H$_8$O$_5$·2(C$_5$H$_9$NO$_2$)
M$_r$	616.57	414.41
Wavelength	0.71073 Å	0.71073 Å
Temperature	298,00	298,00
Crystal system, space group	Triclinic, *P*1	Orthorhombic, *P*2$_1$2$_1$2$_1$
a, b, c (**Å**)	6.8784 (3), 10.2802 (5), 10.9541 (6)	10.0509 (11), 10.3000 (12), 18.942 (3)
α, β, γ (°)	78.452 (5), 81.487 (4), 72.448 (4)	90, 90, 90
V (**Å³**)	720.37 (6)	1960.9 (4)
Z, Z′	1, 1	4, 1
μ (**mm^{-1}**)	0.12	0.11
Crystal size (mm)	0.42 × 0.30 × 0.28	0.63 × 0.41 × 0.23
No. of measured, independent and observed reflections and number of parameters	17425, 9373, 6997, 404	10265, 3360, 2760, 294
R$_1$, wR$_2$ Goof	0.056, 0.154, 1.03	0.039, 0.094, 1.03
Δρ$_{max}$, Δρ$_{min}$ (e Å^{-3})	0.46, −0.23	0.16, −0.19
Absolute structure parameter	−0.2 (7)	0.0 (10)

2.2.3 IR spectroscopy

IR-ATR spectra were collected on a Fourier transform Equinox 55 (Bruker) spectrophotometer equipped with an ATR device; resolution was set at 2 cm^{-1} for all spectra. A spectral range of 400–4000 cm^{-1} was scanned, using a KBr beam splitter. IR-ATR spectra were processed with Bruker's OPUS Version 7.0 software. The IR technique was exclusively used to monitor the formation of the cocrystals during the screening; the relative spectra are reported in Figures A1.4 and A1.5 in Appendix I.

2.2.4 Solid-state NMR experiments

SSNMR spectra were collected on a Bruker Avance II 400 Ultra Shield instrument, working at 400.23, 100.63 and 40.56 MHz for ^{1}H, ^{13}C, and ^{15}N, respectively. For the ^{13}C and ^{15}N experiments, samples were packed in cylindrical zirconia rotors (4 mm o.d.), with a sample volume of 80 µL. [13]C and ^{15}N spectra were acquired at room temperature with a rotation frequency of 12 kHz and 9 kHz, respectively. A ramp CP pulse sequence was used with a [1]H 90° pulse of 3.80 µs. The two-pulse phase modulation (TPPM) decoupling scheme[42] was used for both nuclei, with a frequency field of 66 and 62 kHz for ^{13}C and ^{15}N, respectively. Detailed acquisition parameters are reported in Table A1.5 in Appendix I.

[13]C and ^{15}N chemical shift scales were referenced to glycine (^{13}C methylene signal at 43.5 ppm and ^{15}N signal at 33.4 ppm with respect to NH_3) used as external standard.

2.2.5 Hirshfeld surface and energy framework analyses

The Hirshfeld surface analysis and the energy framework calculation were performed by using the CrystalExplorer17 program.[43] The so called CE-HF(3-21G) method, as implemented in CrystalExplorer17 program, was used to calculate pairwise interaction energies. This method, although less accurate than the CE-B3LYP (based on DFT methods) was proven to be faster in presence of a large number of pairwise interactions, correct for a qualitative comparison between similar patterns (especially when dispersive forces are not the principal component) and only fairly worse than the second one.[44]

2.2.6 Thermal analyses

DSC curves were collected on a DSC Q200 TA Instrument. Samples were accurately weighted (5–10 mg) and put into sealed aluminium pans. Calibration for temperature and heat flow was performed using a high purity
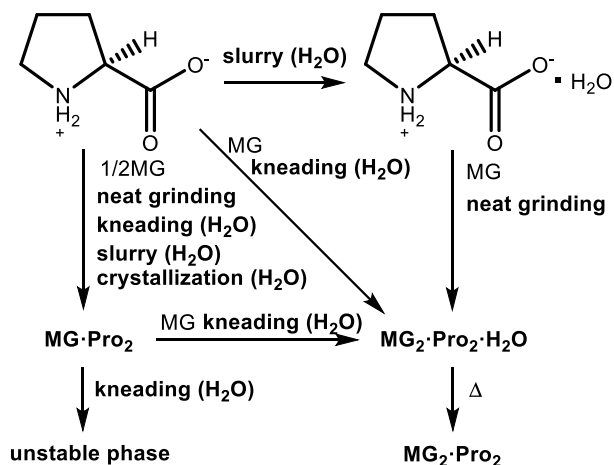
standard of indium. All measurements were performed in a 40–350 °C temperature range, with heating/cooling rates of 10 °C·min^{-1}.

TGA measurements were performed over a temperature range of 40–400 °C under 50 mL·min^{-1} N$_2$ flow, on a Q600 SDT TA instrument equipped with a DSC heat flow analyzer. Samples (5–10 mg of weight) were placed into the furnace inside alumina crucibles and heated with a ramp of 10 °C·min^{-1}.

2.3 Results and discussion

MG exhibits several HB acceptor moieties, i.e., a carboxylic and three phenolic OH groups, while Pro displays an NH$_2$$^+$ group that behaves as a HB donor. The NH$_{pyrrolidine}$···OOC heterosynthon seems likely to be favoured in the formation of a HB interaction; however, only 6 hits are found if this synthon is searched on the CSD. The same can be said for the NH$_{pyrrolidine}$···OH synthon, which returns just 2 hits on the CSD. Nonetheless, two novel crystal forms of MG were obtained using Pro as a coformer: a 2:2 MG-Pro hemihydrate cocrystal (MG$_2$·Pro$_2$·H$_2$O) and a 1:2 MG-Pro anhydrous cocrystal (MG·Pro$_2$). The results of mechanochemical experiments involving Pro and MG are represented in Scheme 2.2, while Table A1.6 in Appendix I reports all of the synthetic trials and the respective outcomes. Interestingly, MG$_2$·Pro$_2$·H$_2$O is obtained either by starting with Pro·H$_2$O in any synthetic condition (presence or absence of water and different stoichiometries) or by using Pro, but only in the presence of H$_2$O during the synthesis and provided that the correct MG:Pro 1:1 stoichiometry is matched. On the other hand, MG·Pro$_2$ is obtained only when starting from anhydrous Pro regardless of the stoichiometry and of the method of preparation. To the best of our knowledge, a similar behaviour was reported only for theophylline with citric acid,[45] in which the presence of water in one or both the starting materials led to the

32

corresponding hydrate cocrystal and *vice versa*. Thus, we took an interest in deepening our comprehension of the phenomenon and testing different approaches for introducing/removing water molecules into the MG-Pro system. No conversion between the two cocrystals was observed in any experimental condition (slurry, kneading…), probably also due to the different stoichiometry. Indeed, adding MG to MG·Pro$_2$, in order to reach the correct stoichiometry, and kneading them with water led to the formation of MG$_2$·Pro$_2$·H$_2$O. Several other techniques, such as crystallization in water, slurry in water, etc., were tested in order to obtain MG$_2$·Pro$_2$·H$_2$O, but to no success. Kneading MG·Pro$_2$ with drops of water provided a new unstable phase, which was characterized only by ATR-IR (Figure A1.6 in Appendix I), as it promptly converted back to the anhydrous cocrystal. The ATR-IR data, although clearly different, show similar features to those of MG$_2$·Pro$_2$·H$_2$O, which points to identifying the powder as a hydrated MG·Pro$_2$ unstable phase (perhaps MG·Pro$_2$·nH$_2$O). Heating MG$_2$·Pro$_2$·H$_2$O (120 °C for 24 h) led to a new stable anhydrous form, MG$_2$·Pro$_2$, which did not revert to the hydrated cocrystal for weeks if it was kept under ambient conditions.

Scheme 2.2 Cocrystal syntheses involving Pro or Pro·H$_2$O with MG and the respective outcomes.

A thorough solid-state characterization of $MG_2 \cdot Pro_2 \cdot H_2O$, $MG \cdot Pro_2$, and $MG_2 \cdot Pro_2$ including PXRD, ^{13}C and ^{15}N CPMAS SSNMR, and infrared (IR) spectroscopy (Figure A1.6 in Appendix I), was carried out, in order to detect whether cocrystallization occurred and to elucidate the local HB network.

PXRD (see Figure A1.7 in Appendix I), and ^{13}C and ^{15}N CPMAS NMR analyses (see Figures 2.1 and 2.2, respectively) were used to assess the formation of a new crystalline phase. Full (^{13}C and ^{15}N) SSNMR assignments for $MG_2 \cdot Pro_2 \cdot H_2O$ and $MG \cdot Pro_2$ are reported in Table 2.2. For both phases, crystallization from ethanol solutions afforded single crystals of good quality for X-ray crystallography. The agreement between the powder patterns calculated from the structures and the experimental ones proved the crystals to be representative of the bulk materials (see Figure A1.8 in Appendix I). As per $MG_2 \cdot Pro_2$, all data confirm that this is indeed a new crystal form of the MG-Pro system. SSNMR was able to confirm that it contains two independent molecules of MG and two of Pro in its unit cell.
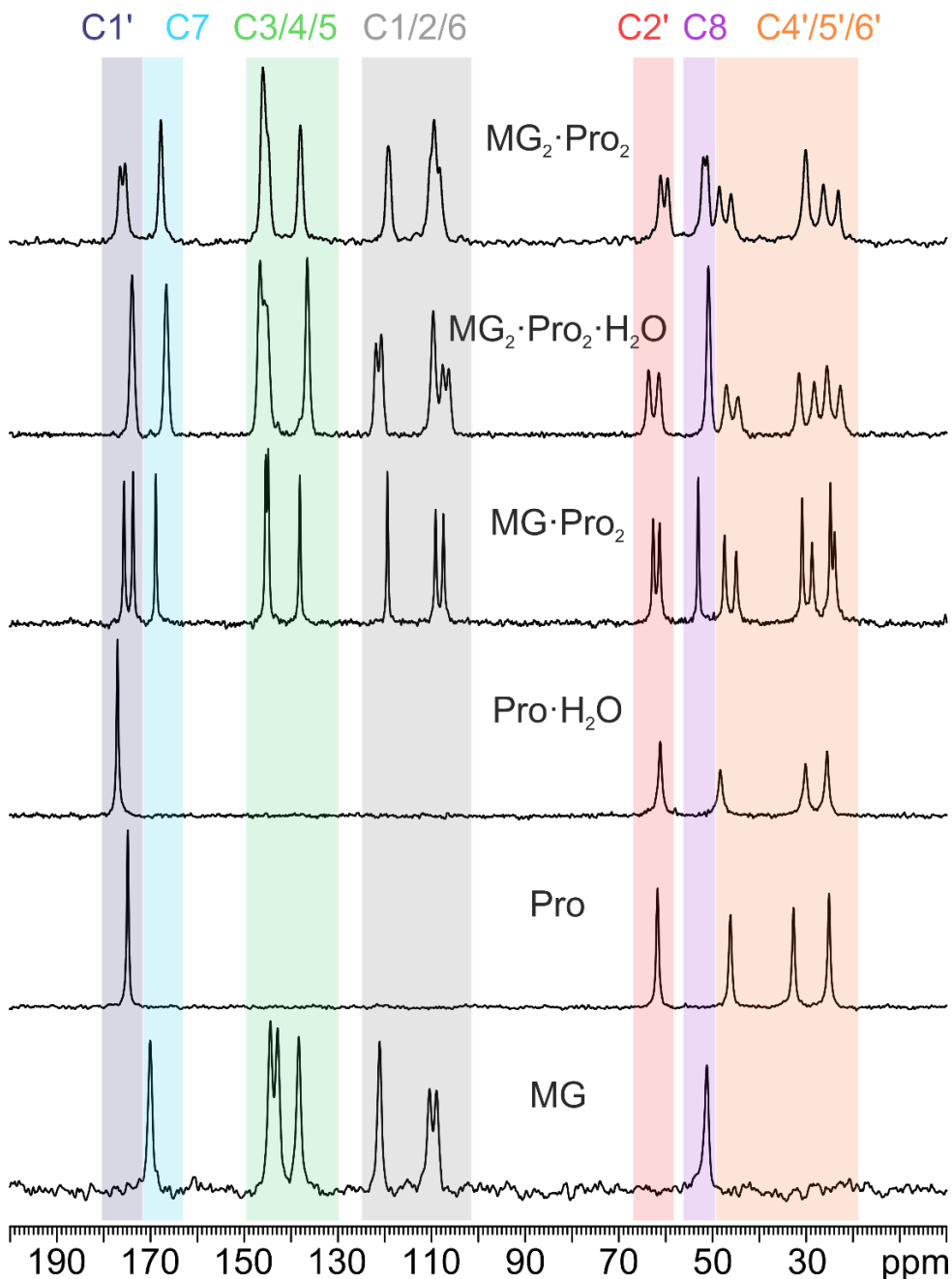
Figure 2.1 ^{13}C (100.6 MHz) CPMAS SSNMR spectra of MG, Pro, Pro·H_2O, MG·Pro_2, MG_2·Pro_2·H_2O and MG_2·Pro_2, recorded at 12 kHz at room temperature. Assignments are reported by means of colored boxes and labels.

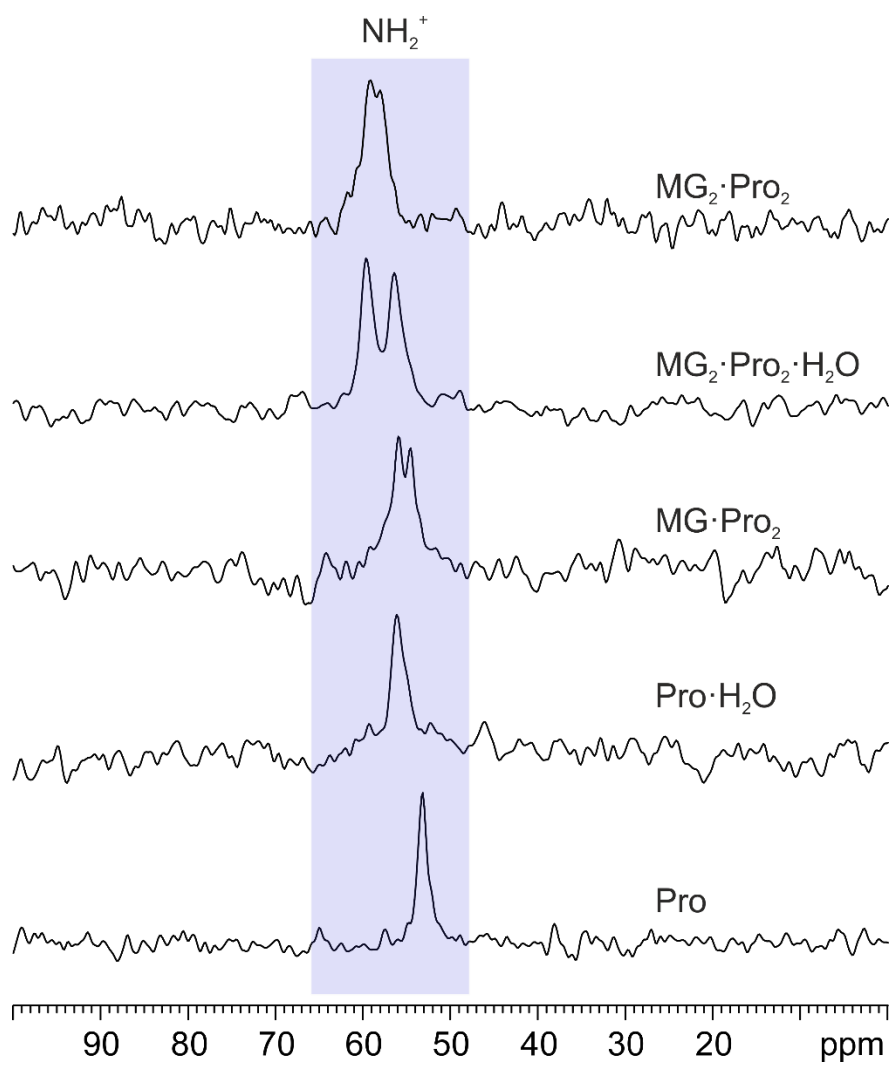**Figure 2.2** ^{15}N (40.6 MHz) CPMAS SSNMR spectra of Pro, Pro·H$_2$O, MG·Pro$_2$, MG$_2$·Pro$_2$·H$_2$O and MG$_2$·Pro$_2$, recorded at 9 kHz at room temperature.

Table 2.2 ^{13}C and ^{15}N SSNMR chemical shift (ppm) assignments for MG·Pro$_2$ and MG$_2$·Pro$_2$·H$_2$O.

MG·Pro$_2$		MG$_2$·Pro$_2$·H$_2$O	
^{13}C CPMAS			
Chemical shift	**Atom**	**Chemical shift**	**Atom**
175.7	1'	173.8	1'
173.8	1'	166.5	7
168.9	7	146.5	3 or 5
145.4	3 or 5	145.6	3 or 5
144.9	3 or 5	145.0	3 or 5
138.2	4	136.4	4
119.5	1	121.8	1
109.2	2 or 6	120.7	1
107.5	2 or 6	111.6	2 or 6
62.8	2'	107.5	2 or 6
61.3	2'	106.2	2 or 6
53.1	8	63.7	2'
47.5	4'	61.4	2'
45.0	4'	50.9	8
30.9	6'	47.0	4'
28.8	6'	44.5	4'
24.9	5'	31.5	6'
24.0	5'	28.3	6'
		25.6	5'
		22.7	5'
^{15}N CPMAS			
55.9	3'	59.7	3'
54.6	3'	56.4	3'

2.3.1 MG$_2$·Pro$_2$·H$_2$O

MG$_2$·Pro$_2$·H$_2$O crystallizes in the triclinic space group $P1$ with five molecules in its unit cell (Figure 2.3a): two zwitterionic Pro (A and C), two MG (B and D) and one water molecule. The corresponding ^{13}C and ^{15}N CPMAS NMR spectra (Figures 2.1 and 2.2, respectively) are in nice agreement with

37

SCXRD data, since they indicate the presence of two independent molecules of both MG and Pro from the splitting of ^{13}C signals related to C1 (121.8 and 120.7 ppm), C2 or C6 (107.5 and 106.2 ppm), and C3 or C5 (145.6 and 145.0 ppm) of MG and C2' (63.7 and 61.4 ppm), C4' (47.0 and 44.5 ppm), C5' (25.6 and 22.7 ppm) and C6' (31.5 and 28.3 ppm) of Pro and of the ^{15}N peak of the NH$_2$$^+$ group (59.7 and 56.4 ppm). The ^{13}C chemical shift of the C=O groups of the two Pro (at 173.8 ppm), typical of a COO$^-$, as well as the ^{15}N chemical shift (usually associated with a protonated aliphatic nitrogen atom) are extremely similar to that of pure Pro/Pro·H$_2$O (53.2 and 56.2 ppm, repectively), confirming the zwitterionic character of both Pro molecules in the adduct.

The two MG molecules are arranged in a perfectly planar way to maximize the conjugation of electrons, while the two Pro molecules display a half-chair conformation of the five-membered ring. As observed in Figure 2.3b, a plethora of HB (Table A1.2 in Appendix I) characterize the packing: every MG (B) is linked to two Pro (C), with one O···H-N$^+$ and two O-H···O$^-$ HBs, and to MG (D), with one O···H-O and one O-H···O HBs. On the other hand, MG (D) molecules are connected to two Pro (A), with one O···H-N$^+$ and one O-H···O$^-$ HBs; to Pro (C), with one O-H···O$^-$ HB; to MG (B), with one O···H-O and one O-H···O HBs; and to a water molecule, with one O-H···O HB. The two zwitterionic Pro molecules do not directly interact with each other; instead, they are only bridged by water and MG molecules. Pro (A) forms 4 HBs: two N$^+$-H···O, with MG (D) and one H$_2$O, and two O$^-$···H-O, with MG (D) and one H$_2$O. Pro (C) is involved in 5 contacts: two N$^+$-H···O, with MG (B) and (D), and three O$^-$···H-O, with two MG (B) and one H$_2$O. This complex network of HBs forms strongly bonded 2D layers that can be simplified by considering molecular centroids in a 2D pentanodal topology with the complex Point Symbol $\{3.4.5.6^2.7\}\{3.4^2.5.7^4.8^2\}\{3.4^2.6^2.7\}\{4.6^2\}\{4^2.5.6^2.7\}$ by considering HBs as defining interactions (Figure A1.9 in Appendix I). These layers interact

38

with each other through a N-H⋯O HB between Pro D and water molecules of the nearby layer, forming a 3D network (Figure 2.3c).
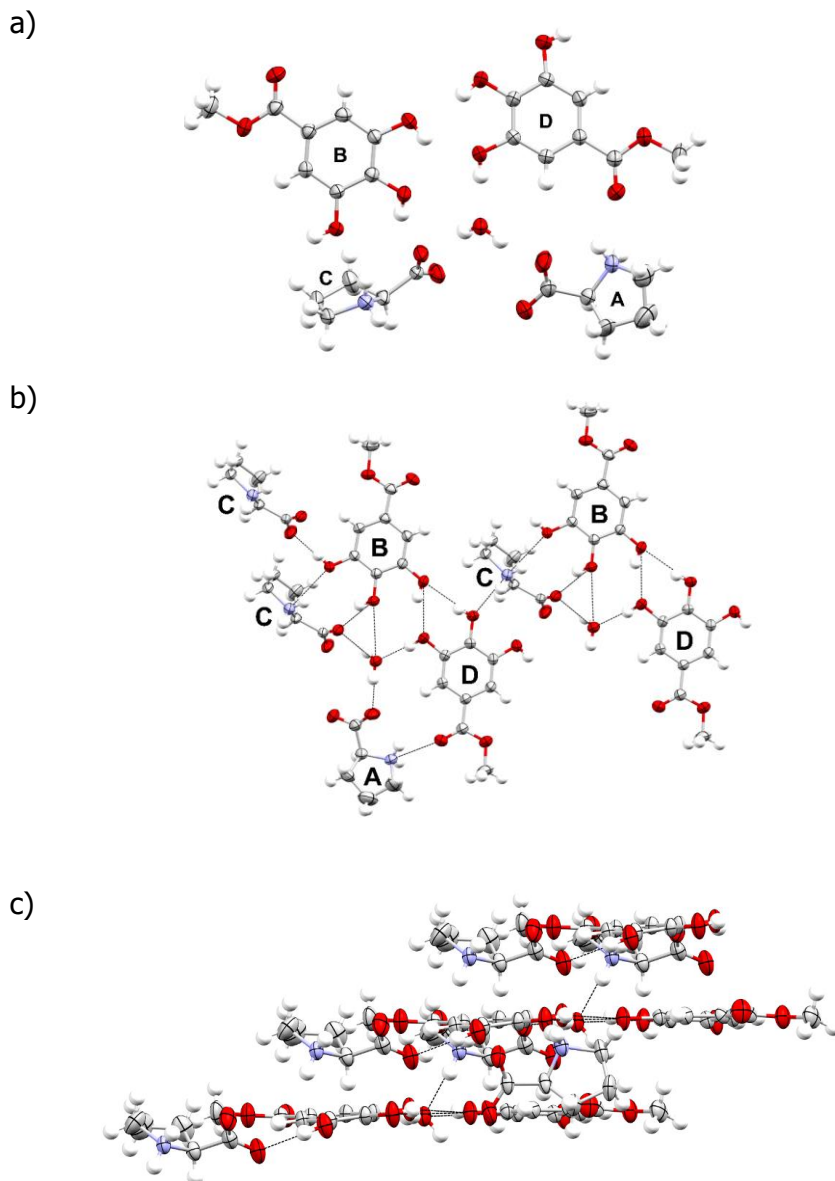
a)

b)

c)

Figure 2.3 (a) Crystallographic independent molecules of $MG_2 \cdot Pro_2 \cdot H_2O$; (b) 2D HB network of $MG_2 \cdot Pro_2 \cdot H_2O$; (c) Perpendicular view of the packing showing the stacking of the layers.

Although the two couples of Pro and MG are similar in terms of geometrical parameters and number of contacts, their interaction patterns are substantially different, as emphasized through the Hirshfeld surface and its fingerprints (Figures A1.10-A1.13 in Appendix I). These analyses are more sensitive to subtle variations of the molecular environment with respect to the usual point of view of crystallochemistry.[46,47] Even if the main interactions for both Pro molecules are the N^+-H···O HBs with MG (see Table A1.2 in Appendix I), in Pro (C) the C-H···H-C components (highlighted by the central symmetric tail in Figure A1.10d in Appendix I) are more significant than in Pro (A) (Figure A1.11d in Appendix I). On the other hand, the two MG molecules differ in the shape index representation on the Hirshfeld surface and in their fingerprints (Figures A1.12 and A1.13 in Appendix I): MG (B) is characterized by strong C-H···π interactions, lateral wings on the fingerprint, while MG (D) by π···π interactions, blue and red triangles in the shape index figure (Figure A1.13b in Appendix I).[48]

2.3.2 MG·Pro$_2$

The anhydrous phase is very different in the molecular packing with respect to the hydrated one. MG·Pro$_2$ crystallizes in the shape of large prisms in the orthorhombic space group $P2_12_12_1$ and the asymmetric unit contains one MG and two Pro molecules (Figure 2.4a). The two Pro molecules (B and C) are zwitterionic and different in geometry: Pro (B) displays disorder, determined by the two possible inverted half chairs for the ring, while Pro (C) presents a half-chair conformation.

Once again, an SSNMR analysis confirmed the SCXRD information. Indeed, the ^{13}C signals of all the C atoms (Figure 2.1) of Pro appear as split, confirming the presence of two independent molecules of Pro in the unit cell. On the contrary, the resonances ascribable to MG are consistent with just one MG molecule in the asymmetric unit. The carboxylic signals of both Pro

40

molecules fall at chemical shifts that are ascribable to carboxylate moieties (175.7 and 173.8 ppm). ^{15}N CPMAS (Figure 2.2) chemical shifts (55.9 and 54.6 ppm) agree with the presence of two Pro molecules in the asymmetric unit and their zwitterionic state. Similar to $MG_2 \cdot Pro_2 \cdot H_2O$, the overall pattern is dominated by a complex network of HBs (see Figure 2.4b and Table A1.3 in Appendix I): Pro (B) is linked to two Pro (C), with one $O^- \cdots H\text{-}N^+$ and one $N^+\text{-}H \cdots O^-$ HB; to MG (A), with one $O^- \cdots H\text{-}O$ HB; and to two other Pro (B), with two weaker $O^- \cdots H\text{-}N^+$ and $N^+\text{-}H \cdots O^-$ HBs ($N \cdots O$ distance = 3.087 Å). Pro (C) forms one $O^- \cdots H\text{-}N^+$ and one $N^+\text{-}H \cdots O^-$ HB with Pro (B); one $O^- \cdots H\text{-}O$ HB with MG (A); and two weaker $O^- \cdots H\text{-}N^+$ and $N^+\text{-}H \cdots O^-$ HBs ($N \cdots O$ distance = 3.150 Å) with two other Pro (C). On the other hand, MG (A) is connected to Pro (C), with one $O\text{-}H \cdots O^-$ HB, to Pro (B), with one $O\text{-}H \cdots O^-$ HB, and to two other MG, with one $O\text{-}H \cdots O^-$ and one $O \cdots H\text{-}O$ HB.
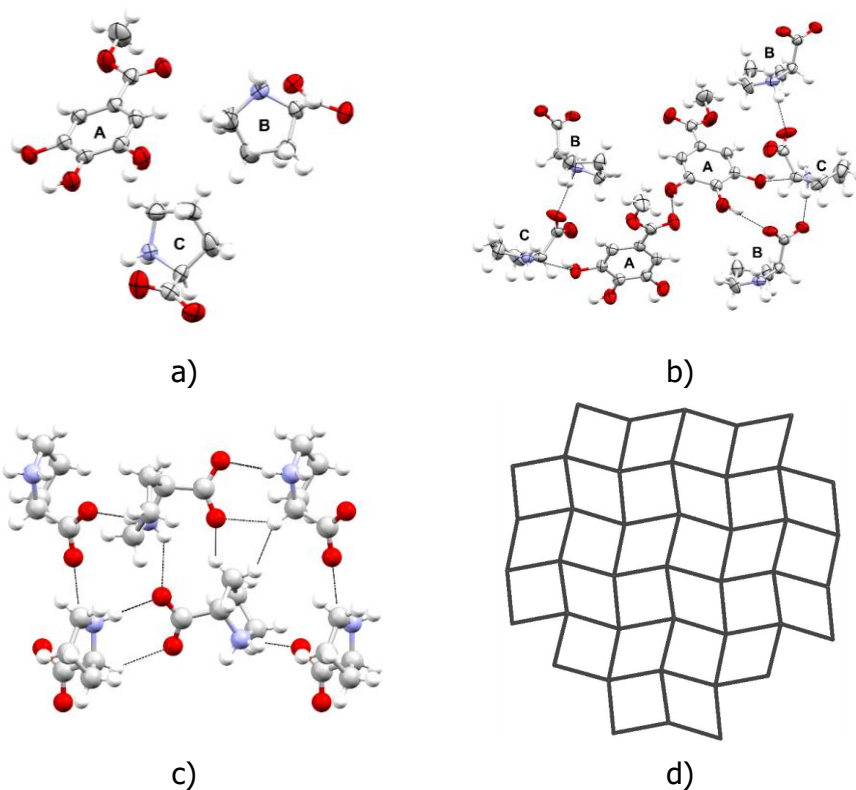
Figure 2.4 (a) Asymmetric unit of MG·Pro$_2$; (b) Representation of the 3D HB network of MG·Pro$_2$; (c) Layers of tetraconnected Pro molecules; (d) Representation of the underlying net of the Pro layers along the b axis.

The resulting complex packing can be represented by layers of Pro molecules, where each of them, either B or C, is connected to 4 other Pro (Figures 2.4c and 2.4d), in turn two B and two C. These layers interact with each other through the presence of MG, which provides a fifth interaction with each Pro: hence, this acts as a pentacoordinated node.

The derived 3D underlying graph is a binodal net with Point Symbol $\{4.6^5\}\{4^6.6^4\}_2$ (Figure A1.14 in Appendix I), which presents the plane of Pro molecules as a $\{4^4\}$ net in the (001) plane (Figure 2.4d).

Considering the Hirshfeld surface analysis, in the case of MG, the $\pi\cdots\pi$ interaction component is completely absent in the shape index representation

42

(Figure A1.15 in Appendix I), differing from $MG_2 \cdot Pro_2 \cdot H_2O$. The Hirshfeld surface is dominated by C-H···π and C-H···H-C, evidenced in the fingerprint plot and in red hollows in the shape index representation. However, the shortest and most stable interactions are the strong HBs to the oxygen sites. On the other hand, the two Pro molecules are both characterized by short O^-···H-O and N^+-H···O^-, as can be observed by the long stripes in the fingerprints (see Figures A1.16d and A1.17d in Appendix I), but they differ in the C-H···H-C dispersive contacts of the ring. In the case of Pro (C) these contacts are weaker and more inhomogeneous, while in Pro (B) they are more directional and can be observed not only in the fingerprint plot, but also in the shape index representation (see Figure A1.16b in Appendix I).

Both Pro and MG are highly soluble in water (Pro 162 g/L (at 25 °C); MG 10.6 g/L) highlighting an effective solvation process. However, the experimental syntheses show that the water molecules cannot be easily included in the structure if coming from outside; surely, they can be incorporated if already in interaction with Pro.

In order to rationalize this behavior, an energy framework analysis was performed on Pro (CSD code: PROLIN),[49] Pro·H_2O (CSD code: RUVGEW),[50] $MG \cdot Pro_2$, and $MG_2 \cdot Pro_2 \cdot H_2O$. Energy frameworks both provide the energetic components of interactions (i.e., electrostatic, dispersive, repulsive and polarization) between molecular pairs and allows visualizing them as cylinders with a radius which is proportional to the magnitude of the interaction energy. This method has been recently employed for its speed and reliability in facing different problems in a great number of systems: from mechanical properties of crystals,[30] polymorphism[51] and calculation of lattice energies[52] to the effectiveness of specific supramolecular synthons in stabilizing and directing the overall packing.[53]

Comprehensive energy framework data are reported in Appendix I (Tables A1.7-A1.10 and Figures A1.18-A1.25). In the case of Pro, the packing is

characterized by columns of stacked Pro molecules laterally connected by HBs to form layers of tetraconnected Pro molecules (Figure 2.5a), observed also in MG·Pro$_2$ (see above) and which are typical of Pro-containing structures (~70 % of the 117 organic cases found in the CSD).[18,54] The main energetic interaction component in this molecular arrangement is electrostatic (see Table 2.3 and Figure 2.6a), between both stacked and lateral Pro. The molecular packing of Pro·H$_2$O consists of columns of Pro molecules alternating with columns of water molecules (Figure 2.5b). Beside the strong Pro-Pro electrostatic interactions along the columns, the water molecules present quite strong electrostatic interactions with nearby Pro (Table 2.3 and Figure 2.6b) as well, leading to the disarrangement of the intercolumnar network. In MG$_2$·Pro$_2$·H$_2$O, water-Pro interactions (E_{ele} = -35.4 kJ·mol^{-1}) represent the main contribution to the total energy of the structure, even stronger than Pro-Pro (E_{ele} = -33.4 kJ·mol^{-1}) and MG-Pro (E_{ele} = -10.3 kJ·mol^{-1}) interactions (Table 2.3), supporting the evidence that, if water is present in the starting reagent, it is maintained in the final products. This is likely due to the drastic change in the crystal packing of Pro molecules, which do not form the typical columnar motif.
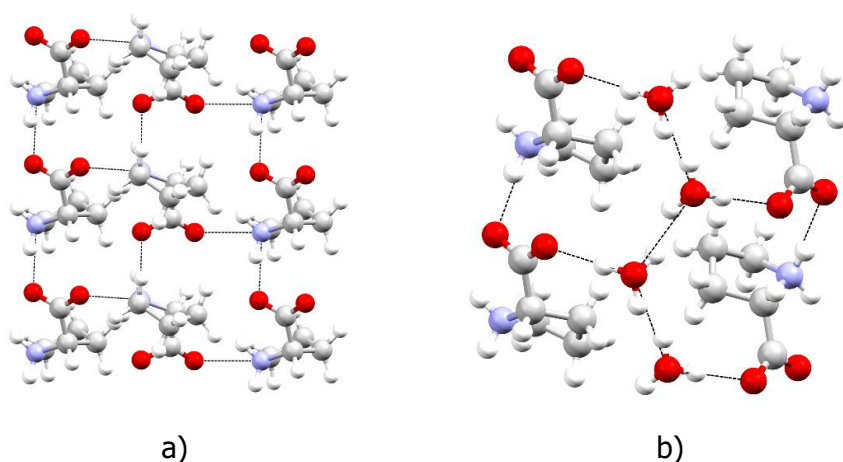

a)   b)

**Figure 2.5** (a) Layer of Pro molecules in Pro; (b) Columns of Pro molecules interacting with water in Pro·H$_2$O.

In MG·Pro$_2$, where the layers of Pro molecules are maintained, dispersive MG-Pro and electrostatic Pro-Pro interactions are dominant (-23.4 and -52.5 kJ·mol^{-1}, respectively, Table 2.3). This suggests that, when anhydrous Pro is used as starting material, water cannot be incorporated since it would disrupt the stable structural Pro motif in pure Pro, which, in turn, is not severely altered by the presence of MG (see Figure A1.26 in Appendix I for the comparison between Pro layers in Pro and MG·Pro$_2$). However, this is in contradiction with the experimental outcomes: indeed, when the correct stoichiometry is matched, kneading in water leads to MG$_2$·Pro$_2$·H$_2$O. A possible explanation is offered by the readiness with which pure Pro is hydrated if it is kneaded in water. Our hypothesis is that the driving force of the MG$_2$·Pro$_2$·H$_2$O formation consists of three steps: (a) solubilization of the anhydrous reagents (Pro or MG·Pro$_2$), (b) formation of Pro·H$_2$O, and (c) cocrystallization of Pro·H$_2$O with MG. In this process, the stoichiometry still plays a pivotal role: indeed, when MG·Pro$_2$ is ground in the presence of water, an unstable phase is obtained rather than MG$_2$·Pro$_2$·H$_2$O plus excess Pro.
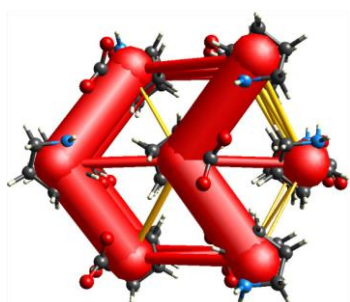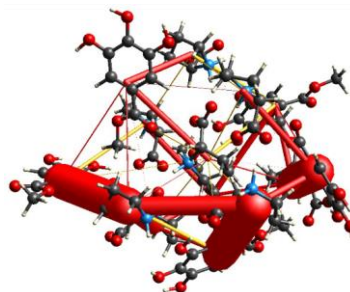
a)

b)
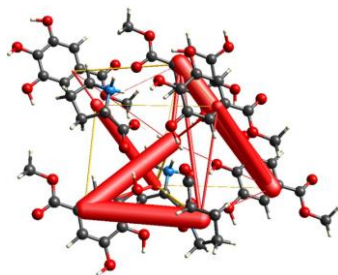
c)

d)

Figure 2.6 Electrostatic (red cylinders) and repulsive (yellow cylinders) components in the energy frameworks of (a) Pro (CSD code: PROLIN); (b) Pro·H_2O (CSD code: RUVGEW); (c) MG_2·Pro_2·H_2O; (d) MG·Pro_2.

Table 2.3 Energetic contribution (kJ·mol^{-1}) of the main interactions (electrostatic, E_{ele}; polarization, E_{pol}; dispersion, E_{dis}; repulsive, E_{rep}; total, E_{tot}) in Pro (CSD code: PROLIN), Pro·H_2O (CSD code: RUVGEW), MG_2·Pro_2·H_2O and of MG·Pro_2.

Pro					
Interaction	E_{ele}	E_{pol}	E_{dis}	E_{rep}	E_{tot}
Pro-Pro (stacked)	-105.4	-31.2	-15.8	24.8	-121.8
Pro-Pro (lateral)	-112.6	-50.6	-21.3	58.5	-119.4
Pro·H_2O					
Interaction	E_{ele}	E_{pol}	E_{dis}	E_{rep}	E_{tot}
Water-Pro	-33.2	-7.4	-3.3	1.7	-40.3
Water-Pro	-34.2	-7.4	-3.3	1.7	-41.3
Water-Water	-106.1	-48.5	-23.4	60.7	-111.6
Pro-Pro (stacked)	-109.1	-47.5	-23.4	60.7	-113.6
MG_2·Pro_2·H_2O					
Interaction	E_{ele}	E_{pol}	E_{dis}	E_{rep}	E_{tot}
Pro-water	-35.4	-16.3	-8.1	8.4	-47.1
Pro-MG	-33.4	-15.3	-8.1	8.4	-44.1
Pro-Pro	-10.3	-3.4	-13.7	2.7	-22.8
MG·Pro_2					
Interaction	E_{ele}	E_{pol}	E_{dis}	E_{rep}	E_{tot}
Pro-Pro (stacked)	-52.5	-15.3	-7.0	4.3	-66.3
Pro-MG	-18.1	-5.3	-23.4	12.3	-33.0

The thermic profile of MG_2·Pro_2·H_2O was assessed by means of DSC and TGA experiments (Figures A1.27-A1.29 in Appendix I). It exhibits two main endothermic events: at 92 °C a slight weight loss (~3%) is observed, which is consistent with the release of one water molecule; at 251 °C melting/decomposition of the cocrystal starts. As for MG·Pro_2, the TGA curve does not exhibit any weight loss below 100 °C, while a single DSC endothermic event occurs at 148 °C, which is associated to its melting.

Finally, the phase obtained by heating MG_2·Pro_2·H_2O was analyzed: no weight loss could be observed in the TGA curve, while the melting of the cocrystal can be observed as an endothermic peak (140 °C) in the

respective DSC thermogram. This confirms this phase to be an anhydrous phase of the MG-Pro system.

2.4 Conclusions

Two new cocrystals, $MG \cdot Pro_2$ and $MG_2 \cdot Pro_2 \cdot H_2O$, were obtained from L-proline and methyl gallate by mechanochemical methods. The compelling behavior of the system consisted of the fact that starting from $Pro \cdot H_2O$ is a sufficient condition to obtain $MG_2 \cdot Pro_2 \cdot H_2O$. On the other hand, the employment of Pro proves to be a necessary condition for the achievement of $MG \cdot Pro_2$. The energy framework and crystal packing analyses suggest that, on starting from $Pro \cdot H_2O$, in which water is already interacting with Pro and the peculiar intercolumnar network is disarranged, the result is a crystal packing where Pro−water interactions prevail. On the other hand, on starting from Pro, where Pro molecules are connected to each other to form layers (as in Pro and $MG \cdot Pro_2$), Pro−Pro interactions prevail. However, the stoichiometry strongly drives the final outcome if water is involved in the synthesis: 1:1 can lead to a stable hydrated structure, while 1:2 only provides an anhydrous form. Hopefully, this will open up fascinating perspectives for the rational use of Pro or $Pro \cdot H_2O$ in designing new cocrystals of APIs. Such prospects concern driving the pseudopolymorphism of the achieved phases, as well as engineering the final crystal packings (i.e., with Pro columns/layers or not), and thus the macroscopic properties of the systems. The last statement is statistically verified by a CSD survey of Pro-containing cocrystals which suggests that using anhydrous Pro as a reagent leads to a 70% probability of achieving phases characterized by Pro columns/layers.

References

[1] G. R. Desiraju, *Angew. Chem. Int. Ed.* **2007**, *46*, 8342–8356.

[2] T. S. Thakur; R. Thakuria, C*ryst. Growth Des.* **2020**, *20*, 6245–6265.

[3] J. Wojnarska; M. Gryl; T. Seidler; A. Rydz; M. Oszajca; K. M. Stadnicka; M. Marzec; I. Matulková; I. Němec; P. Němec, Cryst. Growth Des. 2019, 19, 6831–6836.

[4] S. Y. Chang; C. C. Sun, *Mol. Pharm.* **2017**, *14*, 2047–2055.

[5] D. Hasa; D. Voinovich; B. Perissutti; M. Grassi; A. Bonifacio; V. Sergo; C. Cepek; M. R. Chierotti; R. Gobetto; S. Dall'Acqua; S. Invernizzi, *Pharm. Res.* **2011**, *28*, 1870–1883.

[6] F. Grifasi; M. R. Chierotti; K. Gaglioti; R. Gobetto; L. Maini; D. Braga; E. Dichiarante; M. Curzi, *Cryst. Growth Des.* **2015**, *15*, 1939–1948.

[7] D. Bernasconi; S. Bordignon; F. Rossi; E. Priola; C. Nervi; R. Gobetto; D. Voinovich; D. Hasa; N. T. Duong; Y. Nishiyama; M. R. Chierotti, *Cryst. Growth Des.* **2020**, *20*, 906–915.

[8] D. Braga; L. Chelazzi; F. Grepioni; E. Dichiarante; M. R. Chierotti; R. Gobetto, *Cryst. Growth Des.* **2013**, *13*, 2564–2572.

[9] K. T. Holman, *J. Am. Chem. Soc.* **2008**, *130*, 2878.

[10] S. Aitipamula; R. Banerjee; A. K. Bansal; K. Biradha; M. L. Cheney; A. R. Choudhury; G. R. Desiraju; A. G. Dikundwar; R. Dubey; N. Duggirala *et al., Cryst. Growth Des.* **2012**, *12*, 2147–2152.

[11] D. Braga; L. Maini; G. de Sanctis; K. Rubini; F. Grepioni; M. R. Chierotti; R. Gobetto, *Chem. Eur. J.* **2003**, *9*, 5538–5548.

[12] M. Baldrighi; G. Cavallo; M. R. Chierotti; R. Gobetto; P. Metrangolo; T. Pilati; G. Resnati; G. Terraneo, *Mol. Pharm.* **2013**, *10*, 1760–1772.

[13] T. S. Thakur; Y. Azim; T. Srinu; G. R. Desiraju, *Curr. Sci.* **2010**, *98*, 793–802.

[14] F. Rossi; P. Cerreia Vioglio; S. Bordignon; V. Giorgio; C. Nervi; E. Priola; R. Gobetto; K. Yazawa; M. R. Chierotti, *Cryst. Growth Des.* **2018**, *18*, 2225–2233.

[15] S. Bordignon; P. Cerreia Vioglio; E. Priola; D. Voinovich; R. Gobetto; Y. Nishiyama; M. R. Chierotti, *Cryst. Growth Des.* **2017**, *17*, 5744–5752.

[16] S. Bordignon; P. Cerreia Vioglio; E. Amadio; F. Rossi; E. Priola; D. Voinovich; R. Gobetto; M. R. Chierotti, *Pharmaceutics* **2020**, *12*, 818–835.

[17] P. Cerreia Vioglio; M. R. Chierotti; R. Gobetto, *Adv. Drug Delivery Rev.* **2017**, *117*, 86–110.

[18] A. Tilborg; B. Norberg; J. Wouters, *Eur. J. Med. Chem.* **2014**, *74*, 411–426.

[19] R. Thakuria; B. Sarma, *Crystals* **2018**, *8*, 101–139.

[20] C. Wang; S. Paul; D. J. Sun; S. O. Nilsson Lill; C. C. Sun, *Cryst. Growth Des.* **2020**, *20*, 4217–4223.

[21] A. O. Surov; A. P. Voronin; M. V. Vener; A. V. Churakov; G. L. Perlovich, *CrystEngComm* **2018**, *20*, 6970–6981.

[22] N. Tumanova; N. Tumanov; F. Fischer; F. Morelle; V. Ban; K. Robeyns; Y. Filinchuk; J. Wouters; F. Emmerling; T. Leyssens, *CrystEngComm* **2018**, *20*, 7308–7321.

[23] A. Tilborg; T. Leyssens; B. Norberg; J. Wouters, *Cryst. Growth Des.* **2013**, *13*, 2373–2389.

[24] X. Zhu; X. Li; T. Zhang; F. Yuan, *Dapagliflozin Crystalline Form and Preparation Method Thereof*. US9550747B2, January 24, **2017**.

[25] M. R. Shimpi; S. L. Childs; D. Boström; S. P. Velaga, *CrystEngComm* **2014**, *16*, 8984–8993.

[26] H. He; Y. Huang; Q. Zhang; J. R. Wang; X. Mei, *Cryst. Growth Des.* **2016**, *16*, 2348–2356.

[27] J. Hernández-Paredes; A. L. Olvera-Tapia; J. I. Arenas-García; H. Höpfl; H. Morales-Rojas; D. Herrera-Rui; A. I. Gonzaga-Morales; L. Rodríguez-Fragoso, *CrystEngComm* **2015**, *17*, 5166–5186.

[28] J. G. Choi; S. H. Mun; H. S. Chahar; P. Bharaj; O. H. Kang; S. G. Kim; D. W. Shin; D. Y. Kwon, *Plos One* **2014**, *9*, e102697.

[29] H. Lee; H. Lee; Y. Kwon; J. H. Lee; J. Kim; M. K. Shin; S. H. Kim; H. Bae, *J. Immunol.* **2010**, *185*, 6698–6705.

[30] S. H. Lee; J. K. Kim; D. W. Kim; H. S. Hwang; W. S. Eum; J. Park; K. H. Han; J. S. Oh; S. Y. Choi, *Biochim. Biophys. Acta-Gen. Subj.* **2013**, *1830*, 4017–4029.

[31] D. Bebout; S. Pagola, *Acta Crystallogr. Sect. E-Struct. Rep. Online* **2009**, *65*, O317-U2094.

[32] *CrysAlisPro Software System*; Agilent Technologies UK Ltd.: Oxford UK, **2012**.

[33] G. M. Sheldrick, *SHELX97: Program for Crystal Structure Solution and Refinement*; University of Göttingen: Göttingen, Germany, **2004**.

[34] V. A. Blatov; A. P. Shevchenko; D. M. Proserpio, *Cryst. Growth Des.* **2014**, *14*, 3576–3586.

[35] M. C. Etter; J. C. MacDonald; J. Bernstein, *Acta Crystallogr. B* **1990**, *46*, 256–262.

[36] C. F. Macrae; P. R. Edgington; P. McCabe; E. Pidcock; G. P. Shields; R. Taylor; M. Towler; J. van de Streek, *J. Appl. Crystallogr.* **2006**, *39*, 453–457.

[37] A. L. Spek, *J. Appl. Crystallogr.* **2003**, *36*, 7–13.

38 C. Capillas; E. S. Tasci; G. de la Flor; D. Orobengoa; J. M. Perez-Mato; M. I. Aroyo, *Z. Für Krist. - Cryst. Mater.* **2011**, *226*, 186–196.

39 R. E. Marsh, *Acta Crystallogr. B* **1999**, *55*, 931–936.

40 G. R. Desiraju, G. R. *CrystEngComm* **2006**, *9*, 91–92.

41 A. Bennett; C. Rienstra; M. Auger; K. Lakshmi; R. Griffin, *J. Chem. Phys.* **1995**, *103*, 6951–6958.

42 M. J. Turner; J. J. McKinnon; S. K. Wolff; D. J. Grimwood; P. R. Spackman; D. Jayatilaka; M. A. Spackman, *CrystalExplorer*; University of Western Australia, **2017**.

43 M. J. Turner; S. Grabowsky; D. Jayatilaka; M. A. Spackman, *J. Phys. Chem. Lett.* **2014**, *5*, 4249–4255.

44 M. A. Spackman; D. Jayatilaka, *CrystEngComm* **2009**, *11*, 19–32.

45 S. Karki; T. Friščić; W. Jones; W. D. S. Motherwell, *Mol. Pharm.* **2007**, *4*, 347–354.

46 J. J. McKinnon; F. P. A. Fabbiani; M. A. Spackman, *Cryst. Growth Des.* **2007**, *7*, 755–769.

47 M. A. Spackman; J. J. McKinnon, *CrystEngComm* **2002**, *4*, 378–392.

48 R. L. Kayushina; B. K. Vainshtein *Kristallografiya* **1965**, *883*, 10–25.

49 J. Janczak; P. Luger, *Acta Crystallogr. C* **1997**, *53*, 1954–1956.

50 D. Dey; S. P. Thomas; M. A. Spackman; D. Chopra, *Chem. Commun.* **2016**, *52*, 2141–2144.

51 S. P. Thomas; P. R. Spackman.; D. Jayatilaka; M. A. Spackman, *J. Chem. Theory Comput.* **2018**, *14*, 1614–1623.

52 S. P. Thomas; D. Jayatilaka; T. N. G. Row, *Phys. Chem. Chem. Phys.* **2015**, *17*, 25411–25420.

53 C. H. Görbitz, *Crystallogr. Rev.* **2015**, *21*, 160–212.

Chapter 3

Ethionamide: a poorly soluble drug that proves versatile in the formation of new crystal forms

3.1 Introduction

The obtainment of novel crystal forms is a well-consolidated strategy in the quest for solid molecular materials with enhanced physicochemical properties with respect to those of the pure components. The crystal engineering approach, i.e., the rational design and synthesis of new crystal forms[1], is viable for any molecule that is employed in the solid state, ranging from pigments to explosives,[2] from pharmaceuticals to energy storage materials.[3] In the case of active pharmaceutical ingredients (APIs), crystal engineering has proved to be successful in modulating and improving their performances in terms of water solubility,[4,5] dissolution rate,[6,7] hygroscopicity,[8] thermal stability,[9] flow properties,[10] etc. An important point of this strategy is the fact that some APIs are often doomed to obsolescence because of their poor biopharmaceutical and/or physicochemical properties.[11] Improving them represents a way to restore their value, in some cases even to reduce side effects due to a decrease in the administered doses and to extend rights on the intellectual property. This aspect gains particular importance in today's economic and scientific context, where the R&D costs in the pharmaceutical industry increase annually,[12] yet the number of approved drugs kept constant throughout 60 years.[13,14] Therefore, the revamping of old drugs represents a chance to reduce costs and also introduce new therapies.[15]

The crystal engineering approach can deliver many different crystal forms, namely polymorphs, salts, solvates/hydrates and cocrystals. The

latter, in particular, are more and more commonly pursued as an alternative to salts in the quest for performance enhancement of APIs, because cocrystallization offers greater opportunities than salification: (i) it is viable for molecules that do not display any ionizable moiety; (ii) the possible coformers (i.e., molecules selected to cocrystallize with the API) are more numerous than the possible counterions; (iii) cocrystallization can significantly improve the solubility of the APIs without altering their permeability. As of today, many pharmaceutical cocrystals have been successfully prepared and reported in the literature,[7,16–20]

This work focuses on the preparation and solid-state characterization of multicomponent crystal forms of ethionamide (2-ethylpyridine-4-carbothioamide, ETN) (Scheme 3.1). ETN is an anti-tubercular drug used in the treatment of drug-resistant tuberculosis; hence, it is frequently administered in association with other antibacterial agents. Indeed, multidrug- and extensively drug-resistant tuberculosis are addressed by the World Health Organization as major global issues.[21] Since ETN belongs to class II of the BCS (Biopharmaceutical Classification System), comprising of compounds with low solubility and high permeability, efforts in the improvement of the dissolution properties of ETN clearly become crucial to help the treatment of such aggressive forms of the disease. ETN crystallizes in space group *Cc*,[22] without any polymorphic forms known to date. On the other hand, there are several examples in the literature of salts and cocrystals of ETN, namely ETN hydrochloride,[23] hydrobromide,[24] nitrate,[25] oxalate,[26,27] maleate[27] and saccharinate;[27]; ETN·adipic acid,[26] ETN·fumaric acid[26] and ETN·suberic acid.[26] Notably, in all salts reported in the literature, N5 of ETN appears to be protonated, while in all cocrystal structures of ETN with carboxylic acids, the COOH group is involved in hydrogen bond (HB) contacts with both N5 (COOH···N) and N10 (C=O···HN). Most recently, some of us managed to selectively obtain both a salt and a cocrystal for the ETN−salicylic

acid system, which display remarkable *in vitro* bioavailability properties.[16] This further proves ETN to be a very feasible molecule to undergo the crystal engineering approach. In this work, three new crystal forms of ETN were obtained by solution or mechanochemical techniques through the combination with glutaric (GLU), malonic (MAL) and tartaric (TAR) acid (see Scheme 3.1). Notably, the cocrystallization of ETN with TAR yielded a rare kryptoracemic cocrystal: to date, only one kryptoracemic cocrystal has been reported.[28] Notably, all three new crystal forms are characterized by significantly higher dissolution rates than pure ETN.

These three novel forms were compared with two previously reported crystal forms of ETN with dicarboxylic acids fumaric (FUM) and maleic (MLE) acid,[26,27] to observe similarities and differences with respect to our novel forms in terms of spectroscopic and physicochemical properties. All five forms were analyzed by single-crystal X-ray diffraction (SCXRD), while all but ETN·TAR, which could not be reproduced as a bulk powder (see Materials and Methods section), underwent solid-state NMR (SSNMR). The latter technique was instrumental in clarifying the nature (neutral or ionic) of the obtained products, since the position of the H atoms along the HB axis was in general not clearly detected in SCXRD structures. Finally, the thermal stability and the dissolution rate were evaluated for all crystal forms (except for ETN·TAR) by means of DSC and TGA analyses and dissolution kinetic tests (DKTs), respectively.
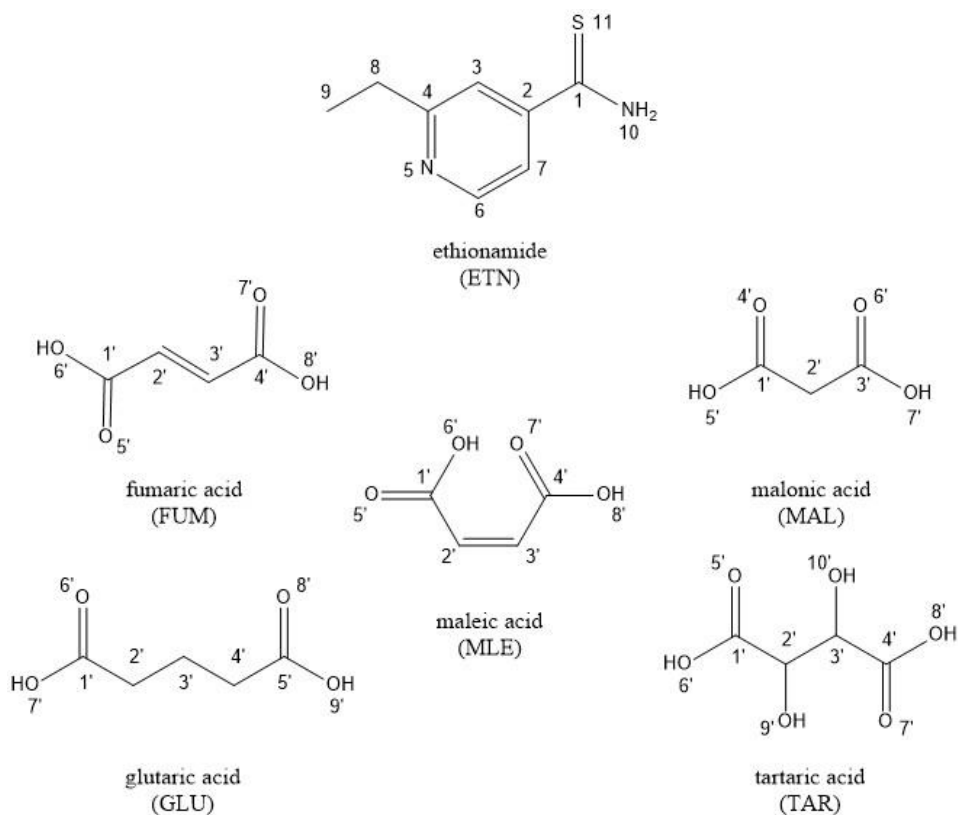
Scheme 3.1 Representation of the employed molecules, with atom numbering.

3.2 Materials and methods

FUM, GLU, MLE, MAL and all solvents were purchased from Sigma-Aldrich (Milan, Italy,); ETN was purchased from Alfa Aesar (Thermo Fisher Scientific, Kendal, Germany); TAR was purchased from Schiapparelli (Carlo Erba, Cornaredo (MI), Italy). All reagents were used without further purification.

3.2.1 Synthesis procedures

ETN·GLU: A yellow microcrystalline powder was obtained by manually dry grinding 30 mg (0.18 mmol) of ETN and 24 mg (0.18 mmol) of GLU for 60 min. Crystals were obtained through seeding crystallization of the ground product in ethanol.

ETN·MAL: An orange microcrystalline powder was obtained by the slurry technique: 50 mg (0.3 mmol) of ETN and 31 mg (0.3 mmol) of MAL were stirred for 4 h with a few drops of ethanol. Crystals, suitable for SCXRD, were obtained through seeding crystallization of the slurried product in ethyl acetate.

ETN·TAR: Crystals were obtained through slow evaporation at room temperature of a methanol solution containing 30 mg (0.18 mmol) of ETN and 27 mg (0.18 mmol) of TAR. Despite many attempts, ETN·TAR could not be reproduced in pure form to undergo further analyses.

ETN·FUM: Crystals were obtained through slow evaporation at room temperature of a methanol solution containing 30 mg (0.18 mmol) of ETN and 21 mg (0.18 mmol) of FUM.

ETN·MLE: An orange microcrystalline powder was obtained by manually dry grinding 30 mg (0.18 mmol) of ETN and 21 mg (0.18 mmol) of MLE for 30 min. Crystals, suitable for SCXRD, were obtained through slow evaporation at room temperature of an acetone solution containing 15 mg (0.09 mmol) of ETN and 10.5 mg (0.09 mmol) of MLE.

3.2.2 Screening techniques

3.2.2.1 Raman spectroscopy

Raman spectra were registered with a Bruker Vertex 70 instrument (Bruker, Billerica, MA, USA), equipped with a RAM II module. An excitation source at 1064 nm was used, with a laser power between 10 and 50 mW and a number of scans between 80 and 500, depending on the analyzed sample,

56

with a resolution of 4 cm^{-1}. The employed spectral range is comprised between 50 and 4500 cm^{-1}, using a CaF$_2$ beam splitter. Raman spectra are not discussed as they were used only for screening purposes, but they are reported in Figures A2.1–A2.4.

3.2.3 Characterization techniques

3.2.3.1 X-ray diffraction (SCXRD and PXRD)

Single crystals of ETN·GLU, ETN·MAL and ETN·TAR were analyzed with a Gemini R Ultra diffractometer (Rigaku Oxford Diffraction, Abingdon, Oxfordshire, England) operating at 293(2) K, using a Mo Kα source (λ = 0.71073 Å). Data collection and reduction were performed using the CrysAlisPro software (Rigaku Oxford Diffraction, Abingdon, Oxfordshire, England). The crystal structure was solved by direct methods and refined with the full matrix least-squares technique on F^2 using the SHELXS-97 and SHELXL-97 programs (Structural Chemistry Department at the University of Göttingen, Germany). All non-hydrogen atoms were refined anisotropically; hydrogen atoms bonded to unambiguous sites were placed in geometrical positions and refined using the riding model. Hydrogen atoms between pyridinic nitrogen and carboxylic oxygen sites of nearby molecules have been detected in the Fourier maps, and their position has been further confirmed through SSNMR. See Table 3.1 for the crystal data and structure refinement parameters for ETN·GLU, ETN·MAL and ETN·TAR, and Tables A2.1–A2.6 for the measured crystallographic distances and angles (refer to Scheme 3.1 for atom numbering).

Table 3.1 Crystal data and structure refinement parameters for ETN·GLU, ETN·MAL and ETN·TAR.

	ETN·GLU
Empirical formula	$C_{13}H_{18}N_2O_4S$
Formula weight	298.35
Temperature/K	293(2)
Crystal system	triclinic
Space group	$P\bar{1}$
a/Å	5.3818(3)
b/Å	11.4336(6)
c/Å	13.2901(9)
α/°	78.196(5)
β/°	80.618(5)
γ/°	77.435(5)
Volume/Å³	775.28(8)
Z	2
ρ_{calc} g/cm³	1.278
μ/mm⁻¹	0.222
F(000)	316.0
Crystal size/mm³	0.50 × 0.22 × 0.21
Radiation	Mo Kα (λ = 0.71073)
2θ range for data collection/°	6.74 to 50.06
Index ranges	$-6 \leq h \leq 6$, $-13 \leq k \leq 13$, $-14 \leq l \leq 15$
Reflections collected	5457
Independent reflections	2739 (R_{int} = 0.0228, R_{sigma} = 0.0543)
Data/restraints/parameters	2739/25/238
Goodness-of-fit on F^2	1.043
Final R indexes [I >= 2σ (I)]	R_1 = 0.0448, wR_2 = 0.1131
Final R indexes [all data]	R_1 = 0.0593, wR_2 = 0.1236
Largest diff. peak/hole/e Å⁻³	0.18/−0.18
	ETN·MAL
Empirical formula	$C_{11}H_{14}N_2O_4S$
Formula weight	270.30

Temperature/K	293(2)
Crystal system	triclinic
Space group	$P\bar{1}$
a/Å	7.0008(12)
b/Å	8.8110(13)
c/Å	11.1507(13)
α/°	88.116(11)
β/°	77.358(12)
γ/°	68.930(15)
Volume/Å³	625.48(16)
Z	2
ρ$_{calc}$ g/cm³	1.435
μ/mm⁻¹	0.267
F(000)	284.0
Crystal size/mm³	0.256 × 0.210 × 0.203
Radiation	Mo Kα (λ = 0.71073)
2θ range for data collection/°	6.66 to 50.04
Index ranges	−8 ≤ h ≤ 7, −10 ≤ k ≤ 10, −13 ≤ l ≤ 10
Reflections collected	4108
Independent reflections	2204 (R_{int} = 0.0343, R_{sigma} = 0.0743)
Data/restraints/parameters	2204/0/170
Goodness-of-fit on F^2	1.038
Final R indexes [I ≥ 2σ (I)]	R_1 = 0.0422, wR_2 = 0.0974
Final R indexes [all data]	R_1 = 0.0551, wR_2 = 0.1065
Largest diff. peak/hole/e Å⁻³	0.19/−0.23
ETN·TAR	
Empirical formula	$C_{24}H_{32}N_4O_{12}S_2$
Formula weight	632.66
Temperature/K	293(2)
Crystal system	monoclinic
Space group	$P2_1$
a/Å	4.8561(3)
b/Å	24.2003(13)

c/Å	12.1304(6)
α/°	90.00
β/°	92.671(5)
γ/°	90.00
Volume/Å³	1424.00(14)
Z	2
ρ_{calc} g/cm³	1.475
μ/mm⁻¹	0.257
F(000)	664.0
Crystal size/mm³	0.42 × 0.41 × 0.21
Radiation	Mo Kα (λ = 0.71073)
2θ range for data collection/°	6.72 to 50.04
Index ranges	−4 ≤ h ≤ 5, −28 ≤ k ≤ 26, −14 ≤ l ≤ 14
Reflections collected	11036
Independent reflections	4925 (R_{int} = 0.0420, R_{sigma} = 0.0)
Data/restraints/parameters	4925/1/395
Goodness-of-fit on F^2	1.036
Final R indexes [I ≥ 2σ (I)]	R_1 = 0.0475, wR_2 = 0.0852
Final R indexes [all data]	R_1 = 0.0659, wR_2 = 0.0918
Largest diff. peak/hole/e Å⁻³	0.23/−0.22
Flack parameter	0.07(7)

ETN·TAR presents a kryptoracemic structure, and the absence of an inversion center (although quite certain from the near 0 Flack parameter)[29] or other second-type symmetry elements has been checked by pseudosymmetry search using the PSEUDO program[30] of Bilbao Crystallographic Server, and no centrosymmetric supergroup compatible with the experimental atomic positions has been found.

Powder diffractograms were obtained on the same Gemini R Ultra diffractometer (Rigaku Oxford Diffraction, Abingdon, Oxfordshire, England),

equipped with an X-ray source using Cu Kα radiation (λ = 1.54 Å). Data were collected and processed through the CrysAlisPro software.

CCDC accession codes 2019883, 2019884 and 2019885 contain the supplementary crystallographic data for ETN·MAL, ETN·GLU and ETN·TAR, respectively. These data can be obtained free of charge *via* www.ccdc.cam.ac.uk/data_request/cif, or by e-mailing data_request@ccdc.cam.ac.uk, or by contacting The Cambridge Crystallographic Data Centre, 12 Union Road, Cambridge CB2 1EZ, UK; fax: +44 1223 336033.

3.2.3.2 Solid-state NMR measurements

^{13}C CPMAS and ^{15}N CPMAS SSNMR spectra were collected on a Bruker Avance II 400 Ultra Shield instrument (Bruker, Billerica, MA, USA), working at 400.23, 100.63, and 40.56 MHz for ^{1}H, ^{13}C and ^{15}N, respectively. Samples were packed in cylindrical zirconia rotors (4 mm o.d., Bruker, Billerica, MA, USA), with a sample volume of 80 µL. ^{13}C and ^{15}N spectra were acquired at room temperature with a rotation frequency of 12 and 9 kHz, respectively. All ^{13}C and ^{15}N experiments employed the RAMP-CP pulse sequence (^{1}H 90° pulse = 3.6 µs; contact time = 4 ms) with the TPPM ^{1}H decoupling (rf field = 69.4 kHz) during the acquisition period. Detailed acquisition parameters (number of scans, relaxation delays, contact times) may be found in Table A2.7. All employed relaxation delay values were optimized on each sample by means of ^{1}H saturation recovery experiments and obtained by multiplying the measured T_1 ^{1}H values by 1.27, to ensure full relaxation. ^{13}C and ^{15}N chemical shift scales were referenced with the resonance of glycine (^{13}C methylene signal at 43.5 ppm), $(NH_4)_2SO_4$ (^{15}N signal at 24.6 ppm with respect to NH_3), respectively, as external standards.

3.2.3.3 Thermal analyses

TGA measurements (TA Instruments, New Castle, UK) were performed over a temperature range of 30–350 °C under a 50 mL·min^{-1} N$_2$ flow, on a Q600 SDT TA instrument equipped with a DSC heat flow analyzer. Samples (5–10 mg of weight) were placed into the furnace inside alumina crucibles and heated with a ramp of 10 °C·min^{-1}.

DSC curves were collected on a DSC Q200 TA Instrument (TA Instruments, New Castle, UK). Samples were accurately weighed (5–10 mg) and put into sealed aluminum pans. Calibration for temperature and heat flow was performed using high purity standards of *n*-decane, benzene and indium. All measurements were performed in a 30–350 °C temperature range, with heating rates of 10 °C·min^{-1}.

3.2.3.4 Dissolution Kinetic Tests (DKTs)

DKTs were carried out in phosphate buffer (pH = 7.4). For each measurement, 4 mg of either ETN or its adducts were added to 100 mL of the thermostatically controlled (at 37 °C) dissolution medium. Dissolution parameters were evaluated for 60 min. The solution was kept homogeneous by continued stirring at 100 rpm, and concentrations were measured using an optical fiber system (HELLMA, Milan, Italy) linked to a spectrophotometer. UV measurements (ZEISS, Wetzlar, Germany) were performed at the maximum absorption wavelength of ETN, namely 288 nm. A calibration curve (Figure A2.5) was obtained with five diluted ETN solutions in phosphate buffer (the concentrations used were the following: 8, 10, 16, 20 and 40 mg/L), while pure phosphate buffer was used as the blank.

3.3 Results and Discussion

Three novel crystal forms were obtained by means of solution or mechanochemical techniques. These are a salt of ETN with malonic acid (ETN·MAL), a cocrystal between ETN and glutaric acid (ETN·GLU) and a salt cocrystal of ETN with tartaric acid (ETN·TAR). Two crystal forms of ETN were reproduced from the literature, namely a salt of ETN with maleic acid (ETN·MLE)[27] and a cocrystal between ETN and fumaric acid (ETN·FUM).[26] Table 3.2 summarizes the techniques used for preparing the new crystal forms and the outcome, in terms of stoichiometry and ionization state.

Table 3.2 Summary of the employed techniques used for the solid-state preparations, with final stoichiometry and ionization state for all obtained adducts.

Crystal Form	Preparation Technique	Final Stoichiometry	Outcome
ETN·GLU	Dry grinding	1:1	Cocrystal
ETN·MAL	Slurry in ethanol	1:1	Salt
ETN·TAR	Slow evaporation from methanol	1:1	Salt cocrystal

The crystal structures of all the adducts were obtained through SCXRD. Moreover, for each adduct, except ETN·TAR, which, despite several attempts, could not be reproduced to undergo further analysis, the XRD powder patterns calculated from crystal structures were compared to the experimental powder diffractograms obtained from bulk powders to confirm that the selected crystals were representative of the whole product (see Figures A2.6–A2.9).

3.3.1 SCXRD

3.3.1.1 ETN·GLU

ETN·GLU crystallizes in the centrosymmetric triclinic space group $P\bar{1}$. The asymmetric unit (Figure 3.1) includes one molecule of ETN and one of GLU, which interact with each other through a HB between pyridinic N5 and one of the carboxylic moieties (d N5–O7' = 2.654 (4) Å). The neutral nature of the adduct is confirmed by the C–O (d C1'–O6' = 1.203 (3) Å, d C1'–O7' = 1.295 (3) Å, d C5'–O9' = 1.315 (3) Å, d C5'–O8' = 1.217 (2) Å) distances, consistent with the distribution of distances obtained by the CSD results for neutral COOH groups; this is supported by the ^{15}N CPMAS NMR spectrum as well (see the SSNMR paragraph). Notably, ETN displays rotational disorder around the axis formed by atoms C1, C2, N5 and O7', as represented by the doubling of the thermal ellipsoids (Figure 3.1).
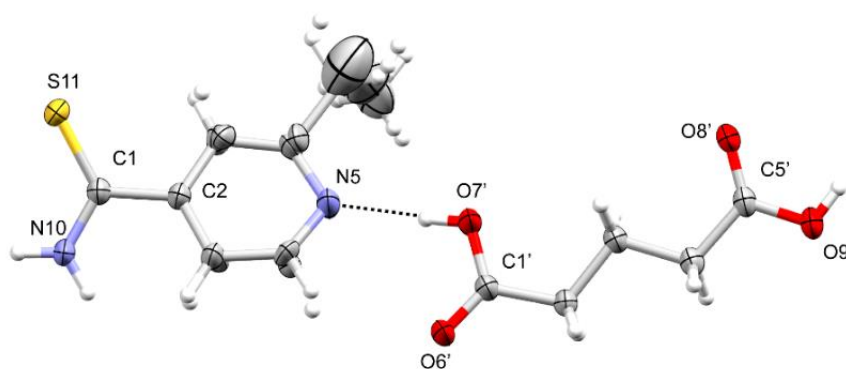
Figure 3.1 Asymmetric unit of ETN·GLU.

The HB pattern (Figure 3.2) is characterized by the presence of a centrosymmetric $R_2^2(8)$ dimer, formed between the carboxylic groups of two GLU molecules (d O8'–O9' = 2.667 (4) Å). Additionally, the COOH groups of GLU molecules, that are not involved in the formation of the dimers, interact with the NH$_2$ groups (d N10–O6' = 2.932 (4) Å) and with the pyridinic N5

(see above) of two different ETN molecules. The result is the formation of $R_4^4(22)$ cyclic motifs, as visible in Figure 3.2.
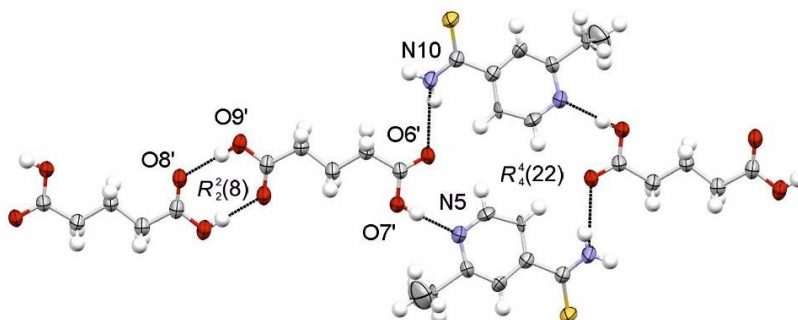

Figure 3.2 Hydrogen bond (HB) pattern of ETN·GLU, highlighting the centrosymmetric $R_2^2(8)$ dimer and the $R_4^4(22)$ cyclic motif.

3.3.1.2 ETN·MAL

ETN·MAL crystallizes in the centrosymmetric triclinic space group $P\bar{1}$. The asymmetric unit (Figure 3.3) contains one ETN molecule, protonated on N5 (d N5–O7′ = 2.657(4) Å) and one MAL molecule, characterized by a carboxylate group (d C3′–O7′ = 1.264(3) Å and C3′–O6′ = 1.234(3) Å) and a carboxylic moiety (d C1′–O4′ = 1.196 (3) Å and d C1′–O5′ = 1.329 Å).
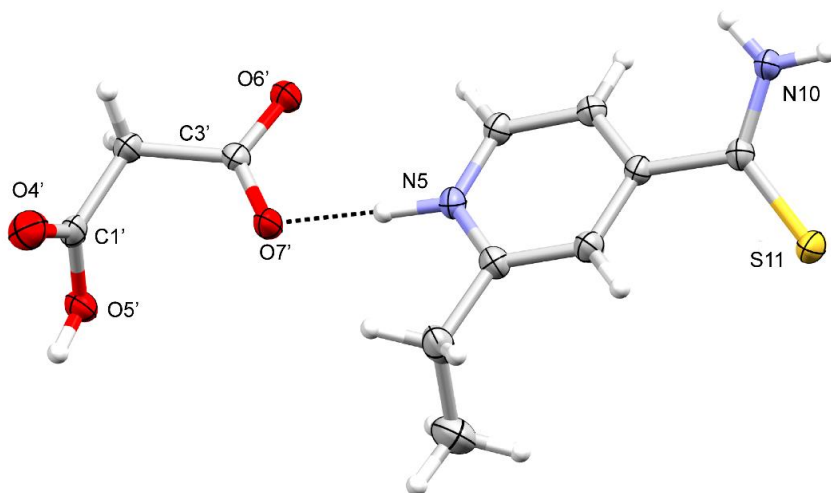
Figure 3.3 Asymmetric unit of ETN-MAL.

The HB pattern (Figure 3.4) is characterized by the presence of two O–H⋯O⁻ interactions between two molecules of MAL through their COOH and COO⁻ groups, which form a centrosymmetric $R_2^2(12)$ dimer (d O6'–O5' = 2.653 (3) Å). The carboxylate group also interacts with the N5 and N10 centers of ETN molecules forming N5⁺–H⋯O⁻ and N10–H⋯O contacts (d N5–O6' = 2.657 (4) Å; d N10–O7' = 2.844 (4) Å), leading to the formation of the $R_4^4(22)$ cyclic motifs already observed in ETN·GLU.
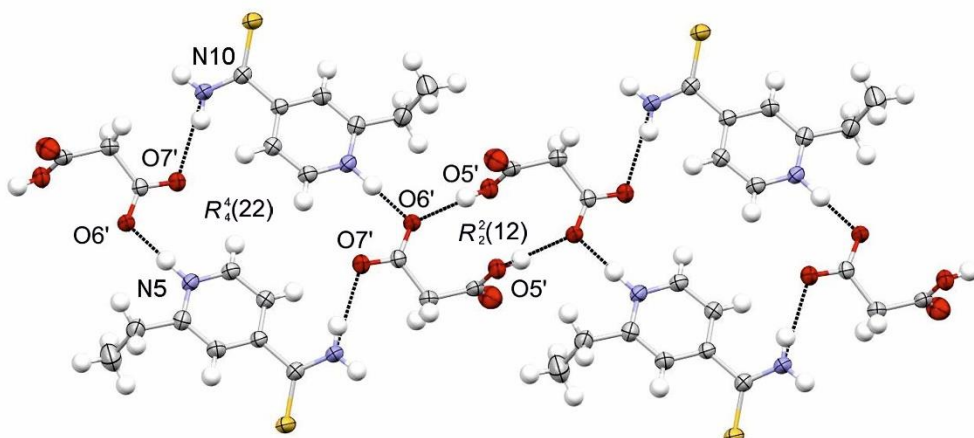
Figure 3.4 HB pattern of ETN·MAL, highlighting the centrosymmetric $R_2^2(12)$ dimer and the $R_4^4(22)$ cyclic motif.

3.3.1.3 ETN·TAR

ETN·TAR crystallizes in a monoclinic non-centrosymmetric $P2_1$ space group. The structure is a kryptoracemate, i.e., a compound that crystallizes in a non-centrosymmetric space group containing only symmetry elements of the first type (Sohnke group), despite containing both the enantiomers of a molecule in the same lattice.[31] This phenomenon is still rarely detected in both organic[31] and organometallic[32] crystals (0.1% of all the structure reported in the CSD database), although some attempt to rationally develop some functional material based on this peculiarity has been considered.[33,34] Its explanation is deeply debated, although it is clearly related to the existence of high Z' structures and pseudosymmetry.[35] However, the existence of the first kryptoracemic cocrystal has been reported only in 2016,[28] making our result quite peculiar. In the asymmetric unit (Figure 3.5), four molecules are present: two ETN molecules and two TAR molecules (both enantiomers).
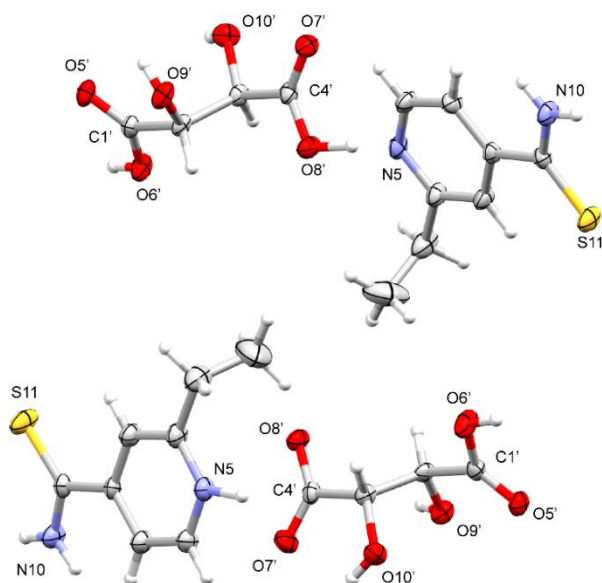
Figure 3.5 Asymmetric unit of ETN·TAR.

The two crystallographically independent TAR molecules significantly differ in the C–O distances of the carboxylic moieties. Indeed, for one molecule (top in Figure 3.5), d C4′–O7′ = 1.215 (2) Å, d C4′–O8′ = 1.291 (2) Å, d C1′–O6′ = 1.325 (2) Å and d C1′–O5′ = 1.211 (2) Å, while, for the other one (bottom in Figure 3.5), d C1′–O5′ = 1.188 (2) Å, d C1′–O6′ = 1.327 (2) Å, d C4′–O7′ = 1.228 (2) Å and d C4′–O8′ = 1.260 (2) Å. This introduces a degree of uncertainty in the position of the H atoms along the HB axes, which makes it complicated to assess the neutral or ionic nature of the adduct. Unfortunately, it was not possible to confirm those positions by means of SSNMR. As far as the X-ray analysis is concerned, the structure can be defined as a salt cocrystal as ETN is present is in both its neutral and ionic forms. In the HB pattern (Figure 3.6), chains of alternated ETN and TAR molecules are present. They are linked by HB N5$^+$–H···O$^-$ interactions and $R_2^2(8)$ motifs involving the thioamidic (ETN) and the carboxylic (TAR) groups. Since TAR is

present in both its enantiomeric forms, the two strands differ in terms of chirality, making the distances not equivalent. The bottom molecule in Figure 3.5 displays the following distances: d N5–O8' = 2.571 (4) Å, d S11–O6' = 3.144 (2) Å and d N10–O5' = 3.025 (4) Å. The top molecule in Figure 3.5 presents the following distances: d N5–O8' = 2.549 (4) Å, d S11–O6' = 3.088 (2) Å and d N10–O5' = 2.960 (4) Å.

The chains interact with a complex pattern of HBs involving all OH and carboxylic groups of TAR and the thioamidic group of ETN.
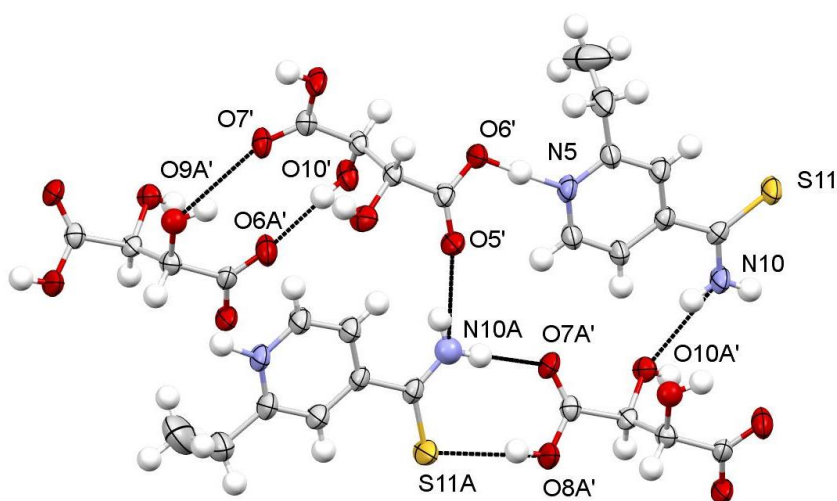

Figure 3.6 HB interactions between chains in ETN·TAR.

The presence of both enantiomers of TAR distinguishes the chains in the disposition of the OH groups, generating a double layer (Figure 3.7).
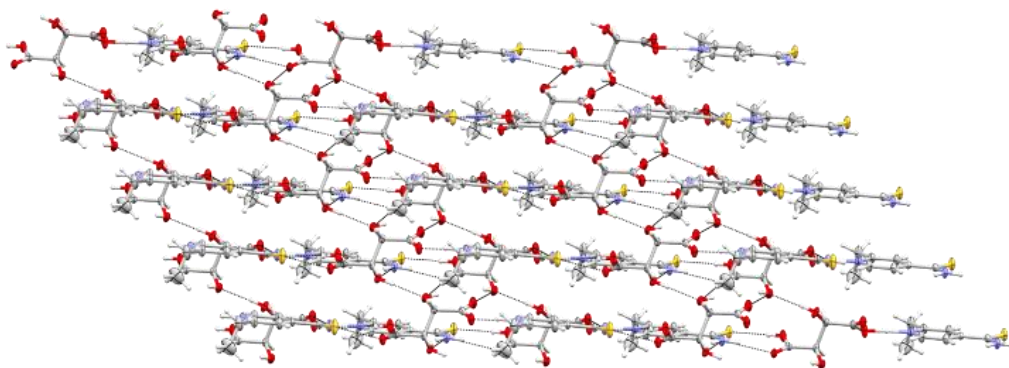
Figure 3.7 Links between chains through HBs in ETN·TAR.

The structures of ETN·FUM and ETN·MLE are already discussed in references 26 and 27. For the sake of clarity, the asymmetric units and the HB networks are reported in Figures A2.10–A2.13.

3.3.2 SSNMR

SSNMR was useful to verify the neutral or ionic nature of all adducts, except ETN·TAR, strengthening the X-ray evidence.[36–39] Indeed, the position of the H atoms along the HB axis was not always clearly detected from X-ray analyses. Through 1D ^{13}C CPMAS (Figure 3.8) and ^{15}N CPMAS (Figure 3.9) experiments, the SSNMR analysis focused on the ^{13}C resonances of the carboxylic groups of the acids and the ^{15}N signals of N5 (pyridinic) and N10 (thioamidic) of ETN. Indeed, these chemical shifts are very sensitive to the protonation state of the corresponding moieties.[37] All ^{13}C and ^{15}N chemical shifts with their relative assignments are reported in Table 3.3.
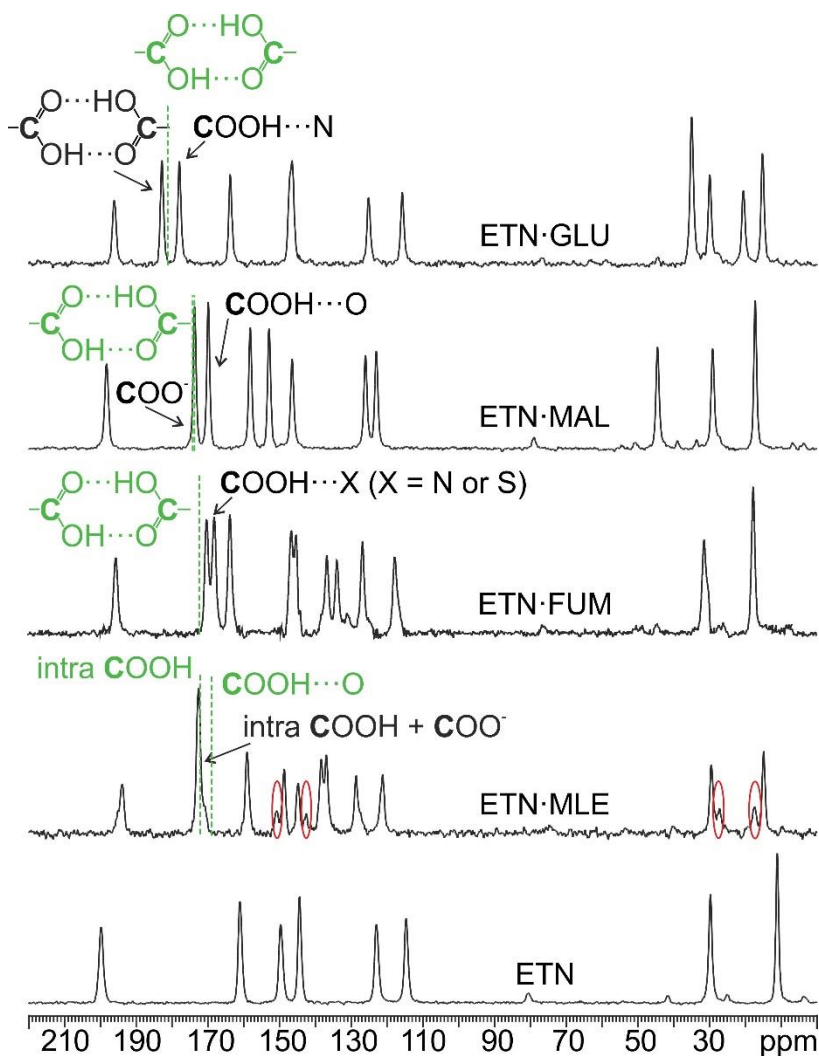
Figure 3.8 ¹³C CPMAS spectra of the analyzed compounds. Dashed green lines and green writings refer to carboxylic signals of the pure acids. Red ovals highlight extra peaks due to crystalline disorder.
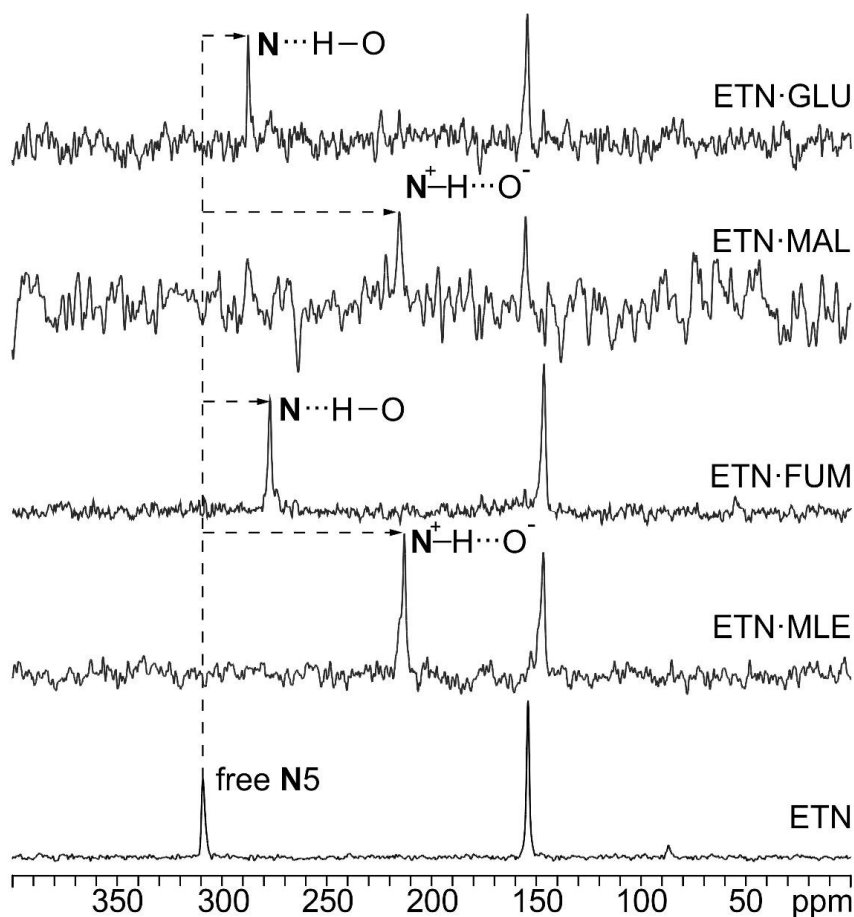
Figure 3.9 ^{15}N CPMAS spectra of the analyzed compounds. Dashed lines highlight the chemical shift of N5 in pure ETN.

Table 3.3 ^{13}C and ^{15}N SSNMR chemical shift values for all analyzed powders. The atom numbering is referred to as Scheme 3.1.

Atom	ETN (ppm)	MAL (ppm)	GLU (ppm)	MLE (ppm)	FUM (ppm)	ETN·MAL (ppm)	ETN·GLU (ppm)	ETN·MLE (ppm)	ETN·FUM (ppm)
					^{13}C				
1	199.7					198.1	196	193.8	195.3
2	149.6					152.8	147	148.6	146.4
3	122.9					125.9	125.1	128.5	126.6
4	161					158	163.6	159	163.5
6	144.4					146.4	146.4	144.7	144.9
7	114.6					122.9	115.7	121.1	117.6

8	29.7					29.1	29.9	29.5	31.3
9	11.1					17.2	15.2	14.9	17.6
1'		174.3	181.4	169.2	172.3	169.8	177.8	172.5	167.9
2'		40.6	33.8	133.1	136.2	44.5	34.9	136.8	133.7
3'		174.8	18.7	140	136.2	173.6	20.6	138.2	136.4
4'			33.8	172.7	172.3		34.9	172.5	170
5'			181.4				182.7		
^{15}N									
5	308.9					215.4	287.4	212.7	276.9
10	153.8					154.6	153.8	146.2	146.2

[13]C CPMAS spectra offer the chance to assess the involvement of the carboxylic groups of the coformers in deprotonation or HB contacts. The spectrum of ETN·GLU exhibits two carboxylic resonances at 182.7 and 177.8 ppm. This can be explained by the variation in the network of interactions engaging the two COOH moieties. The former is assigned to a COOH group (182.7 ppm) forming a homodimeric $R_2^2(8)$ synthon with neighboring GLU molecules, as also observed in pure GLU (181.4 ppm).[40] This translates into high-frequency chemical shifts for carboxylic groups, comparable to those typical of carboxylate moieties.[37] In ETN·GLU, the second resonance (177.8 ppm) is typical of neutral COOH groups, in this case engaging in a COOH···N HB. This nicely agrees with X-ray data as in the case of ETN·MAL. As a matter of fact, pure MAL displays carboxylic homodimers (δ = 174.3/174.8 ppm),[41] while, in ETN·MAL, we attribute the signal at 173.6 ppm to a COO⁻ group and the remaining peak (169.8 ppm) to a COOH moiety involved in a $R_2^2(12)$ dimeric COOH···O HB. Homodimers are also characteristic of pure FUM[42] (172.3 ppm); on the contrary, in ETN·FUM,[26] both COOH groups stay protonated and are no longer involved in homodimeric interactions, which explains the low-frequency shift of their resonances (170.0 and 167.9 ppm). Pure MLE represents an exception, since it does not exhibit homodimeric synthons,[43] which justifies the relatively low chemical shift of one of the COOH groups (169.2 ppm); the other COOH is involved in a COOH···O

intramolecular interaction, bringing its chemical shift up to 172.7 ppm. In ETN·MLE,[27] a single resonance can be observed, at 172.5 ppm. This can be traced back to the high symmetry of the hydrogenmaleate group, which leads the two carboxylic groups to be very similar (d C4′–O8′= 1.272 Å; d C4′–O7′= 1.241 Å and d C1′–O6′= 1.285 Å; d C1′–O5′= 1.233 Å, atom numbering in Figure A2.12) despite the deprotonation of one of them. Notably, the spectrum of the salt exhibits extra peaks in the aliphatic and aromatic regions with lower intensity, specifically those centered at about 17, 27, 142 and 151 ppm (highlighted with red ovals in Figure 3.8). These are due to disorder associated to the ethyl and pyridyl groups, as also observed in the crystal structure (see Figure A2.12).

In SSNMR, the ^{15}N chemical shift is recognized as being particularly sensitive and highly reliable on the position of neighboring protons.[37] As indicated by the drastic low-frequency shift ($\Delta\delta > 80$ ppm) of the N5 signal of ETN from 308.9 ppm (pure ETN) to 215.4 ppm (ETN·MAL) and 212.7 ppm (ETN·MLE), the two adducts are confirmed to be salts, in fair agreement with X-ray measurements;[27] in ETN·FUM and ETN·GLU, the N5 signal shifts to lower frequencies as well (276.9 and 287.4 ppm, respectively), but the variation is lower than for ETN·MAL or ETN·MLE ($\Delta\delta \sim 32$ and 21 ppm), and it is consistent with the formation of a HB involving N5 rather than a proper proton transfer.[26] This indicates the neutral nature of ETN·FUM and ETN·GLU, which are to be considered cocrystals, confirming the X-ray findings.

3.3.3 Thermal analyses

Thermal analyses were run to evaluate the thermal behavior of the adducts with respect to pure ETN, which melts at 165.6 °C. The corresponding curves are reported in Figures A2.14–A2.21. Table 3.4 reports all the obtained values. In all cases, endothermic DSC peaks, corresponding to lower melting points than for pure ETN, are observed. This behavior is

74

recurrent for ETN as all the adducts reported in literature are characterized by lower melting points.[16,25–27]

Table 3.4 TGA onset points and DSC signal max values for pure ETN and all obtained adducts. See Figures A2.14–A2.21.

TGA Onset Points (°C)		DSC Signal Max (°C)	
ETN	195.1	ETN	165.6
ETN·FUM	183.6	ETN·FUM	148.9
ETN·GLU	191	ETN·GLU	105.6
ETN·MLE	162.8	ETN·MLE	142.3
ETN·MAL	165.2	ETN·MAL	95.2

3.3.4 Dissolution kinetic tests

The dissolution rate for all obtained adducts, except for ETN·TAR, was evaluated in order to assess its variation with respect to pure ETN. Dissolution tests were already performed at pH = 1.2 for ETN·FUM[23] and ETN·GLU.[23] To the best of the authors' knowledge, this is the first time they are conducted at physiological pH values (7.4). Concentrations (mg/L) were plotted against time (min), as shown in Figure 3.10. The dissolution rate of ETN in ETN·MLE is the highest among the obtained adducts. Nonetheless, a significant improvement in the dissolution rate of ETN is observed for all of them. The ratios between the Area Under the Curve (AUC) values of each adduct and pure ETN are reported in Table 3.5. This parameter allows one to assess the increase in the *in vitro* bioavailability of ETN in the crystal forms.[44] In all cases, a remarkable increase from two up to eight times is observed.
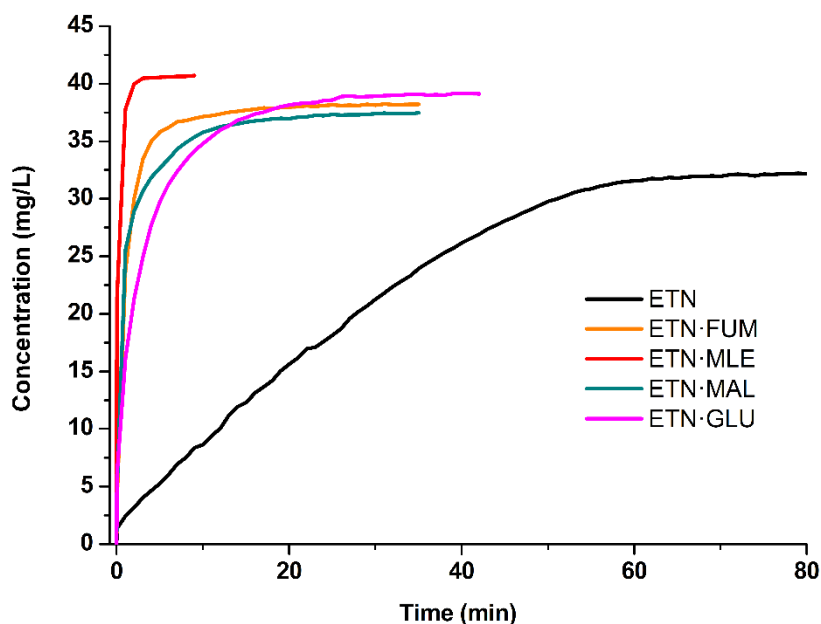
Figure 3.10 Dissolution profiles of pure ETN and all obtained adducts.

Table 3.5 Normalized Area Under the Curve (AUC) values obtained by the dissolution curves of the obtained ETN adducts.

	AUC/AUC$_{ETN}$
ETN·FUM	2.7
ETN·GLU	2.3
ETN·MLE	7.8
ETN·MAL	2.6

3.4 Conclusions

ETN proved promising to engineer new crystal forms with enhanced physicochemical properties. The presence in its molecular structure of a thioamidic moiety and of a heterocyclic N atom makes it easy to salify or cocrystallize with dicarboxylic acids. Three new crystal forms were obtained—

namely, a salt (ETN-MAL), a cocrystal (ETN-GLU) and a salt-cocrystal (ETN-TAR). As in all cases reported in the literature, in ETN-MAL and ETN-TAR, N5 is protonated, while, in ETN-GLU and ETN-TAR, COOH···N and C=O···HN contacts are present. The salt cocrystal with TAR presents the rare characteristic to be a kryptoracemic cocrystal, a racemate that crystallizes into a Sohnke group; this behavior can be attributed to the concomitant presence of both the enantiomers in the asymmetric unit with some degree of distortion between each other, preserving their generation through an inversion center, a mirror plane or a glide.

The solid-state characterization of all the adducts was performed by SCXRD analyses and supported by ^{13}C and ^{15}N CPMAS SSNMR experiments. The latter are particularly informative, since they provide unambiguous results. These made it possible to assess the purity, the degree of crystallinity and the ionic/neutral nature, clarifying the exact position of protons, which were often uncertain in the obtained X-ray structures.

As for their physicochemical properties, all analyzed adducts show lower melting points than pure ETN. In this sense, by also comparing literature data (more than 10 adducts), we can affirm that cocrystallization systematically decreases its melting point. The dissolution profile for each analyzed adduct was evaluated. Their dissolution rates all proved significantly higher than for the pure API. In particular, ETN·MLE stands out as eight times more bioavailable (*in vitro*) than pure ETN.

References

1   G. R. Desiraju; J. J. Vittal; A. Ramanan, *Crystal Engineering: A Textbook*; World Scientific Publishing, Singapore, **2011**.

2   H. Qiu; R. B. Patel; R. S. Damavarapu; V. Stepanov, *CrystEngComm* **2015**, *17*, 4080–4083.

3   S. Cherukuvada; R. Kaur; T. N. Guru Row, *CrystEngComm* **2016**, *18*, 8528–8555.

4   F. Grifasi; M. R. Chierotti; K. Gaglioti; R. Gobetto; L. Maini; D. Braga; E. Dichiarante; M. Curzi, *Cryst. Growth Des.* **2015**, *15*, 1939–1948.

5   K. Gaglioti; M. R. Chierotti; F. Grifasi; R. Gobetto; U. J. Griesser; D. Hasa; D. Voinovich, *CrystEngComm* **2014**, *16*, 8252–8262.

6   S. Golob; M. Perry; M. Lusi; M. R. Chierotti; I. Grabnar; L. Lassiani; D. Voinovich; M. J. Zaworotko, *J. Pharm. Sci.* **2016**, *105*, 1–8.

7   S. Bordignon; P. Cerreia Vioglio; E. Priola; D. Voinovich; R. Gobetto; Y. Nishiyama; M. R. Chierotti, *Cryst. Growth Des.* **2017**, *17*, 5744–5752.

8   J. Lu; S. Rohani, *Org. Process. Res. Dev.* **2009**, *13,* 1269–1275.

9   D. Braga; E. Dichiarante; G. Palladino; F. Grepioni; M. R. Chierotti; R. Gobetto; L. Pellegrino, *CrystEngComm* **2010**, *12*, 3534–3536.

10 C. Chen; S. Ghosh; C. Malla Reddy; M. J. Buehler, *Phys. Chem. Chem. Phys.* **2014**, *16*, 13165–13171.

11 I. J. Onakpoya; C. J. Heneghan; J. K. Aronson, J. *BMC Med.* **2016**, *14*, 10.

12 J. A. DiMasi; H. G. Grabowski; R. W. Hansen, *J. Health Econ.* **2016**, *47*, 20–33.

13 E. J. Griffen; A. G. Dossetter; A. G. Leach; S. Montague, *Drug Discov. Today* **2018**, *23*, 1373–1384.

14 L. M. McNamee; M. J. Walsh; F. D. Ledley, *PLoS ONE* **2017**, *12*, e0177371.

15 S. Domingos; V. André; S. Quaresma; I. C. B. Martins; M. F. Minas da Pietade; M. T. Duarte, *J. Pharm. Pharmacol.* **2015**, *67*, 830–846.

16 D. Bernasconi; S. Bordignon; F. Rossi; E. Priola; C. Nervi; R. Gobetto; D. Voinovich; D. Hasa; N. Tuan Dong; Y. Nishiyama; M. R. Chierotti, *Cryst. Growth Des.* **2020**, *20*, 906–915.

17 A. O. Surov; K. A. Solanko; A. D. Bond; A. Bauer-Brandl; G. L. Perlovich, *CrystEngComm* **2016**, *18*, 4818–4829.

18 L. F. Diniz; M. S. Souza; P. S. Carvalho Jr.; C. C. P. da Silva; R. F. D'Vries; J. Ellena, *J. Mol. Struct.* **2018**, *1153*, 58–68.

19 R. Takuria; B. Sarma, *Crystals* **2018**, *8*, 101–139.

20   T. Grecu; H. Adams; C. A. Hunter; J. F. McCabe; A. Portell; R. Prohens, *Cryst. Growth Des.* **2014,** *14*, 1749–1755.

21   Y. Adebayo Adebisi; I. Agumage; T. D. Sylvanus; I. J. Nawaila; W. A. Ekwere; M. Nasiru; E. E. Okon; A. M. Ekpenyong; D. E. Lucero-Prisno III, *Int. J. Infect.* **2019**, *6*, e92250–e92257.

22   M. Allèaume; F. Leroy; M. Gadret; M. Goursolle, *Acta Crystallogr. Sect. B* **1973**, *29*, 1994–2000.

23   J. C. Colleter; M. Gadret, *Acta Crystallogr. Sect. B* **1968**, *24*, 513–519.

24   J. C. Colleter; M. Gadret, *Acta Crystallogr. Sect. B* **1968**, *24*, 519–525.

25   L. F. Diniz; P. S. Carvalho Jr.; C. C. de Melo; J. Ellena, *J. Mol. Struct.* **2017**, *1137*, 119–125.

26   M. K. Chaitanya Mannava; K. Suresh; A. Nangia, *Cryst. Growth Des.* **2016**, *16*, 1591–1598.

27   C. C. De Melo; C. C. P. da Silva; C. C. S. S. Pereira; P. C. P. Rosa; J. Ellena, *Eur. J. Pharm. Sci.* **2016**, *81*, 149–156.

28   U. B. R. Khandavilli; M. Lusi; B. R. Bhogala; A. R. Maguire; M. Stein, *Chem. Commun.* **2016**, *52*, 8309–8312.

29   H. D. Flack; G. Bernardinelli; D. A. Clemente; A. Linden; A. L. Spek, *Acta Crystallogr. Sect. B* **2006**, *62*, 695–701.

30   C. Capillas; E. S. Tasci; G. de la Flor; D. Orobengoa; J. M. Perez-Mato; M. I. Aroyo, *Z. Kristallogr.* **2011**, *226*, 186–196.

31   L. Fábián; C. P. Brock, *Acta Crystallogr. Sect. B* **2010**, *66*, 94–103.

32   I. Bernal; S. Watkins, *Acta Crystallogr. Sect. C* **2015**, *71*, 216–221.

33   R. Gautier; J. M. Klingsporn; R. P. Van Duyne; K. R. Poeppelmeier, *Nat. Mat.* **2016**, *15*, 591–592.

34   R. Gautier; A. J. Norquist; K. R. Poeppelmeier, *Cryst. Growth Des.* **2012**, *12*, 6267–6271.

35   B. Dalhus; C. H. Görbitz, *Acta Crystallogr. Sect. B* **2000**, *56*, 715–719.

36   F. G. Vogt; J. S. Clawson; M. Strohmeier; A. J. Edwards; T. N. Pham; S. A. Watson, *Cryst. Growth Des.* **2009**, *9*, 921–937.

37   P. Cerreia Vioglio; M. R. Chierotti; R. Gobetto, *Adv. Drug Delivery Rev.* **2017***, 117*, 86–110.

38   Y. Xu; S. A. Southern; P. M. J. Szell; D. L. Bryce, *CrystEngComm* **2016**, *18*, 5236–5252.

39   S. D. Gumbert; M. Körbitzer; E. Alig; M. U. Schmidt; M. R. Chierotti; R. Gobetto; X. Li; J. van de Streek, *Dyes Pigm.* **2016**, *131*, 364–372.

40   P. Espeau; P. Négrier; Y. Corvis, *Cryst. Growth Des.* **2013**, *13*, 723–730.

[41]   J. A. Goedkoop; C. H. MacGillavry, *Acta Crystallogr.* **1957**, *10*, 125–127.

[42]   A. L. Bednowitz; B. Post, *Acta Crystallogr.* **1966**, *21*, 566–571.

[43]   M. Shahat, *Acta Crystallogr.* **1952**, *5*, 763–768.

[44]   S. Fahmy; E. Abu-Gharbieh, *BioMed Res. Int.* **2014**, 590848.

Chapter 4

Beyond the pK_a rule: driving protonic transfer in the ethionamide-salicylic acid system

4.1 Introduction

Crystal engineering has established itself as a valuable tool in the design of functional molecular solids. In particular, tuning physicochemical properties of a crystalline material by changing the arrangement of its components, based on their molecular shapes and functional groups, is of outmost importance in the pharmaceutical industry.[1-3] Indeed, the solubility, stability, bioavailability and manufacturability of an active pharmaceutical ingredient (API) can be properly modified using different solid forms, such as polymorphs, cocrystals and salts.[4-6] In particular, the latter two are examples of multicomponent systems, namely formed by the API and a second GRAS ("Generally Recognized as Safe") molecule, that are neutral in the case of cocrystals or ionic in the case of salts. The distinction between these two types of crystalline forms is crucial for pharmaceutical companies, not only because they are often characterized by different physicochemical and pharmacokinetic performances, but also from the legal and regulatory point of view, connected to intellectual property issues.[7-9] Furthermore, it is also important under an academic perspective, related to the study of structure-property relationships, molecular recognition mechanisms and weak interactions.[9-13] In fact, in many cases, the main distinction between salts and cocrystals depends on whether a complete proton transfer has occurred or not along the axis of a hydrogen bond (HB) interaction between the API and the molecular partner.[14] This will generate ionized species in the former case and neutral ones in the latter. Usually, a specific pair of molecules produces

either a salt or a cocrystal, although the neutral or ionic character of the adduct can be modulated by temperature or stoichiometry.[15,16] However, to the best of our knowledge, there are only four examples in the literature in which the same chemical species can crystallize both as a cocrystal and a salt with the same composition and stoichiometry and at the same temperature: tartaric acid-β-alanine,[17] sulfamethazine-saccharin,[18] isonicotinamide-citric acid[19] and dinitrobenzoic acid-haloanilines.[20] Only for the first two, the authors managed to obtain the salt or cocrystal on purpose, while for the other two cases the achievement remained stochastic.

Here we present the ethionamide (ETH)-salicylic acid (SAL) system, for which we managed to selectively drive the synthesis toward both the salt (ETH$^+$SAL$^-$) and the cocrystal (ETH·SAL) forms. ETH (Scheme 4.1, left) is an important anti-tubercular drug, included in the Essential Medicine List by the World Health Organization. Tuberculosis still represents one of the most dangerous infective diseases and new therapies have continuously been investigated.[21] ETH is an analogue of isoniazid and it is employed specifically for the treatment of multi-drug resistant tuberculosis (MDR-TB).[22,23] Due to its limited water solubility (0.84 mg/mL),[24] and consequent unfavorable bioavailability, ETH has been extensively investigated and a series of cocrystals and salts, both organic and inorganic, have been reported.[25–28] We selected SAL (Scheme 4.1, right) as a coformer since ETH bears a pyridine moiety and the pyridine-carboxylic acid heterosynthon is one of the most robust and reliable available synthon.[29,30] Furthermore, SAL is a GRAS phenolic acid with analgesic and anti-inflammatory properties.[31,32]
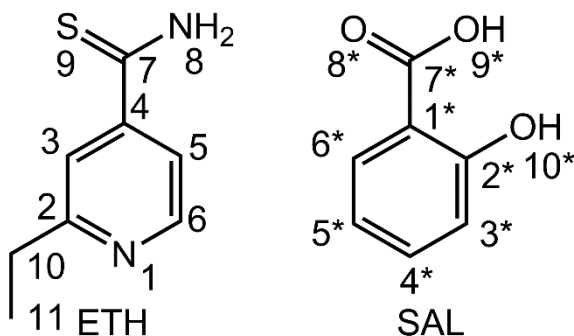
Scheme 4.1 Chemical structures of ethionamide (ETH) and salicylic acid (SAL), with atom numbering.

In order to fully identify and characterize the structural features of the two polymorphs, a complementary X-ray diffraction (PXRD and SC-XRD) and solid-state NMR (SSNMR) approach, supported by DFT calculations, was employed. From the SSNMR point of view, both common and advanced techniques (^{1}H MAS, ^{13}C and ^{15}N CPMAS, ^{1}H-{^{14}N} J- and D-HMQC, ^{1}H-^{14}N PM-S-RESPDOR) were applied to discriminate between the neutral or ionic nature of the adducts. In particular, the ^{1}H-^{14}N PM-S-RESPDOR is a new sequence,[33,34] which allows one to determine ^{1}H-^{14}N distances through the ^{1}H detected signal at a very high spinning speed (70 kHz) and here it was tested on a natural abundance real system.

The relative stability of the two polymorphs was assessed by calorimetric analyses (DSC and TGA), competitive slurry experiment and DFT calculations, while their solubility properties were inquired by dissolution kinetic tests (DKT).

4.2 Materials and methods

SAL (purity > 99%) and all used solvents were purchased from Sigma Aldrich, while ETH (purity > 98%) was purchased from Alfa Aesar. All reagents were used as received, without purification.

4.2.1 Syntheses and competitive slurry

For ETH^+SAL^-, the bulk powder was achieved by kneading 50 mg (0.3 mmol) of ETH and 42 mg (0.3 mmol) of SAL with few drops of MeOH for 20 min. Crystals suitable for SCXRD were obtained through seeding crystallization at room temperature of 5 mL of an iPrOH-MeOH (1:3) solution using the bulk powder as seed.

For ETH·SAL, the bulk powder was prepared by employing a rotavapor for rapid evaporation of 30 mL of a MeOH solution containing 50 mg (0.3 mmol) of ETH and 42 mg (0.3 mmol) of SAL. Single crystals were obtained by evaporation of a MeOH solution at room temperature (5 mL).

For the competitive slurry experiment, a mixture of 40 mg of ETH·SAL and 40 mg of ETH^+SAL^- was stirred with few mL of MeOH. After 48 hours, the resulting sample was filtered and analyzed by FTIR-ATR (see Figure A3.1 in Appendix III).

4.2.2 FTIR-ATR

FTIR-ATR spectra were collected on a Fourier transform Equinox 55 (Bruker) spectrophotometer equipped with an ATR device; the resolution was set at 2 cm^{-1} for all spectra. A spectral range of 400–3800 cm^{-1} was scanned, using KBr as a beam splitter. All spectra were acquired with 16 scans.

4.2.3 X-ray diffraction

Single crystals of ETH·SAL and ETH⁺SAL⁻ were analyzed with a Gemini R Ultra diffractometer operating at 293(2) K, using a Mo Kα source (λ = 0.71073 Å). Data collection and reduction were performed using the CrysAlisPro software.[35] The crystal structures were solved by direct methods and refined with the full matrix least-squares technique on F^2 using the SHELXS-97 and SHELXL-97 programs.[36,37] All non-hydrogen atoms were refined anisotropically; hydrogen atoms bonded to unambiguous sites were placed in geometrical positions and refined using the riding model. Hydrogen atoms between pyridinic nitrogen and carboxylic oxygen sites of nearby molecules were detected in the Fourier maps, and their position was checked through SSNMR. See Table 4.1 for the crystallographic data of ETH⁺SAL⁻ and ETH·SAL, and Tables A3.1a-A3.4a and A3.1b-A3.4b in Appendix III for more details, i.e., bond distances and angles (refer to Scheme 4.1 for the atom numbering). The powder diffractogram of ETH was obtained on the same Gemini R Ultra diffractometer, equipped with an X-ray source using Cu Kα radiation (λ = 1.54 Å). Data were collected and processed through the CrysAlisPro software. The powder patterns of SAL, ETH·SAL and ETH⁺SAL⁻ were obtained on a Philips X'Pert PW3020 Bragg−Brentano instrument, equipped with an X-ray source using Cu Kα radiation (λ = 1.54506 Å) operating at 40 kV and 30 mA. Measurements were carried out in $\theta/2\theta$ mode, with a scanning range of 5−40° for 2θ.

4.2.4 SSNMR measurements

All SSNMR measurements were recorded at room temperature on a solid-state NMR spectrometer (JNM-ECZ600R, JEOL RESONANCE Inc.) at a magnetic field of 14.1 T, equipped with 3.2 or 1 mm ¹H/X double-resonance probes, operating at ¹H, ¹³C, ¹⁵N and ¹⁴N Larmor frequencies of 600.1, 150.9, 60.8 and 43.4 MHz, respectively. For 2D ¹H-{¹⁴N} D-HMQC and PM-S-

RESPDOR experiments, ETH·SAL and ETH$^+$SAL$^-$ were separately packed into 1 mm zirconia rotors and spun at a MAS frequency of 70 kHz. The ^{1}H radio frequency (rf) field for $\pi/2$ and π pulses was 208 kHz for ETH$^+$SAL$^-$ and 278 kHz for ETH·SAL while it was 140 kHz for the SR4$^2_1$ recoupling sequence for both samples. For D-HMQC experiments, the ^{14}N pulse length was 8 µs and the highest technically possible rf power on ^{14}N was used. The mixing time (τ) and recycling delay were (171 µs; 20 s) and (342 µs; 25 s) for ETH$^+$SAL$^-$ and ETH·SAL, respectively. The two-dimensional ^{1}H-{^{14}N} D-HMQC spectra were recorded with 24 scans, 32-42 t_1 points, and rotor-synchronized t_1 increment of 14.3 µs. The dummy scans were 8 and 4 for ETH$^+$SAL$^-$ and ETH·SAL, respectively. The States-TPPI method was employed for the quadrature detection along the indirect dimension. The experimental times were 11.2 hours for ETH$^+$SAL$^-$ and 10.7 hours for ETH·SAL. For PM-S-RESPDOR experiments, the length of the PM pulse was $10t_R$ (0.14 ms) and ^{14}N rf-field was 80 kHz (calibrated through NH$_4$Cl) for both samples. In order for the experiments to reach the steady state, prior to the PM-S-RESPDOR measurements, 32 or 54 dummy scans were applied on ETH$^+$SAL$^-$ and ETH·SAL samples, respectively. The mixing time (τ) was varied from 0 to 1.0 ms for ETH$^+$SAL$^-$ and from 0 to 1.5 ms for ETH·SAL. The number of scans and recycling delays were (32, 75 s) for ETH$^+$SAL$^-$ and (36, 72 s) for ETH·SAL. The total experimental times were 26 and 40 hours for ETH$^+$SAL$^-$ and ETH·SAL, respectively. ^{1}H MAS spectra were performed at 70 kHz with an echo pulse sequence (90°-τ-180°-τ) to remove the probe background (^{1}H 90° pulse = 0.77 µs; 3 transients for all samples). 1D ^{13}C CPMAS and ^{15}N CPMAS measurements were performed on cylindrical 3.2 mm o.d. zirconia rotors with a sample volume of 60 µL spun at 20 (^{13}C) and 12 (^{15}N) kHz. All experiments employed the ramped CP pulse sequence with a ^{1}H 90° pulse of 3.8 µs, a contact time in the range 3.5–4.5 ms, a number of scans in the range 325–1150 for ^{13}C spectra and 1253–13000 for ^{15}N spectra and a recycle delay

86

ranging between 4.2 and 12.5 s, depending on the sample. The two-pulse phase modulation (TPPM) ^{1}H decoupling scheme[38] was used for ^{13}C while SPINAL64[39] was employed for ^{15}N, both with a rf field of 119 kHz. [1]H, ^{13}C, ^{14}N, and ^{15}N chemical shift scales were referenced through the resonances of adamantane (^{1}H signal at 1.87 ppm), glycine (^{13}C methylene signal at 43.5 ppm), $(NH_4)_2SO_4$ (^{14}N signal at 0 ppm and ^{15}N signal at 24.6 ppm with respect to NH_3), respectively, which were used as external standards.

4.2.5 DFT calculations

Periodic lattice calculations were performed with Quantum Espresso version 6.4.1,[40,41] adopting the non-local vdW-DF2 method,[42–48] choosing the b86r functional of Hamada.[49] Geometry optimizations were performed starting from the solid-state crystal structures, with a full geometry optimization with cell relaxation. The relaxed cells are in substantial agreement with experimental data, with a volume smaller of 4.6% and 4.8% for the salt and the cocrystal, respectively. The PBE PAW pseudopotentials from the PS Library 1.0.0[50] were adopted, with a cutoff of 60 Ry. The Brillouin zones were automatically sampled with the Monkhorst–Pack scheme[51] in a similar approach as previously described.[52] Geometry optimizations were performed with a grid mesh of 1×3×1 and 1×2×1 for ETH·SAL and ETH[+]SAL[-], respectively. Magnetic shieldings were calculated using the GIPAW method,[53] with a cut off energy of 80 Ry. The theoretical absolute ^{13}C magnetic shielding (σ) values were converted into the corresponding chemical shifts (δ) using the following conversion: $\delta_{(calc)} = \sigma_{ref} - \sigma$. Here, σ_{ref} is the reference shielding, obtained by plotting the experimental chemical shifts $\delta_{(exp)}$ against the GIPAW-calculated chemical shieldings (σ). A linear regression model with slope constrained to (−1) was applied to find the best fit to the data. The value of σ_{ref} is determined by the intercept with the y

axis.[54,55] The obtained values are 167.13 and 165.86 ppm for the salt and cocrystal, respectively (see Figure A3.2).

4.2.6 Thermal analyses

TGA measurements were performed over a temperature range of 35–350 °C under a 50 mL·min^{-1} N$_2$ flow, on a Q600 SDT TA instrument equipped with a DSC heat flow analyzer. Samples (5–10 mg of weight) were placed into the furnace inside alumina crucibles and heated with a ramp of 10 °C·min^{-1}. DSC curves were collected on a DSC Q200 TA Instrument. Samples were accurately weighed (5–10 mg) and put into sealed aluminum pans. Calibration for temperature and heat flow was performed using high purity standards of *n*-decane, benzene and indium. All measurements were performed in a 40–130 °C temperature range, with heating rates of 10 °C·min^{-1}.

4.2.7 Dissolution kinetic tests (DKTs)

DKT were carried out in phosphate buffer (pH = 7.4). For each measurement, an equivalent amount of solid to give 4 mg of ETH were added to 100 mL of the thermostatically controlled (at 37 °C) dissolution medium. Each test lasted 60 min. The solution was kept homogeneous by continued stirring at 100 rpm, and concentrations were measured using an optical fiber system (HELLMA, Milan, Italy) linked to a spectrophotometer (ZEISS, Germany). UV measurements were performed at the maximum absorption wavelength of ETH, namely 288 nm. A calibration curve (Figure A3.3) was obtained with five diluted ETH solutions in phosphate buffer (the concentrations used were the following: 8, 10, 16, 20 and 40 mg/L), while pure phosphate buffer was used as blank.

Table 4.1 Crystallographic data of ETH⁺SAL⁻ and ETH·SAL.

	ETH⁺SAL⁻	ETH·SAL
Empirical formula	$C_{15}H_{16}N_2O_3S$	$C_{15}H_{16}N_2O_3S$
Formula weight	304.36	304.36
Temperature/K	295	295
Crystal system	monoclinic	monoclinic
Space group	$P2_1/c$	$P2_1/n$
a/Å	13.6128(14)	12.931(6)
b/Å	7.1563(9)	4.3009(14)
c/Å	16.3031(19)	28.040(7)
α/°	90	90
β/°	107.078(12)	92.65(4)
γ/°	90	90
Volume/Å³	1518.2(3)	1557.7(10)
Z	4	4
ρ_{calc} g/cm³	1.332	1.298
μ/mm⁻¹	0.224	0.219
Crystal size/mm³	0.34 × 0.22 × 0.21	0.35 × 0.34 × 0.22
Radiation	Mo Kα (λ = 0.71073)	Mo Kα (λ = 0.71073)
2θ range for data collection/°	6.498 to 50.04	6.824 to 50.044
Reflections collected	6564	6087
Independent reflections	2687 [R_{int} = 0.0510, R_{sigma} = 0.0674]	2742 [R_{int} = 0.0373, R_{sigma} = 0.0484]
Data/restraints/parameters	2687/0/201	2742/0/203
Goodness-of-fit on F^2	1.030	1.028
Final R indexes [I>=2σ (I)]	R_1 = 0.0571, wR_2 = 0.1068	R_1 = 0.0522, wR_2 = 0.1219
Final R indexes [all data]	R_1 = 0.1118, wR_2 = 0.1313	R_1 = 0.0909, wR_2 = 0.1451
Largest diff. peak/hole / e Å⁻³	0.15/-0.17	0.17/-0.17

4.3 Results and discussion

Both the salt (ETH$^+$SAL$^-$) and the cocrystal (ETH·SAL) forms of the ETH-SAL system were selectively obtained. The salt was achieved by manual liquid-assisted grinding (LAG), employing methanol, acetonitrile, dichloromethane or *n*-pentane as solvent. However, this easiness of formation in the solid state was not reflected in solution, since many crystallization trials at room temperature using a variety of polar and apolar solvents failed in giving the compound (see Table 4.2). On the contrary, at first the cocrystal stochastically appeared while trying to crystallize the salt with methanol, ethanol or dichloromethane as solvents (see Table 4.2). To obtain the pure bulk powder, rapid evaporation of a methanol solution by means of a rotary evaporator was employed.[56] The large supersaturation generated in this way ensured quantitative precipitation of ETH·SAL. A competitive slurry experiment in methanol at room temperature (see Figure A3.1 for the FTIR-ATR spectra) confirmed that the salt is the thermodynamic phase while the cocrystal is a kinetic product in these conditions (see Thermal Analyses for further discussion). Therefore, this system seems to follow the Oswald rule of stages,[57,58] which states that the less stable form tends to crystallize first. It is also worth noting that the proton transfer is not influenced by the character of the solvent, i.e., polar/apolar or protic/aprotic. Actually, it is the method itself, promoting either the kinetic or thermodynamic form, that seems to determine the position of the hydrogen atom along the main N···H···O interaction. Although simple grinding is often employed to obtain thermodynamic polymorphs,[59–61] LAG can generate different polymorphs upon changing the solvent.[62,63] In this case, however, all trials led to the same thermodynamically stable polymorph.[64]

Table 4.2 List of the different solvents employed in the two preparation methods, liquid-assisted grinding (LAG) and solution crystallization (SOL), and of the corresponding products.[a]

Solvent	Product (LAG)	Product (SOL)
methanol	salt	SM + cocrystal
ethanol	salt	SM + cocrystal
dichloromethane	salt	SM + cocrystal
acetonitrile	salt	SM
n-penthane	salt	
isopropanol		SM
chloroform		SM
tetrahydrofurane		SM
diethylether		SM

[a] All SOL trials were conducted at room temperature. The products were analyzed by FTIR-ATR (data not shown). SM stands for starting materials.

The outcome of the reaction between an acid and a base has been historically proposed to be predictable, at least to a certain degree, by employing the so called "pK_a rule". Such rule states that the larger the difference between the pK_a values of the two components, the greater the chance to obtain a salt (*vice versa*, cocrystal is favoured).[65–67] According to a model suggested by Cruz-Cabeza *et al*,[66] for -1 < ΔpK_a < 4 the probability of cocrystal or salt formation can be quantitatively computed using the following formula: P_{obs} (AB, %) = −17*ΔpK_a + 72 and P_{obs} (A⁻B⁺, %) = 17*ΔpK_a + 28, respectively. As shown in Table 4.3, the ETH-SAL system well fits in the pK_a model, which calculates an almost equal chance of salt and cocrystal formation. For the sake of comparison, the same model was applied to the other examples of salt/cocrystal polymorphism. It is apparent that all the reported systems fall in the region of uncertain prediction, with ΔpK_a values around 1. This is somewhat expected, since in this region there is not a clear

predominance of either salt or cocrystal formation, meaning that both forms are theoretically obtainable. Although the reported samples are not statistically relevant, satisfying the pK_a rule seems necessary to achieve salt/cocrystal polymorphism. However, it is worth keeping in mind that it is the crystalline environment as a whole that plays a decisive role in defining the hydrogen position along an HB at room temperature, as proposed by Childs and co-workers.[67]

Table 4.3 Cruz-Cabeza model applied on examples of salt-cocrystal polymorphism. (P_{obs} = observed probability)

Adduct	ΔpK_a[a]	P_{obs} (AB, %)	P_{obs} (A⁻B⁺, %)	Expected product
ethionamide salicylic acid	2[b]	38	62	salt or cocrystal
tartaric acid β-alanine	0.63[c,d]	61.3	38.7	salt or cocrystal
sulfamethazine saccharin	0.8[18]	58.4	41.6	salt or cocrystal
isonicotinamide citric acid	0.4[e]	65.2	34.8	salt or cocrystal
3,5-dinitrobenzoic acid 4-iodoaniline	0.99[19]	55.2	44.8	salt or cocrystal
3,5-dinitrobenzoic acid 4-bromoaniline	1.07[19]	53.8	46.2	salt or cocrystal
3,5-dinitrobenzoic acid 4-iodo-2-methylaniline	0.84[19]	57.7	42.3	salt or cocrystal
3,5-dinitrobenzoic acid 4-bromo-2-methylaniline	0.89[19]	56.9	43.1	salt or cocrystal

[a] ΔpK_a = pK_a (protonated base) – pK_a (acid); [b] pK_a (ethionamide) = 5.0;[24] pK_a (salicylic acid) = 3;[31] [c] pK_a (β-alanine) = 3.63;[76] pK_a (tartaric acid) = 3.0.[77] [d] For β-alanine, the selected pK_a value is relative to the carboxylic group. In fact, a careful analysis of the reported structures indicates that, in the salt, the transferred proton is shared between the carboxylate moieties of two zwitterionic β-alanine molecules. [e] pK_a (isonicotinamide) = 3.45[78] (calculated); pK_a (citric acid) = 3.05[78] (calculated).

The appearance of the new crystalline forms was confirmed by different techniques, namely FTIR-ATR (Figure A3.4 in Appendix III), PXRD

(Figures A3.5-A3.6) and solid-state NMR (SSNMR) (see below). The ionic or neutral character of the products was investigated by SC-XRD, supported by ^{15}N CPMAS, ^{1}H-$\{^{14}$N$\}$ D-HMQC and N-H distances measurements by ^{14}N-^{1}H PM-S-RESPDOR SSNMR experiments, which account for very accurate ^{1}H-^{14}N distance values on natural abundance samples.[33,34] For both forms, the comparison of the experimental and calculated PXRD patterns (Figures A3.5-A3.6) indicates that the single crystal structures are representative of the bulk powders.

4.3.1 Crystal structure analysis

Yellow block-shaped crystals of ETH^{+}SAL^{-}, suitable for SC-XRD, were obtained by crystallization from an iPrOH-MeOH (1:3) solution with the addition of a seed of the ground powder. It crystallizes in a monoclinic $P2_1/c$ space group (see Table A3.1a in the Appendix III) with one ETH cation and one SAL anion in the asymmetric unit (Figure 4.1, top). The S1 sulfur is disordered over two positions. The main intermolecular interaction is the predicted charge-assisted heterosynthon O9*⋯H-N1 (O9*⋯N1 = 2.592(4) Å), as shown by the similar C-O distances of the carboxylate moiety (C7*-O8* = 1.234(4) Å and C7*-O9* = 1.278(3) Å), and the ^{14}N-^{1}H distance by PM-S-RESPDOR SSNMR analysis (see below). These distances are consistent with a proton transfer to the ETH pyridinic nitrogen. A weaker HB is also observed between the ETH thioamidic group as donor and a carboxylate of a second SAL anion as acceptor (O8*⋯N8 = 2.868(4) Å). This secondary HB interaction involving the SAL carboxylate, which is absent in the cocrystal (see below), helps in favoring the proton transfer and in stabilizing the charged species.[68] The analysis of the crystal packing (Figure 4.1, middle) highlights the presence of $R_4^4(22)$, tetrameric rings, formed by pairs of ETH^{+}SAL^{-} units, and a contribute from π- π stacking interactions (Figure 4.1, bottom) between contiguous rings (intercentroid distances: 3.615(4) Å and 3.588(4) Å).

94
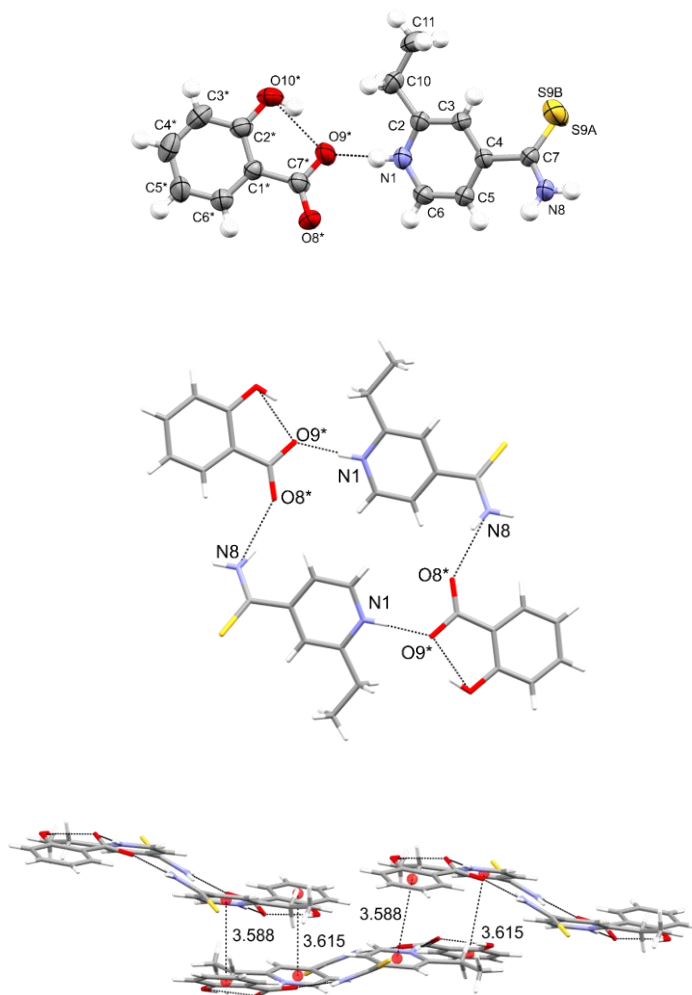
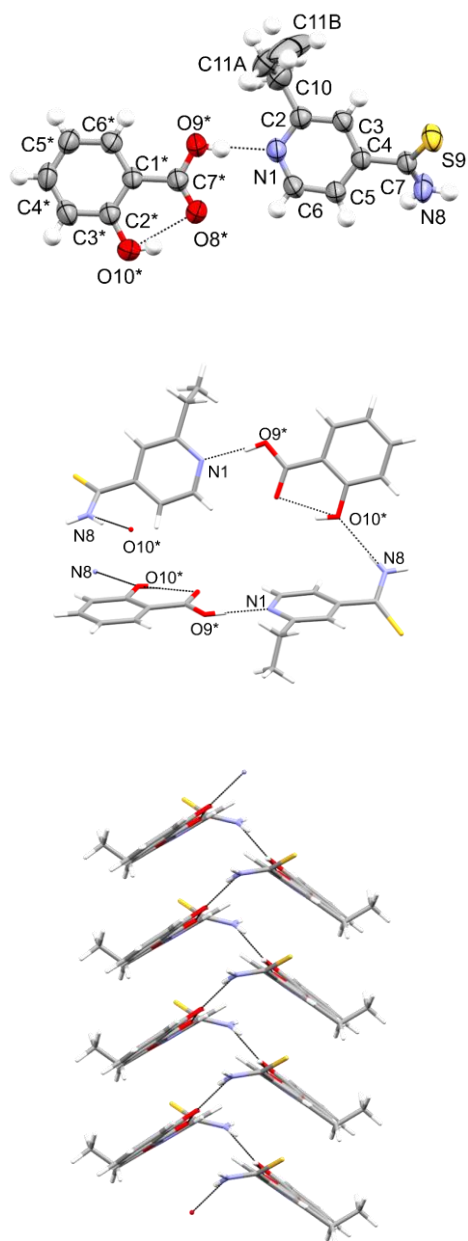**Figure 4.1** Asymmetric unit of ETH⁺SAL⁻ represented by ellipsoids at 50% of probability, highlighting the main heterosynthon and the sulphur atom disorder (top). Details of the tetrameric rings (middle) and the π- π stacking interactions (the disorder is removed for clarity) (middle and bottom).

On the other hand, ETH·SAL, whose crystals were obtained by crystallization from a MeOH solution, crystallizes in a monoclinic $P2_1/n$ space group. The asymmetric unit (Figure 4.2, top) contains one ETH and one SAL molecule. The ETH ethyl group shows disorder over two positions. The main

interaction still corresponds to the aforementioned O···N heterosynthon, no longer charge-assisted (O9*···N1 = 2.646(4) Å) as shown by the larger difference between C-O distances of the carboxylic moiety (C7*-O9* = 1.303(4) Å and C7*-O8* = 1.222(4) Å) and confirmed by the ^{14}N-^{1}H distances measured by SSNMR (see below). These evidences clearly indicate that, in this case, the proton transfer does not occur. A further weaker HB involves the ETH thioamidic group as donor and a hydroxyl oxygen of a second SAL molecule as acceptor (O10*···N8 = 2.919(4) Å). The tetrameric rings are substituted by spiral-shaped structures (Figure 4.2, middle and bottom), due to the torsion of the thioamidic moiety with respect to the ETH ring (C3-C4-C7-N8 dihedral angle = -132°).

Figure 4.2 Asymmetric unit of ETH·SAL represented by ellipsoids at 50% of probability, highlighting the main heterosynthon and the ethyl group disorder (top). Details of the packing and of the spiral-shaped structures (the disorder is removed for clarity) (middle and bottom).

4.3.2 Solid-state NMR characterization

A complete SSNMR characterization (^{1}H MAS, ^{13}C and ^{15}N CPMAS spectra, 2D [1]H-{[14]N} D-HMQC spectra and [14]N-^{1}H PM-S-RESPDOR experiments) was performed. All chemical shifts are listed in Table A3.5, while the ^{13}C CPMAS and ^{1}H MAS spectra are reported in Figures A3.7-A3.8 in Appendix III. The main evidence of the ionic/neutral nature of the compounds is provided by ^{15}N CPMAS spectra (Figure 4.3). Indeed, pyridinic ^{15}N chemical shift is recognized in being particularly sensitive to its protonation state. For ETH$^+$SAL$^-$, the N1 signal exhibits a marked shift of almost 100 ppm toward lower frequencies (from 309.0 ppm for pure ETH down to 211.9 ppm), consistent with a complete proton transfer to the pyridinic nitrogen. For ETH·SAL, the low-frequency shift is much less pronounced (from 309.0 ppm to 273.4 ppm), indicating the formation of a neutral HB.[69]
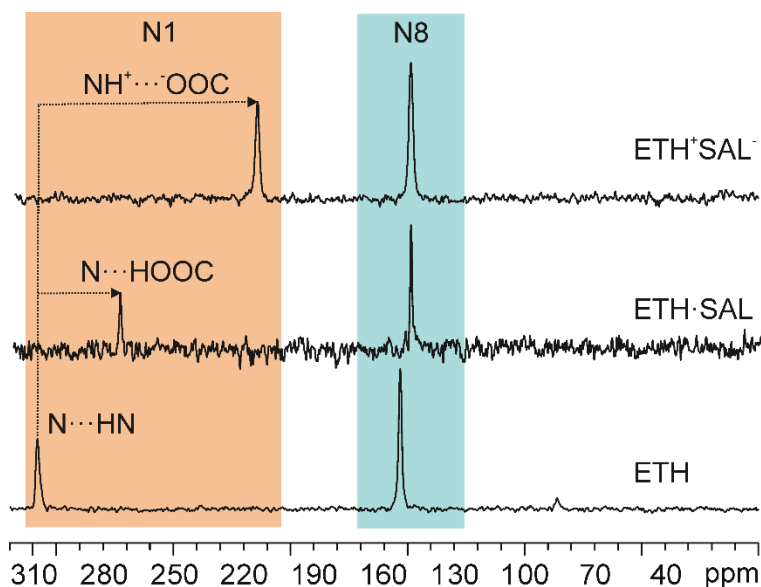
Figure 4.3 [15]N (60.8 MHz) CPMAS spectra of ETH·SAL, ETH$^+$SAL$^-$ and pure ETH with assignments, recorded at 12 kHz at room temperature. The pyridinic

nitrogen (N1) shift is highlighted, to remark the different chemical shifts in the two polymorphs, with respect to pure ETH.

This qualitative analysis is further expanded by 2D ^{1}H-{^{14}N} D-HMQC spectra (Figure 4.4), which allow for the ^{1}H assignment of the thioamidic N-H (H8) and pyridinic N$^+$-H or N$\cdots$H (H9*) resonances as follows: at 10.8 (H8) and 18.4 (H9*) ppm for ETH$^+$SAL$^-$ and at 10.3/8.7 (H8) and 17.3 (H9*) ppm for ETH$\cdot$SAL (see Appendix III for further discussion).
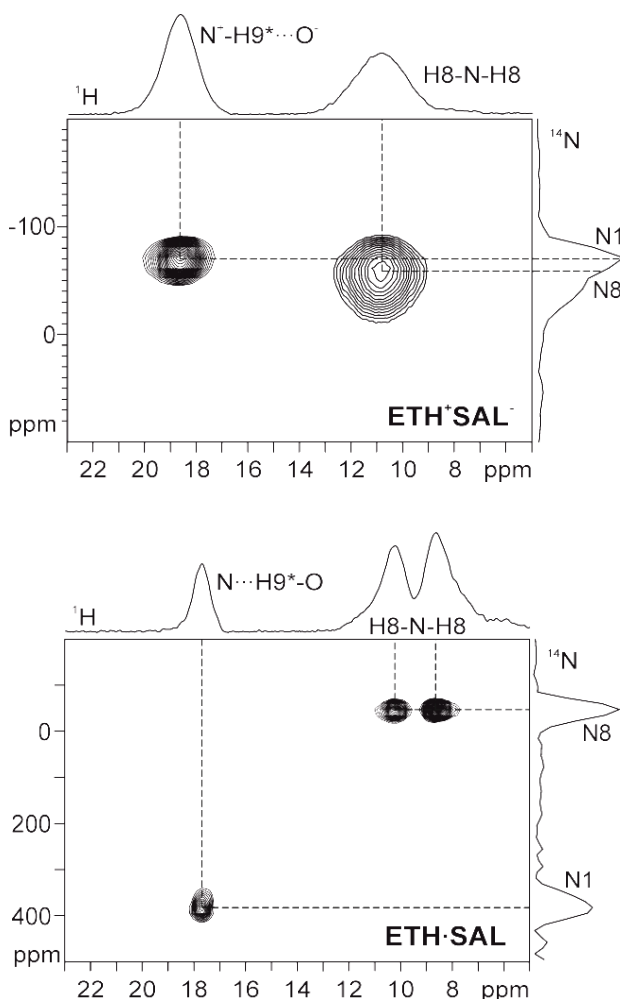
Figure 4.4 2D ^{1}H-{^{14}N} D-HMQC spectra (^{1}H = 600.1 MHz, ^{14}N = 43.4 MHz, ν_R = 70 kHz) of ETH$^+$SAL$^-$ (top) and ETH$\cdot$SAL (bottom).

Finally, the N-H distances were measured by ^{14}N-^{1}H PM-S-RESPDOR SSNMR experiments, which provide very accurate ^{1}H-^{14}N distances, leveraging the ^{1}H detected signal at a very high spinning speed (70 kHz). Details of the experimental setup of the pulse sequence are given elsewhere.[33,34] In short, the method based on the PM-S-RESPDOR sequence requires the acquisition of two sets of data to extract the distance information. Firstly, the experiment is run without irradiation on the ^{14}N channel, resulting in the ^{1}H signal $S_0(\tau)$. Secondly, the same experiment is run with the ^{14}N PM-pulse which prevents the refocusing of the ^{1}H-^{14}N heteronuclear dipolar coupling, leading to the ^{1}H signal $S'(\tau)$. The PM-S-RESPDOR fraction curves are obtained by plotting $\Delta S/S_0 = (S_o(\tau) - S'(\tau))/S_o(\tau))$ as a function of mixing time, τ. These fraction curves are then matched by analytical curves where the dipolar coupling between ^{1}H and ^{14}N ($b_{1H-14N}/(2\pi)$) is the only fitting parameter. Once experimental and analytical curves match, the extracted dipolar coupling ($b_{1H-14N}/(2\pi)$) is used in the following equation to obtain accurate ^{1}H-^{14}N distances:

$$^{1}\text{H-}^{14}\text{N distance} / \text{Å} = \left(\frac{120.1}{b_{1H-14N}/(\frac{2\pi}{\text{kHz}})} \frac{\gamma_{14N}}{\gamma_{1H}} \right)^{1/3}$$

where γ_X (X = ^{1}H or ^{14}N) represents the gyromagnetic ratio of the X nucleus.

Herein, the N-H distances are extracted by matching the experimental and analytical fitting $\Delta S/S_0$ fraction curves of the ^{1}H signals of H9* at 18.4 (ETH$^+$SAL$^-$) and 17.3 (ETH·SAL) ppm, as assigned from the 2D ^{1}H-{^{14}N} D-HMQC spectra. The extracted values were obtained by considering mixing time (τ) values up to 0.4 and 1.0 ms for ETH$^+$SAL$^-$ and ETH·SAL, respectively. The experimental and simulated $\Delta S/S_0$ fraction curves are represented in Figure 4.5 as black dots and solid red lines, respectively. The best fittings are obtained with N-H distances of 1.07 Å for ETH$^+$SAL$^-$ and of 1.50 Å for

ETH·SAL. The same analysis was also carried out for the NH_2 group (^1H peaks at 10.8 and 10.3 ppm for ETH^+SAL^- and ETH·SAL, respectively) for which the $\Delta S/S_0$ fraction curves are reported in Figure A3.9, together with the obtained N-H distances. These NMR distance values perfectly agree with the reference mean values (1.128 Å for the salts; 1.491 Å for the cocrystals) extrapolated from a CSD survey (CSD version 5.40, updated in September 2019 on the N-H and N-D distances of pyridine-carboxylic acid interactions in neutron structures, see Figure A3.10 in Appendix III for the 29 found structures).
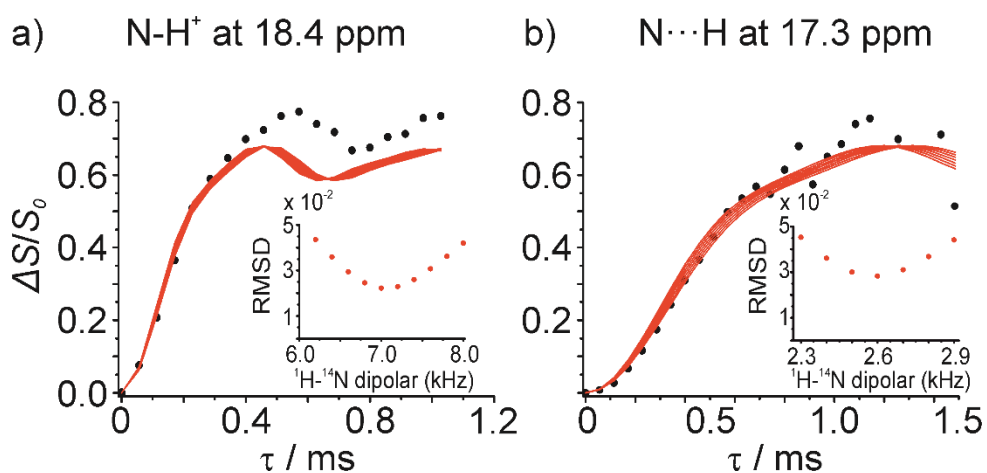
Figure 4.5 Experimental ^{14}N-^1H $\Delta S/S_0$ fraction curves (black dots) achieved by PM-S-RESPDOR of (a) ETH^+SAL^- and (b) ETH·SAL at ^1H chemical shifts of 18.4 and 17.3 ppm, respectively and analytical fitting curves (red solid lines). The insets show the best fitting ^1H-^{14}N dipolar coupling based on root mean square deviation analysis.

4.3.3 DFT calculations

We employed DFT-D non-local vdW-df2-b86r method with a fully relaxed cell in order to optimize the single crystal structures (see Figures A3.11-A3.12 for superpositions). Our objective was 3-fold: i) to support chemical shift assignments by calculating chemical shielding and shift; ii) to

obtain reference values for the N-H distances, and compare them to the SSNMR extrapolated ones; iii) to investigate the two polymorphs' relative stability by computing their lattice energy difference. The reliability of the optimized structures is provided by the calculated chemical shifts, which show agreement with the experimental ones, displaying RMS values (for ^{13}C) of 2.09, for the salt, and 1.46, for the cocrystal. The optimized N-H distances display values of 1.087 and 1.488 Å for N^+-H and $N \cdots H$, respectively (see Table 4.4), which again demonstrate the remarkable accuracy of the PM-RESPDOR experiments. Finally, the DFT-D calculations indicate that the salt form has a lower energy by 4.95 kJ/mol per molecule with respect to the cocrystal. This result, along with the higher density of the salt (salt = 1.332 g/cm^{-3}; cocrystal = 1.298 g/cm^{-3}) confirms the stability relationship derived by the competitive slurry and thermal analysis (see below).

Table 4.4 Comparison among N-H distances values from neutron diffraction structures (mean values), NMR and DFT data.

	Neutron diffraction (Å)	SSNMR (Å)	DFT-D (Å)
ETH$^+$SAL$^-$	1.128	1.07	1.087
ETH·SAL	1.491	1.50	1.488

4.3.4 Thermal analyses

A DSC run up to 130 °C was conducted on the samples. As shown in Figure A3.13, both forms display a melting point around 104 °C, while the salt presents an additional broad endothermic event around 99 °C due to salt-cocrystal polymorphic conversion. Indeed, the FTIR-ATR spectrum of the salt sample after heating to 100 °C matches the cocrystal one (Figure A3.14). Thus, the two phases are enantiotropically related,[70] with the salt being the most stable one at room temperature. The cocrystal is kinetically stable, as no reverse transitions are observed on cooling. If compared to the melting

point of pure ETH (around 165 °C), it is apparent that the new adducts lead to a lower thermal stability, as do almost all ETH multicomponent forms reported in literature.[24-27] The TGA experiments do not show weight loss before 150 °C, confirming that both adducts are free from solvents (Figure A3.15).

4.3.5 Dissolution kinetic tests

DKTs were carried out in water (pH 7.4 phosphate buffer) at 37 °C for both forms, to evaluate the dissolution rate with respect to pure ETH (Figure 4.6). As expected, pure ETH exhibits a slow dissolution rate. On the other hand, both salt and cocrystal display a pronounced improvement, providing an ETH concentration of 32 mg/L, which is reached in 24 min, while the concentration of pure ETH after the same time is about 22 mg/L. Interestingly, both ETH$^+$SAL$^-$ and ETH·SAL show almost identical dissolution profiles, i.e., the protonation state does not affect the overall *in vitro* dissolution properties in agreement with previous findings.[67] A number of works have questioned the widespread belief that pharmaceutical salts are more soluble than cocrystals.[71–74] All of these articles are based on systems made by different components, i.e., one API and a series of coformers, while our adducts are formed by the same components, thus offering a decisive support to their claims. Indeed, the complexity of the solubilization process cannot be restricted to the position of a hydrogen along a single HB.

In addition, more generally, a similar dissolution performance does not necessarily mean that other physicochemical properties are the same. In fact, several examples showed that cocrystals and salts display different properties. For instance, Sandhu *et al.*[75] reported that the hygroscopicity of a solid can be significantly reduced through cocrystallization. Additionally, in a structural analysis of over 80 cocrystals and salts, Aakeröy *et al.*[12] indicated that the frequency of solvate formation among the salt forms was 19%, while

such frequency decreased to 5% in the case of cocrystals. While analyzing several physicochemical properties such as hygroscopicity of ETH^+SAL^- and $ETH \cdot SAL$ would be interesting for comparison purposes, this type of information is beyond the scope of the present study.

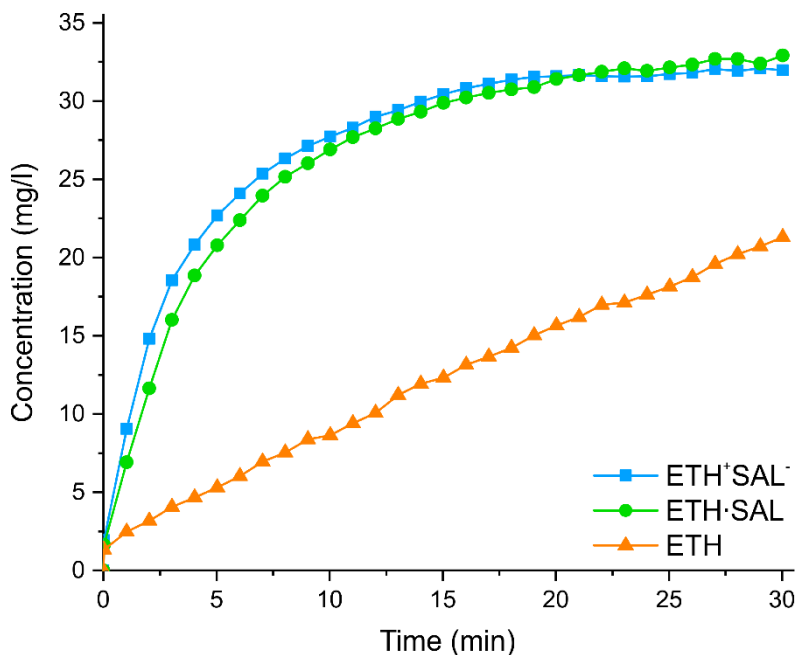**Figure 4.6** Dissolution profiles of (blue) ETH^+SAL^- and (green) $ETH \cdot SAL$, with respect to pure (orange) ETH. DKT were carried out in water (pH 7.4 phosphate buffer) at 37 °C.

4.4 Conclusions

In conclusion, the ethionamide-salicylic acid system is a rare example of salt/cocrystal polymorphism. The two forms have the same stoichiometry, composition and are both stable at room temperature, with the salt being the thermodynamic phase and the cocrystal being the kinetic one. We managed to optimize the synthetic procedure to selectively obtain both forms. Thus,

the method itself, promoting either the kinetic or thermodynamic form, seems to determine the position of the hydrogen atom along the main N···H···O interaction, rather than the character of the solvent (protic/aprotic or polar/apolar). We have unraveled the different ionic and neutral character of the two polymorphs, by a combined X-ray diffraction and SSNMR approach by leveraging the impressive robustness of the PM-RESPDOR sequence for ^{1}H-^{14}N distance measurements. Their thermodynamic relationship was investigated from the experimental and computational points of view, enabling one to characterize the two polymorphs as enantiotropically related. The performances of the two forms in terms of dissolution rate are comparable to each other and significantly higher with respect to the pure ETH. This is further evidence that packing, HBs, ionic or neutral character and dispersion forces are intimately connected in determining the macroscopic properties of molecular crystals and should not be considered independently.

References

1   P. Cerreia Vioglio; M. R. Chierotti; R. Gobetto, *Adv. Drug Deliv. Rev* **2017**, *117*, 86–110.

2   O. N. Kavanagh; D. M. Croker; G. M. Walker; M. J. Zaworotko, *Drug Discov. Today* **2019**, *24*, 796–804.

3   S. Bordignon; P. Cerreia Vioglio; E. Priola; D. Voinovich; R. Gobetto; Y. Nishiyama; M. R. Chierotti, *Cryst. Growth Des.* **2017**, *17*, 5744–5752.

4   I. Sathisaran; S. Dalvi, *Pharmaceutics* **2018**, *10*, 108–181.

5   D. J. Good; N. Rodríguez-Hornedo, *Cryst. Growth Des.* **2009**, *9*, 2252–2264.

6   D. P. Elder; R. Holm; H. L. de Diego, *Int. J. Pharm.* **2013**, *453*, 88–100.

7   N. Schultheiss; A. Newman, *Cryst. Growth Des.* **2009**, *9*, 2950–2967.

8   A. Kumar; S. Kumar; A. Nanda, *Adv. Pharm. Bull.* **2018**, *8*, 355–363.

9   D. J. Berry; J. W. Steed, *Adv. Drug Deliv. Rev* **2017**, *117*, 3–24.

10 E. Grothe; H. Meekes; E. Vlieg; J. H. ter Horst; R. de Gelder, *Cryst. Growth Des.* **2016**, *16*, 3237–3243.

11 S. Aitipamula; R. Banerjee; A. K. Bansal; K. Biradha; M. L. Cheney; A. R. Choudhury; G. R. Desiraju; A. G. Dikundwar; R. Dubey; N. Duggirala *et al.*, *Cryst. Growth Des.* **2012**, *12*, 2147–2152.

12 C. Aakeröy; M. E. Fasulo; J. Desper, *Mol. Pharm.* **2007**, *4*, 317–322.

13 S. P. Kelley; A. Narita; J. D. Holbrey; K. D. Green; W. M. Reichert; R. D. Rogers, *Cryst. Growth Des.* **2013**, *13*, 965–975.

14 V. R. Hathwar; R. Pal; T. N. Guru Row, *Cryst. Growth Des.* **2010**, *10*, 3306–3310.

15 D. Wiechert; D. Mootz, *Angew. Chem., Int. Ed.* **1999**, *38*, 1974–1976.

16 T. Steiner; I. Majerz; C. C. Wilson, *Angew. Chem., Int. Ed.* **2001**, *40*, 2651–2654.

17 E. A. Losev; E. V. Boldyreva, *CrystEngComm* **2018**, *20*, 2299–2305.

18 S. R. Perumalla; C. Wang; Y. Guo; L. Shi; C. C. Sun, *CrystEngComm* **2019**, *21*, 2089–2096.

19 P. Stainton; T. Grecu; J. McCabe; T. Munshi; E. Nauha; I. J. Scowen; N. Blagden, *Cryst. Growth Des.* **2018**, *18*, 4150–4159.

20 C. L. Jones; J. M. Skelton; S. C. Parker; P. R. Raithby; A. Walsh; C. C. Wilson; L. H. Thomas, *CrystEngComm* **2019**, *21*, 1626–1634.

21 K. Zaman, *J. Health Popul. Nutr.* **2010**, *28*, 111–113.

22 F. Wang; R. Langley; G. Gulten; L. G. Dover; G. S. Besra; W. R. Jacobs; J. C. Sacchettini, *J. Exp. Med.* **2007**, *204*, 73–78.

23   M. L. Bastos; H. Hussain; K. Weyer; L. Garcia-Garcia; V. Leimane; C. C. Leung; M. Narita; J. M. Peñã; A. Ponce-de-Leon; K. J. Seung *et al.*, *Clin. Infect. Dis.* **2014**, *59*, 1364–1374.

24   Ethionamide - DrugBank https://www.drugbank.ca/drugs/DB00609.

25   M. K. C. Mannava; K. Suresh; A. Nangia, *Cryst. Growth Des.* **2016**, *16*, 1591–1598.

26   L. F. Diniz; P. S. Carvalho; C. C. de Melo; J. Ellena, *J. Mol. Struct.* **2017**, *1137*, 119–125.

27   M. Alléaume; F. Leroy; M. Gadret; M. Goursolle, *Acta Cryst. B* **1973**, *29*, 1994–2000.

28   C. C. de Melo; C. C. P. da Silva; C. C. S. S. Pereira; P. C. P. Rosa; J. Ellena, *Eur. J. Pharm. Sci.* **2016**, *81*, 149–156.

29   C. B. Aakeröy; A. M. Beatty; B. A. Helfrich, *J. Am. Chem. Soc.* **2002**, *124*, 14425–14432.

30   C. B. Aakeröy; A. M. Beatty; B. A. Helfrich, *Angew. Chem., Int. Ed.* **2001**, *40*, 3240–3242.

31   F. Spinelli; E. Dichiarante; M. Curzi; S. L. Giaffreda; M. R. Chierotti; R. Gobetto; F. Rossi; L. Chelazzi; D. Braga; F. Grepioni, *Cryst. Growth Des.* **2017**, *17*, 4270–4279.

32   A. O. Surov; N. A. Vasilev; A. V. Churakov; J. Stroh; F. Emmerling; G. L. Perlovich, *Cryst. Growth Des.* **2019**, *19*, 2979–2990.

33   N. T. Duong; F. Rossi; M. Makrinich; A. Goldbourt; M. R. Chierotti; R. Gobetto; Y. Nishiyama, *J. Magn. Reson.* **2019**, 106559.

34   E. Nimerovsky; R. Gupta; J. Yehl; M. Li; T. Polenova; A. Goldbourt, *J. Magn. Reson.* **2014**, *244*, 107–113.

35   CrysAlis PRO 1.171.38.46 (Rigaku OD, 2015).

36   G. M. Sheldrick, *Acta Cryst. A* **2008**, *64*, 112–122.

37   G. M. Sheldrick, *Acta Cryst. C* **2015**, *71*, 3–8.

38   A. E. Bennett; C. M. Rienstra; M. Auger; K. V. Lakshmi; R. G. Griffin, *J. Chem. Phys.* **1995**, *103*, 6951–6958.

39   B. M. Fung; A. K. Khitrin; K. Ermolaev, *J. Magn. Reson.* **2000**, *142*, 97–101.

40   P. Giannozzi; S. Baroni; N. Bonini; M. Calandra; R. Car; C. Cavazzoni; D. Ceresoli; G. L. Chiarotti; M. Cococcioni; I. Dabo *et al.*, *J. Phys. Condens. Matter* **2009**, *21*, 395502.

41   P. Giannozzi; O. Andreussi; T. Brumme; O. Bunau; M. Buongiorno Nardelli; M. Calandra; R. Car; C. Cavazzoni; D. Ceresoli; M. Cococcioni *et al.*, *J. Phys. Condens. Matter* **2017**, *29*, 465901.

42   M. Dion; H. Rydberg; E. Schröder; D. C. Langreth; B. I. Lundqvist, *Phys. Rev. Lett.* **2004**, *92*, 246401.

107

43 K. Lee; É. D. Murray; L. Kong; B. I. Lundqvist; D. C. Langreth, *Phys. Rev. B* **2010**, *82*, 081101(R).

44 T. Thonhauser; S. Zuluaga; C. A. Arter; K. Berland; E. Schröder; P. Hyldgaard, *Phys. Rev. Lett.* **2015**, *115*, 136402.

45 T. Thonhauser; V. R. Cooper; S. Li; A. Puzder; P. Hyldgaard; D. C. Langreth, *Phys. Rev. B* **2007**, *76*, 125112.

46 K. Berland; V. R. Cooper; K. Lee; E. Schröder; T. Thonhauser; P. Hyldgaard; B. I. Lundqvist, *Rep. Prog. Phys.* **2015**, *78*, 066501.

47 D. C. Langreth; B. I. Lundqvist; S. D. Chakarova-Käck; V. R. Cooper; M. Dion; P. Hyldgaard; A. Kelkkanen; J. Kleis; L. Kong; S. Li *et al.*, *J. Phys. Condens. Matter* **2009**, *21*, 084203.

48 R. Sabatini; E. Küçükbenli; B. Kolb; T. Thonhauser; S. de Gironcoli, *J. Phys. Condens. Matter* **2012**, *24*, 424209.

49 I. Hamada, *Phys. Rev. B* **2014**, *89*, 121103(R).

50 A. Dal Corso, *Comp. Mater. Sci.* **2014**, *95*, 337–350.

51 H. J. Monkhorst; J. D. Pack *Phys. Rev. B* **1976**, *13*, 5188–5192.

52 F. Franco; M. Baricco; M. R. Chierotti; R. Gobetto; C. Nervi, *J. Chem. Phys. C* **2013**, *117*, 9991–9998.

53 C. J. Pickard; F. Mauri, *Phys. Rev. B* **2001**, *63*, 245101.

54 R. K. Harris; P. Hodgkinson; C. J. Pickard; J. R. Yates; V. Zorin, *Magn. Reson. Chem.* **2007**, *45 Suppl. 1*, S174–S186.

55 G. N. M. Reddy; D. S. Cook; D. Iuga; R. I. Walton; A. Marsh; S. P. Brown, *Solid State Nucl. Magn. Reson.* **2015**, *65*, 41–48.

56 S. F. Chow; L. Shi; W. W. Ng; K. H. Y. Leung; K. Nagapudi; C. C. Sun; A. H. L. Chow, *Cryst. Growth Des.* **2014**, *14*, 5079–5089.

57 M. Kitamura, *CrystEngComm* **2009**, *11*, 949–964.

58 P. T. Cardew; R. J. Davey, *Cryst. Growth Des.* **2019**, *19*, 5798–5810.

59 M. U. Schmidt; J. Brüning; J. Glinnemann; M. W. Hützler; P. Mörschel; S. N. Ivashevskaya; J. van de Streek; D. Braga; L. Maini; M. R. Chierotti; R. Gobetto, *Angew. Chem., Int. Ed.* **2011**, *50*, 7924–7926.

60 T. Stolar; S. Lukin; M. Tireli; I. Sovic; B. Karadeniz; I. Kerekovic; G. Matijasič; M. Gretic; Z. Katancič; I. Dejanovic; M. di Michiel; I. Halasz; K. Uzarevic, *ACS Sustain. Chem. Eng.* **2019**, *7*, 7102–7110.

61 N. Kaneniwa; M. Otsuka, *Chem. Pharm. Bull.* **1985**, *33*, 1660–1668.

62 D. Hasa; G. Schneider Rauber; D. Voinovich; W. Jones, *Angew. Chem., Int. Ed.* **2015**,

54, 7371–7375.

63   F. Fischer; G. Scholz; S. Benemann; K. Rademann; F. Emmerling, *CrystEngComm* **2014**, *16*, 8272–8278

64   D. Hasa; E. Miniussi; W. Jones, *Cryst. Growth Des.* **2016**, *16*, 4582–4588.

65   B. R. Bhogala; S. Basavoju; A. Nangia, *CrystEngComm* **2005**, *7*, 551–562.

66   A. J. Cruz-Cabeza, *CrystEngComm* **2012**, *14*, 6362–6365.

67   S. L. Childs; G. P. Stahly; A. Park, *Mol. Pharm.* **2007**, *4*, 323–338.

68   O. N. Kavanagh; G. Walker; M. Lusi, *Cryst. Growth Des.* **2019**, *19*, 5308–5313.

69   M. R. Chierotti; R. Gobetto, *Chem. Comm.* **2008**, *14*, 1621–1634.

70   S. Aitipamula; A. B. H. Wong; P. S. Chow; R. B. H. Tan, *CrystEngComm* **2012**, *14*, 8193–8198.

71   K. L. Cavanagh; C. Maheshwari; N. Rodríguez-Hornedo, *J. Pharm. Sci.* **2018**, *107*, 113–120.

72   R. Chadha; A. Saini; S. Khullar; D. S. Jain; S. K. Mandal; T. N. Guru Row, *Cryst. Growth Des.* **2013**, *13*, 858–870.

73   G. Bolla; P. Sanphui; A. Nangia, *Cryst. Growth Des.* **2013**, *13*, 1988–2003.

74   S. Mittapalli; M. K. C. Mannava; U. B. R. Khandavilli; S. Allu; A. Nangia, *Cryst. Growth Des.* **2015**, *15*, 2493–2504.

75   B. Sandhu; A. S. Sinha; J. Desper; C. B. Aakeröy, *Chem. Comm.* **2018**, *54*, 4657–4660.

76   Beta-Alanine - DrugBank https://www.drugbank.ca/drugs/DB03107

77   N. Variankaval; R. Wenslow; J. Murry; R. Hartman; R. Helmy; E. Kwong; D. Clas; C. Dalton; I. Santos, *Cryst. Growth Des.* **2006**, *6*, 690–700.

78   Marvin 19.22, 2019, ChemAxon (http://www.chemaxon.com).

Chapter 5

Salt/cocrystal polymorphism of a system of pharmaceutical interest: the case of ketoprofen-L-lysine

5.1 Introduction

During the last decade, cocrystallization has emerged and established itself in the field of pharmaceutical solid-state chemistry as an advanced and valuable method to modify the physicochemical characteristics of drugs.[1] Like pharmaceutical salts, cocrystals are multi-component crystalline solid materials formed by two or more molecules, of which at least one is an active pharmaceutical ingredient (API) that is combined with generally recognized as safe (GRAS), organic molecules used as cocrystallizing agents, or coformers.[2] Pharmaceutical salts and cocrystals, thus, preserve the intrinsic activities of the APIs, while their physicochemical properties can be tailored systematically by varying the coformers.[3] Contrary to salts, however, in which the molecules within the crystal lattice predominantly interact through ion pairing,[4] in cocrystals, the components are combined *via* other noncovalent interactions (e.g., hydrogen bonds, van der Waals forces, π-stacking, and electrostatic interactions) in a definite stoichiometric ratio.[5,6] Thus, particularly when hydrogen bonds (HBs) are involved, cocrystals can be distinguished from salts because, in the latter, a complete proton transfer occurs along the axis of the HB interaction between the API and the molecular partner, whereas, in cocrystals, a neutral adduct is formed by the components.[7]

Most commonly, when a specific pair of molecules is combined with the same stoichiometry and at the same temperature, the outcome is either a salt (ionic) or a cocrystal (neutral).[8] However, to predict whether the outcome will be one or the other can be difficult. For this reason, a "pK_a rule"

has been proposed to provide, at least to some extent, reliable indications about the possibility of obtaining a salt and *vice versa*. Accordingly, a larger ΔpK_a (i.e., pK_a (protonated base) − pK_a (acid)) leads to a greater chance of obtaining a salt and *vice versa*,[9–11] while the probability can also be quantitatively estimated formulas as follows (for the salt and the cocrystal, respectively):[10]

$$P_{obs}(AB)/\% = -17\Delta pK_a + 72 \text{ and } P_{obs}(A^- B^+)/\% = 17\Delta pK_a + 28$$

These formulas identify a region of uncertainty around $\Delta pK_a = 1$, wherein the chances to get a salt or a cocrystal are very similar. In this region usually fall the rare cases in which the same chemical species can give rise to both a cocrystal and a salt (salt/cocrystal polymorphism), which have the same composition and stoichiometry at the same temperature, depending on the crystallization protocol. Stainton *et al.* were the first to report a cocrystal and a salt of the same chemical composition (isonicotinamide and citric acid)[12] and, subsequently, other cases of salt/cocrystal polymorphisms were found for β-alanine and DL-tartaric acid,[13,14] sulfamethazine and saccharine,[15] dinitrobenzoic acid and haloanilines,[16] and ethionamide and salicylic acid.[8] Some of these systems were analyzed for their thermodynamic stability,[14] moisture sorption and compaction properties,[15] or dissolution rate,[8] and cocrystals resulted in having superior or similar properties compared to those of the polymorphic salts. Only a limited number of these studies, however, compare head-to-head salt and cocrystal polymorphic forms originated from the same chemical species in terms of physicochemical properties and *in vivo* pharmacokinetic and pharmacodynamic properties, leaving still open the question about the actual impact that the physicochemical difference between salt and cocrystal polymorphic forms can have on the clinical performance/pharmacological properties of a drug. Answering this question is of particular interest, not only because of the regulatory and legal

implications of intellectual property rights related to the discovery of a new polymorph,[17] but most importantly because it could lead to the development of a drug that, while maintaining the same chemical composition of the polymorphic one, can have different pharmacokinetic and pharmacological characteristics. According to its physicochemical and pharmacokinetic properties, the polymorphic form may allow for the development of different formulations,[18] which can be characterized, for example, by a slower or faster drug release in the blood; on the other hand, depending on its taste, a different coating process or flavor can be used to mask the drug taste, thus possibly affecting drug manufacturing costs and patient compliance.[19] Lastly, on the basis of all the pharmacokinetic and physicochemical characteristics of the new polymorph, new therapeutic indications can potentially be hypothesized.

With the aim of deeply studying the solid-state characteristics of ketoprofen–L-lysine salt (KLS) to identify its already known and new crystalline forms and, thus, possibly discover new polymorphic drugs, we thoroughly investigated, for the first time, the existence of polymorphs of the ketoprofen (KET)–lysine (LYS) system (Scheme 5.1). KET belongs to the group of nonsteroidal anti-inflammatory drugs (NSAIDs), widely used anti-inflammatory, analgesic, and antipyretic compounds that are usually marketed in different forms with sodium, lysine, arginine, and others, to improve the physicochemical and pharmacological profile of the APIs.[20,21] Indeed, salts of KET and LYS, like commercial KLS, have significantly higher solubility compared to KET, allowing for a more rapid absorption of the drug and a subsequent faster onset of the therapeutic effects after oral administration.[22]

Here, we report the method of crystallization and characterization of two distinct KET–LYS polymorphic forms, with salt and cocrystal structural characteristics, and we compare their physicochemical properties, their

112

organoleptic characteristics by electronic tongue analysis, and their pharmacokinetics *in vivo*.
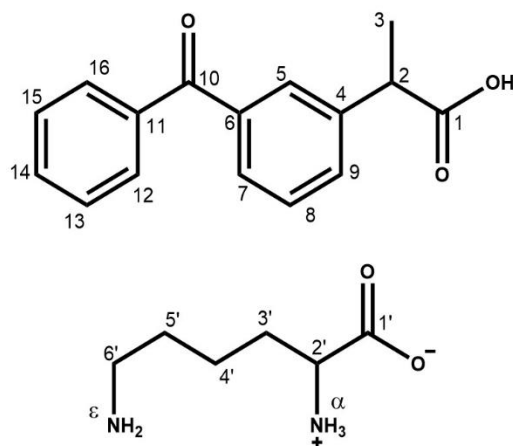
Scheme 5.1 Molecular representation of KET (top) and LYS (bottom), with C and N atom labeling.

5.2 Materials and methods

5.2.1 Crystallization conditions screened to identify potential polymorphs

To deeply investigate the solid-state characteristics of KLS, we conducted a polymorph screening study to identify all the crystalline forms that this API can adopt. To this end, several crystallization conditions were tested on the basis of the solubility properties of the compounds (Table A4.1, Appendix IV). Experiments were performed by (i) dry grinding, in which solid forms of both coformers were combined for manual/mechanical grinding for a fixed period, (ii) kneading (liquid-assisted grinding), in which solid forms of both coformers were combined in the presence of a very small amount of solvent for manual/mechanical grinding for a fixed period, (iii) slurry, in which

solid forms of both coformers were added to a solvent/solvent mixture for a fixed period of equilibration with the solid remaining in excess for the duration of the experiment, (iv) evaporation at low/room/high temperature (based on boiling point), in which the solvent was removed from an undersaturated solution of both coformers *via* evaporation at various temperatures, and (v) precipitation by antisolvent addition, in which cocrystallization directly resulted after the addition of an antisolvent to a solution of both coformers.

For all the compounds, various stoichiometric ratios were investigated in the range of 0.5 to 2 equivalents with respect to the amount of KET or LYS. The slurry experiment with saturated solutions in various solvents was performed when possible.

5.2.2 General procedure for the preparation of KET-LYS polymorph 1 (P1)

First, 50 g of (*RS*)-KET was added to 350 mL of ethanol, and the mixture was stirred at RT until complete solubilization. Then, 29 g of DL-LYS, 50% *w/w* in water (1:1 ratio), was added, and the solution was stirred at RT until the first precipitation occurred. The mixture was left under these conditions for 3 h and then cooled to 5 °C. After 5 h, the product was recovered by filtration, washed with 60 mL of ethanol, and dried under reduced pressure at 40 °C. The final KET–LYS P1 was obtained as a white powder (69 g, yield of 88%).

5.2.3 General procedure for the preparation of KET–LYS polymorph 2 (P2)

First, 1.2 g of (*RS*)-KET and 0.69 g of DL-LYS (1:1 ratio) were suspended in 20 mL of methanol and left under stirring at 40 °C for 1 h. The suspension was then filtered (0.45 µm filter) directly in a Mettler Toledo Easymax 102 reactor. The solution was left under stirring for 5 min in the

114

reactor; then, 100 mL of ethyl acetate was added, and the solution was cooled to −5 °C without solid formation. Ethyl acetate (20 mL) was added through a pipette in two aliquots (10 mL and 10 mL) to trigger nucleation. The system was left under stirring until the suspension became "milky". An additional 30 min of stirring was applied. The precipitate was then filtered, and the collected sample was stored in a sealed vial at room temperature. The final KET–LYS P2 was obtained as a white powder (1.3 g, yield of 69%).

5.2.4 X-ray powder diffraction (XRPD)

XRPD experiments were performed on a powder X-ray diffractometer (Rigaku MiniFlex600, Applied Rigaku Technologies, Inc., Austin, TX, USA) using Cu Kα radiation (1.540598 Å). Samples were scanned with a step size of 0.01° (2θ) and speed of 10.0°/min (2θ) from 3° to 40° 2θ. The tube voltage and amperage were 40 kV and 15 mA, respectively.

5.2.5 Thermal analyses

The analyses were carried out using the Mettler Toledo TGA/DSC1. Samples were weighed in an aluminum pan hermetically sealed with an aluminum pierced cover. The analyses were performed heating the sample from 25 °C to 320 °C at 10 °C/min.

5.2.6 Fourier-transform infrared spectroscopy (FT-IR)

The analyses were carried out using a Thermo Nicolet iS50 ATR module spectrometer equipped with a Smart Performer Diamond, DTGS KBr detector, IR source, and KBr beam splitter.

5.2.7 Solid-state NMR characterization

Solid-state NMR (SSNMR) spectra of KET, LYS, Na$^+$KET$^-$, and KET– LYS P1 were acquired with a Bruker Avance II 400 Ultra Shield instrument,

operating at 400.23, 100.63, and 40.56 MHz, respectively, for ^{1}H, ^{13}C, and ^{15}N nuclei.

Powder samples were packed into cylindrical zirconia rotors with a 4 mm o.d. and an 80 μL volume. A certain amount of sample was collected from each batch and used without further preparation to fill the rotor. [13]C CPMAS spectra were acquired at a spinning speed of 12 kHz, using a ramp cross-polarization pulse sequence with a 90° [1]H pulse of 3.60 μs, a contact time of 3 ms, optimized recycle delays between 1.5 and 3.5 s, and a number of scans in the range 430–640, depending on the sample. [15]N CPMAS spectra were acquired at a spinning speed of 9 kHz using a ramp cross-polarization pulse sequence with a 90° [1]H pulse of 3.60 μs, a contact time between 1 and 4 ms, optimized recycle delays between 1.1 and 3.4 s, and a number of scans in the range 14330–22770, depending on the sample. For every spectrum, a two-pulse phase modulation (TPPM) decoupling scheme was used, with a radiofrequency field of 69.4 kHz. The ^{13}C chemical shift scale was calibrated through the methylenic signal of external standard glycine (at 43.7 ppm). The ^{15}N chemical shift scale was calibrated through the signal of external standard glycine (at 33.4 ppm with reference to NH_3).

The 2D [1]H−[13]C on- and off-resonance (short and long range, respectively) HETCOR spectra were measured with contact times of 0.1 and 7 ms, respectively, and FSLG t1 decoupling and TPPM t2 decoupling (rf fields of 82 kHz). Accordingly, 288 and 384 scans were averaged for 88 and 128 increments, respectively, with 3.4 s of relaxation delay. The indirect ^{1}H chemical shift scale in the HETCOR spectra was experimentally corrected by a scaling factor of $1/\sqrt{3}$ because the ^{1}H chemical-shift dispersion is scaled by a factor of $1/\sqrt{3}$ during FSLG decoupling.

The ^{13}C CPMAS spectrum of KET–LYS P2 was acquired with a Jeol ECZR 600 instrument, operating at 600.17 and 150.91 MHz, respectively, for ^{1}H and ^{13}C nuclei. The powder sample was packed into a cylindrical zirconia

116

rotor with a 3.2 mm o.d. and a 60 µL volume. A certain amount of sample was collected from the batch and used without further preparations to fill the rotor. The ^{13}C CPMAS spectrum was acquired at 273 K, at a spinning speed of 20 kHz, using a ramp cross-polarization pulse sequence with a 90° ^{1}H pulse of 2.19 µs, and a contact time of 3.5 ms. An optimized recycle delay of 6 s was used, for a number of scans of 240. A two-pulse phase modulation (TPPM) decoupling scheme was used, with a radiofrequency field of 108.5 kHz. The ^{13}C chemical shift scale was calibrated through the methylenic signal of external standard glycine (at 43.7 ppm).

The well-known ^{15}N-NMR low sensitivity together with the poorly crystalline nature of KET–LYS P2 prevented a proper parameter optimization of the CPMAS experiment. Several attempts were made for acquiring the ^{15}N CPMAS spectrum of KET–LYS P2 by changing several parameters (contact time, number of scans, and Hartmann–Hahn conditions), without succeeding.

5.2.8 Intrinsic dissolution rate

KET–LYS P1 and KET–LYS P2 were tested for intrinsic dissolution rate (IDR). The IDR experimental method was performed using a 150 mg powder sample; this was compacted by means of a hydraulic press in a round Ø = 11 mm matrix, under approximately 2 tons of force for 3 min. The obtained compacts were maintained inside the matrix and tested in a USP42 Apparatus 2 (Distek Dissolution System 2100B, Distek, Inc., NJ, USA) under the following conditions: 500 mL of gastric simulated fluid (GSF) without pepsin, 37 °C, and 30 rpm paddle rotation speed. The amount of solid dissolved at each time point was determined spectrophotometrically at 260 nm. The test was performed in three replicates. Statistical analysis of the data was performed by Microsoft Excel.

5.2.9 Multisensory analysis

The composition and properties of tested samples (KET–LYS P1 and KET–LYS P2) are listed in Table A4.2 (Appendix IV). The response of E-tongue system was tested in model solutions of salty, bitter, and sweet taste for which aqueous solutions of 0.001 mol/L NaCl, 0.001 mol/L MgCl$_2$, and 0.06 mol/L of fructose were used, respectively. Millipore-grade water was used for aqueous solution preparation. All the other chemicals were of analytical grade and used without further purification.

Membrane components, high-molecular-weight poly(vinyl chloride) (PVC), bis(2-ethylhexyl) sebacate (DEHS) plasticizer, tridodecylmethyl ammonium chloride (TDMACl), potassium tetrakis-(4-chlorophenyl)borate (TpClPBK) lipophilic additives, and nonactine ionophore were purchased from Sigma-Aldrich (Rome, Italy). Tetrahydrofuran (THF) used for PVC membrane preparation was obtained from Carlo Erba Reagents (Rome, Italy) and distilled prior to use. 5,10,15,20-tetraphenylporphyrin manganese(III) chloride ionophore (Mn(TPP)Cl) was synthesized in our laboratories and fully characterized according to the literature procedure.[23] Millipore-grade water was used for aqueous solution preparation. All the other chemicals were of analytical grade and used without further purification.

The potentiometric E-tongue system was composed of eight sensors with three different types of sensing membranes: PVC-based solvent polymeric membranes doped with Mn(TPP)Cl (sensor A1) and nonactin (sensor C1) ionophores, chalcogenide glass membranes doped with different metal salts (G2-Cu, G7-Tl, G8-Ag, G10-Cd, G11-Pb), and sensor A7 with polycrystalline LaF$_3$ membrane. The PVC-based solvent polymeric membranes were prepared according to the previously reported procedures.[24,25] For this, all the membrane components (PVC 30–33 wt.%, plasticizer 60–66 wt.%, ion-exchanger 0.1–10 wt.%, and ionophore 1 wt.%) were dissolved in THF. The membrane cocktails were then cast in a 24 mm i.d. glass ring on a glass

slide, and the solvent was evaporated overnight. The polymeric membrane discs of 8 mm in diameter were cut out from the parent membrane and fixed with 10 wt.% PVC in cyclohexanone glue onto hollow PVC tubes that served as electrode bodies, filled with 0.01 mol/L solutions of NaCl and NH_4Cl for sensor A1 and sensor C1, respectively. The sensor A1 and C1 membrane potential was registered against the internal, homemade Ag/AgCl reference electrode.

Chalcogenide glass sensors and sensor A7 with a polycrystalline LaF_3 membrane had solid Cu-wire/Ag-paste solid contacts and were purchased from Sensor Systems (St. Petersburg, Russia). The potentials of E-tongue system sensors were measured *versus* a saturated calomel reference electrode (SCE, AMEL, Milan, Italy), in a standard two-electrode configuration cell. Potentiometric measurements were performed with a LiquiLab (ECOSENS srl, Rome, Italy) high-impedance analog-to-digital potentiometer. Prior to measurements, the sensors were soaked in 0.01 mol/L NaCl aqueous solution for at least 24 h.

The quantity of samples KET–LYS P1 and KET–LYS P2 corresponded to the standard dosage of administration of commercial KLS (40 mg). This amount of sample was dissolved in 20 mL of distilled water.

All analyses were performed in analytical triplicate for all the above time conditions. The pH value and electrical conductivity of the t24 h and t48 h solutions were also measured. The samples were stored in closed containers at room temperature (+22 °C) during the study period.

5.2.10 Pharmacokinetics

For the pharmacokinetics studies, Sprague Dawley male rats (body weights 250–275 g at the time of the treatment) were used. The animals were originally supplied by Harlan, Italy. The animals were acclimatized to local housing conditions for approximately 5 days.

The animals were housed in a single, exclusive room, air-conditioned to provide a minimum of 15 air changes/h. The environmental controls were set to maintain temperature within 22 °C and relative humidity within the range 50–60% with an approximate 12 h light and 12 h dark cycle that was controlled automatically. Food (Mucedola Standard GLP diet) and water were available *ad libitum* throughout the study. All animals were weighed on the day of each treatment. Clinical signs were monitored at regular intervals throughout the study in order to assess any reaction to treatment. Each animal was uniquely identified with a colored spray on the back before the experiment.

The compounds were administered at a dose of 3.5 mg/kg as KET free acid in gelatin capsules (size 9, Torpac®). To perform this, capsules were individually filled and weighed up with the substances and then filled with rice starch up to about 20 mg, weighed again, and closed. After administration, blood (approximately 60–80 µL) was sampled from tail vein at the following timepoints: 15 min, 30 min, 1 h, 2 h, 4 h, 6 h, 8 h, 24 h, and 48 h. Blood samples were collected in heparinized Eppendorf tubes (Heparin Vister 5000 UI/mL), gently mixed, and placed immediately on ice; then, Eppendorf tubes were centrifuged (3500× g, at 4 °C for 15 min), and the resulted plasma was collected and transferred to uniquely labeled Eppendorf tubes, before being frozen at −20 °C till the HPLC–MS analysis.

At the end of the study animals were sacrificed by exsanguination under deep isoflurane anesthesia.

The experiment was carried on in agreement with the Italian Law D. L.vo 4 marzo 2014, no. 26.

5.2.11 Statistics

For IDR experiments, the statistical analysis of the data was performed by *Microsoft Excel* (Microsoft Excel for Office 365 MSO

(16.0.11929.20836)). For pharmacokinetics experiments, data were expressed as the mean ± standard error of the mean (SEM). Multiple statistical comparisons between groups were performed by two-tailed unpaired Student's t-test. All data collected followed good approximation to a normal distribution, being included in the 95% confidence interval of the mean; this generally allowed for the clear identification of outliers, if any, and for the application of the statistical analyses described above. No outliers were found during the present study. Missing data in the results were then related only to overt technical issues during the experimental procedures, which led to the exclusion of those specific samples from the analysis.

5.3 Results and discussion

5.3.1 Crystallization conditions and identification of KET–LYS polymorphs

As part of a project aimed at the identification of new polymorphs of the KET–LYS system, we obtained two polymorphic forms of KET–LYS, KET–LYS P1 and KET–LYS P2, through different crystallization techniques (Table A4.1, Appendix IV). We performed more than 230 experiments and analyzed all the collected solids by X-ray powder diffraction (XRPD) analysis and compared them with the starting material. Mechanochemistry methods were ineffective, as grinding and kneading experiments led to the isolation of solids having the same diffraction pattern of the starting material albeit presenting a lower crystallinity degree. Evaporation and slurry experiments in different conditions led to only unstable and amorphous phases. The best results were obtained performing several precipitation experiments by antisolvent addition as described in Section 5.2. We analyzed the solids obtained using this latter method and deeply characterized them using advanced crystalline solid-state technologies.

121

5.3.2 Characterization of synthesized KET–LYS P1 and P2

According to the pK_a rule, the reaction between KET and LYS should result in a salt, as the ΔpK_a of these molecules is 5.84 (pK_a (protonated LYS ε-NH$_2$) − pK_a (KET COOH) = 10.29 − 4.45). However, since the model suggested by Cruz-Cabeza *et al.*[10] is validated only for −1 < ΔpK_a < 4 and the ΔpK_a in this case is higher than 4, the probabilities of obtaining a salt or a cocrystal cannot be quantitatively estimated.

Since crystals of suitable size for single-crystal X-ray diffraction could not be produced, we performed an XRPD analysis to investigate the microstructure and properties of the powders. The non-superimposition of the XRPD diffraction patterns (Figure 5.1) showed the presence of two different phases with different crystalline degrees that were called KET–LYS Polymorph 1 (P1) and KET–LYS Polymorph 2 (P2). From its XRPD pattern, KET–LYS P2 seemed a less crystalline form compared to KET–LYS P1, and we can speculate that this can be due to the faster precipitation of KET–LYS P2 (30 min) compared to that of KET–LYS P1 (3 h).
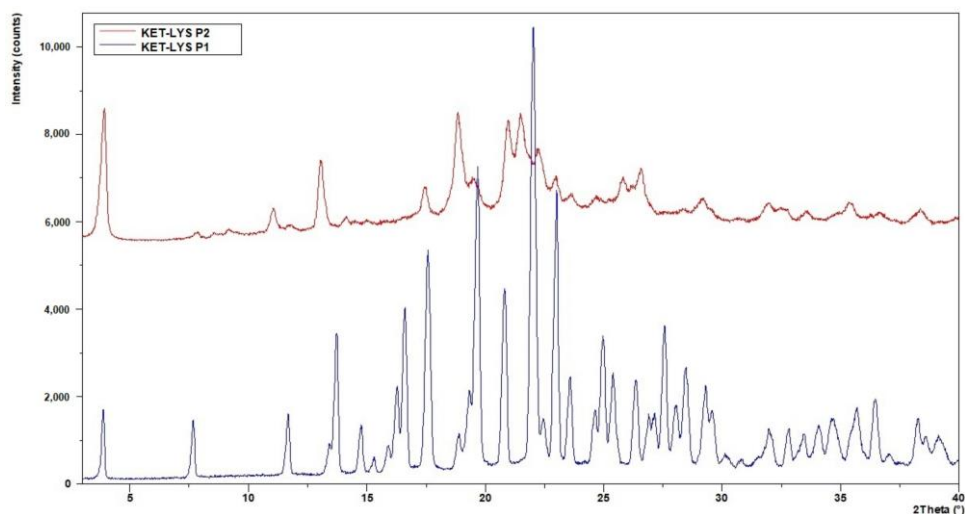
Figure 5.1 Comparison of XRPD patterns of KET–LYS P1 and KET–LYS P2. The diffraction patterns of KET–LYS P1 and KET–LYS P2 are non-superimposable.

To define the nature of these two polymorphs, we firstly performed differential scanning calorimetry (DSC). Interestingly, the DSC profile of KET–LYS P1 showed an endothermic event at 170.7 °C (onset 164.1 °C) that was associated with sample melting and degradation (Figure A4.1, Appendix IV), whereas the DSC profile of KET–LYS P2 showed multiple endothermic peaks, with the first one at 110.9 °C (onset 100.5 °C), while, above 120 °C, multiple partially overlapped endothermic peaks were detectable due to degradation steps (Figure A4.2, Appendix IV).

We then performed an FT-IR analysis and observed that the vibration peaks of characteristic functional groups (O–H, N–H, and COOH) of the KET–LYS system significantly differed between the two polymorphs, and this could be attributable to hydrogen bonding and salt formation (Figures A4.3 and A4.4, Appendix IV). Indeed, in KET–LYS P1, the IR band was centered around 3160 cm^{-1} and could represent the OH stretching in carboxylic acid dimer bands; on the contrary, this band was not detectable in KET–LYS P2, which showed instead a very broad band at 3400–3660 cm^{-1}. Lastly, in KET–LYS P2, the strong band at 1550 cm^{-1} could be due to the KET carboxylate anion group.[26]

Starting from this preliminary evidence, we then performed solid-state nuclear magnetic resonance (SSNMR), relying on the accuracy of this technique[27] to undoubtedly determine the ionic or neutral nature of our samples. Both ^{13}C and ^{15}N chemical shifts are in fact very sensitive to the protonation state of carboxylic and N-containing functional groups.[28] In general, the carboxylic ^{13}C chemical shift undergoes a high-frequency shift in the following order: neutral carboxylic groups (COOH) < COOH involved in HB interactions (COOH···X) < formation of a dimer through a homosynthon (COOH···HOOC) ≈ carboxylate groups (COO⁻);[27] the ^{15}N chemical shift is even more sensitive, as protonation induces shifts that can be as large as 25 ppm toward higher frequencies for aliphatic amines in agreement with the minor

contribution of the lone pair to σ^p_{loc}.[27] Here, 1D (^{13}C and ^{15}N CPMAS) and 2D (^{1}H–^{13}C HETCOR) experiments were acquired for KET–LYS P1, and the ^{13}C CPMAS spectrum was acquired for KET–LYS P2. For comparison, we also analyzed pure KET, its sodium salt (Na$^+$KET$^-$), DL-LYS·2HCl, and pure L-LYS, the latter being selected as a reference due to its crystal structure displaying a free ε-NH$_2$ group (Figure A4.5, Appendix IV). Table 5.1 lists ^{13}C and ^{15}N chemical shifts of KET–LYS P1 and KET–LYS P2 with assignments.

Table 5.1 ^{13}C and ^{15}N SSNMR chemical shift assignments for KET–LYS P1 and KET–LYS P2. Please refer to Scheme 5.1 for atom labeling. The ^{15}N CPMAS peak assignment for KET–LYS P2 is not reported as the spectrum could not be acquired (see Section 5.2 for further details).

KET–LYS P1		KET–LYS P2	
^{13}C			
^{13}C δ (ppm)	C atom	^{13}C δ (ppm)	C atom
196.1	10	194.5	10
177.6	1	181.5	1
174.5	1'	176.1	1'
147.4	6	145.1	6
141.0	11	139.7	11
134.8	4	138.1	4
133.0	Aromatic CH	133.4	Aromatic CH
128.8	Aromatic CH	131.8	Aromatic CH
128.3	Aromatic CH	129.8	Aromatic CH
128.0	Aromatic CH	128.8	Aromatic CH
126.8	Aromatic CH	127.7	Aromatic CH
55.1	2'	53.2	2'
50.2	2	47.4	2
38.8	6'	34.5	6'
32.2	5'	25.9	5' + 3'
29.6	3'	21.2	3
24.7	3	16.6	4'
22.3	4'	/	/
^{15}N			
^{15}N δ (ppm)	N atom		
43.0	α		
32.8	ε		

The ^{13}C CPMAS spectra of KET–LYS P1 and KET–LYS P2 exhibited consistent shifts in the resonances associated both with KET and with L-LYS carbon atoms (Figure A4.6, Appendix IV). These data are in line with the formation of two novel crystal forms that differed from each other and from the starting materials. The samples were pure, as no residual peaks of the starting materials were present, and both crystal forms contained one independent molecule of KET and one of LYS. The fact that the starting materials were racemic suggests the presence of an inversion center in both crystal forms. Moreover, the average full width at half maximum (FWHM) value for the signals indicated a high and a low degree of crystallinity for KET–LYS P1 (~65 Hz) and KET–LYS P2 (~130 Hz), respectively.

In Figure 5.2, the C=O regions (170–210 ppm) of the ^{13}C CPMAS spectra of KET, L-LYS, Na$^+$KET$^-$, KET–LYS P1, and KET–LYS P2 are reported. Analyzing the ^{13}C CPMAS spectrum of KET, a signal is detectable at 184.0 ppm, a high value that is typical and, thus, indicative of a carboxylic group involved in a homodimeric interaction (as is the case for KET, Figure A4.7, Appendix IV);[29] on the other hand, its sodium salt Na$^+$KET$^-$ displays two peaks at 181.4 and 180.5 ppm, which indicate the presence of two independent molecules in the unit cell. Both these chemical shifts are consistent with the unprotonated nature of a carboxylate group (COO$^-$). In the case of KET–LYS P1, we observed two peaks in the carboxylic region, at 174.5 and 177.6 ppm.
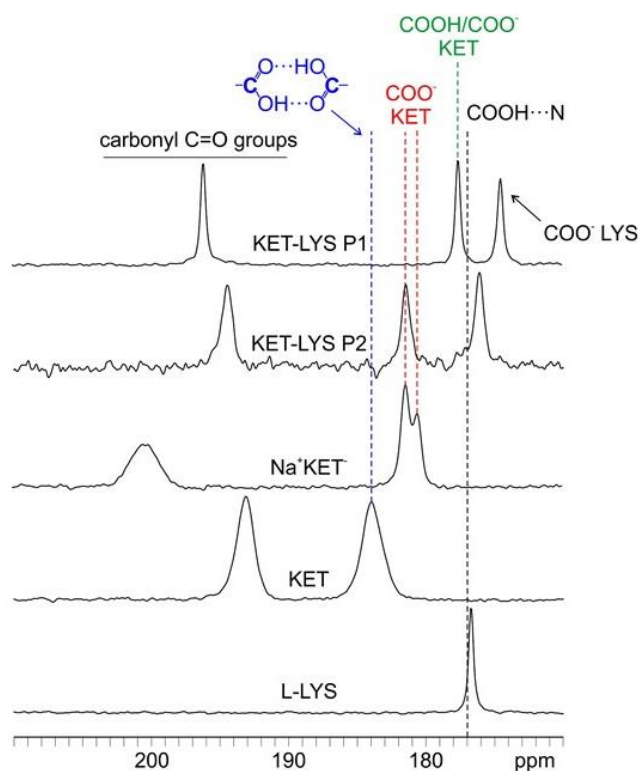
Figure 5.2 Carboxylic region (170–210 ppm) of the ^{13}C CPMAS spectra of samples KET, L-LYS, Na$^+$KET$^-$, KET–LYS P1, and KET–LYS P2. The black dashed line at *ca.* 177 ppm refers to the chemical shift reported in the literature for the protonated carboxylic group of ibuprofen, involved in an HB interaction with a nitrogen atom, in a (ibuprofen)$_2$(4,4'-bipyridyl) cocrystal.[30]

To understand which signal refers to the carboxylic group of KET and which refers to that of LYS, we performed a 2D experiment (i.e., ^{1}H–^{13}C FSLG HETCOR) in two different versions, with on- and off-resonance CP conditions; the first (Figure A4.8, Appendix IV) allowed observing short-range correlations only between covalently bonded C atoms and protons, while the second (Figure 5.3) also provided signals for long-range interactions between C and H nuclei which were spatially close, within 3–4 Å. The short-range

127

experiment (Figure A4.8, Appendix IV) made it possible to correlate the ^{13}C signals of the CH groups of LYS (55.1 ppm) and KET (50.2 ppm) to the corresponding protonic peaks, leading to their assignment at 3.4 and 3.6 ppm, respectively. Being the CH groups closest to the carboxylic moieties in both KET and LYS, we were then able, through the long-range version of the experiment (Figure 5.3), to identify the carboxylic signal of LYS at 174.5 ppm (correlating with the protonic signal at 3.4 ppm) and that of KET at 177.6 ppm (correlating with the protonic signal at 3.6 ppm). The carboxylic peak of LYS agrees with the typical chemical shift of the COO⁻ in pure LYS (176.7 ppm), which, together with the ^{15}N data (see below), confirms the zwitterionic nature of LYS in KET–LYS P1. The KET signal resonates at a frequency which is much lower than that of both the COO⁻ groups of Na⁺KET⁻ (181.4/180.5 ppm) and the homodimeric COOH group of pure KET (184.0 ppm). In particular, the KET signal is very similar to that unambiguously assigned to a neutral carboxylic group involved in an HB, observed at *ca.* 177 ppm in the (ibuprofen)₂(4,4′-bipyridyl) cocrystal.[30] Since the carboxylic environment of ibuprofen is very similar to that of KET, the comparison we made is definitely reliable. Thus, these data suggest that the carboxylic group of KET in KET–LYS P1 is in a protonated state (COOH) and involved in HBs with LYS, making KET–LYS P1 better defined as a cocrystal rather than a salt.
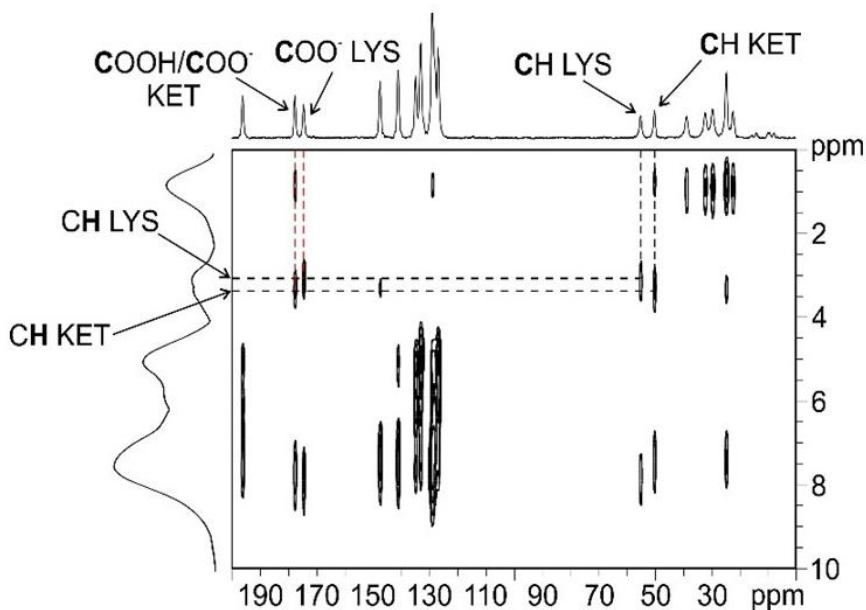
Figure 5.3 Off-resonance ^{1}H–^{13}C FSLG HETCOR spectrum (contact time = 7 ms) of KET–LYS P1. Above, ^{13}C spectrum; on the left, ^{1}H spectrum. Black dashed lines represent significant correlations among covalently bonded protons and C atoms in the crystal structure; red dashed lines represent significant correlations among protons and C atoms spatially close in the crystal structure (see main text). Spinning speed of 12 kHz, room temperature.

To confirm this assumption, we further investigated the system by ^{15}N CPMAS SSNMR analysis, which usually offers the chance to discriminate between deprotonated and protonated N atoms and, thus, in this case, between the NH_2 and NH_3^+ moieties of L-LYS and KET–LYS P1. Figure 5.4 shows the ^{15}N CPMAS NMR spectra of samples L-LYS, DL-LYS·2HCl, and KET–LYS P1. L-LYS itself contains both types of moieties; its ε-NH_2 group, free from HBs (as observable in its crystal structure, Figure A4.5, Appendix IV; see also ref 31),[31] resonates at 27.2 ppm, while its α-NH_3^+ falls at 41.0 ppm.

The ^{15}N CPMAS spectrum of KET–LYS P1 allowed confirming the protonated nature of the α-NH$_3^+$ of LYS in KET–LYS P1 (43.0 ppm), and it showed that the ε-N signal falls at 32.8 ppm, which is intermediate between the chemical shifts of α-NH$_3^+$ and ε-NH$_2$ of pure L-LYS. Although ambiguous, its chemical shift suggests the presence of a neutral NH$_2$ group involved in HB interactions, i.e., H$_2$N···H–X. Indeed, a proper ε-NH$_3^+$ signal falls at 41.3 ppm as observed in the spectrum of DL-LYS·2HCl. Thus, it can be said that this system falls in the salt/cocrystal continuum but points more toward a neutral nature, again supporting the concept that the KET–LYS P1 structure is more referable to a cocrystal rather than to a salt.
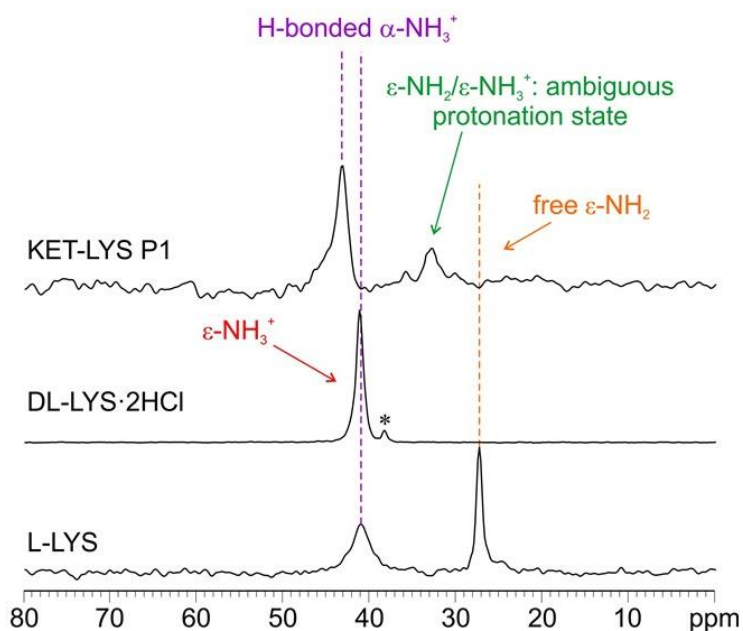
Figure 5.4 ^{15}N (40.6 MHz) CPMAS spectra of samples L-LYS, DL-LYS·2HCl, and KET–LYS P1. Acquisition at room temperature at a spinning speed of 9 kHz. The asterisk in the middle spectrum identifies a small signal due to an

impurity. The ^{15}N CPMAS spectrum of KET–LYS P2 could not be acquired (see Section 5.2 for further details).

From the comparison among the ^{13}C CPMAS spectra, it can be observed how, in KET–LYS P2, the signal at 181.5 ppm (referred to KET) is quite close to the signal of pure KET (184.0 ppm) and especially of Na^+KET^- (181.4/180.5 ppm). This suggests that, in KET–LYS P2, the COOH of KET is in a carboxylate form, since dimeric COOH groups and COO^- moieties resonate at similar frequencies.

Altogether, these data clearly demonstrate that the crystallization outcome of the reaction between KET and LYS is a case of salt/cocrystal polymorphism. This result is unexpected if we consider the pK_a rule and the fact that the ΔpK_a of our system is higher than 4, for which a salt is to be definitely expected. Thus, while the pK_a rule has a statistical and predictive value that is fundamental in the design phase, once the adduct is obtained, the characterization of the protonation state must be always supported by diffraction and/or spectroscopic data. This is because, as also for this system, the influence of the crystalline environment in defining the hydrogen position along an HB is more important than the strength of the acidic and basic sites.[11]

Surprisingly, the subsequent analysis of commercial samples of KLS from different manufacturers showed that it is representative of KET–LYS P1 (Figure A4.9, Appendix IV), thus revealing that commercial KLS, which was introduced in the market as a KET salt, should instead be more appropriately defined as a cocrystal. The existence of a stable cocrystal structure of KET–LYS was not predictable on the basis of the typical "pK_a rule", which has been validated only for a limited ΔpK_a range.[10] Thus, these new findings highlight the importance of conducting specific studies to assess the salt/cocrystal polymorphism possibility for species with a ΔpK_a outside the $-1 < \Delta pK_a < 4$ range.

5.3.3 Intrinsic dissolution rates of cocrystal KET–LYS P1 and salt KET–LYS P2

Having identified two distinct polymorphs of the KET–LYS system, we then analyzed them with regard to some of the intrinsic chemical and physical properties that have to be considered before the development of a pharmaceutical formulation. Among these properties, the dissolution rate of a drug is usually modified by cocrystallization processes.[2] Thus, we investigated whether the cocrystal form of the KET–LYS system (KET–LYS P1) has different intrinsic dissolution rate (IDR) compared to its salt polymorph (KET–LYS P2). The results showed two different IDRs for the two compact forms, having constant surface area exposed to the GSF medium (Figure 5.5 and Table 5.2). In particular, the IDR comparative profile (Table 5.2) between KET–LYS P1 and KET–LYS P2 shows that the release of KET from KET–LYS P2 was significantly faster than from KET–LYS P1 at pH 1.2 (SGF), and KET–LYS P2 seemed to have a higher IDR than KET–LYS P1.

Table 5.2 IDR (slope) mg/($cm^2 \cdot$ min) of cocrystal KET–LYS P1 and salt KET–LYS P2.

Compound	IDR (slope) mg/($cm^2 \cdot$ min)	Confidence Interval (95%)	
Cocrystal KET–LYS P1	1.453	1.411	1.495
Salt KET–LYS P2	1.907	1.813	2.002

These results further confirm that the outcomes of KET and LYS crystallization are two different structural entities and demonstrate that the two forms are characterized by different IDRs. *In vitro* dissolution is an important factor in defining drug absorption, distribution, metabolism, and excretion (ADME), and different IDRs among drugs can allow for the

development of formulations with different release kinetic profiles.[32] Commercial KLS (representative of KET–LYS P1) has been reported to exhibit fast *in vivo* absorption and onset of action;[22] thus, the faster dissolution observed for KET–LYS P2 compared to KET–LYS P1 may suggest that the newly synthesized salt form (KET–LYS P2) could be characterized by a faster absorption compared to the commercialized KLS.
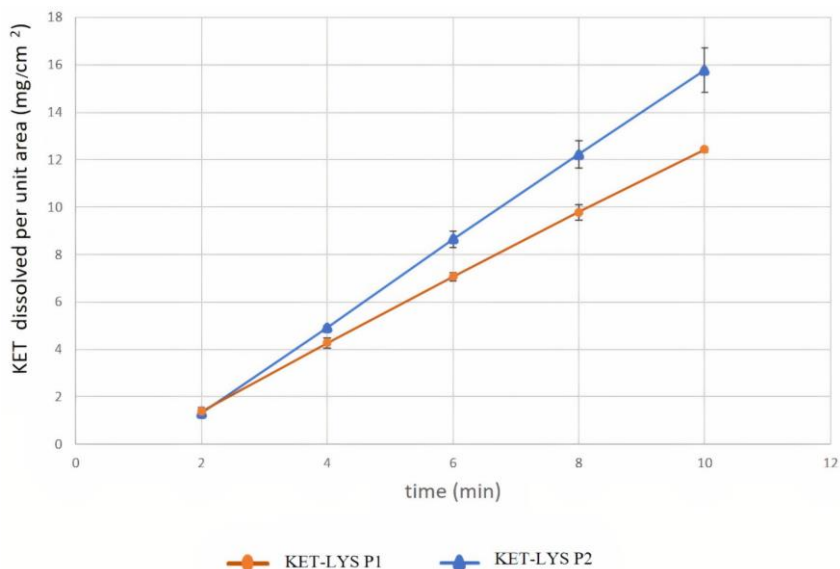
Figure 5.5 Intrinsic dissolution rates of cocrystal KET–LYS P1 and salt KET–LYS P2. Dissolution profiles of KET for KET–LYS P1 and KET–LYS P2, having constant surface area exposed to the dissolution medium. Three analytical replicates were performed for all the time points. Values are expressed as the mean ± SD.

5.3.4 Taste and sensorial kinetic analysis of KET–LYS P1 and KET–LYS P2

One of the central challenges of drug manufacturing is to sweeten the unpleasant taste of APIs, which can be bitter, salty, sour, and even metallic or astringent, as it negatively affects the compliance of patients, especially in

pediatric and geriatric populations.[33] Technologies have been developed to mask unpleasant drug tastes and odors, such as the use of physical barriers (coating) or the addition of sweeteners and flavoring excipients,[34] but modifying the taste of a drug is not an easy, straightforward process, as it strongly depends on the target patient age and geographic location[35] and, of course, on the API itself.[36] Thus, drugs that, at the beginning of their development, have different tastes, will potentially allow for different subsequent coating processes or flavor addition.

As some studies have reported, the taste of a drug is among the chemical properties that cocrystallization can modify.[2] For example, cocrystals of hydrochlorothiazide obtained using sucralose as a coformer had increased dissolution rate and taste masking compared to the API,[37] while taste sensing experiments revealed the sweetness of the cocrystal of paracetamol with trimethylglycine due to the presence of the latter in the structure,[38] as well as of the cocrystal obtained from theophylline and saccharine.[39]

We thus investigated and compared the taste and the sensorial kinetics of KET–LYS P1 and KET–LYS P2, to assess whether the substitution of an ionic bond (salt) with a neutral HB (cocrystal), rather than the substitution or the addition of coformers as described in the above examples, can alter these characteristics. To analyze the variation of bitterness and palatability characteristics of KET and LYS pharmaceutical preparations, we used a potentiometric E-tongue system application, a method that was successfully employed in previous researches dedicated to the evaluation of soft cheese salinity,[40] water toxicity, and organoleptic potability screening.[41,42] The response of the E-tongue system to the two polymorphs was analyzed by a pattern recognition method called principal component analysis (PCA), to detect the similarities or differences in taste of the sample solutions from time 0 (t0, just solubilized) to 30 min (t30) and after 60 min (t60). The PCA score plot representing the dispersion of E-tongue data obtained for the two

134

polymorphs shows completely different sensorial kinetics between KET–LYS P1 and KET–LYS P2. Firstly, the position on the gustatory map (determined by modeling sweet, bitter, and salty solutions on the PCA score plot) was significantly different at t0 between the cocrystal and the salt forms, as KET–LYS P1 started in the right lower quadrant of the map, while KET–LYS P2 was in the upper part of the left quadrant in an opposite position compared to KET–LYS P1 (Figure 5.6). These data demonstrate that the cocrystal at t0 is sweeter than the salt and, for this reason, different coating processes and/or flavor addition can be envisioned for the potential subsequent development of the new salt KET–LYS P2 form compared to that usually followed during the manufacturing of the commercialized KLS (KET–LYS P1). Secondly, analysis at t30 and t60 shows that KET–LYS P1 underwent smaller variations in the first 60 min after preparation of the solution compared to KET–LYS P2, as, over time, KET–LYS P1 remained in the same quadrant, while KET–LYS P2 made a significant change in its position on the gustatory map in the first 30 min, moving from the upper part of the left quadrant to the lower right quadrant (Figure 5.6). This phenomenon could be due to the formation of intimate ion pairs in solution that maintain over time (from t0 to t60) the memory of the different stereochemistry of the original crystalline structures, and this results in a different solvation and shielding of the ion and the counterion of the KET–LYS P1 and KET–LYS P2 systems.[43]
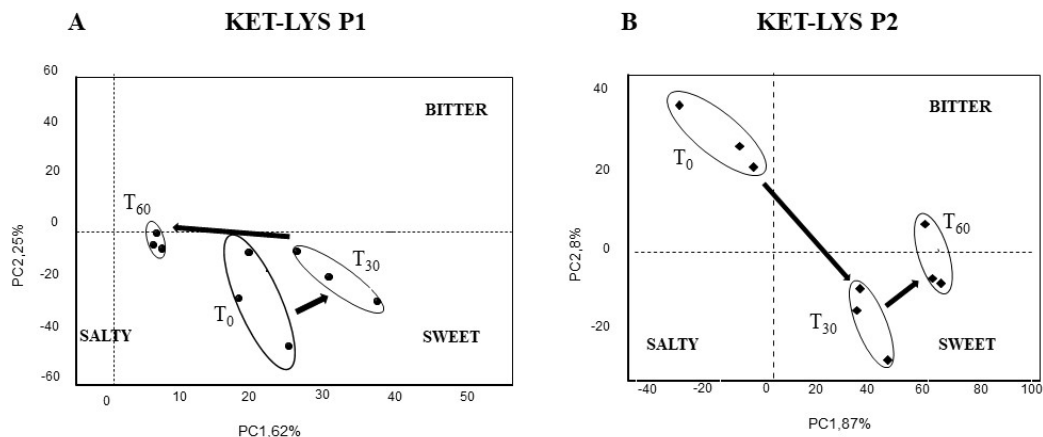
Figure 5.6 Taste and sensorial kinetic analysis by electronic tongue of cocrystal KET–LYS P1 (A) and salt KET–LYS P2 (B). PCA score plot of KET–LYS P1 and KET–LYS P2 over the time lapsed after dissolution preparation. T0, just solubilized; T30, 30 min in solution; T60, 60 min in solution. PC1: first principal component; PC2: second principal component. Three analytical replicates were performed for all the time points.

5.3.5 Pharmacokinetics *in vivo* of KET–LYS P1 and KET–LYS P2

Having assessed the differences in IDRs between the polymorphic salt and cocrystal forms of KET and LYS, we studied and compared the *in vivo* pharmacokinetics. We analyzed the major pharmacokinetic parameters after oral administration of the two compounds at the dose of 3.5 mg/kg to not fasted Sprague Dawley male rats. Results showed that the two polymorphs were comparable in terms of C_{max}, $T_{1/2}$, and mean residence time (MRT); however, notably, the dose-normalized area under the curve to infinity (AUC-inf) and T_{max} values of KET–LYS P1 were significantly higher than those of KET–LYS P2 (74,076 ± 5931 ng/mL·h vs. 50,434 ± 4439 ng/mL·h, $p < 0.01$,

136

for AUC-inf, and 3.1 ± 0.97 h vs. 0.64 ± 0.34 h, $p < 0.05$ for T_{max}, for P1 and P2, respectively, $n = 6$, mean ± SEM) (Figure 5.7). After single oral administration, AUC-inf measures the absorbed drug amount and is calculated from administration time to infinity (inf), whereas the peak time (T_{max}) depends on the rate of drug absorption. Thus, the lower AUC-inf of KET–LYS P2 compared to that of commercial KET–LYS P1 could probably mean a lower bioavailability of KET–LYS P2, in addition to a lower T_{max} that indicates a faster absorption of this latter compared to commercial KLS. These data agree with IDR data and show the potential advantages of KET–LYS P2 for a further improvement of fast-acting formulations for the treatment of acute inflammation conditions.
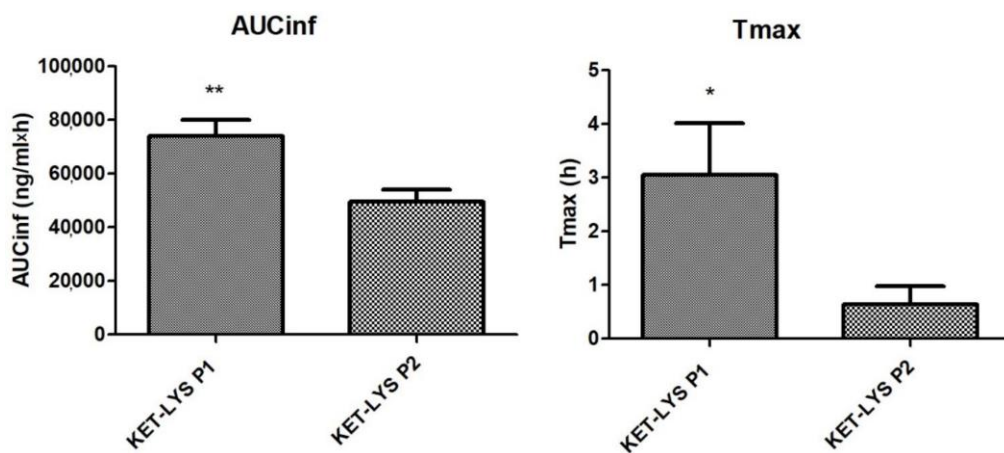
Figure 5.7 Pharmacokinetics *in vivo* of cocrystal KET–LYS P1 and salt KET–LYS P2. AUC-inf and T_{max} values of KET–LYS P1 and KET–LYS P2. * $p < 0.05$ and ** $p < 0.01$. Analyses were performed in $n = 6$ rats, and values are expressed as the mean ± SEM.

While it can be expected that cocrystals and salts with different coformers have different physicochemical and pharmacokinetic characteristics, finding significant differences in the IDR, taste, and pharmacokinetics of a salt and its cocrystal polymorph surely opens new

perspectives. Altogether, these differences clearly highlight the actual impact that (in this case) the substitution of one ionic bond (salt) with a neutral HB (cocrystal) can have on drug clinical performance, to the extent that different formulations and different coating processes or flavor addition can be suggested for the two polymorphs. KLS is a widely used NSAID that is already known, as also confirmed by our data on KET–LYS P1 T_{max}, for its rapid absorption and subsequent therapeutic action,[22] which make it indicated for the treatment of acute inflammatory and painful conditions. From our data, we can hypothesize that new polymorphic form KET–LYS P2 could further emphasize the property of KLS for the treatment of acute inflammatory and painful conditions.

5.4 Conclusions

In this study, we synthesized and characterized, for the first time, two different polymorphic forms of KLS, a cocrystal, KET–LYS P1, and a salt, KET–LYS P2. Through advanced analyses, we were able to define the structural characteristics of the two polymorphs and compare their physicochemical characteristics, in terms of dissolution rate and taste, and pharmacokinetic profiles *in vivo*. What emerged is that, from a structural point of view, the commercial KLS, which was introduced in the market as a KET salt, should instead be more appropriately defined as a cocrystal (KET–LYS P1), and that the newly identified salt KET–LYS P2 has significantly different chemical and pharmacokinetic characteristics compared to KET–LYS P1. The faster dissolution rate and reduced T_{max} *in vivo* of KET–LYS P2 suggest potential advantages of this new form for fast-acting formulations of the drug. Nevertheless, it should be considered that this new polymorph may exhibit a more bitter taste and a lower AUC compared to the commercially available KLS form, and this should prompt the design of specific formulation studies

138

to hypothesize different potential formulations (faster release) and coating or flavoring processes, according to the specific characteristics of the starting API material.

The present study advances our knowledge regarding the solid-state characteristics of KLS and gives a comprehensive view of its polymorphic diversity; while doing this, it led to the discovery of a new polymorph of KLS, KET–LYS P2, thus opening the way for the development of a new potential KET–LYS polymorph drug, the pharmacological and pharmacokinetic characteristics of which will be further investigated to define the appropriate formulation and the conditions that would most benefit from the treatment with this drug.

References

1   N. K. Duggirala; M. L. Perry; Ö. Almarsson; M. J. Zaworotko, *Chem. Commun.* **2015**, *52*, 640–655.

2   M. Karimi-Jafari; L. Padrela; G. Walker; D. M. Croker, *Cryst. Growth Des.* **2018**, *18*, 6370–6387.

3   X. L. Dai; J. M. Chen; T. B. Lu, *CrystEngComm* **2018**, *20*, 5292–5316.

4   C. B. Aakeröy; M. E. Fasulo; J. Desper, *Mol. Pharm.* **2007**, *4*, 317–322.

5   R. Chadha; S. Bhandari; J. Haneef; S. Khullar; S. Mandal, *CrystEngComm* **2014**, *16*, 8375–8389.

6   M. Zaworotko, *Chem. Commun.* **2004**, *35*, 1889–1896.

7   S. Tothadi; T. R. Shaikh; S. Gupta; R. Dandela; P. V. Chathakudath; A. K. Nangia, *Cryst. Growth Des.* **2021**, *21*, 735–747.

8   D. Bernasconi; S. Bordignon; F. Rossi; E. Priola; C. Nervi; R. Gobetto; D. Voinovich; D. Hasa; N. T. Duong; Y. Nishiyama; M. R. Chierotti, *Cryst. Growth Des.* **2020**, *20*, 906–915.

9   B. R. Bhogala; S. Basavoju; A. Nangia, *CrystEngComm* **2005**, *7*, 551–562.

10   A. J. Cruz-Cabeza, *CrystEngComm* **2012**, *14*, 6362–6365.

11   S. L. Childs; A. G. P. Stahly; A. Park, *Mol. Pharm.* **2007**, *4*, 323–338.

12   P. Stainton; T. Grecu; J. McCabe; T. Munshi; E. Nauha; I. J. Scowen; N. Blagden, *Cryst. Growth Des.* **2018**, *18*, 4150–4159.

13   E. Losev; E. Boldyreva, *Acta Crystallogr. C Struct. Chem.* **2018**, *74*, 177–185.

14   E. A. Losev; E. V. Boldyreva, *CrystEngComm* **2018**, *20*, 2299–2305.

15   S. R. Perumalla; C. Wang; Y. Guo; L. Shi; C. C. Sun, *CrystEngComm* **2019**, *21*, 2089–2096.

16   C. L. Jones; J. Skelton; S. C. Parker; P. R. Raithby; A. Walsh; C. C. Wilson; L. H. Thomas, *CrystEngComm* **2019**, *21*, 1626–1634.

17   A. V. Trask, *Mol. Pharm.* **2007**, *4*, 301–309.

18   K. Raza; P. Kumar; S. Ratan; R. Malik; S. Arora, *SOJ Pharm. Pharm. Sci.* **2014**, *1*, 1–10.

19   K. S. Seo; R. Bajracharya; S. H. Lee; H. K. Han, *Pharmaceutics* **2020**, *12*, 853–872.

20   L. Miles; J. Hall; B. Jenner; R. Addis; S. Hutchings, *Curr. Med. Res. Opin.* **2018**, *34*, 1483–1490.

21   R. Altman; B. Bosch; K. Brune; P. Patrignani; C. Young, *Drugs* **2015**, *75*, 859–877.

22   G. Varrassi; E. Alon; M. Bagnasco; L. Lanata; V. Mayoral-Rojals; A. Paladini; J. V.

Pergolizzi; S. Perrot; C. Scarpignato; T. Tölle, *Adv. Ther.* **2019**, *36*, 2618–2637.

23 J. E. Falk, *Porphyrins and Metalloporphyrins: A New Edition Based on the Original Volume by J. E. Falk*; Elsevier: Amsterdam, The Netherlands, **1975**.

24 S. Levitchev; A. Smirnova; V. Khitrova; L. Lvova; A. Bratov; Y. Vlasov, *Sens. Actuators B Chem.* **1997**, *44*, 397–401.

25 L. Lvova; C. Di Natale; A. D'Amico; R. Paolesse, *J. Porphyr. Phthalocyanines* **2009**, *13*, 1168–1178.

26 R. M. Silverstein; F. X. Webster; D. J. Kiemle; D. L. Bryce, *Spectrometric Identification of Organic Compounds*; Wiley: Hoboken, NJ, USA, **2015**.

27 P. Cerreia Vioglio; M. R. Chierotti; R. Gobetto, *Adv. Drug Deliv. Rev.* **2017**, *117*, 86–110.

28 M. R. Chierotti; R. Gobetto, *Chem. Commun.* **2008**, *14*, 1621–1634.

29 P. Briard; J. C. Rossi, *Acta Crystallogr. C* **1990**, *46*, 1036–1038.

30 S. Chen; H. Xi; R. F. Henry; I. Marsden; G. G. Z. Zhang, *CrystEngComm* **2010**, *12*, 1485–1493.

31 W. Pa; H. Ce; H. Kd, *Angew. Chem. Int. Ed. Engl.* **2015**, *54*, 3973–3977.

32 P. Pudjiastuti; S. Wafiroh; E. Hendradi; H. Darmokoesoemo; M. Harsini; M. A. R. D. Fauzi; L. Nahar; S. D. Sarker, *Open Chem.* **2020**, *18*, 226–231.

33 R. Chauhan, *J. Stem Cell Biol. Transplant.* **2017**, *1*, 12.

34 H. Sohi; Y. Sultana; R. K. Khar, *Drug Dev. Ind. Pharm.* **2004**, *30*, 429–448.

35 A. R. Baharuddin; S. Shaarani, *Int. Food Res. J.* **2015**, *22*, 731–738.

36 M. Maniruzzaman; J. Boateng; B. Z. Chowdhry; M. J. Snowden; D. Douroumis, *Drug Dev. Ind. Pharm.* **2013**, *40*, 145–156.

37 M. F. Arafa; S. A. El-Gizawy; M. A. Osman; G. El Maghraby, *Drug Dev. Ind. Pharm.* **2015**, *42*, 1225–1233.

38 Y. Maeno; T. Fukami; M. Kawahata; K. Yamaguchi; T. Tagami; T. Ozeki; T. Suzuki; K. Tomono, *Int. J. Pharm.* **2014**, *473*, 179–186.

39 S. Aitipamula; A. B. Wong; P. Kanaujia, *J. Pharm. Sci.* **2018**, *107*, 604–611.

40 L. Lvova; S. Denis; A. Barra; P. Mielle; C. Salles; C. Vergogian; C. Di Natalle; R. Paolesse; P. Temple-Boyer; G. Feron, *Talanta* **2012**, *97*, 171–180.

41 L. Lvova; C. G. Gonçalves; K. Petropoulos; L. Micheli; G. Volpe; D. Kirsanov; A. Legin; E. Viaggiu; R. Congestri; L. Guzzella *et al.*, *Biosens. Bioelectron.* **2016**, *80*, 154–160.

42 L. Lvova; I. Jahatspanian; L. H. Mattoso; D. S. Correa; E. Oleneva; A. Legin; C. Di Natale; R. Paolesse, *Sensors* **2020**, *20*, 821–830.

43 J. Hack; D. C. Grills; J. R. Miller; T. Mani, *J. Phys. Chem. B* **2016**, *120*, 1149–1157.

Chapter 6

Drug/prodrug solid solutions: a valid alternative to salts and cocrystals

6.1 Introduction

Modern medical therapies rely on increasingly complex pharmaceutical regimens that include multiple drugs with synergistic or complementary effects. In the case of chronic conditions, such therapies may be continued throughout the patient's life. Multidrug formulations could reduce drug dosage and potential side effects whilst simplifying administration regimens.[1–3] Such products can often be prepared as physical mixtures of the active pharmaceutical ingredients (APIs) in the desired dose, although the resulting multiphase system might be difficult to process and to store over time.[4] Alternatively, a stable crystalline phase can be obtained by combining multiple active ingredients in a cocrystal.[5,6] Cocrystals possess the advantages of a single phase but their fixed stoichiometry does not allow for the adjustment of the APIs dose, which is necessarily dictated by therapeutic considerations rather than crystallographic ones.[7] A third approach can be imagined that involves crystalline molecular solid solutions,[8] which combine the simplicity of a single crystalline phase with the stoichiometry variability of a physical mixture.

Solid solutions are commonly employed in inorganic chemistry and metallurgy, whereas their molecular subgroup remains largely understudied. Besides a few notable exceptions,[9–11] the dominant perception around these phases is that they are difficult to make.[12] Indeed, empirical rules originally formulated by Hume-Rothery[13] and Kitaigorodsky[14] prescribe that only atoms and molecules of the same size, charge and shape can mutually substitute each other in the solid state. Moreover, complete solubility is only deemed

possible for those compounds that produce isostructural (and/or isomorphous) crystals.[14] In particular, it was suggested that in order to form a mixed crystal, molecules must have equivalent hydrogen-bond donors and acceptors. From a crystal-engineering perspective, such a requirement can be seen as a direct consequence of Etter's rule for hydrogen bonds: 'All good proton donors and acceptors are used in hydrogen bonding'[15] – a rule that is generally followed in the known crystal structures with a few exceptions owing to steric hindrance.[16] Ultimately, only a subset of molecules, often differing by a methyl or a halogen substituent, would fulfil Hume-Rothery and Kitaigorodsky prescriptions. Such conditions represent a bottleneck to the development of pharmaceutical solid solutions.[15]

In contrast, recent work shows that appropriate design strategies can enable mixed crystals despite the lack of isostructurality[17] or large size difference[18] of the parent components. Other works show that the appropriate synthetic conditions could afford long-lasting metastable products – as an example, solvent-assisted grinding can afford solid solutions that are not available by conventional techniques.[19] In fact, for non-stoichiometric systems, the complex equilibria between liquid and solid phases often hinders the preparation of a uniform product. In those cases, mechanochemical reactions might afford better control over the product by avoiding a liquid phase.[12] Similarly, the kinetic control possible through rapid expansion of supercritical solutions (RESS) processes affords high miscibility in the solid solutions of anthracene/phenanthrene,[20] L-leucine/L-isoleucine and L-leucine/L-valine.[21]

With these premises we believe that the investigation of novel pharmaceutical solid solutions and their potential scale-up by such methods is meritable of attention. In particular, we wanted to test whether solid solutions could be formed for molecules that have different hydrogen-

bonding capabilities and are not isostructural. To this end, our attention was directed to two steroids: cortisone (C) and hydrocortisone (HC).

Owing to their extensive use in medicine, many steroids are synthesized and commercialized as slow-releasing formulations that help in maintaining the ideal blood concentration for prolonged periods of time.[22,23] Over five decades ago, steroids were among the earliest APIs to be co-crystallized as solid solutions and eutectic mixtures.[24,25] Interestingly, solid solutions are also reported for pairs of steroids such as arenobufagin/gamabufotalin and cinobufagin/cinobufotalin,[26] which are 'essentially isostructural' despite their different hydrogen-bond capabilities. In fact, for large and non-polar molecules such as steroids, the role of dispersive forces may become predominant over hydrogen bonds.[27]

C was the first steroid to be employed as a replacement in adrenocortical deficiency states.[28,29] Nowadays, it is largely substituted by its more soluble metabolite: cortisol (HC), the most widely used steroidal antiinflammatory drug, listed by the World Health Organization as an essential medicine.[30] For this drug, the topical market alone is estimated at ~3 billion USD globally.

C and HC differ only in the substituent in the C11 position, a carbonyl and a hydroxyl moiety, respectively (Scheme 6.1), and their metabolism is closely related. In fact, C can be seen as a prodrug[31] of HC, being converted to the latter by the 11-hydroxysteroid dehydrogenase.[32,33]
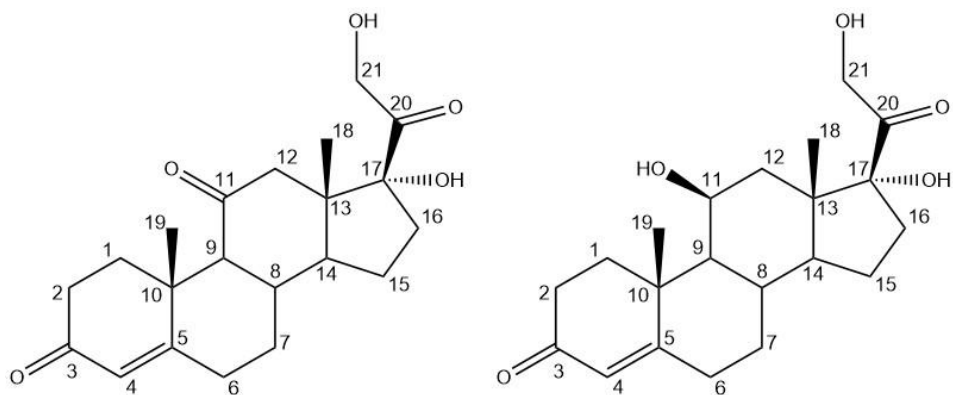
Scheme 6.1 Schematic representations of C (left) and HC (right), with C atom numbering.

From a pharmaceutical perspective, it can be imagined that a solid form that includes both molecules could help maintain the desired plasma concentration for a prolonged period reducing the number of doses and simplifying their administration.

6.2 Materials and methods

All reagents grade products were used as purchased without further purification.

6.2.1 Solution synthesis

Single crystals of pure C and pure HC were recrystallized from a solution of ~0.2 mmol (72 mg) of the commercial products in ethanol, by slow evaporation in ambient conditions. The mixed crystals of C and HC in the 2:1, 1:1 and 1:2 ratios were obtained in the same conditions from ethanol solutions containing: (*a*) 72.0 mg (0.2 mmol) of C and 36.3 mg (0.1 mmol) of HC, (*b*) 54.1 mg (0.15 mmol) of C and 54.4 mg (0.15 mmol) of HC, and (*c*) 36.1 mg (0.1 mmol) of C and 72.6 mg (0.2 mmol) of HC, respectively.

Good-quality single crystals were isolated from the liquid phase as soon as they formed (within two or three days).

6.2.2 Mechanochemical synthesis

Solid-solution synthesis of C and HC in the 2:1, 1:1 and 1:2 ratios was attempted by manually grinding in an agate mortar: (*a*) 72.0 mg (0.2 mmol) of C and 36.3 mg (0.1 mmol) of HC, (*b*) 54.1 mg (0.15 mmol) of C and 54.4 mg (0.15 mmol) of HC, and (*c*) 36.1 mg (0.1 mmol) of C and 72.6 mg (0.2 mmol) of HC, respectively. In each case, four to five (Pasteur pipette) drops of ethanol were added to the mixture and machination continued until a dry powder was obtained (~5–10 min).

6.2.3 SASD synthesis

Solutions of either pure C or HC where prepared by dissolving 150.0 mg of as-received powder in 20 mL of ethanol. Solutions of the mixed steroids in the 2:1, 1:1 and 1:2 ratios were prepared in 20 mL of ethanol by dissolving: (*a*) 100.0 mg (0.28 mmol) of C and 50.0 mg (0.14 mmol) of HC, (*b*) 75.0 mg (0.21 mmol) of C and 75.0 mg (0.21 mmol) of HC, and (*c*) 50.0 mg (0.14 mmol) of C and 100.0 mg (0.28 mmol) of HC, respectively. Full dissolution was completed in an ultrasonic bath (~15 min). The solutions were then filtered through a 0.2 mm pore-size nylon filter (Whatman Inc., Florham Park, New Jersey). An Agilent Technologies 1260 Infinity II pump was used to pass the solutions at a flow rate of 0.2 mL min^{-1} through a 0.1 cm^3 high-pressure nozzle equilibrated at 70 °C with heating resistors. In the nozzle, the solutions were mixed with a stream of CO_2 compressed to 12 MPa using a SFE Process DoseHPP 400-C pump. The supercritical mixture was depressurized in a 1000 cm^3 chamber in equilibrium with a water jacket at 70 °C, and the product collected on 0.2 mm filter paper. The samples were harvested and stored in

a desiccator prior to characterization to prevent exposure to humidity that results in solid-state transformation over time.

6.2.4 XRD analysis

Single-crystal XRD was performed in Bruker D8 Quest single-crystal X-ray diffractometers with an Mo anode for C, and a Cu anode for HC. Measurements were taken at an ambient temperature. The intensities were integrated with *SHELX* and *SAINT* in the Bruker *APEX3*[34] suite of programs and a solution was found using direct methods. Atomic positions and occupancies were refined against all the F^2_{obs} values, and all non-hydrogen atoms were treated anisotropically in *SHELXL*[35] using the *X-SEED*[36] interface.

Powder XRD patterns were collected on a X'Pert Pro instrument at 40 kV and 40 mA, with Cu Kα, λ = 1.54056 Å, in a $\theta°–\theta°$ geometry. Data were measured from 4 and 40 2$\theta°$ with a step size of 0.0167113° and a scan time of 19.685 seconds step^{-1}. Samples were placed in a zero-background disc. Rietveld refinement for mixture samples was performed in *HighScore Plus*.[37] Rietveld refinement was performed for the mixture samples against the pure C and HC crystal structures.

6.2.5 Hirshfeld surface analysis and energy calculation

Hirshfeld surface analysis was calculated with *Crystal Explorer 17*[42] for the molecules of C and HC in the pure compounds and in the solid solutions. Since the hydrogen-atom position cannot be reliably refined by XRD, the hydrogen atoms were fixed according to the riding model and their bond lengths normalized to the average neutron data. In particular, for the HC molecule, the H-C11-O11-H torsion angle was fixed to 45°: the most common value obtained as a result of the structure refinement. This precaution allows a more direct comparison of the structural change as a function of composition.

Interaction energies were calculated in *Crystal Explorer 17* for a cluster containing the reference molecule and neighbour molecules within a radius of 3.8 Å using the default setting and the HF/3-21G basis set.

6.2.6 Solid-state NMR

Solid-state NMR spectra were acquired with a Bruker Avance II 400 Ultra Shield instrument, operating at 400.23 and 100.63 MHz for ^{1}H and ^{13}C nuclei, respectively.

The powder samples were packed into cylindrical zirconia rotors with a 4 mm outer diameter and an 80 µL volume. A certain amount of sample was collected from each batch and used without further preparations to fill the rotor. [13]C CPMAS spectra were acquired at room temperature at a spinning speed of 12 kHz, using a ramp cross-polarization pulse sequence with a 90° [1]H pulse of 3.6 µs, a contact time of 3 ms, optimized recycle delays ranging from 2.5–5.6 s and a number of scans in the range 200–6500, depending on the sample. For every spectrum, a two-pulse phase modulation decoupling scheme was used, with a radiofrequency field of 69.4 kHz. The ^{13}C chemical shift scale was calibrated through the methylenic signal of external standard glycine (at 43.7 ppm). As for the [13]C T_1-^{1}H analysis of the 1:1 solid solution, ^{13}C spectra were acquired for 320 scans with different relaxation delays, included in the range 0.2–60 s and calculated by Bruker *TopSpin* 2.1 software through an exponential algorithm.

In order to assess the relative amounts of C and HC in the solid solutions, a deconvolution was performed on the signals in the 120–130 ppm range. By considering the resonances to be the result of slightly different contributions, the deconvolution allowed us to determine that the C:HC ratio for the SASD products is equal to 66.0:34.0, 49.7:50.3 and 35.2:64.8, in accordance with the nominal ones (2:1, 1:1 and 1:2, respectively).

6.2.7 Thermal analyses

Thermogravimetric analysis was performed on a TA Instrument Q50 with aluminium sample pans. Samples were heated to 400 °C with a rate of 10 °C min^{-1} and nitrogen gas flow rates of 60 mL min^{-1}. Differential scanning calorimetry was performed on a TA Instrument Q2000 in sealed aluminium pans with a heating rate of 10 °C min^{-1} and nitrogen gas flow rates of 60 mL min^{-1}.

6.2.8 Solubility measurements

Intrinsic solubility measurements were performed in sink conditions. 20 mg of each sample was dissolved in 1000 mL of deionized water at 37 °C at 150 rev min^{-1}. The sample was collected at minutes 1, 3, 5, 10, 15, 30, 45 and 60 and filtered through a 0.2 μm nylon filter. The HPLC system used was Agilent Technologies 1260 Infinity with column MachereyNagel EC100/4.6 Nucleodur 100-5C18ec. The mobile phase used was methanol and water with a ratio of 1:1 at 1.0 mL min^{-1} flow rate. 20 μL of the sample was injected into the HPLC system. The system and the autosampler were at an ambient temperature. Chromatograms were recorded at 248 nm with a run time of 12 min. The processing of the chromatographic data was carried out in the software *Chemstation* for liquid chromatography (Agilent Technologies).

6.3 Results and discussion
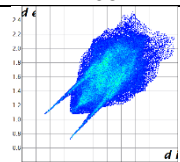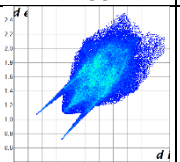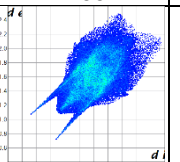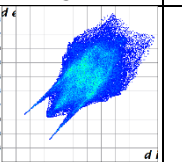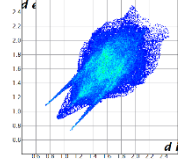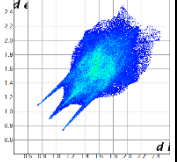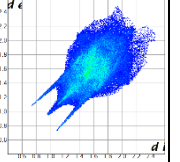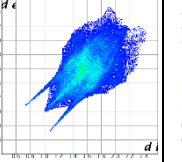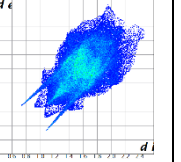
6.3.1 Single-crystal analysis

Despite their similar biochemical functions, C and HC are rather different from a supramolecular point of view. They crystallize in different structures and show different polymorphism. C has only one known polymorph in the $P2_12_12_1$ space group (CCDC refcode DHPRTO),[38,39] while three polymorphs of HC are known: forms I (CCDC refcode ZZZPNG01) and

III (CCDC refcode ZZZPNG03) in the $P2_12_12_1$ space group and form II (CCDC refcode ZZZPNG02) in the monoclinic $P2_1$ space group.[40] No evident structural similarity is recognisable in these structures,[26] phenomena that can be explained in terms of the different hydrogen-bond capabilities of the substituents, carbonyl and hydroxyl, on the C11.

Slow solvent evaporation of alcoholic solutions of C and HC in 2:1, 1:1 and 1:2 ratios provided colourless crystals. Single-crystal X-ray diffraction (XRD) revealed that the crystals are all isomorphous to the C structure (CCDC refcode DHPRTO). The C11–O11 bond lengths for the single crystals isolated from the solutions measure 1.25, 1.29 and 1.31 Å, respectively (Table 6.1).

Table 6.1 Crystallographic data for single crystals of C, HC and their solid solutions.

	C	C:HC ≃ 2:1	C:HC ≃ 1:2	C:HC ≃ 1:3	HC form I
a (Å)	7.7819 (4)	7.7442 (6)	7.7308 (7)	7.76953 (9)	10.1439 (14)
b (Å)	10.0468 (5)	10.0968 (8)	10.1237 (9)	10.1258 (11)	12.4255 (16)
c (Å)	23.6401 (13)	23.6750 (19)	23.694 (2)	23.694 (3)	30.496 (5)
Volume (Å³)	1848.26 (17)	1851.2 (3)	1854.4 (3)	1854.4 (3)	3843.8 (10)
Space group	$P2_12_12_1$	$P2_12_12_1$	$P2_12_12_1$	$P2_12_12_1$	$P2_12_12_1$
Moiety formula	$C_{21}H_{28}O_5$	0.63($C_{21}H_{28}O_5$) 0.37($C_{21}H_{30}O_5$)	0.36($C_{21}H_{28}O_5$) 0.64($C_{21}H_{30}O_5$)	0.26($C_{21}H_{28}O_5$) 0.74($C_{21}H_{30}O_5$)	$C_{21}H_{30}O_5$
M_r	360.43	361.18	361.71	361.92	359.42
D_x (g·cm⁻³)	1.295	1.296	1.296	1.306	1.242
Z	4	4	4	4	8
R (reflections)	0.0504 (3395)	0.0747 (2479)	0.0715 (1824)	0.0715 (1824)	0.0969 (931)
Temperature (K)	296	296	296	296	296
C-O distance (Å)	1.208	1.255	1.288	1.311	1.457
Hirshfeld plot of cortisone					
Hirshfeld plot of hydrocortisone					

These values fall between those of pure C (C=O = 1.21 Å) and those of pure HC (C–O = 1.43 Å) and suggest the formation of a solid solution. The poor resolution of standard XRD does not allow for the refinement of the oxygen substituent as a split atom (carbonyl versus hydroxyl group), nor for the reliable refinement of hydrogen-atoms occupancy.[41] Similarly, the single crystals are too small for high-performance liquid chromatography (HPLC) analysis. The occupancy refinement for the hydrogen atoms on C11 and on the adjacent O11 was attempted for a mere aesthetical end. The single crystals, isolated at the beginning of the crystallization, appear enriched in HC. Incidentally, when the C–O bond lengths are plotted against the calculated occupancy, a second-order relation emerges (see Figure A5.1 in Appendix V).

A qualitative understanding of the structure modifications that occur with substitution can be proposed using Hirshfeld surface analysis (see Figure A5.2 in Appendix V). Here the (virtual) replacement of a HC molecule in the structure of C would result in a short H···H contact (~1.8 Å) between the hydroxyl group O11 and C7 in the adjacent molecule (Figure 6.1).
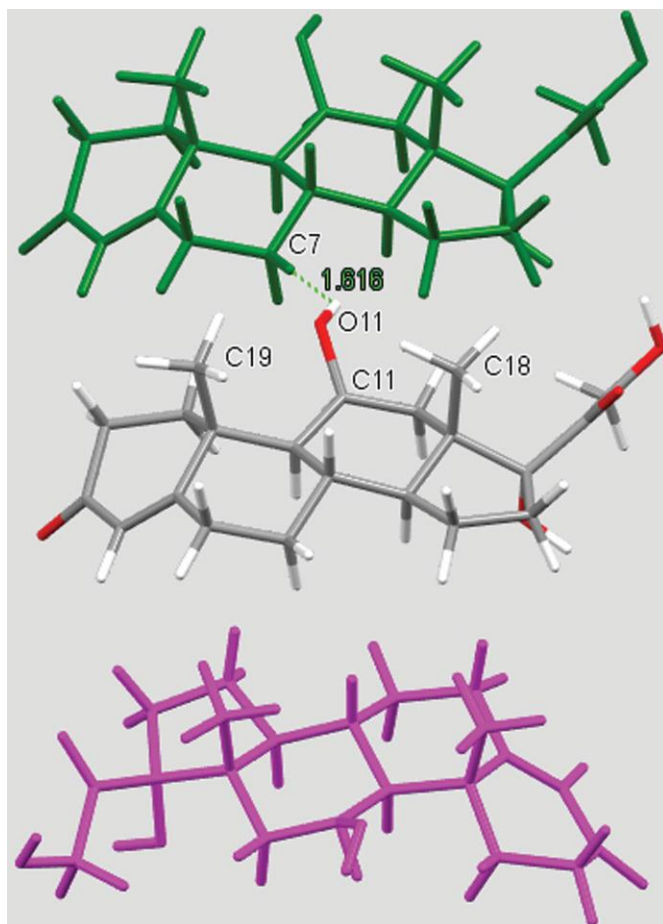
Figure 6.1 Part of the packing features of HC in the structure of C. The green molecule is generated by translation along *a* and the purple molecule is generated by screw symmetry along *b*.

This value is ~20% shorter than the expected contact distance based on the Bondi radius (1.1 Å). At the same time, any rotation of the OH group is sterically hindered by the presence of the adjacent methyl carbons C18 and C19, which suggests that the substitution would rapidly increase the enthalpy of the crystal. As a response, when the amount of HC increases, the structure progressively relaxes to accommodate the bulkier hydroxyl substituent (Table 6.1). The structure adjustments have negligible effects on the contact surface

of C but the H···H contact distance for HC increases to above 2 Å. A similar phenomenon was observed in the phenazine/acridine system, confirming the importance of structure modulability for the successful realization of solid solutions.[17]

The correct identification and quantification of all the energy contributions in such a disordered system is not straightforward and it is beyond the scope of this work, though an estimate of the energies can be performed in Crystal Explorer[42] for the C and HC molecules in the different structures. The results indicate that the overall interaction energy for the HC molecule in the structure of pure C is ~12 kJ mol^{-1} higher than that of the C molecule (see Tables A5.1a and A5.1b in Appendix V). The main difference is caused by the higher repulsion occurring with another HC molecule related by simple translation along the *a* axis (identified as *x*, *y* and *z* in Tables A5.1a and A5.1b and coloured in green in Figure 6.1). Although, part of the repulsion is compensated by a greater dispersive contribution. As the substitution increases and the structure adjusts, the repulsion contribution between this pair of HC molecules is progressively reduced and, eventually, the total interaction energy calculated for HC becomes comparable with the one calculated for C. Notably, the structural and compositional variations along the series seem to have little effect on the other molecular interactions. Invariantly, the largest contribution to the molecular packing comes from the dispersive interaction with the molecule along the *b* screw axis (identified as -*x*, *y* + 1/2, *z* + 1/2 in Tables A5.1a and A5.1b and coloured in violet in Figure 6.1).

6.3.2 Bulk synthesis and properties

Based on previous experience, solvent assisted co-grinding of the two molecules was attempted to make a bulk product with homogenous 2:1, 1:1

and 1:2 ratio compositions. The persistence of a diffraction peak at 17.5°
shows that a phase mixture was obtained (Figure 6.2).

PXRD
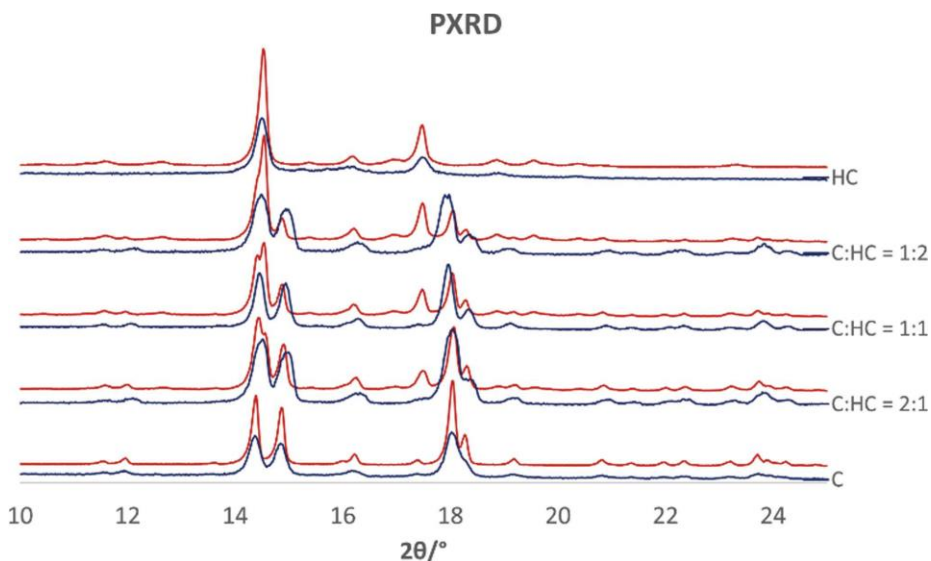
Figure 6.2 Powder XRD patterns measured for microcrystalline powder
generated by the SASD method (blue) and the mechanochemical product
(red).

Such qualitative conclusions are confirmed by Rietveld refinement, according
to which the relative amount of each phase coincides with that of the starting
materials (Tables A5.1a, A5.1b and A5.2). On the contrary, the same
technique indicates that a single microcrystalline phase is obtained when CO_2
is employed in a supercritical CO_2 assisted spray drying (SASD) process[43–45]
(Figure 6.2). In this case, peak broadening indicates smaller crystallites.

The spray-drying methods ensure that the overall stoichiometry of the
microcrystalline product coincides with that of the liquid phase. Within the
bulk, product uniformity is confirmed by solid-state nuclear magnetic
resonance (SSNMR). [13]C cross-polarization magic angle spinning (CPMAS)

spectra of the solid solutions are consistent with those of pure C, but with apparent differences, especially in the number of signals (Figure 6.3).
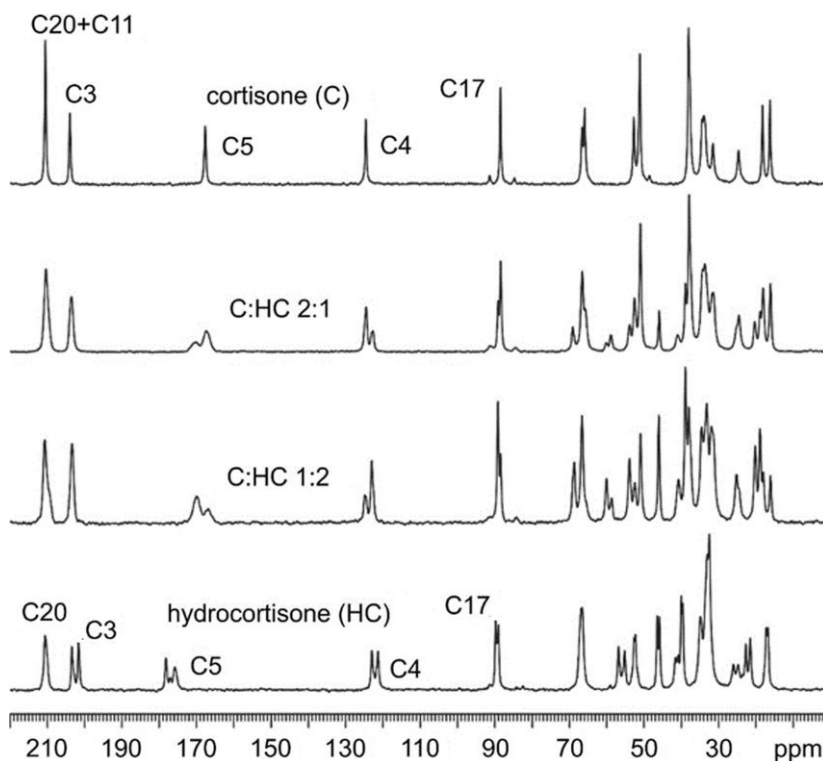
Figure 6.3 ^{13}C (100.63 MHz) CPMAS SSNMR spectra measured for the microcrystalline powder generated by the SASD method. The labels refer to assignments of relevant peaks (see Scheme 6.1 for atom numbering).

This agrees with the fact that the structure of pure C is maintained in the solid solutions, with HC as a guest molecule. The homogeneous nature of the microcrystalline product was further confirmed by ^{1}H T_1 relaxation measurements acquired through ^{13}C (not shown). Indeed, the ^{1}H T_1 values are the same for each ^{13}C signal, indicating active spin diffusion processes, i.e., homogeneous domains over a 100 nm scale. The CPMAS technique is

intrinsically non-quantitative, since the intensity of each spectral resonance depends both on their T_{XH} (the cross-polarization rate) and their $T_{1\rho}{}^{H}$ (the proton spin-lattice relaxation in the rotating frame). However, the two CH groups in C and HC are the same functional group (namely, the olefinic CH group – C4), in the same chemical environment of two almost identical and rigid molecules (or in any case with very similar mobility) in the same unit cell. Therefore, it is reasonable and safe to think that the two CH groups in the two molecules have almost identical T_{XH} and $T_{1\rho}{}^{H}$ values and the same cross-polarization rate. Thus, ^{13}C spectra were used to achieve reliable quantitative information.[46] Specifically, in order to assess the relative amounts of C and HC in the solid solutions, a deconvolution was performed on the signals in the 120–130 ppm range. By considering the resonances to be the result of slightly different contributions, the deconvolution allowed the determination of the C:HC ratio for the SASD products, in accordance with the nominal ones (see Figure A5.3).

Thermal analyses reveal that the solid solutions are marginally lower melting than the pure compounds but remain stable until ~180 °C (see Figures A5.4 and A5.5). Finally, the solubility of the new phase was assessed by measuring the intrinsic solubility of C and HC in the solid solution and physical mixture. Notably, in the solid solution the initial dissolution rate of HC is twice that of pure HC (form I). On the contrary, the dissolution rate of C is reduced in the solid solution (Figure 6.4). This agrees with the common understanding that the properties of solid solutions often vary regularly between those of the pure components.
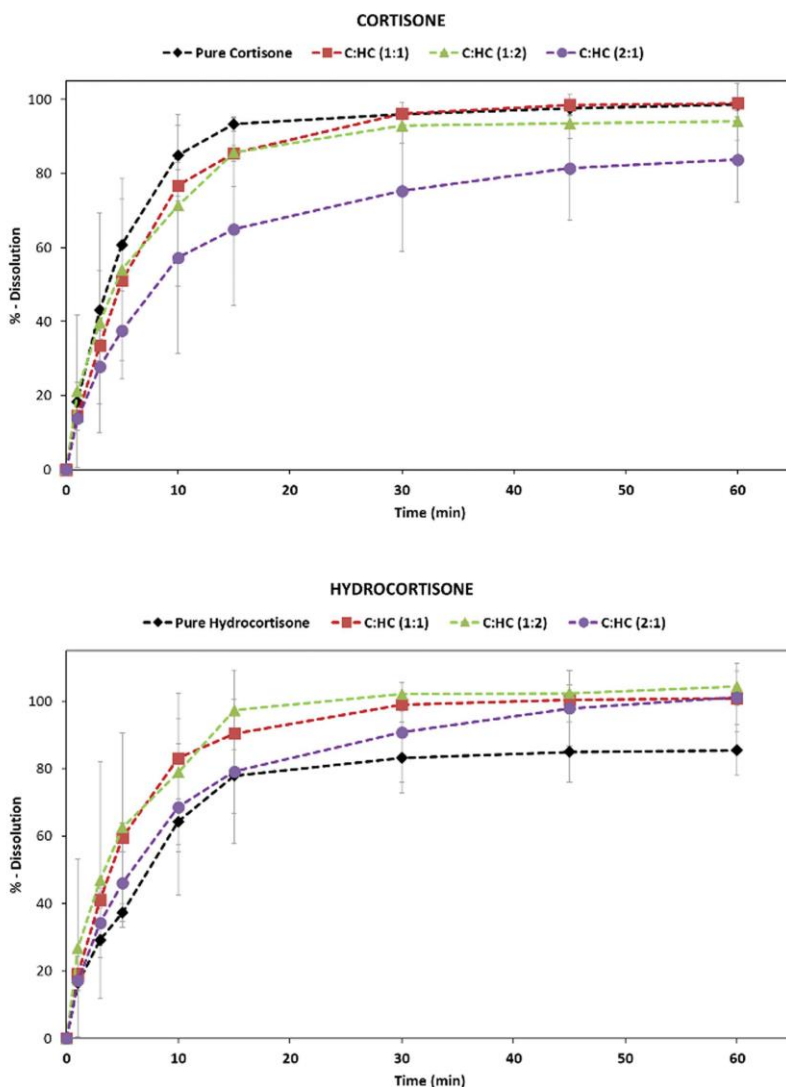
Figure 6.4 Dissolution profiles of C and HC for the products generated by the SASD method.

6.4 Conclusions

Drug/prodrug solid solutions of C and HC were prepared in different stoichiometric ratios. The mixed-crystals results are stable in spite of the different hydrogen-bond capabilities of the two molecules and the different crystal structures of their pure phases. We believe that the formation of the

solid solution is possible because in large and non-polar molecules the contribution of dispersive forces becomes predominant over that of hydrogen bonds. Moreover, the host structure of C can adjust to accommodate the hydroxyl group of the HC molecule. Interestingly, a uniform polycrystalline phase could be obtained by the SASD method, whereas the solvent evaporation and mechanochemical techniques resulted in a large compositional spread or a mixture of the pure components, respectively.

From a pharmaceutical point of view, the solid solution enables a faster dissolution rate of HC, which is up to twice that measured for the pure compound. We speculate that the higher solubility could increase the bioavailability of HC, while the compresence of C could prolong the desired concentration of the anti-inflammatory API in plasma. The variable ratio of the solid solutions would then allow the optimization of the correct dosage.

Ultimately, this work shows that mixed crystals represent a viable alternative to physical mixtures and cocrystals to formulate multidrug products. In particular, drug–prodrug solid solutions would be particularly targetable because of the structural similarity that is often observed between an active molecule and its biological precursors.

References

1. I. A. Aljuffali; C. F. Lin; C. H. Chen; J. Y. Fang, *Expert Opin. Drug Deliv.* **2016**, *13*, 1311–1325.

2. T. Okuda; S. Kidoaki, *J. Biomater. Nanobiotechnol.* **2012**, *3*, 50–60.

3. N. Das; M. Dhanawat; B. Dash; R. C. Nagarwal; S. K. Shrivastava, *Eur. J. Pharm. Sci.* **2010**, *41*, 571–588.

4. B. T. Raimi-Abraham; A. Garcia del Valle; C. Varon Galcera; S. A. Barker; M. Orlu, *J. Pharm. Heal. Serv. Res.* **2017**, *8*, 81–89.

5. O. N. Kavanagh; D. M. Croker; G. M. Walker; M. J. Zaworotko, *Drug Discovery Today* **2019**, *24*, 796–804.

6. S. Bordignon; P. Cerreia Vioglio; E. Priola; D. Voinovich; R. Gobetto; Y. Nishiyama; M. R. Chierotti, *Cryst. Growth Des.* **2017**, *17*, 5744–5752.

7. O. N. Kavanagh; G. Walker; M. Lusi, *Cryst. Growth Des.* **2019**, *19*, 5308–5313.

8. M. Lusi, *Cryst. Growth Des.* **2018**, *18*, 3704–3712.

9. M. K. Mishra; U. Ramamurty; G. R. Desiraju, *J. Am. Chem. Soc.* **2015**, *137*, 1794–1797.

10. D. Braga; F. Grepioni; L. Maini; M. Polito; K. Rubini; M. R. Chierotti; R. Gobetto, *Chem. Eur. J.* **2009**, *15*, 1508–1515.

11. A. Delori; P. Maclure; R. M. Bhardwaj; A. Johnston; A. J. Florence; O. B. Sutcliffe; I. D. H. Oswald, *CrystEngComm* **2014**, *16*, 5827–5831.

12. M. Lusi, *CrystEngComm* **2018**, *20*, 7042–7052.

13. W. Hume-Rothery, *J. Inst. Met.* **1926**, *35*, 295–361.

14. A. I. Kitaigorodsky, *Mixed Crystals.* **1984,** Berlin: Springer-Verlag.

15. M. C. Etter, *Acc. Chem. Res.* **1990**, *23*, 120–126.

16. P. A. Wood; P. T. A. Galek, *CrystEngComm* **2010**, *12*, 2485–2491.

17. E. Schur; E. Nauha; M. Lusi; J. Bernstein, *Chem. Eur. J.* **2015**, *21*, 1735–1742.

18. M. Lestari; M. Lusi, *Chem. Commun.* **2019**, *55*, 2297–2300.

19. M. R. Chierotti; L. Ferrero; N. Garino; R. Gobetto; L. Pellegrino; D. Braga; F. Grepioni; L. Maini, *Chem. Eur. J.* **2010**, *16*, 4347–4358.

20. G. T. Liu; K. Nagahama, *J. Supercrit. Fluids* **1996**, *9*, 152–160.

21. S. A. Raza; U. Schacht; V. Svoboda; D. P. Edwards; A. J. Florence; C. R. Pulham; J. Sefcik; I. D. H. Oswald, *Cryst. Growth Des.* **2018**, *18*, 210–218.

22. J. Paik; S. T. Duggan; S. J. Keam, *Drugs* **2019**, *79*, 455–462.

23. M. Krasselt; C. Baerwald, *Drug. Des. Dev. Ther.* **2016**, *10*, 1047–1058.

24 H. Rudel, US Patent 3800038A, **1974**.

25 E. E. Castellano; P. Main; E. Westbrook, *Acta Cryst. B* **1980**, *36*, 3063–3067.

26 A. Kálmán; L. Párkány, *Advances in Molecular Structure Research*, edited by M. Hargittai & I. Hargittai, **1997**, 3, 189. London: JAI Press Limited.

27 H. P. G. Thompson; G. M. Day, *Chem. Sci.* **2014**, *5*, 3173–3182.

28 T. G. Benedek, *Clin. Exp. Rheumatol.* **2011**, *29*, S5-S12.

29 P. S. Hench; E. C. Kendall; C. H. Slocumb; H. F. Polley, *Proc. Staff Meet. Mayo Clin.* **1949**, *24*, 181–197.

30 M. L. M. Garay; W. Babad; W. Hart, *J. Am. Acc. Derm.* **2007**, *56*, AB85.

31 K. L. Becker, *Principles and Practice of Endocrinology and Metabolism.* **2001**, Philadelphia: Lippincott Williams & Wilkins.

32 V. Lakshmi; C. Monder, *Endocrinology* **1985**, *116*, 552–560.

33 C. R. W. Edwards; D. Burt; M. A. Mcintyre; E. R. De Kloet; P. M. Stewart; L. Brett; W. S. Sutanto; C. Monder, *Lancet* **1988**, *332*, 986–989.

34 Bruker *APEX3.*, **2016**, v2016.5-0.

35 G. M. Sheldrick, *Acta Cryst. C* **2015**, *71*, 3–8.

36 L. J. Barbour, *J. Supramol. Chem.* **2001**, *1*, 189–191.

37 T. Degen; M. Sadki; E. Bron; U. König; G. Nénert, *Powder Diffr.* **2014**, *29*, S13–S18.

38 C. R. Groom; I. J. Bruno; M. P. Lightfoot; S. C. Ward, *Acta Cryst. B* **2016**, *72*, 171–179.

39 J. P. Declercq; G. Germain; M. Van Meerssche, *Cryst. Struct. Commun.* **1972**, *1*, 13–15.

40 V. Suitchmezian; I. Jeß; C. Näther, *J. Pharm. Sci.* **2008**, *97*, 4516–4527.

41 M. Lusi; L. J. Barbour, *Cryst. Growth Des.* **2011**, *11*, 5515–5521.

42 M. J. Turner; J. J. McKinnon; S. K. Wolff; D. J. Grimwood; P. R. Spackman; D. Jayatilaka; M. A. Spackman, *Crystal Explorer 17.* **2017**, University of Western Australia.

43 B. Long; G. M. Walker; K. M. Ryan; L. Padrela, *Cryst. Growth Des.* **2019**, *19*, 3755–3767.

44 B. Long; K. M. Ryan; L. Padrela, *Org. Process Res. Dev.* **2020**, *24*, 1006–1017.

45 L. Padrela; J. Zeglinski; K. M. Ryan, *Cryst. Growth Des.* **2017**, *17*, 4544–4553.

46 C. Anelli; M. R. Chierotti; S. Bordignon; P. Quadrelli; D. Marongiu; G. Bongiovanni; L. Malavasi, *Inorg. Chem.* **2019**, *58*, 944–949.

160

Conclusions

The aim of this doctoral thesis was to improve our rational understanding of some rules among those that stand as a foundation for crystal engineering. A reliable prediction of the outcome of supramolecular syntheses in terms of structural features and physicochemical properties indeed serves as the ultimate goal of this fascinating field of research. The projects that were carried out in this thesis demonstrated how particular focus needs to be put onto the nature of the crystallization partners, with regard, for example, to the state of hydration, the presence of specific moieties favored in the formation of supramolecur synthons, or its pK_a values. Nonetheless, part of this work showed how some basic principles, that often work as guidelines for crystal engineers, can be broken or harnessed in ways that allow for the obtainment of unexpected crystal forms.

In particular, the project presented in **Chapter 2** revealed that the hydration state of coformer L-proline, if combined with the adoption of an adequate stoichiometry, can afford differently hydrated cocrystals with methyl gallate; specifically, the absence of structural water in the employed L-proline was found to be a necessary condition for the obtainment of the anhydrous adduct, otherwise unobtainable by simply treating the hydrated cocrystal.

As for the adducts of ethionamide with dicarboxylic acids, discussed in **Chapter 3**, improved dissolution profiles for the API were achieved by selecting the very robust carboxylic acid-pyridinic nitrogen synthon. Moreover, in the case of the salt cocrystal with tartaric acid, a rare kryptoracemate form was obtained.

Chapters 4 and **5** dealt with selectively driving the supramolecular synthesis towards the obtainment of salt/cocrystal polymorph couples for the ethionamide-salicylic acid and ketoprofen-L-lysine systems, respectively. The

obtained results are surely extremely interesting and important: they represent very uncommon instances of cases in which the well-known pK_a rule fails to predict the ionization state of the intended crystal forms, and is ultimately overturned, since crystal forms characterized by the same chemical composition and stoichiometry, but different ionization states, were produced.

Finally, **Chapter 6** related to a collaboration performed together with the group of Dr. Lusi of Bernal Insitute, in Limerick, Ireland, that well fit in the context of this doctoral thesis. Indeed, the cornerstones of solid solubility, enounced decades ago by Kitaigorodsky and Hume-Rothery, were apparently violated. Carefully designed syntheses allowed for the obtainment of solid solutions of hydrocortisone and its prodrug cortisone, despite them exhibiting different native crystal structures and different hydrogen bond donor/acceptor capabilities.

It is apparent how much effort is still needed to improve the predictability of crystal engineering applications; the carried-out studies confirm how some of its fundamental principles are to be regarded just as explorative tools in the very early stages of the supramolecular design, and not as insurmountable obstacles. Indeed, both in academia and, especially, in the industry field, a common mistake is represented by the dogmatic character given to some empirical rules, which can lead to serious misinterpretation of the data, and also prevent researchers from seizing opportunities to make riveting discoveries.

It is most likely that the current and ever increasing efforts in the development of computational tools, machine learning, and chemometrics will be able to provide extremely precious assistance to crystal engineering. This is especially true in the context of crystal structure prediction and cocrystal formation prediction, two rapidly advancing approaches that have already proved highly helpful in the design step of new crystal forms.

162

Appendix I: Additional data for Chapter 2

Table A1.1 X-ray distances and angles in $MG_2 \cdot Pro_2 \cdot H_2O$. Refer to Figure A1.1 for atom numbering.

Atom1	Atom2	Atom3	Angle (°)	Atom1	Atom2	Length (Å)
C7	O1	C8	117.3(2)	O1	C7	1.335(3)
O1	C7	O2	123.8(2)	O4	C4	1.364(2)
O1	C7	C1	111.6(2)	O3	C3	1.374(2)
O2	C7	C1	124.6(2)	C7	C1	1.489(3)
C7	C1	C2	118.3(2)	C1	C2	1.396(3)
C7	C1	C6	121.1(2)	C1	C6	1.385(3)
C2	C1	C6	120.5(2)	C2	C3	1.381(3)
C1	C2	C3	119.1(2)	C4	C5	1.397(3)
O3	C3	C2	120.6(2)	O8	C13	1.369(3)
O3	C3	C4	118.5(2)	O7	C12	1.375(2)
C2	C3	C4	120.9(2)	O6	C11	1.362(3)
O4	C4	C3	116.8(2)	O9	C15	1.207(3)
O4	C4	C5	123.1(2)	O10	C15	1.331(3)
C3	C4	C5	120.1(2)	O10	C16	1.441(3)
O5	C5	C4	117.4(2)	C9	C10	1.392(3)
O5	C5	C6	123.5(2)	C9	C14	1.396(3)
C4	C5	C6	119.1(2)	C9	C15	1.487(3)
C1	C6	C5	120.3(2)	C10	C11	1.383(3)
C15	O10	C16	116.5(2)	C11	C12	1.395(3)
C10	C9	C14	120.4(2)	C12	C13	1.393(3)
C10	C9	C15	121.5(2)	C13	C14	1.373(3)
C14	C9	C15	118.1(2)	O1'	C1'	1.248(3)
C9	C10	C11	120.1(2)	N3'	C2'	1.502(3)
O6	C11	C10	124.3(2)	C1'	C2'	1.520(3)
O6	C11	C12	116.6(2)	C2'	C6'	1.525(4)
C10	C11	C12	119.1(2)	C6'	C5'	1.539(5)
O7	C12	C11	118.6(2)	C5'	C4'	1.475(5)
O7	C12	C13	121.0(2)	O3'	C7'	1.242(2)
C11	C12	C13	120.4(2)	O4'	C7'	1.254(3)
O8	C13	C12	115.7(2)	N9'	C8'	1.491(3)
O8	C13	C14	124.0(2)	N9'	C10'	1.502(3)
C12	C13	C14	120.3(2)	C7'	C8'	1.511(3)
C9	C14	C13	119.4(2)	C8'	C12'	1.537(3)
O9	C15	O10	123.1(2)	C12'	C11'	1.526(4)
O9	C15	C9	124.6(2)	C11'	C10'	1.500(4)
O10	C15	C9	112.3(2)	O8	C13	1.369(3)
C2'	N3'	C4'	108.9(2)	O7	C12	1.375(2)
O1'	C1'	O2'	128.4(2)	O6	C11	1.362(3)
O1'	C1'	C2'	116.5(2)	O9	C15	1.207(3)
O2'	C1'	C2'	115.0(2)	O10	C15	1.331(3)
N3'	C2'	C1'	109.9(2)	O10	C16	1.441(3)

Atom1	Atom2	Atom3	Angle	Atom1	Atom2	Length
N3'	C2'	C6'	104.2(2)	C9	C10	1.392(3)
C1'	C2'	C6'	113.1(2)	C9	C14	1.396(3)
C2'	C6'	C5'	103.7(3)	C9	C15	1.487(3)
C6'	C5'	C4'	103.1(3)	C10	C11	1.383(3)
N3'	C4'	C5'	105.2(3)	C11	C12	1.395(3)
C8'	N9'	C10'	105.8(2)	C12	C13	1.393(3)
O3'	C7'	O4'	127.0(2)	C13	C14	1.373(3)
O3'	C7'	C8'	117.6(2)	O3'	C7'	1.242(2)
O4'	C7'	C8'	115.4(2)	O4'	C7'	1.254(3)
N9'	C8'	C7'	111.9(2)	N9'	C8'	1.491(3)
N9'	C8'	C12'	102.1(2)	N9'	C10'	1.502(3)
C7'	C8'	C12'	114.2(2)	C7'	C8'	1.511(3)
C8'	C12'	C11'	104.3(2)	C8'	C12'	1.537(3)
C12'	C11'	C10'	107.1(2)	C12'	C11'	1.526(4)
N9'	C10'	C11'	105.4(2)	C11'	C10'	1.500(4)
				O1	C7	1.335(3)
				O1	C8	1.445(3)
				O2	C7	1.197(3)
				O5	C5	1.359(2)
				O4	C4	1.364(2)
				O3	C3	1.374(2)
				C7	C1	1.489(3)
				C1	C2	1.396(3)
				C1	C6	1.385(3)
				C2	C3	1.381(3)
				C3	C4	1.386(3)
				C4	C5	1.397(3)
				C5	C6	1.392(3)
				O1'	C1'	1.248(3)
				O2'	C1'	1.259(3)
				N3'	C2'	1.502(3)
				N3'	C4'	1.485(3)
				C1'	C2'	1.520(3)
				C2'	C6'	1.525(4)
				C6'	C5'	1.539(5)
				C5'	C4'	1.475(5)

Table A1.2 Hydrogen bond distances in MG$_2$·Pro$_2$·H$_2$O. Refer to Figure A1.1 for atom numbering.

Atom1	Atom2	Length	Length-VdW	Symm. op. 1	Symm. op. 2
O5	O4'	2.593	-0.447	x,y,z	x,y,-1+z
O9	N3'	2.853	-0.217	x,y,z	x,-1+y,z
N9'	O7	2.821	-0.249	x,y,z	1+x,y,z
O11	O4	2.996	-0.044	x,y,z	-1+x,y,z
O11	O8	2.650	-0.390	x,y,z	1+x,y,z
O11	N3'	2.770	-0.300	x,y,z	x,-1+y,z
O11	O3'	2.725	-0.315	x,y,z	x,y,-1+z

O8	O3	2.814	-0.226	1+x,y,z	-1+x,y,z
O7	O3	2.998	-0.042	1+x,y,z	-1+x,y,z
O3'	O4	2.632	-0.408	x,y,-1+z	-1+x,y,z
N9'	O5	3.008	-0.062	x,y,-1+z	-1+x,y,z
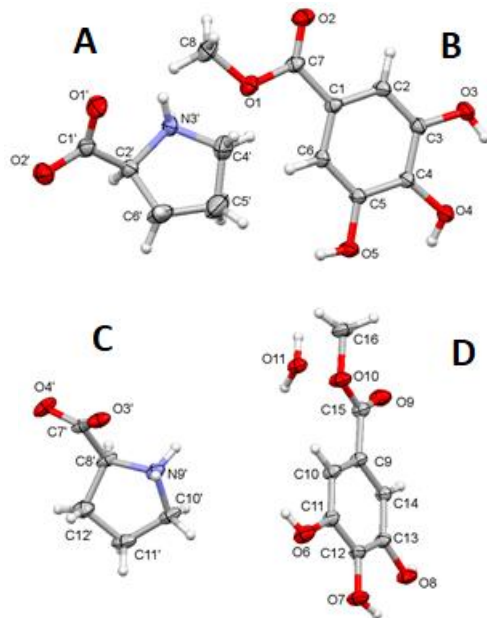
Figure A1.1 Asymmetric unit of $MG_2 \cdot Pro_2 \cdot H_2O$, with atom numbering. Thermal ellipsoids drawn at 70% of probability. (C = grey; H = white; O = red; N = azure).

Table A1.3 X-ray distances and angles in $MG \cdot Pro_2$. Refer to Figure A1.2 for atom numbering.

Atom1	Atom2	Length (A°)	Atom1	Atom2	Atom3	Angle (°)
C18	O1	1.441(4)	C7	C2	C3	120.2(2)
O5	C6	1.350(3)	C7	C2	C1	120.4(2)
C2	C7	1.385(3)	C3	C2	C1	119.5(2)
C2	C3	1.382(3)	C6	C5	O4	123.2(2)
C2	C1	1.467(3)	C6	C5	C4	119.5(2)
C5	C6	1.390(3)	O4	C5	C4	117.4(2)
C5	O4	1.357(3)	C18	O1	C1	117.2(2)
C5	C4	1.387(3)	O5	C6	C5	116.5(2)
O3	C4	1.367(3)	O5	C6	C7	123.3(2)
O1	C1	1.325(3)	C5	C6	C7	120.1(2)
C6	C7	1.372(3)	C2	C7	C6	119.9(2)

C3	C4	1.370(3)	C2	C3	C4	119.9(2)
C1	O2	1.203(3)	C2	C1	O1	112.8(2)
N1	C9	1.499(3)	C2	C1	O2	125.1(2)
N1	C12	1.498(3)	O1	C1	O2	122.1(2)
O6	C8	1.252(3)	C5	C4	O3	120.1(2)
C8	C9	1.517(3)	C5	C4	C3	120.4(2)
C8	O7	1.223(3)	O3	C4	C3	119.5(2)
C9	C10	1.508(4)	C9	N1	C12	108.7(2)
C10	C11	1.506(4)	O6	C8	C9	114.9(2)
C11	C12	1.499(4)	O6	C8	O7	127.7(2)
O9	C13	1.249(3)	C9	C8	O7	117.4(2)
N2	C14	1.497(3)	N1	C9	C8	110.3(2)
N2	C17A	1.43(2)	N1	C9	C10	103.1(2)
O8	C13	1.251(3)	C8	C9	C10	112.9(2)
C14	C15A	1.47(2)	C9	C10	C11	103.8(2)
C16A	C15A	1.54(2)	C10	C11	C12	103.2(2)
C16A	C17A	1.56(2)	N1	C12	C11	104.8(2)
			C14	N2	C17A	109.6(7)
			O9	C13	O8	126.9(2)
			O9	C13	C14	116.5(2)
			O8	C13	C14	116.6(2)
			N2	C14	C13	109.7(2)
			N2	C14	C15A	103.7(6)
			C13	C14	C15A	119.5(7)

Table A1.4 Hydrogen bond distances in MG·Pro$_2$ X-ray structure. Refer to Figure A1.2 for atom numbering.

Atom1	Atom2	Length	Length-VdW	Symm. op. 1	Symm. op. 2
O2	O3	2.809	-0.231	x,y,z	-1/2+x,1/2-y,1-z
O5	O6	2.596	-0.444	x,y,z	x,-1+y,z
O5	N1	2.822	-0.248	x,y,z	1-x,-1/2+y,1/2-z
O4	O9	2.720	-0.320	x,y,z	1/2+x,1/2-y,1-z
N1	O8	2.802	-0.268	x,y,z	1/2-x,1-y,-1/2+z
O7	N2	2.724	-0.346	x,y,z	1.5-x,1-y,-1/2+z
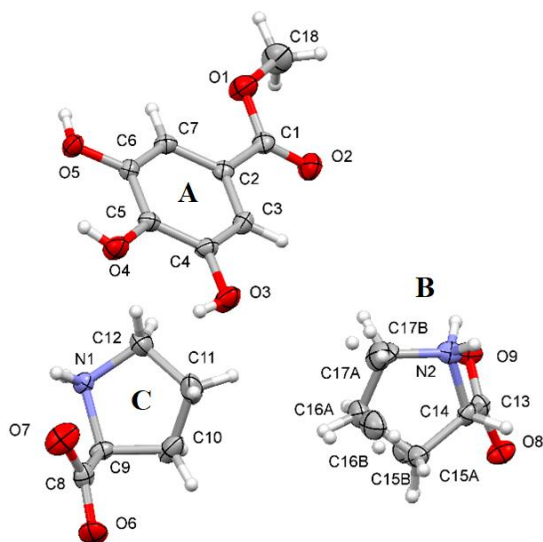
Figure A1.2 Asymmetric unit of MG·Pro$_2$, with atom numbering. Thermal ellipsoids drawn at 70% of probability. (C = grey; H = white; O = red; N = azure).
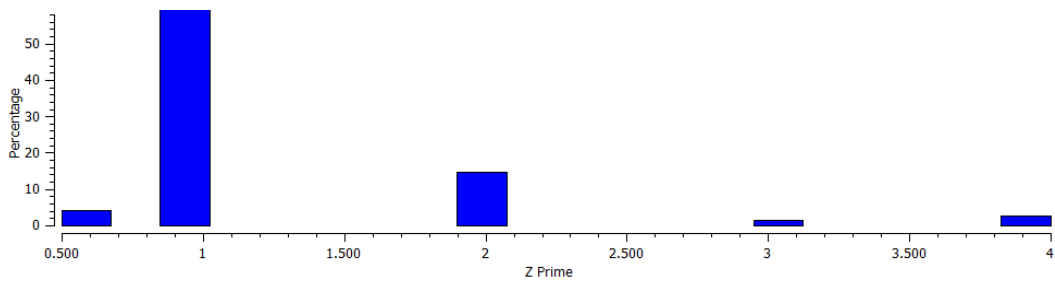
Figure A1.3 Percentage of structures as function of Z' in the 117 organic derivatives of Pro found in the CSD database.
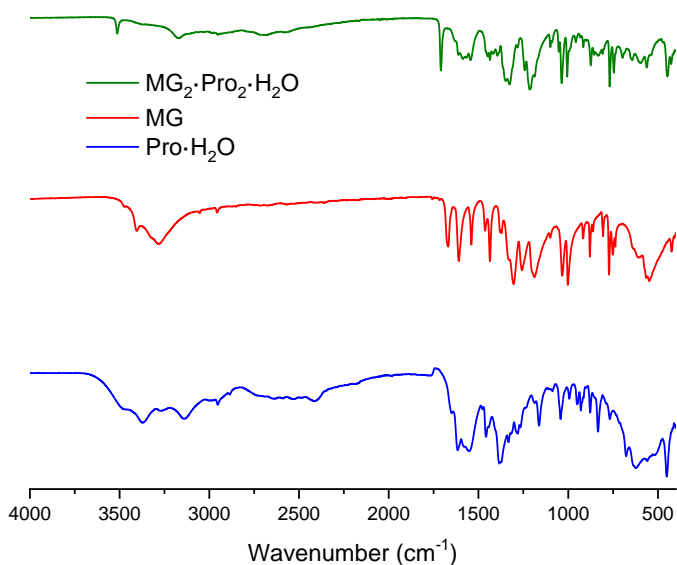
Figure A1.4 ATR-IR spectra of $MG_2 \cdot Pro_2 \cdot H_2O$ (in green), MG (in red) and $Pro \cdot H_2O$ (in blue).
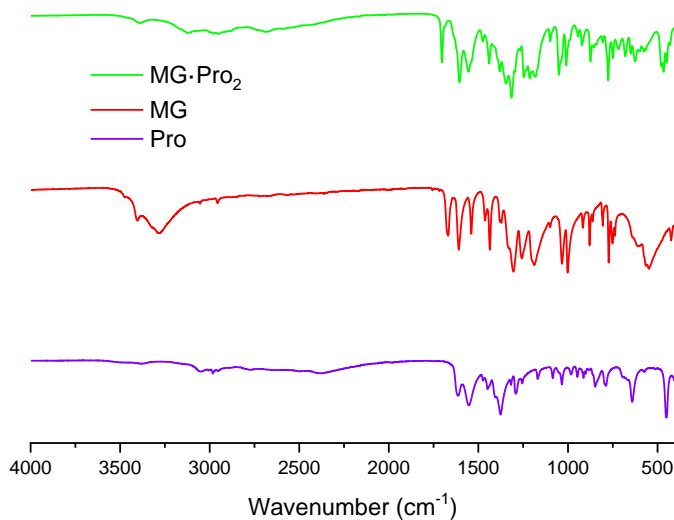
Figure A1.5 ATR-IR spectra of $MG \cdot Pro_2$ (in green), MG (in red) and Pro (in purple).

Table A1.5 ^{13}C and ^{15}N SSNMR detailed acquisition parameters.

	^{13}C CPMAS spectra					
	MG	Pro	Pro·H_2O	MG·Pro_2	MG_2·Pro_2·H_2O	MG_2·Pro_2
Number of scans	284	80	120	100	200	32
Relaxation delay (s)	5	50	18	6	15	28
Contact time (ms)	4	3	3	3	4	3.5
Resolution (Hz)	25	29	29	29	25	34
	^{15}N CPMAS spectra					
Number of scans	/	1706	17650	1594	15328	/
Relaxation delay (s)	/	50	18	6	15	/
Contact time (ms)	/	3	4	4	4	/
Resolution (Hz)	/	26	26	26	25	/

Table A1.6 Experimental outcomes of several attempted mechanochemical (grinding and water-assisted kneading) preparations.

Reagent 1	Reagent 2	Molar ratio	Water	Outcome
MG	Pro	1:2	NO	MG·Pro_2
MG	Pro	1:2	YES	MG·Pro_2
MG	Pro	1:1	YES	MG_2·Pro_2·H_2O
MG	Pro·H_2O	1:1	NO	MG_2·Pro_2·H_2O
MG·Pro_2	MG	1:1	YES	MG_2·Pro_2·H_2O
MG	Pro·H_2O	1:2	NO	MG_2·Pro_2·H_2O + Pro·H_2O
MG·Pro_2	/	/	YES	unstable phase
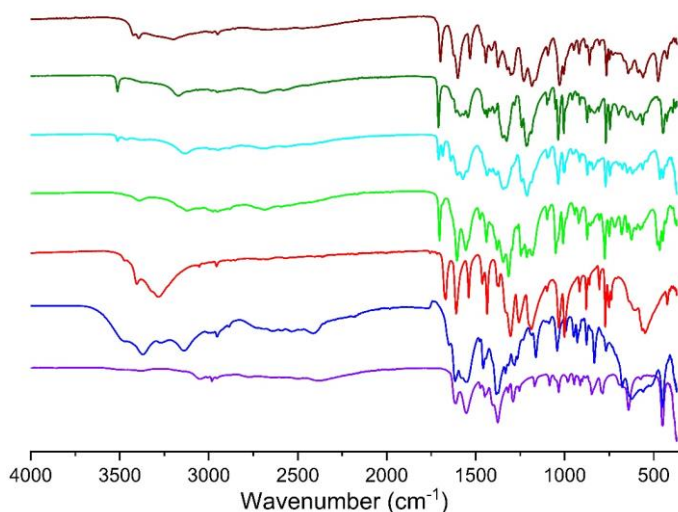
Figure A1.6 ATR-IR spectra of, from bottom to top, Pro (in purple), Pro·H_2O (in blue), MG (in red), MG·Pro_2 (in lime), the unstable phase [obtained by kneading (H_2O) MG·Pro_2, see main text in Chapter 2] (in cyan), MG_2·Pro_2·H_2O (in green), and the anhydrous phase (obtained by heating MG_2·Pro_2·H_2O, see main text in Chapter 2) (in wine).
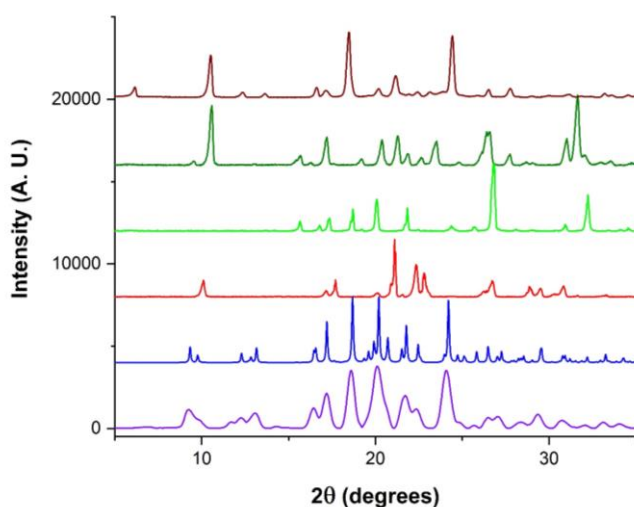
Figure A1.7 Experimental PXRD patterns of, from bottom to top, Pro (in purple), Pro·H_2O (in blue), MG (in red), MG·Pro_2 (in lime), MG_2·Pro_2·H_2O (in green), and the anhydrous phase (obtained by heating MG_2·Pro_2·H_2O, see main text in Chapter 2) (in wine).

170
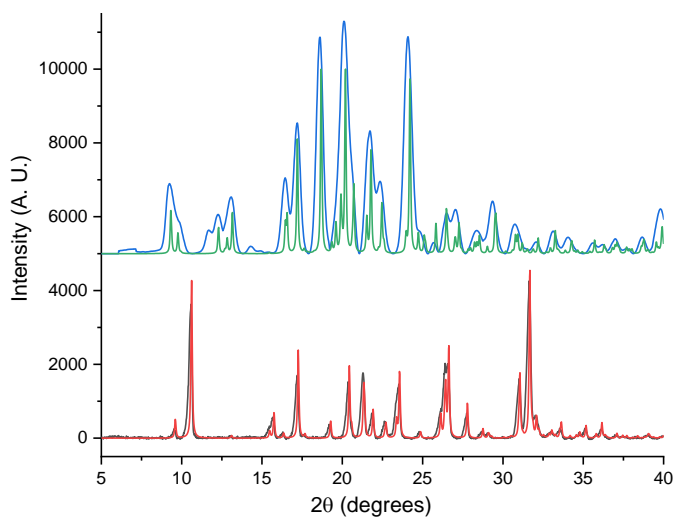
Figure A1.8 Comparison between experimental and calculated (from the single crystal structure) PXRD patterns for $MG_2 \cdot Pro_2 \cdot H_2O$ (black and red, respectively) and $MG \cdot Pro_2$ (blue and green, respectively).
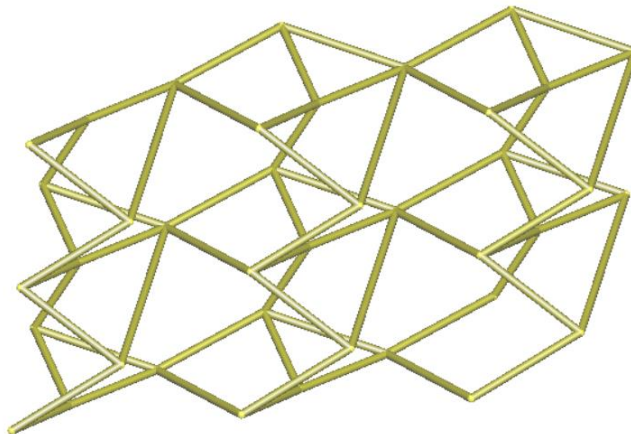
Figure A1.9 Representation of the 2D HB underlying net in $MG_2 \cdot Pro_2 \cdot H_2O$.
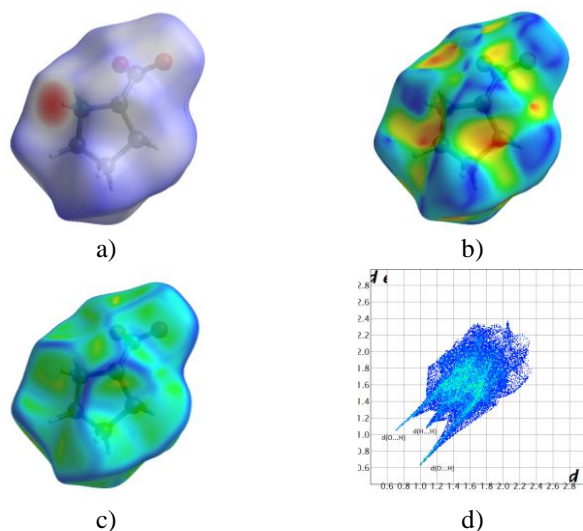
Figure A1.10 Hirshfeld Surface analysis of Pro (C) in MG$_2$·Pro$_2$·H$_2$O (Figure A1.1): representation of d$_{norm}$ (a), Shape Index (b), curvedness (c) and relative fingerprint (d).
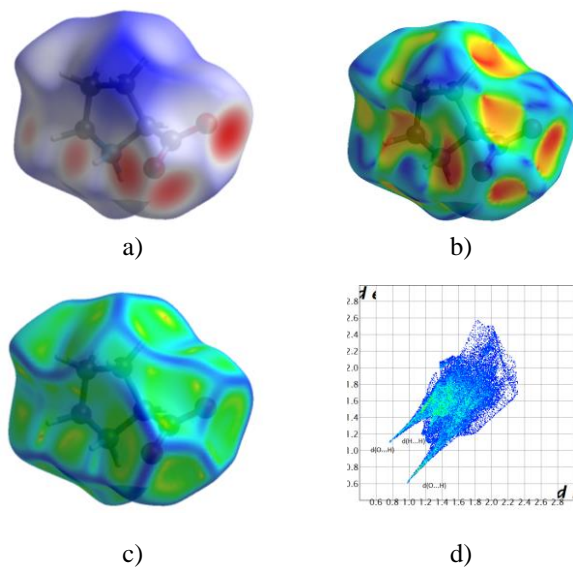
Figure A1.11 Hirshfeld Surface analysis of Pro (A) in MG$_2$·Pro$_2$·H$_2$O (Figure A1.1): representation of d$_{norm}$ (a), Shape Index (b), curvedness (c) and relative fingerprint (d).
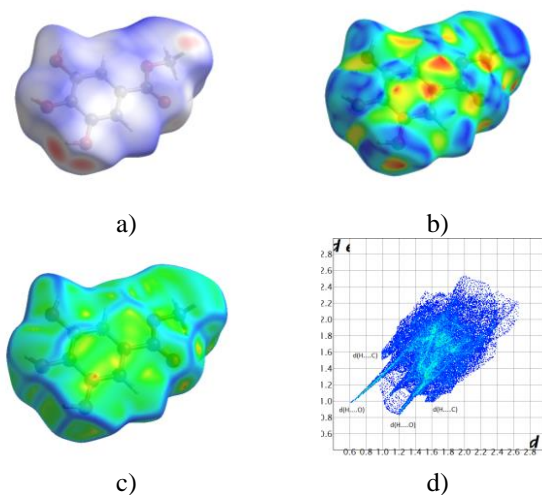
Figure A1.12 Hirshfeld Surface analysis of MG (B) in MG$_2$·Pro$_2$·H$_2$O (Figure A1.1): representation of d$_{norm}$ (a), Shape Index (b), curvedness (c) and relative fingerprint (d).
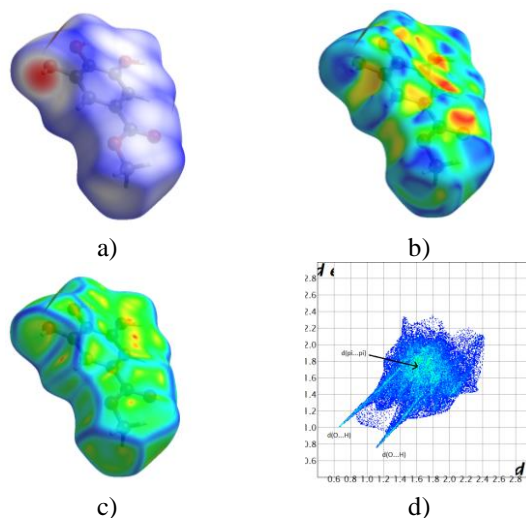
Figure A1.13 Hirshfeld Surface analysis of MG (D) in MG$_2$·Pro$_2$·H$_2$O (Figure A1.1): representation of d$_{norm}$ (a), Shape Index (b), curvedness (c) and relative fingerprint (d).

a)   b)   c)
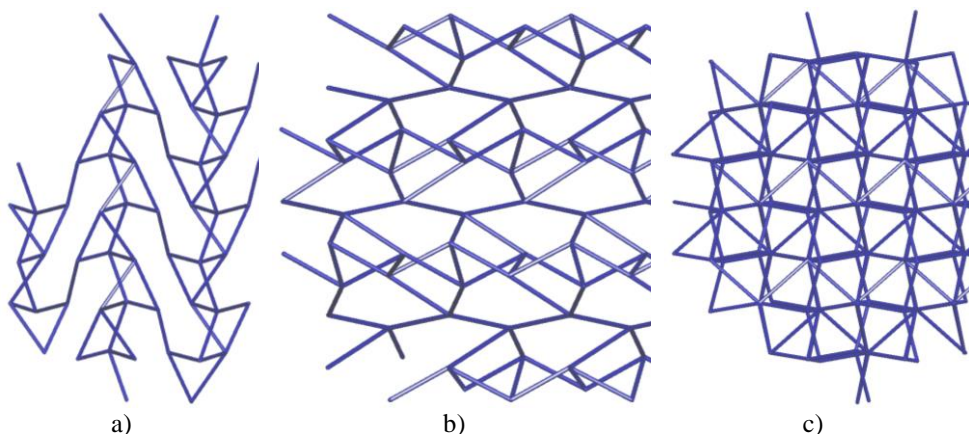
Figure A1.14 Underlying net representation of MG·Pro$_2$ based on HB interactions between molecules along x, y and z (a, b and c, respectively).

a)   b)

c)   d)
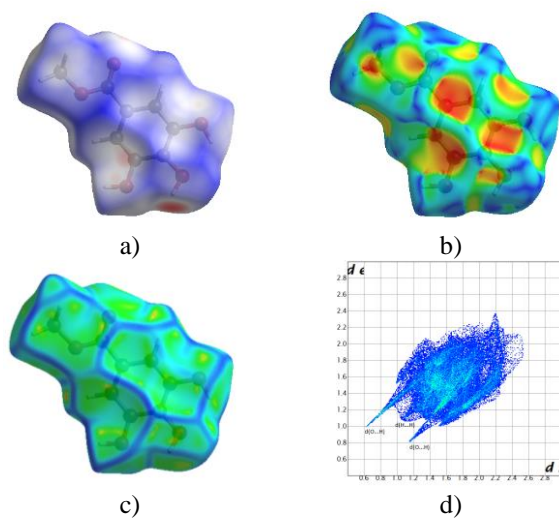
Figure A1.15 Hirshfeld Surface analysis of MG in MG·Pro$_2$ (Figure A1.2): representation of d$_{norm}$ (a), Shape Index (b), curvedness (c) and relative fingerprint (d).
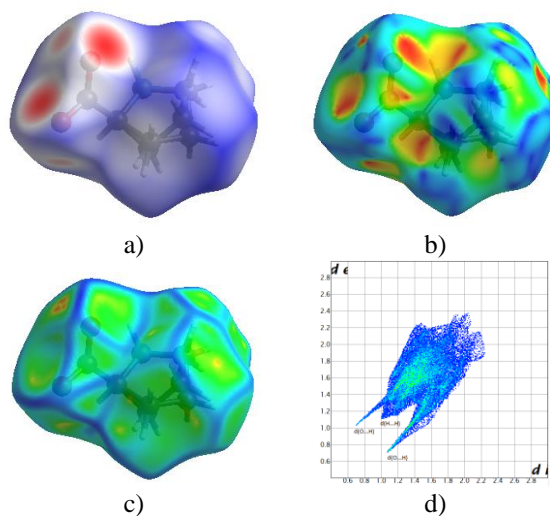
Figure A1.16 Hirshfeld Surface analysis of Pro (B) in MG·Pro$_2$ (Figure A1.2): representation of d_{norm} (a), Shape Index (b), curvedness (c) and relative fingerprint (d).
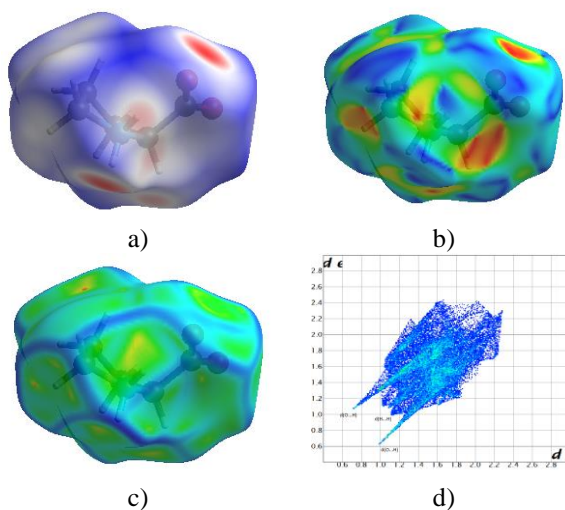
Figure A1.17 Hirshfeld Surface analysis of Pro (C) in MG·Pro$_2$ (Figure A1.2): representation of d_{norm} (a), Shape Index (b), curvedness (c) and relative fingerprint (d).
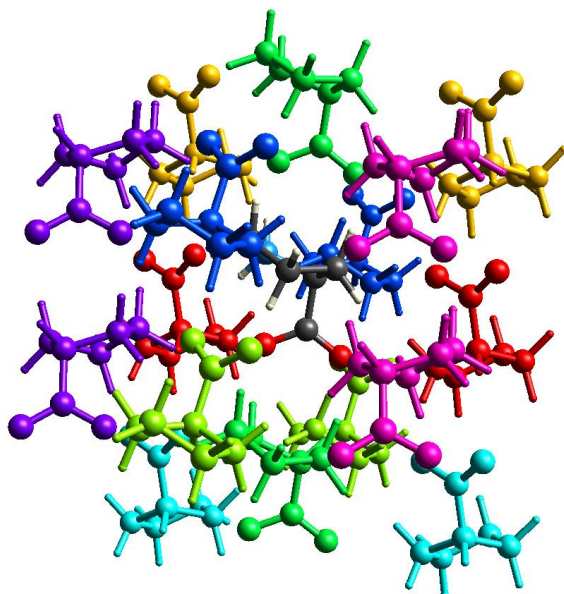
Figure A1.18 Representation of Interaction energies of the molecular pairs calculated for Pro (CSD code: PROLIN). (Colours are connected to lines in Table A1.7).

Table A1.7 Interaction energies (kJ/mol) of the molecular pairs of Pro (CSD code: PROLIN).

|	N	Symop	R	Electron Density	E_ele	E_pol	E_dis	E_rep	E_tot
🟥	2	-x, y+1/2, -z+1/2	5.17	HF/3-21G	-105.4	-31.2	-15.8	24.8	-121.8
🟧	2	-x, y+1/2, -z+1/2	6.86	HF/3-21G	-0.5	-4.2	-3.7	0.1	-6.4
🟨	2	x+1/2, -y+1/2, -z	6.63	HF/3-21G	-26.4	-8.2	-4.5	0.9	-35.5
🟩	2	x, y, z	5.20	HF/3-21G	-112.6	-50.6	-21.3	58.5	-119.4
🟦	2	-x, y+1/2, -z+1/2	7.78	HF/3-21G	27.6	-3.4	-1.1	0.0	24.9
🟦	2	x+1/2, -y+1/2, -z	6.10	HF/3-21G	-20.7	-9.2	-14.4	6.6	-34.7
🟪	2	-x+1/2, -y, z+1/2	6.30	HF/3-21G	15.2	-8.8	-9.9	3.4	3.6
🟥	2	-x+1/2, -y, z+1/2	6.07	HF/3-21G	7.5	-5.0	-14.9	9.0	-1.8
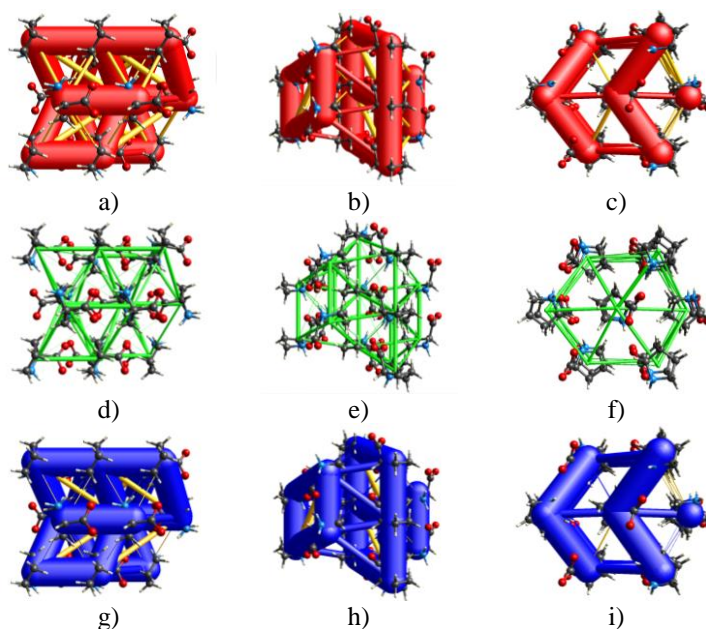
Figure A1.19 Energy Framework of Pro (CSD code: PROLIN) in its electrostatic component along x, y and z axes (a, b and c, respectively), its dispersive component along x, y and z axes (d, e and f, respectively) and in its total energy representation along x, y and z axes (g, h and i, respectively).
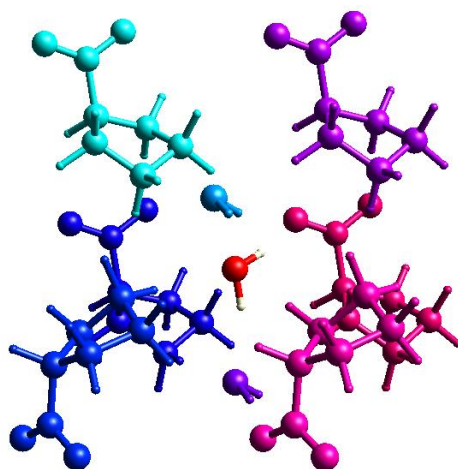

Figure A1.20 Representation of Interaction energies of the molecular pairs calculated for Pro·H_2O (CSD code: RUVGEW). (Colours are connected to lines in Table A1.8)

Table A1.8 Interaction energies (kJ/mol) of the molecular pairs calculated for Pro·H_2O (CSD code: RUVGEW).

	N	Symop	R	Electron Density	E_ele	E_pol	E_dis	E_rep	E_tot
	1	x, y, z	8.04	HF/3-21G	-33.2	-7.4	-3.3	1.7	-40.3
	1	x, y, z	6.19	HF/3-21G	23.9	-6.3	-7.9	2.0	14.7
	1	x, y, z	5.14	HF/3-21G	-106.1	-48.5	-23.4	60.7	-113.6
	1	-	5.24	HF/3-21G	-33.2	-7.4	-3.3	1.7	-40.3
	1	-	5.57	HF/3-21G	-33.2	-7.4	-3.3	1.7	-41.3
	1	x, y, z	5.14	HF/3-21G	-106.1	-48.5	-23.4	60.7	-113.6
	1	-	5.22	HF/3-21G	23.9	-6.3	-7.9	2.0	14.7
	1	-	4.41	HF/3-21G	23.9	-6.3	-7.9	2.0	14.7
	1	-	2.91	HF/3-21G	-106.1	-48.5	-23.4	60.7	-111.6
	1	-	5.26	HF/3-21G	-106.1	-48.5	-23.4	60.7	-111.6
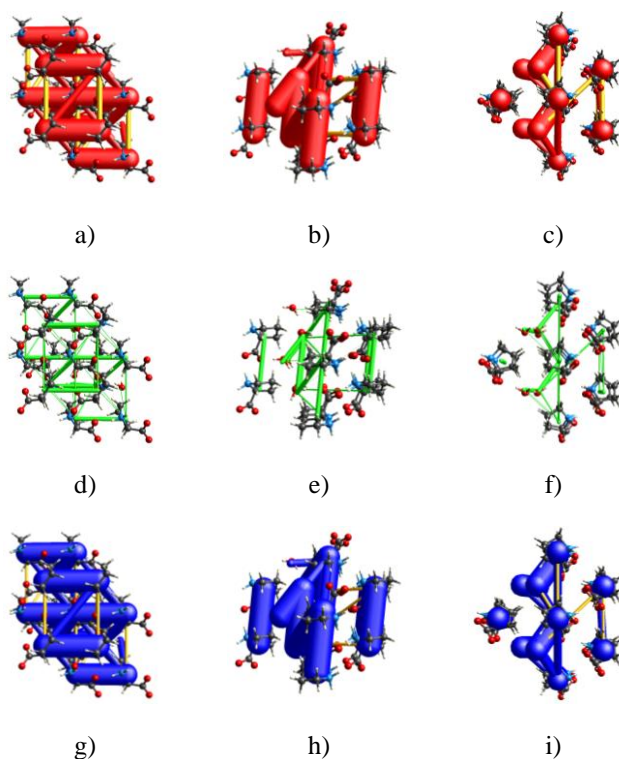
Figure A1.21 Energy Framework of Pro·H$_2$O (CSD code: RUVGEW) in its electrostatic component along x, y and z axes (a, b and c, respectively), its dispersive component along x, y and z axes (d, e and f, respectively) and in its total energy representation along x, y and z axes (g, h and i, respectively).
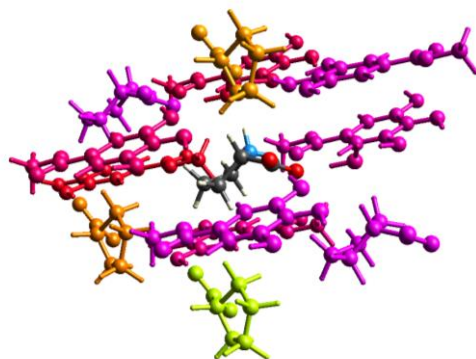
Figure A1.22 Representation of pairwise Interaction energies of the molecular pairs calculated for MG$_2$·Pro$_2$·H$_2$O. (Colours are connected to lines in Table A1.9)

Table A1.9 Interaction energies (kJ/mol) of the molecular pairs calculated for $MG_2 \cdot Pro_2 \cdot H_2O$.

	N	Symop	R	Electron Density	E_ele	E_pol	E_dis	E_rep	E_tot
	1	-	5.15	HF/3-21G	6.8	-0.2	-0.2	0.0	6.6
	1	-	5.91	HF/3-21G	-35.4	-16.3	-8.1	8.4	-47.1
	2	x, y, z	6.88	HF/3-21G	-33.4	-15.3	-8.1	8.4	-44.1
	1	-	5.98	HF/3-21G	4.9	-1.5	-7.3	6.1	2.4
	1	-	6.47	HF/3-21G	1.8	-0.0	-0.0	0.0	1.8
	1	-	6.16	HF/3-21G	-1.8	-0.1	-0.1	0.0	-2.0
	1	-	4.58	HF/3-21G	0.2	-0.0	-0.0	0.0	0.2
	1	-	5.63	HF/3-21G	-2.9	-0.3	-0.1	0.0	-3.2
	1	-	6.14	HF/3-21G	-10.3	-3.4	-13.7	2.7	-22.8
	1	-	7.88	HF/3-21G	1.9	-0.2	-0.2	0.0	1.6
	1	-	3.84	HF/3-21G	6.8	-0.2	-0.2	0.0	6.6
	1	-	9.96	HF/3-21G	-6.9	-0.1	-0.0	0.0	-7.1
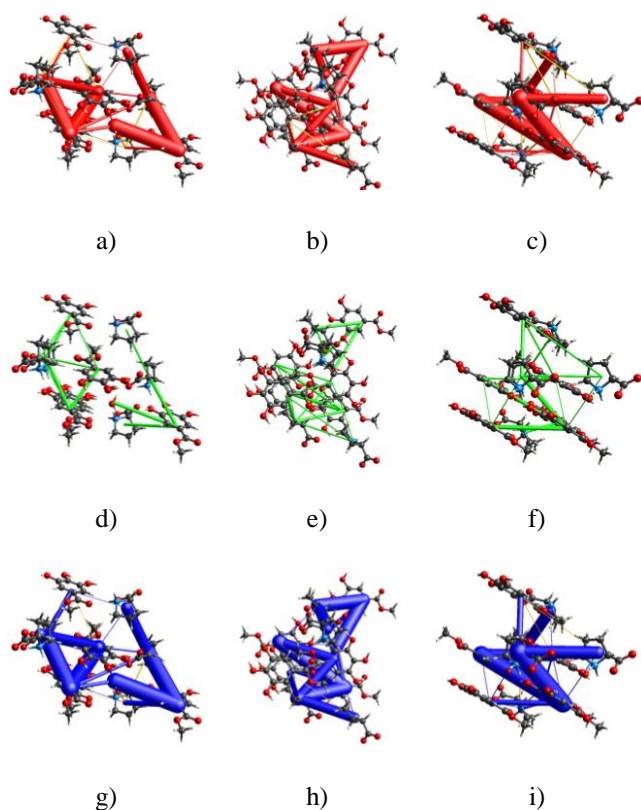
Figure A1.23 Energy Framework of $MG_2 \cdot Pro_2 \cdot H_2O$ in its electrostatic component along x, y and z axes (a, b and c, respectively), its dispersive component along x, y and z axes (d, e and f, respectively) and in its total energy representation along x, y and z axes (g, h and i, respectively).
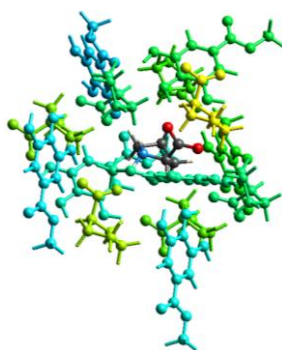
Figure A1.24 Representation of pairwise Interaction energies of the molecular pairs calculated for $MG \cdot Pro_2$. (Colours are connected to lines in Table A1.10)

Table A1.10 Interaction energies (kJ/mol) of the molecular pairs calculated for MG·Pro$_2$.

	N	Symop	R	Electron Density	E_ele	E_pol	E_dis	E_rep	E_tot
	1	-x, y+1/2, -z+1/2	6.36	HF/3-21G	-52.5	-15.3	-7.0	4.3	-66.3
	1	-	5.69	HF/3-21G	-1.8	-0.3	-0.2	0.0	-2.2
	1	-	7.28	HF/3-21G	3.0	-0.2	-0.1	0.0	2.8
	1	-	6.02	HF/3-21G	3.0	-0.2	-0.1	0.0	2.8
	1	-	7.06	HF/3-21G	-4.2	-0.2	-0.2	0.0	-4.6
	1	-	6.80	HF/3-21G	-0.2	-0.9	-1.0	0.0	-1.7
	1	-	6.07	HF/3-21G	11.1	-10.0	-17.5	11.0	-2.0
	2	-x, y+1/2, -z+1/2	5.42	HF/3-21G	3.0	-0.2	-0.1	0.0	2.8
	1	-	6.07	HF/3-21G	-18.1	-5.3	-23.4	12.3	-33.0
	1	-	6.29	HF/3-21G	2.4	-0.1	-0.1	0.0	2.3
	1	-	7.63	HF/3-21G	0.1	-0.4	-0.5	0.0	-0.6
	1	-	8.65	HF/3-21G	1.4	-0.1	-0.2	0.0	1.2
	1	-	6.99	HF/3-21G	-1.1	-0.4	-0.4	0.0	-1.7

a)

b)

c)

d)

e)

f)

g)

h)

i)
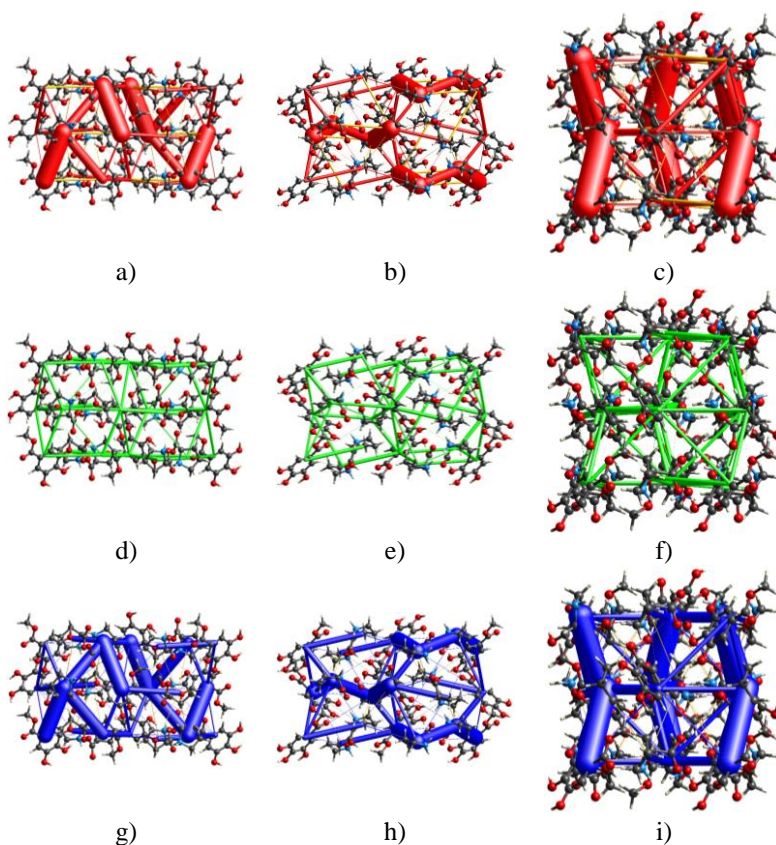
Figure A1.25 Energy framework of MG·Pro$_2$ in its electrostatic component along x, y and z axes (a, b and c, respectively), its dispersive component along x, y and z axes (d, e and f, respectively) and in its total energy representation along x, y and z axes (g, h and i, respectively).

a)

b)
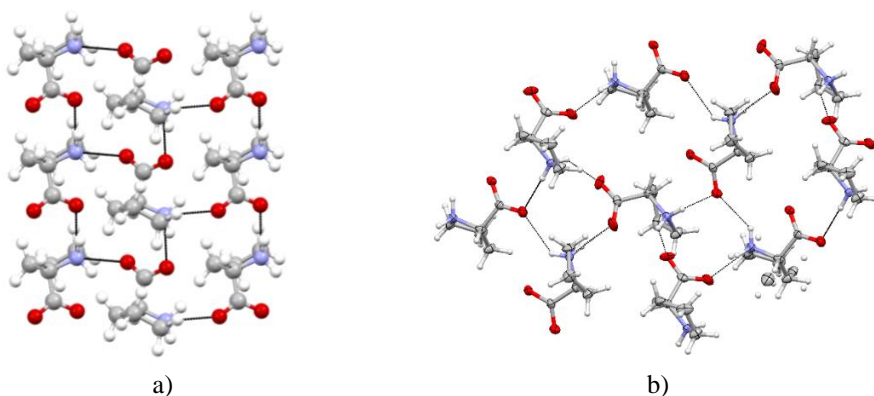
Figure A1.26 Comparison between Pro layer in Pro (a) and in MG·Pro$_2$ (b).
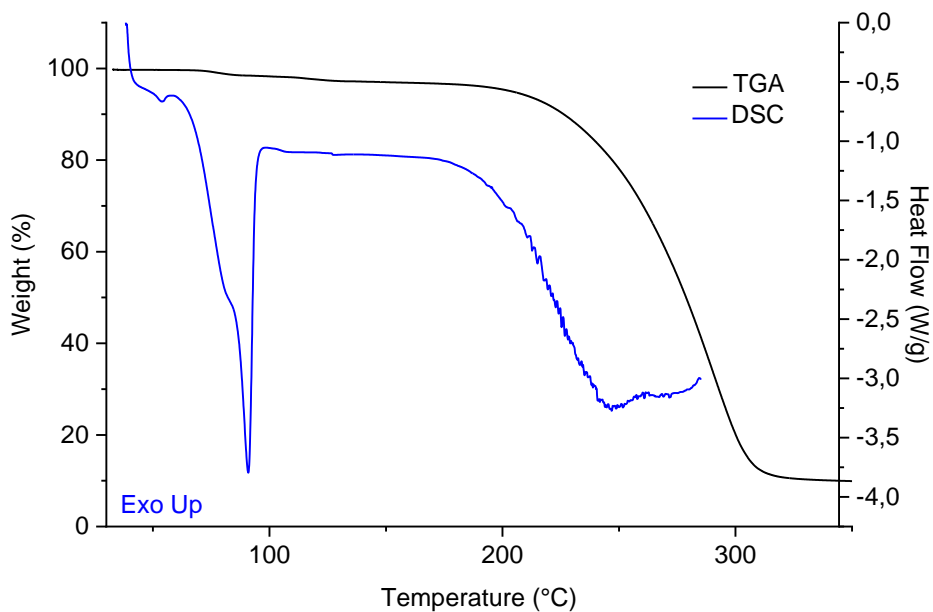
Figure A1.27 DSC and TGA curves for $MG_2 \cdot Pro_2 \cdot H_2O$.
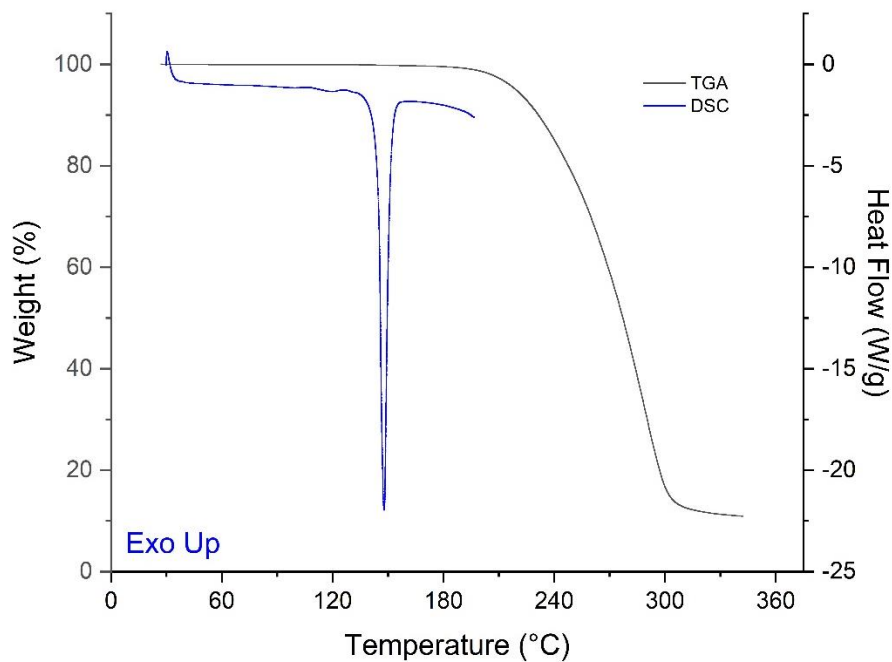
Figure A1.28 DSC and TGA curves for $MG \cdot Pro_2$.
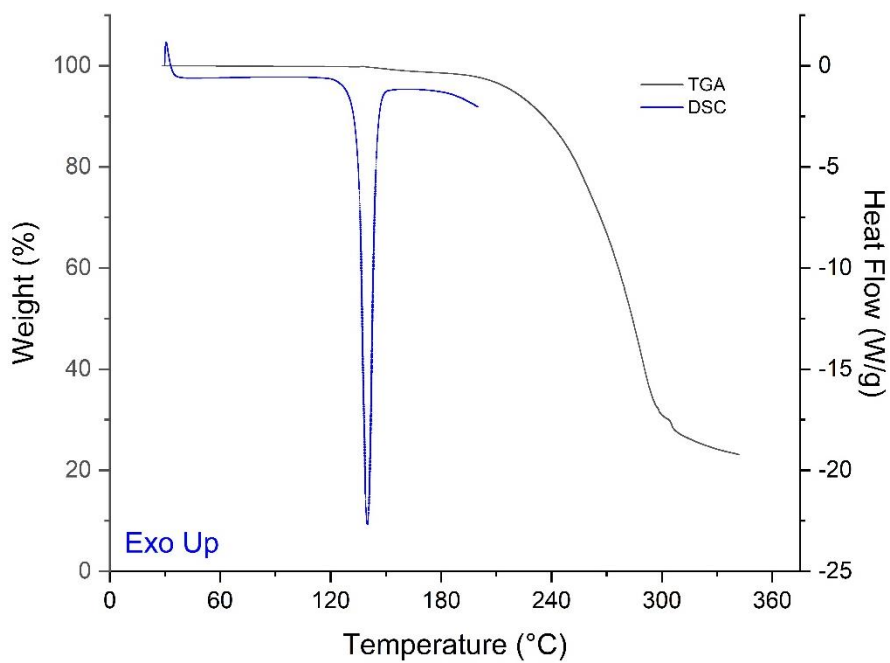
Figure A1.29 DSC and TGA curves for MG$_2$·Pro$_2$.

Appendix II: Additional data for Chapter 3
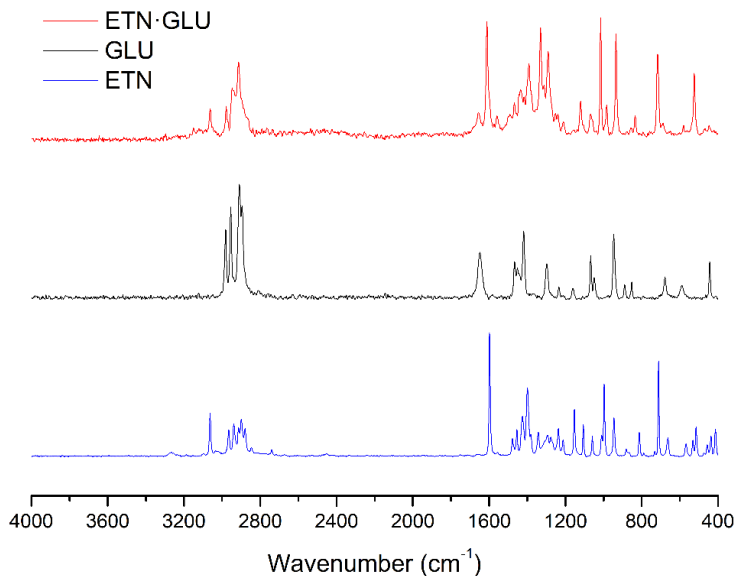
Figure A2.1 Comparison among Raman spectra of ETN (blue), GLU (black) and ETN·GLU (red).
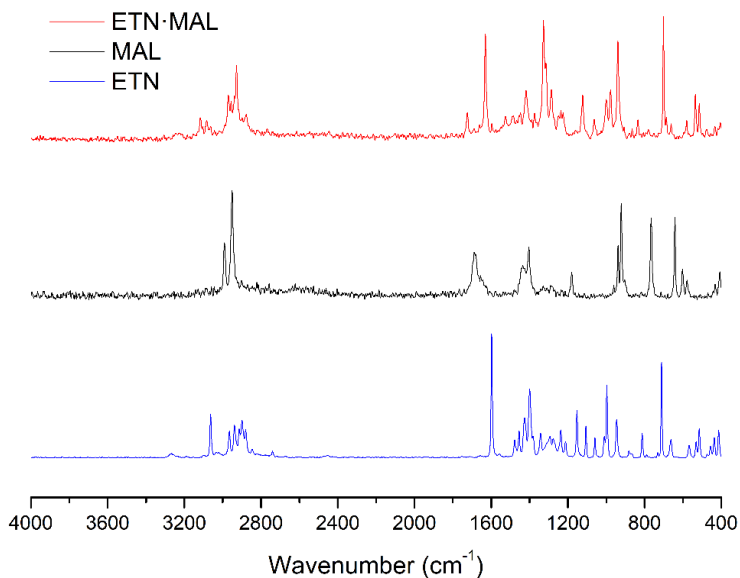
Figure A2.2 Comparison among Raman spectra of ETN (blue), MAL (black) and ETN·MAL (red).
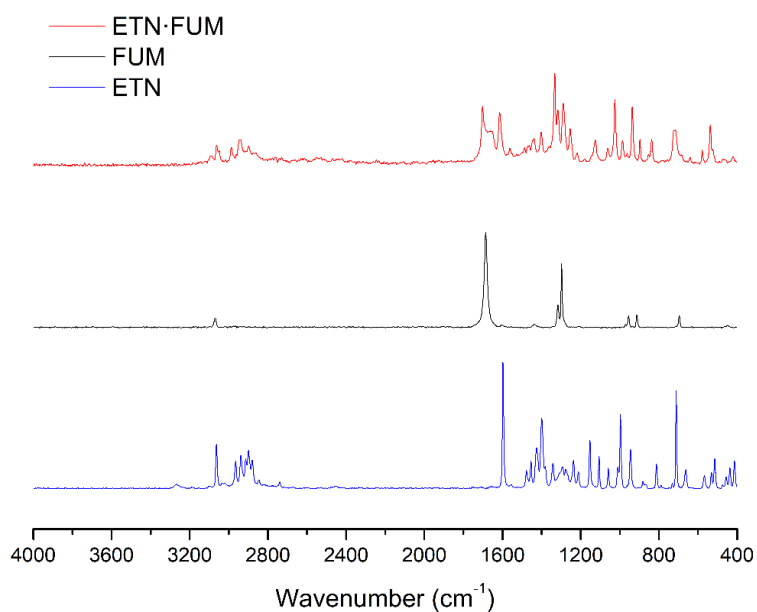
Figure A2.3 Comparison among Raman spectra of ETN (blue), FUM (black) and ETN·FUM (red).
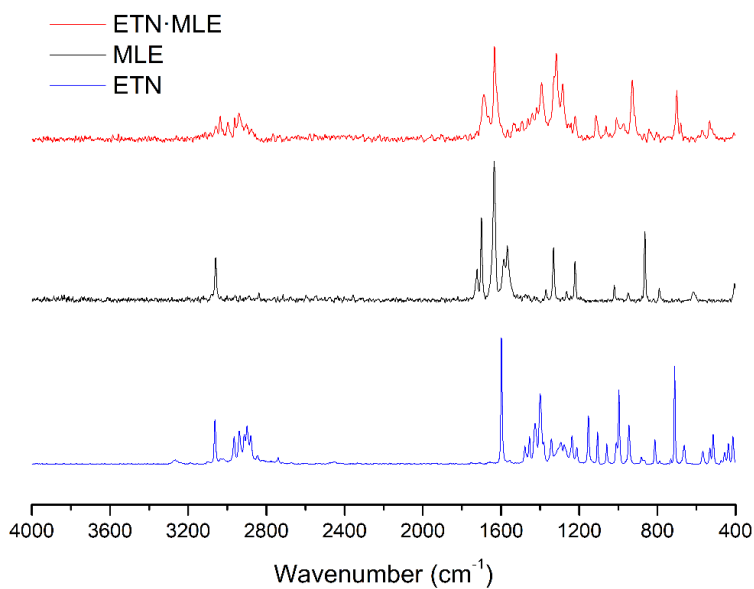
Figure A2.4 Comparison among Raman spectra of ETN (blue), MLE (black) and ETN·MLE (red).

Table A2.1 Values of distances between atoms in ETN·GLU X-ray structure. Refer to Scheme 3.1 in Chapter 3 for atom numbering.

Atom	Atom	Length/Å	Atom	Atom	Length/Å
C4A	N5	1.345(12)	N5	C6B	1.358(13)
C4A	C3A	1.365(14)	C2	C7B	1.371(13)
C4A	C8A	1.561(11)	C2	C3A	1.377(13)
S11	C1	1.661(2)	C2	C3B	1.392(13)
O8'	C5'	1.217(2)	C2	C7A	1.407(12)
O9'	C5'	1.316(2)	C2	C1	1.494(3)
N10	C1	1.308(3)	C3'	C4'	1.504(3)
O6'	C1'	1.203(3)	C7A	C6A	1.381(14)
C2'	C1'	1.490(3)	C8A	C9A	1.479(17)
C2'	C3'	1.506(3)	C3B	C4B	1.391(14)
O7'	C1'	1.294(3)	C4B	C8B	1.624(17)
C5'	C4'	1.489(3)	C7B	C6B	1.368(14)
N5	C6A	1.330(12)	C8B	C9B	1.438(17)
N5	C4B	1.354(14)			

Table A2.2 Values of angles among atoms in ETN·GLU X-ray structure. Refer to Scheme 3.1 in Chapter 3 for atom numbering.

Atom	Atom	Atom	Angle/°	Atom	Atom	Atom	Angle/°
N5	C4A	C3A	126.8(11)	C3B	C2	C1	123.4(7)
N5	C4A	C8A	112.0(9)	C7A	C2	C1	119.3(7)
C3A	C4A	C8A	120.5(10)	C4'	C3'	C2'	111.33(18)
C1'	C2'	C3'	117.35(18)	C5'	C4'	C3'	114.18(18)
O8'	C5'	O9'	122.6(2)	N10	C1	C2	116.23(18)
O8'	C5'	C4'	124.03(19)	N10	C1	S11	122.23(16)
O9'	C5'	C4'	113.34(19)	C2	C1	S11	121.54(15)
C6A	N5	C4A	112.9(7)	O6'	C1'	O7'	122.5(2)
C6A	N5	C4B	116.3(9)	O6'	C1'	C2'	122.02(19)
C4A	N5	C4B	16.4(13)	O7'	C1'	C2'	115.47(19)
C6A	N5	C6B	21.3(14)	C4A	C3A	C2	116.0(12)
C4A	N5	C6B	114.4(8)	N5	C6A	C7A	128.8(11)
C4B	N5	C6B	124.0(10)	C9A	C8A	C4A	109.9(10)
C7B	C2	C3A	114.9(10)	C4B	C3B	C2	126.4(13)
C7B	C2	C3B	112.8(10)	N5	C4B	C3B	114.4(13)
C3A	C2	C3B	16.0(10)	N5	C4B	C8B	121.5(13)
C7B	C2	C7A	19.3(13)	C3B	C4B	C8B	123.7(13)
C3A	C2	C7A	122.2(10)	C2	C7B	C6B	124.6(14)
C3B	C2	C7A	114.6(10)	N5	C6B	C7B	117.6(14)
C7B	C2	C1	123.7(7)	C9B	C8B	C4B	90.2(16)
C3A	C2	C1	118.5(7)				

Table A2.3 Values of distances between atoms in ETN·MAL X-ray structure. Refer to Scheme 3.1 in Chapter 3 for atom numbering.

Atom	Atom	Length/Å	Atom	Atom	Length/Å
S11	C1	1.656(2)	C8	C4	1.500(3)
N5	C4	1.338(3)	C8	C9	1.506(4)
N5	C6	1.338(3)	O5'	C3'	1.234(3)
N10	C1	1.314(3)	O4'	C3'	1.264(3)
C6	C7	1.373(3)	O7'	C1'	1.327(3)
C3	C4	1.381(3)	O6'	C1'	1.198(3)
C3	C2	1.390(3)	C2'	C1'	1.497(3)
C7	C2	1.381(3)	C2'	C3'	1.530(3)
C2	C1	1.495(3)			

Table A2.4 Values of angles among atoms in ETN·MAL X-ray structure. Refer to Scheme 3.1 in Chapter 3 for atom numbering.

Atom	Atom	Atom	Angle/°	Atom	Atom	Atom	Angle/°
C4	N5	C6	122.91(18)	N5	C4	C3	118.3(2)
N5	C6	C7	120.3(2)	N5	C4	C8	118.75(19)
C4	C3	C2	120.5(2)	C3	C4	C8	123.0(2)
C6	C7	C2	119.2(2)	C1'	C2'	C3'	114.00(18)
C7	C2	C3	118.85(19)	O5'	C3'	O4'	124.50(19)
C7	C2	C1	121.29(19)	O5'	C3'	C2'	117.23(19)
C3	C2	C1	119.9(2)	O4'	C3'	C2'	118.26(18)
C4	C8	C9	112.5(2)	O6'	C1'	O7'	124.1(2)
N10	C1	C2	116.21(19)	O6'	C1'	C2'	124.3(2)
N10	C1	S11	124.06(16)	O7'	C1'	C2'	111.6(2)
C2	C1	S11	119.73(15)				

Table A2.5 Values of distances between atoms in ETN·TAR X-ray structure. Refer to Scheme 3.1 in Chapter 3 for atom numbering.

Atom	Atom	Length/Å	Atom	Atom	Length/Å
S11	C1	1.667(4)	C3A	C4A	1.386(6)
S11A	C1A	1.666(4)	C3	C4	1.391(6)
O5A′	C1A'	1.259(4)	C2A'	C3A'	1.533(6)
O10A′	C3A'	1.422(5)	C2A'	C1A'	1.532(6)
O7A′	C4A'	1.187(5)	C4	C8	1.503(6)
N5	C4	1.329(5)	C4A'	C3A'	1.521(6)
N5	C6	1.335(5)	C6A	C7A	1.367(6)
5A	C6A	1.327(5)	C6	C7	1.369(6)

N5A	C4A	1.342(5)	C4A	C8A	1.517(6)
N10	C1	1.304(4)	C8A	C9A	1.438(10)
O8A'	C4A'	1.327(5)	C8	C9	1.465(10)
C2	C1	1.503(6)	O7'	C4'	1.209(5)
C2	C3	1.377(5)	O6'	C1'	1.292(4)
C2	C7	1.391(5)	O3'	C2'	1.405(5)
O9A'	C2A'	1.409(4)	O8'	C4'	1.327(5)
C2A	C1A	1.503(6)	O5'	C1'	1.213(4)
C2A	C3A	1.378(5)	C1'	C2'	1.523(6)
C2A	C7A	1.381(5)	C4'	C3'	1.511(6)
O6A'	C1A'	1.227(4)	O10'	C3'	1.396(5)
C1A	N10A	1.301(4)	C2'	C3'	1.541(6)

Table A2.6 Values of angles among atoms in ETN·TAR X-ray structure. Refer to Scheme 3.1 in Chapter 3 for atom numbering.

Atom	Atom	Atom	Angle/°	Atom	Atom	Atom	Angle/°
C4	N5	C6	120.1(4)	O10A'	C3A'	C2A'	111.4(3)
C6A	N5A	C4A	121.5(4)	O10A'	C3A'	C4A'	108.1(3)
C3	C2	C1	120.0(3)	C4A'	C3A'	C2A'	109.3(3)
C3	C2	C7	117.8(4)	N5	C6	C7	122.5(4)
C7	C2	C1	122.2(3)	C6A	C7A	C2A	119.2(4)
C3A	C2A	C1A	120.5(3)	C6	C7	C2	118.9(4)
C3A	C2A	C7A	117.7(4)	O5A'	C1A'	C2A'	114.8(3)
C7A	C2A	C1A	121.8(3)	O6A'	C1A'	O5A'	127.3(4)
C2A	C1A	S11A	120.4(2)	O6A'	C1A'	C2A'	117.9(4)
N10A	C1A	S11A	122.8(4)	N5A	C4A	C3A	118.0(4)
N10A	C1A	C2A	116.8(3)	N5A	C4A	C8A	118.2(4)
N10	C1	S11	122.7(3)	C3A	C4A	C8A	123.8(4)
N10	C1	C2	116.8(3)	C9A	C8A	C4A	112.4(6)
C2	C1	S11	120.5(3)	C9	C8	C4	111.4(6)
C2A	C3A	C4A	121.7(4)	O6'	C1'	C2'	112.4(3)
C2	C3	C4	120.7(4)	O5'	C1'	O6'	124.5(4)
O9A'	C2A'	C3A'	110.1(3)	O5'	C1'	C2'	123.1(3)
O9A'	C2A'	C1A'	112.7(3)	O7'	C4'	O8'	124.7(4)
C1A'	C2A'	C3A'	110.2(3)	O7'	C4'	C3'	123.8(4)
N5	C4	C3	120.1(3)	O8'	C4'	C3'	111.4(4)
N5	C4	C8	117.5(4)	O3'	C2'	C1'	109.4(3)
C3	C4	C8	122.4(4)	O3'	C2'	C3'	111.4(3)
O7A'	C4A'	O8A'	124.4(4)	C1'	C2'	C3'	107.9(3)
O7A'	C4A'	C3A'	126.3(4)	C4'	C3'	C2'	109.1(3)
O8A'	C4A'	C3A'	109.3(4)	O10'	C3'	C4'	111.5(3)
N5A	C6A	C7A	121.8(4)	O10'	C3'	C2'	112.1(4)

Table A2.7 NMR parameters employed for all SSNMR experiments.

	¹³C CPMAS spectra								
	ETN	**GLU**	**MAL**	**FUM**	**MLE**	**ETN·GLU**	**ETN·MAL**	**ETN·FUM**	**ETN·MLE**
n° scans	216	24	48	24	4	170	1184	609	50
relaxation delay (s)	2.8	73	50	211.2	360	4.8	1.8	2.5	9.7
contact time (ms)	3	3	3	3	5	3	3	3	3
acquisition time (ms)	32	32	55	32	30	32	35	35	32
n° points	2348	2348	3672	2348	2722	2348	2568	2568	2348
spectral width (kHz)	36.8	37	36.8	36.8	45	36.8	36.8	36.8	36.8
	¹⁵N CPMAS spectra								
n° scans	19932	/	/	/	/	1937	531	21932	5892
relaxation delay (s)	2.8	/	/	/	/	4.8	1.8	2.5	9.7
contact time (ms)	4	/	/	/	/	4	4	3	4
acquisition time (ms)	39	/	/	/	/	39	39	39	39
n° points	2048	/	/	/	/	2048	2048	2048	2048
spectral width (kHz)	26.3	/	/	/	/	26.3	26.3	26.3	26.3

$y = 0{,}0243x + 0{,}0021$
$R^2 = 0{,}9998$
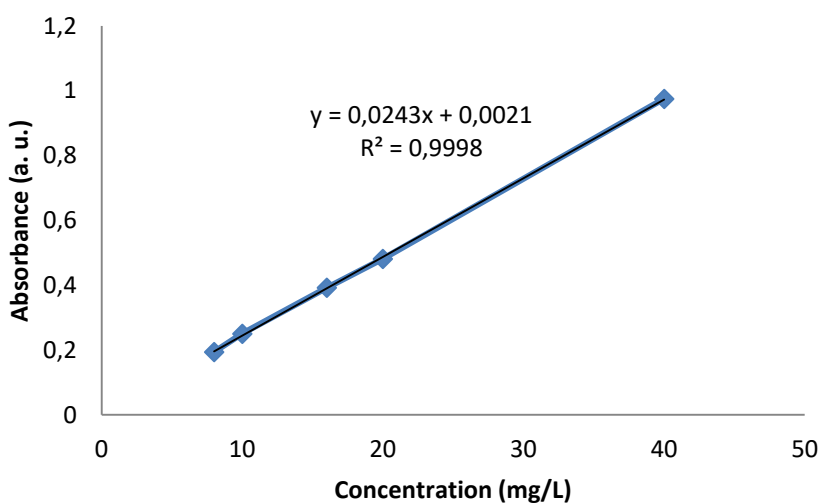
Figure A2.5 Calibration curve for dissolution kinetic tests with correspondent equation for ETN.
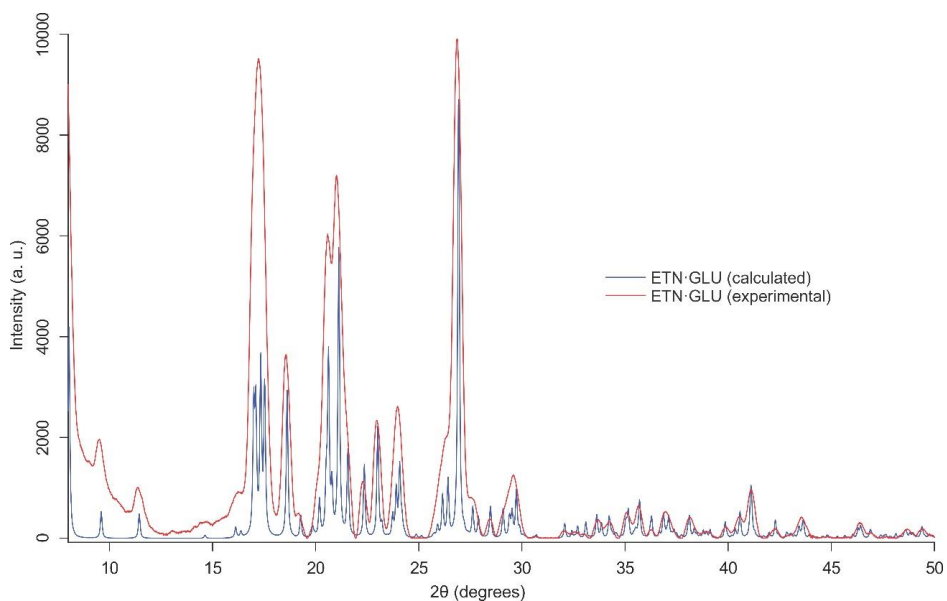
Figure A2.6 Comparison between calculated (blue) and experimental (red) PXRD patterns for ETN·GLU.
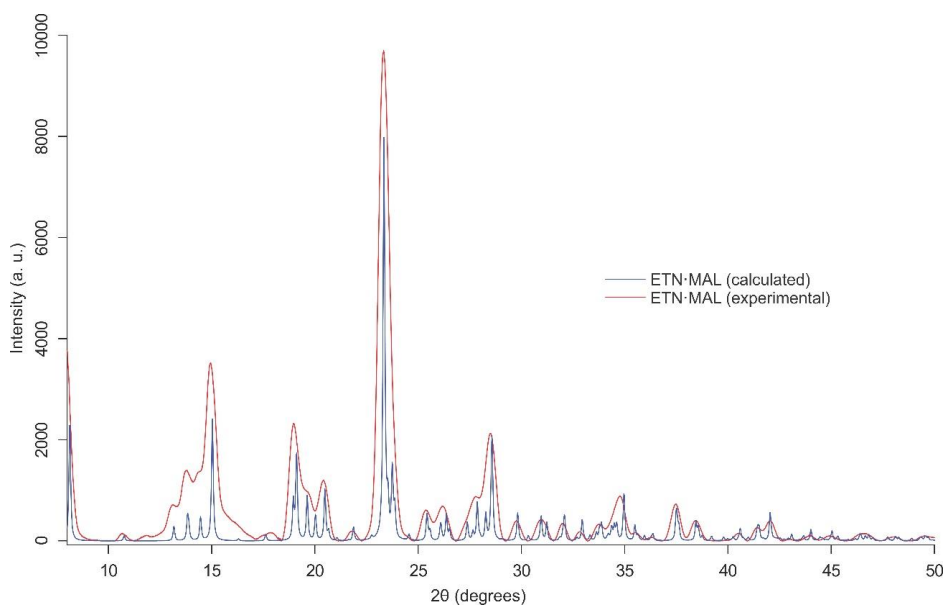
Figure A2.7 Comparison between calculated (blue) and experimental (red) PXRD patterns for ETN·MAL.
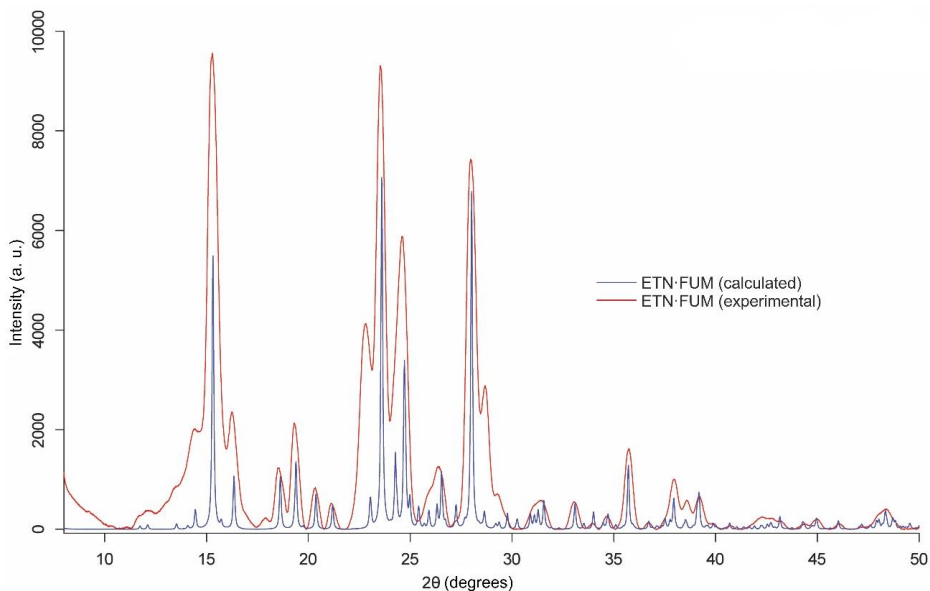
Figure A2.8 Comparison between calculated (blue) and experimental (red) PXRD patterns for ETN·FUM.
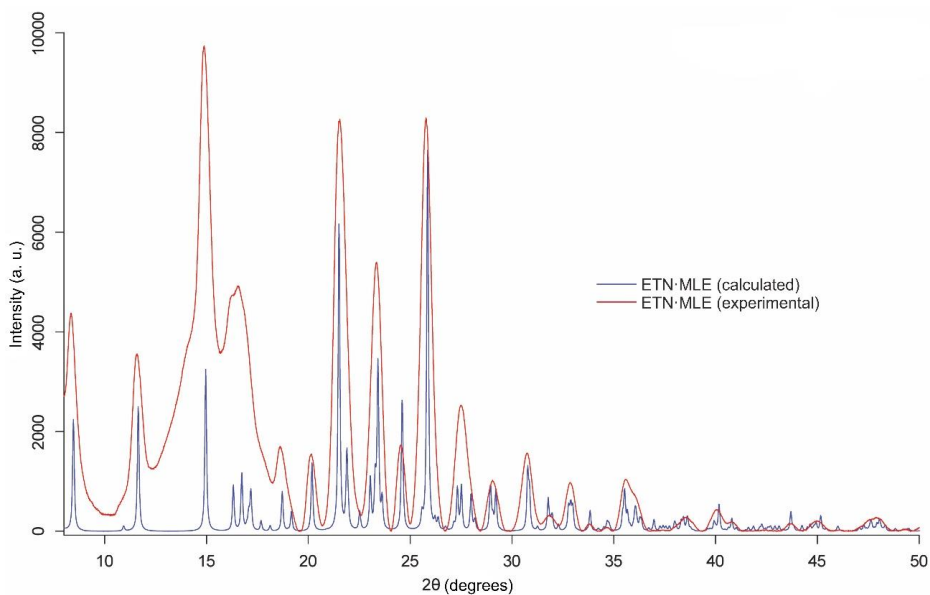
Figure A2.9 Comparison between calculated (blue) and experimental (red) PXRD patterns for ETN·MLE.
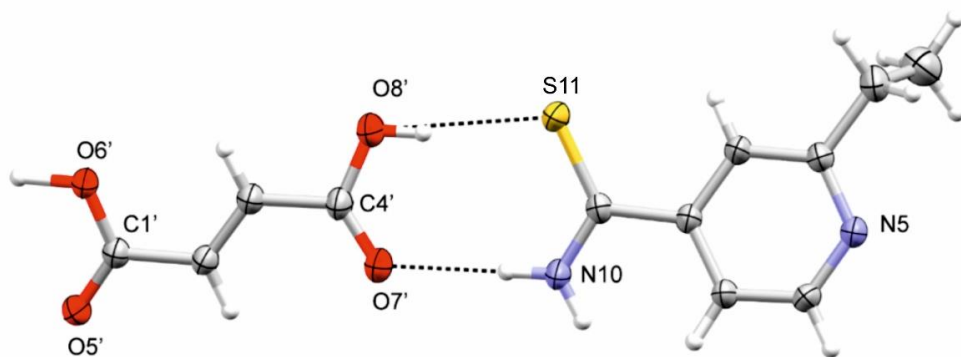
Figure A2.10 Asymmetric unit of ETN·FUM.
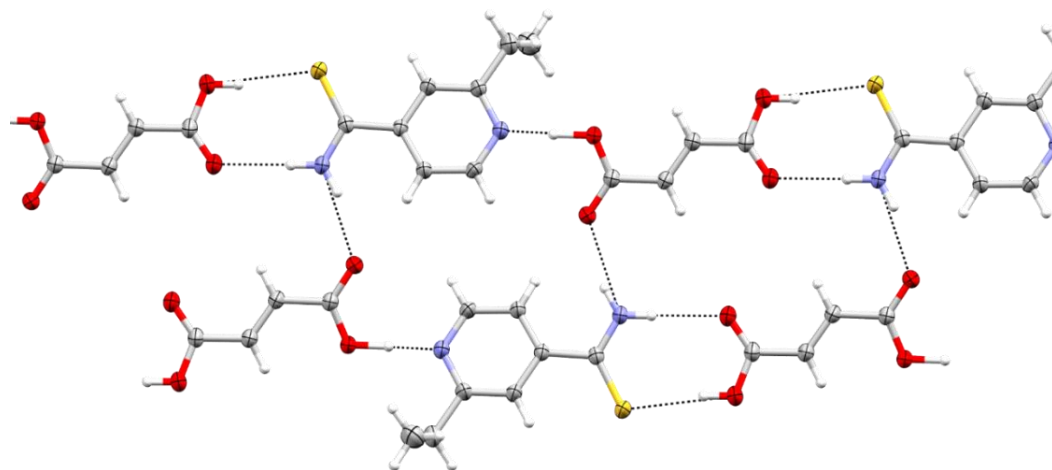
Figure A2.11 HB pattern of ETN·FUM.
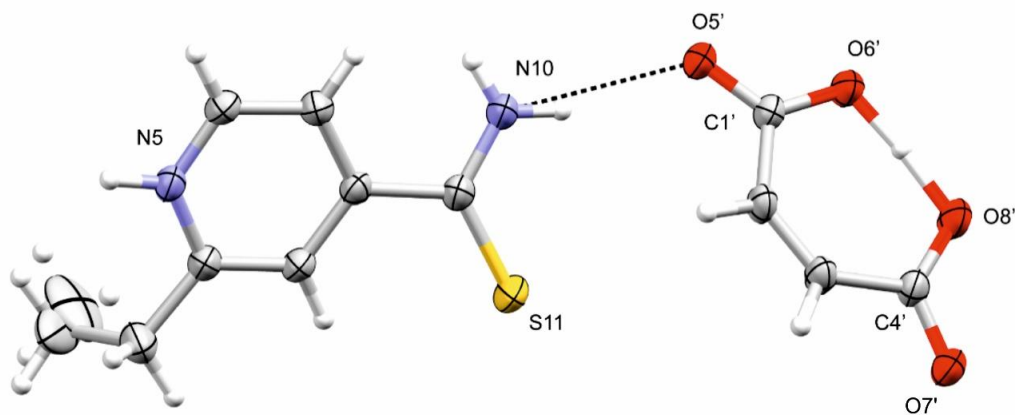
Figure A2.12 Asymmetric unit of ETN·MLE.
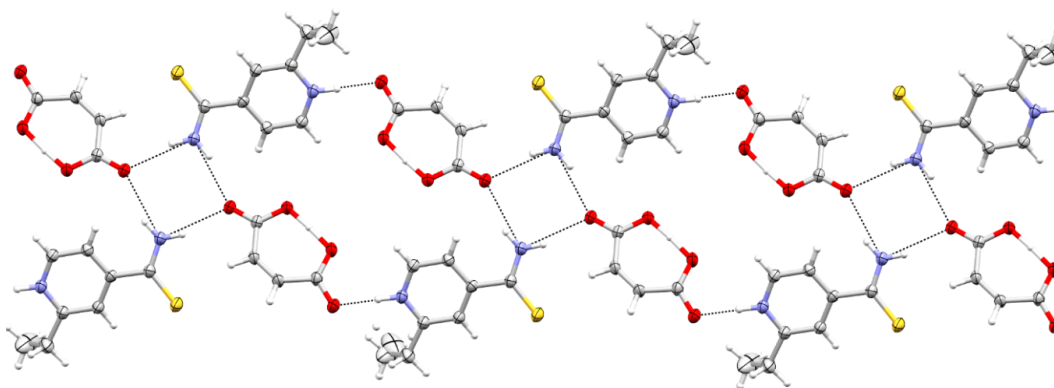
Figure A2.13 HB pattern of ETN·MLE.
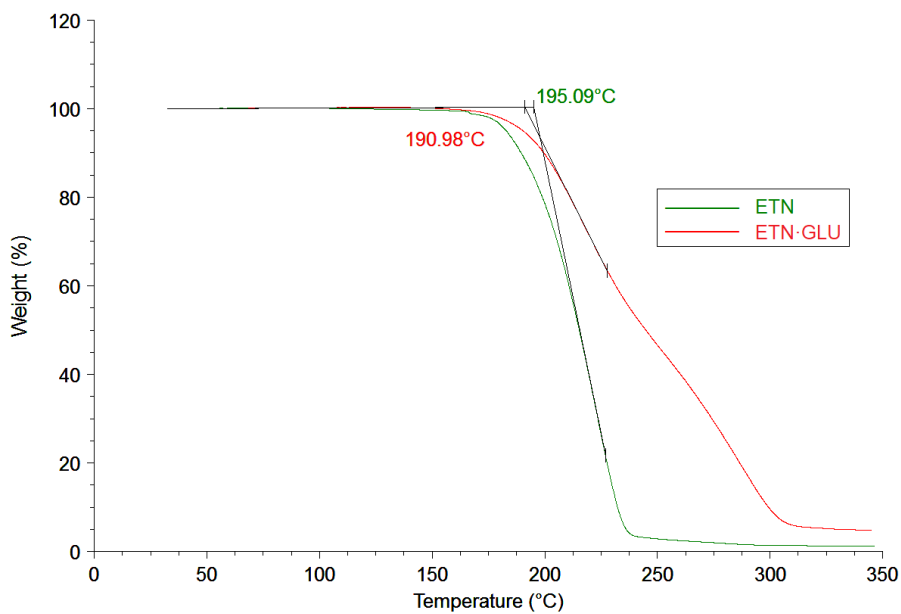
Figure A2.14 Comparison between TGA curves of ETN (green) and ETN·GLU (red).
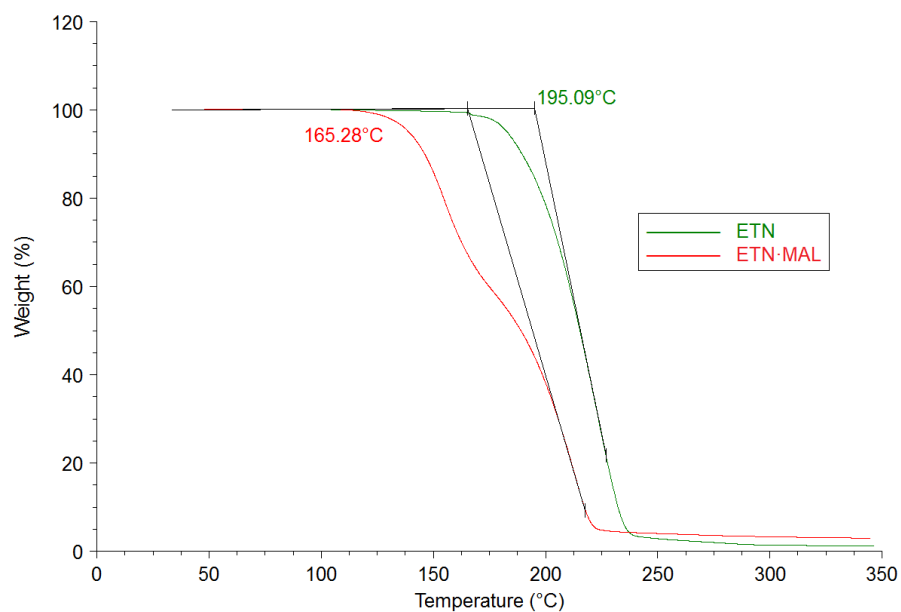
Figure A2.15 Comparison between TGA curves of ETN (green) and ETN·MAL (red).

196
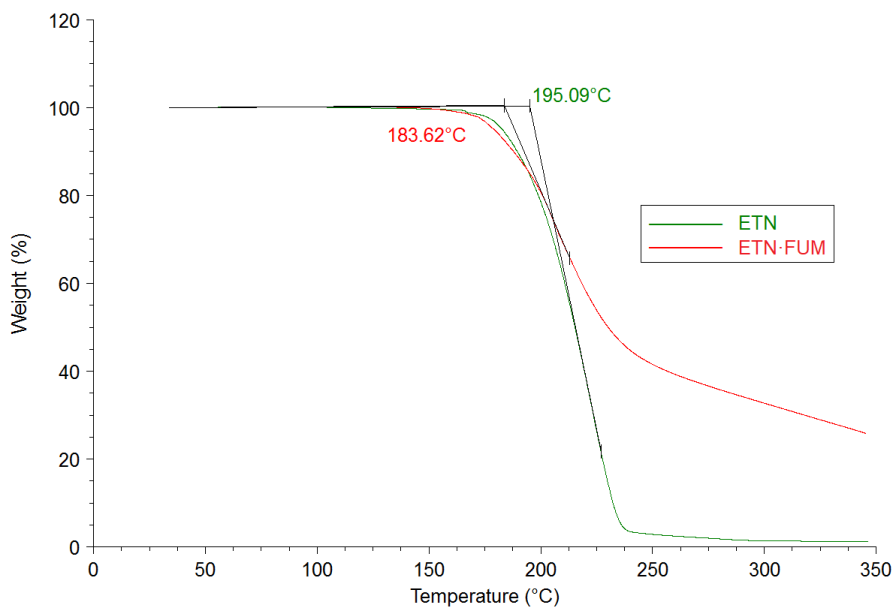
Figure A2.16 Comparison between TGA curves of ETN (green) and ETN·FUM (red).
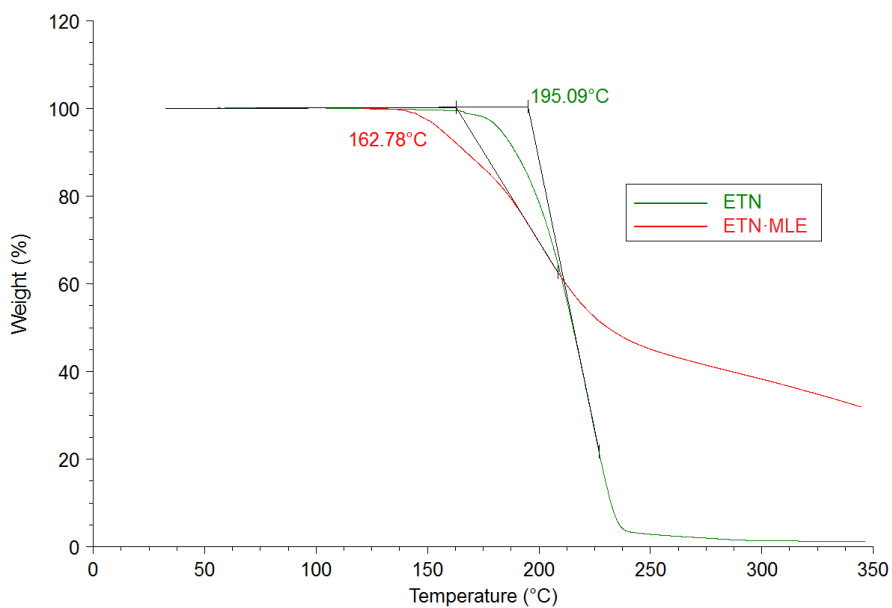
Figure A2.17 Comparison between TGA curves of ETN (green) and ETN·MLE (red).
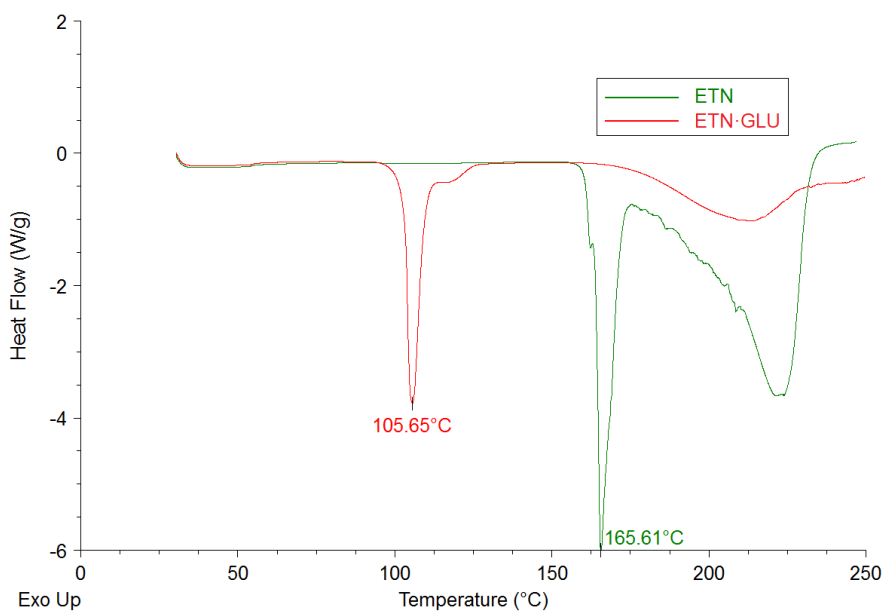
Figure A2.18 Comparison between DSC curves of ETN (green) and ETN·GLU (red).
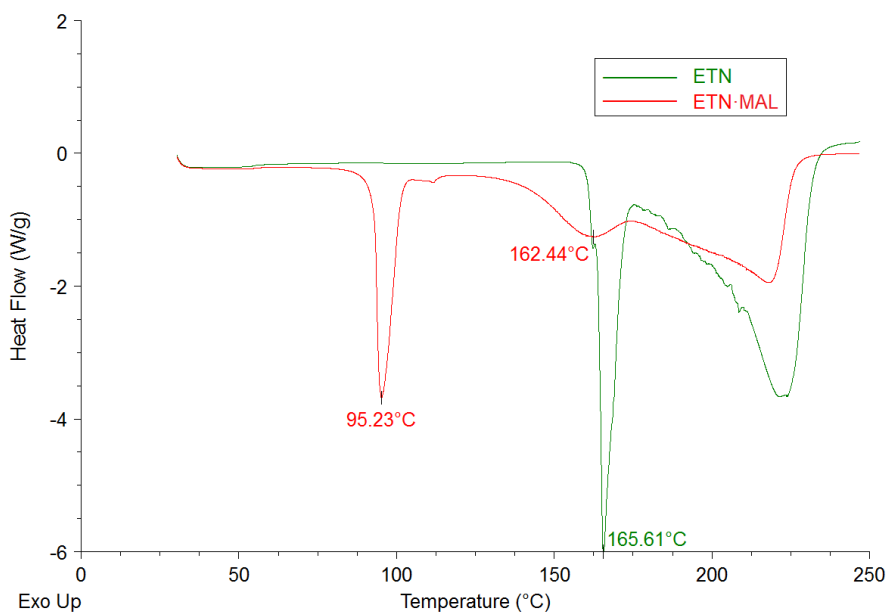
Figure A2.19 Comparison between DSC curves of ETN (green) and ETN·MAL (red).

198
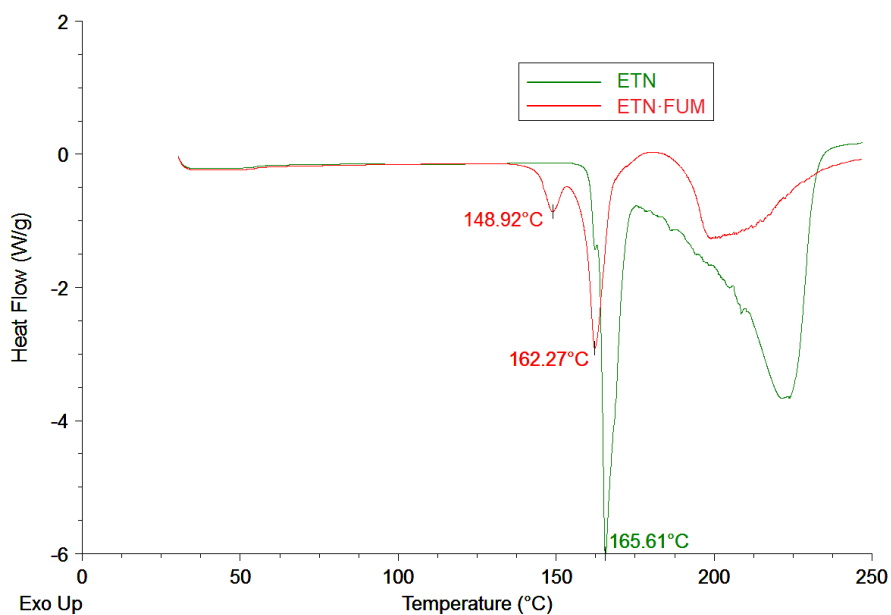
Figure A2.20 Comparison between DSC curves of ETN (green) and ETN·FUM (red).
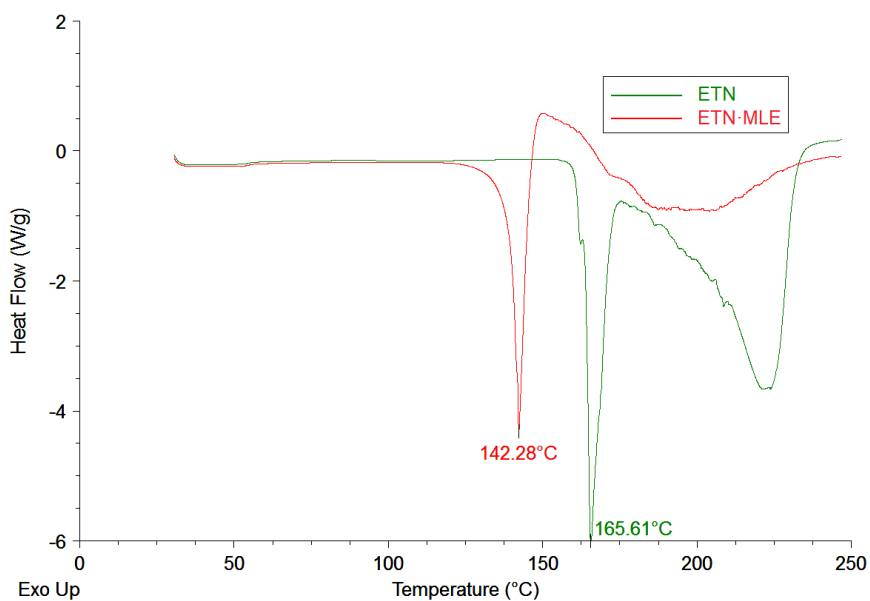
Figure A2.21 Comparison between DSC curves of ETN (green) and ETN·MLE (red).

Appendix III: Additional data for Chapter 4

Table A3.1a Fractional atomic coordinates ($\times 10^4$) and equivalent isotropic displacement parameters ($\text{Å}^2 \times 10^3$) for ETH^+SAL^-. U_{eq} is defined as 1/3 of the trace of the orthogonalized U_{IJ} tensor.

Atom	x	y	z	U(eq)
S9A	4752(5)	1332(8)	6104(4)	71.9(8)
O8*	1468.4(16)	-3769(3)	8574.8(14)	72.2(7)
C6	991(2)	1386(4)	5868(2)	54.5(8)
C1*	1656(2)	-3694(4)	7161.4(18)	44.6(7)
N1	1223.2(17)	1400(3)	6722.1(16)	50.5(7)
O10*	173.0(17)	-3073(4)	5963.6(14)	88.0(8)
O9*	143.7(15)	-2874(3)	7501.1(14)	71.1(7)
C2	2177(2)	1058(4)	7240.1(19)	45.8(7)
C3	2939(2)	731(4)	6863.0(18)	48.9(8)
N8	3372.5(18)	-336(4)	4836.3(16)	65.1(8)
C4	2729.4(19)	720(4)	5981.5(19)	44.9(7)
C5	1729(2)	1040(4)	5474(2)	51.4(8)
C10	2332(2)	1158(4)	8190.2(19)	61.9(9)
C7*	1069(2)	-3447(4)	7805(2)	53.3(8)
C7	3596(2)	459(4)	5598.6(19)	53.0(8)
C3*	1735(3)	-3821(4)	5704(2)	69.3(10)
C2*	1177(2)	-3532(4)	6278(2)	54.1(8)
C4*	2760(3)	-4238(4)	5998(3)	72.4(10)
C6*	2696(2)	-4111(4)	7430(2)	59.6(9)
C11	3433(3)	890(6)	8739(2)	87.2(12)
C5*	3252(3)	-4380(5)	6864(2)	69.6(10)
S9B	4763(17)	760(30)	6204(15)	124(8)

Table A3.2a Anisotropic displacement parameters ($\text{Å}^2 \times 10^3$) for ETH^+SAL^-. The anisotropic displacement factor exponent takes the form: $-2\pi^2 [h^2 a^{*2} U_{11} + 2hka^*b^* U_{12} + \ldots]$.

Atom	U_{11}	U_{22}	U_{33}	U_{23}	U_{13}	U_{12}
S9A	36.1(11)	124.3(17)	57.7(17)	-33.0(14)	17.5(11)	-15.2(10)
O8*	55.2(13)	121(2)	39.7(15)	17.9(13)	13.2(11)	9.3(12)
C6	39.6(17)	75(2)	46(2)	-5.2(16)	8.3(15)	3.3(14)
C1*	44.9(17)	49.2(17)	40.0(19)	6.1(13)	12.9(14)	-3.2(13)
N1	40.9(14)	64.7(16)	50.7(18)	-8.6(13)	20.8(13)	-0.1(11)

O10*	55.5(15)	153(2)	45.8(15)	21.3(16)	0.2(11)	-0.1(15)
O9*	42.4(13)	115.0(18)	59.3(15)	30.6(13)	20.1(11)	8.3(12)
C2	42.7(17)	54.0(18)	42.2(19)	-4.5(13)	14.6(14)	-4.0(14)
C3	39.0(16)	72(2)	34.9(19)	-2.5(14)	9.2(13)	1.3(14)
N8	42.7(14)	111(2)	46.7(18)	-15.5(15)	21.5(13)	-9.8(14)
C4	35.9(16)	57.8(18)	42.2(19)	-5.7(14)	13.5(13)	-2.4(13)
C5	43.4(17)	71(2)	41.1(19)	-2.6(15)	14.9(14)	0.9(15)
C10	66(2)	80(2)	45(2)	-9.8(16)	25.0(17)	-7.0(17)
C7*	40.5(17)	67(2)	52(2)	14.0(16)	13.2(16)	-5.7(15)
C7	41.3(17)	82(2)	36.8(19)	-6.2(16)	12.7(14)	0.5(15)
C3*	87(3)	78(2)	45(2)	0.0(17)	23(2)	-1(2)
C2*	52.2(19)	64(2)	43(2)	7.1(15)	9.2(16)	-3.5(15)
C4*	94(3)	70(2)	69(3)	-3.3(19)	49(2)	9(2)
C6*	52.2(19)	75(2)	51(2)	5.7(16)	14.6(16)	3.7(16)
C11	91(3)	125(3)	39(2)	-3(2)	8(2)	18(2)
C5*	61(2)	88(2)	68(3)	7.2(19)	32(2)	17.9(18)
S9B	51(4)	250(20)	77(6)	-27(10)	23(4)	-16(10)

Table A3.3a Bond lengths for ETH⁺SAL⁻.

Atom	Atom	Length/Å		Atom	Atom	Length/Å
S9A	C7	1.668(7)		C2	C10	1.502(4)
O8*	C7*	1.234(3)		C3	C4	1.381(4)
C6	N1	1.334(3)		N8	C7	1.318(4)
C6	C5	1.366(4)		C4	C5	1.389(4)
C1*	C7*	1.505(4)		C4	C7	1.500(4)
C1*	C2*	1.400(4)		C10	C11	1.515(4)
C1*	C6*	1.386(4)		C7	S9B	1.62(2)
N1	C2	1.347(3)		C3*	C2*	1.383(4)
O10*	C2*	1.352(3)		C3*	C4*	1.368(5)
O9*	C7*	1.278(3)		C4*	C5*	1.377(5)
C2	C3	1.372(4)		C6*	C5*	1.368(4)

Table A3.4a Bond angles for ETH⁺SAL⁻.

Atom	Atom	Atom	Angle/°		Atom	Atom	Atom	Angle/°
N1	C6	C5	120.7(3)		O8*	C7*	O9*	123.0(3)
C2*	C1*	C7*	121.7(3)		O9*	C7*	C1*	115.6(3)
C6*	C1*	C7*	120.5(3)		N8	C7	S9A	123.4(3)
C6*	C1*	C2*	117.8(3)		N8	C7	C4	117.0(2)
C6	N1	C2	122.9(2)		N8	C7	S9B	123.1(8)

N1	C2	C3	117.8(3)		C4	C7	S9A	119.4(3)
N1	C2	C10	117.1(2)		C4	C7	S9B	118.7(8)
C3	C2	C10	125.0(3)		C4*	C3*	C2*	120.1(3)
C2	C3	C4	121.0(3)		O10*	C2*	C1*	121.6(3)
C3	C4	C5	119.0(3)		O10*	C2*	C3*	118.3(3)
C3	C4	C7	119.1(2)		C3*	C2*	C1*	120.1(3)
C5	C4	C7	121.8(3)		C3*	C4*	C5*	121.0(3)
C6	C5	C4	118.6(3)		C5*	C6*	C1*	122.2(3)
C2	C10	C11	114.8(3)		C6*	C5*	C4*	118.8(3)
O8*	C7*	C1*	121.4(3)					

Table A3.1b Fractional atomic coordinates ($\times 10^4$) and equivalent isotropic displacement parameters ($\mathring{A}^2 \times 10^3$) for ETH·SAL. U_{eq} is defined as 1/3 of the trace of the orthogonalized U_{IJ} tensor.

Atom	x	y	z	U(eq)
S9	3215.5(6)	473(2)	-36.3(3)	75.1(3)
N1	1227.3(18)	-3107(6)	1514.4(8)	63.9(6)
C2	1122(2)	-4071(7)	1060.2(10)	59.9(7)
C5	2831(2)	-745(7)	1321.3(9)	62.7(8)
C4	2727(2)	-1730(7)	851.0(9)	53.7(7)
C3	1858(2)	-3399(7)	723.9(9)	59.4(7)
C6	2061(2)	-1468(8)	1637.2(10)	69.6(8)
N8	4480.2(19)	-1558(7)	635.8(8)	79.8(8)
C7	3534(2)	-990(7)	490.2(9)	58.6(7)
C10	161(3)	-5934(9)	940.2(13)	86.8(11)
O10*	4785.5(16)	4881(5)	1517.4(7)	73.5(6)
O9*	5176.0(15)	852(6)	2846.9(7)	76.4(7)
O8*	4176.1(16)	3632(6)	2352.8(7)	79.9(6)
C7*	4969(2)	2140(8)	2432.9(10)	61.9(8)
C1*	5760.4(19)	1692(7)	2067.1(8)	52.8(7)
C2*	5625(2)	3070(7)	1619.3(9)	57.5(7)
C4*	7203(2)	860(8)	1362.0(12)	76.0(9)
C6*	6634(2)	-97(7)	2149.4(10)	64.3(8)
C3*	6356(2)	2638(8)	1268.2(10)	70.1(9)
C5*	7354(2)	-502(8)	1801.2(11)	74.5(9)
C11A	-689(7)	-4230(20)	807(4)	83(3)
C11B	-420(12)	-5050(40)	530(5)	221(11)

Table A3.2b Anisotropic displacement parameters ($Å^2 \times 10^3$) for ETH·SAL. The anisotropic displacement factor exponent takes the form: $-2\pi^2 [h^2a*^2U_{11}+2hka*b*U_{12}+...]$.

Atom	U_{11}	U_{22}	U_{33}	U_{23}	U_{13}	U_{12}
S9	67.1(5)	108.9(7)	50.1(5)	16.6(4)	9.8(4)	10.5(5)
N1	53.7(15)	87.4(17)	51.3(14)	0.7(13)	10.6(11)	1.0(14)
C2	53.7(17)	71.3(19)	54.6(17)	3.1(14)	2.4(13)	1.6(15)
C5	50.4(16)	90(2)	48.3(15)	-3.6(14)	5.6(13)	-5.4(15)
C4	47.6(16)	67.1(17)	46.8(15)	3.2(13)	6.2(12)	6.1(14)
C3	61.3(19)	73.1(18)	44.1(14)	-0.7(14)	5.0(13)	2.6(16)
C6	61.3(19)	103(2)	44.5(15)	-5.8(16)	7.2(14)	-0.4(19)
N8	53.6(16)	133(2)	54.2(14)	24.8(15)	13.0(12)	4.0(16)
C7	51.4(17)	77(2)	47.8(15)	1.7(14)	7.3(13)	4.8(15)
C10	76(2)	99(3)	85(2)	3(2)	5.7(19)	-25(2)
O10*	59.8(13)	102.3(16)	58.6(12)	14.4(11)	3.6(10)	10.2(12)
O9*	59.4(13)	118.9(18)	51.8(12)	8.4(12)	12.2(10)	11.3(12)
O8*	55.3(13)	121.8(18)	63.3(12)	8.1(13)	11.1(10)	19.0(13)
C7*	52.1(18)	82(2)	51.6(17)	-2.3(15)	3.0(14)	-1.6(17)
C1*	43.6(15)	69.5(17)	44.9(14)	-6.3(13)	-0.1(12)	-6.1(14)
C2*	48.9(16)	72.3(18)	51.2(16)	-4.4(14)	1.5(13)	-6.6(15)
C4*	60(2)	103(3)	67(2)	-14.3(19)	21.8(16)	0.1(19)
C6*	58.1(18)	84(2)	50.1(16)	-6.0(14)	-0.3(14)	4.0(16)
C3*	70(2)	91(2)	49.1(16)	-1.0(16)	10.4(15)	-9.0(19)
C5*	57.9(19)	101(3)	64.4(19)	-13.4(18)	5.9(15)	13.5(17)
C11A	51(4)	67(4)	131(8)	15(5)	8(5)	5(4)
C11B	187(16)	320(20)	141(12)	111(13)	-103(10)	-172(15)

Table A3.3b Bond lengths for ETH·SAL.

Atom	Atom	Length/Å	Atom	Atom	Length/Å
S9	C7	1.640(3)	C10	C11B	1.398(13)
N1	C2	1.341(3)	O10*	C2*	1.355(3)
N1	C6	1.320(4)	O9*	C7*	1.303(3)
C2	C3	1.401(4)	O8*	C7*	1.221(3)
C2	C10	1.502(4)	C7*	C1*	1.495(4)
C5	C4	1.386(4)	C1*	C2*	1.392(4)
C5	C6	1.398(4)	C1*	C6*	1.378(4)
C4	C3	1.367(4)	C2*	C3*	1.409(4)
C4	C7	1.520(4)	C4*	C3*	1.351(4)
N8	C7	1.295(3)	C4*	C5*	1.370(4)
C10	C11A	1.359(9)	C6*	C5*	1.390(4)

Table A3.4b Bond angles for ETH·SAL.

Atom	Atom	Atom	Angle/°		Atom	Atom	Atom	Angle/°
C6	N1	C2	117.3(2)		C11B	C10	C2	116.6(6)
N1	C2	C3	122.2(3)		O9*	C7*	C1*	115.9(3)
N1	C2	C10	115.1(3)		O8*	C7*	O9*	121.6(2)
C3	C2	C10	122.7(3)		O8*	C7*	C1*	122.5(3)
C4	C5	C6	119.7(3)		C2*	C1*	C7*	120.2(3)
C5	C4	C7	122.0(2)		C6*	C1*	C7*	122.6(3)
C3	C4	C5	116.8(2)		C6*	C1*	C2*	117.2(2)
C3	C4	C7	121.2(2)		O10*	C2*	C1*	120.1(2)
C4	C3	C2	120.6(2)		O10*	C2*	C3*	119.0(3)
N1	C6	C5	123.4(3)		C1*	C2*	C3*	120.9(3)
C4	C7	S9	121.9(2)		C3*	C4*	C5*	119.8(3)
N8	C7	S9	123.4(2)		C1*	C6*	C5*	121.5(3)
N8	C7	C4	114.7(2)		C4*	C3*	C2*	120.2(3)
C11A	C10	C2	115.0(5)		C4*	C5*	C6*	120.4(3)
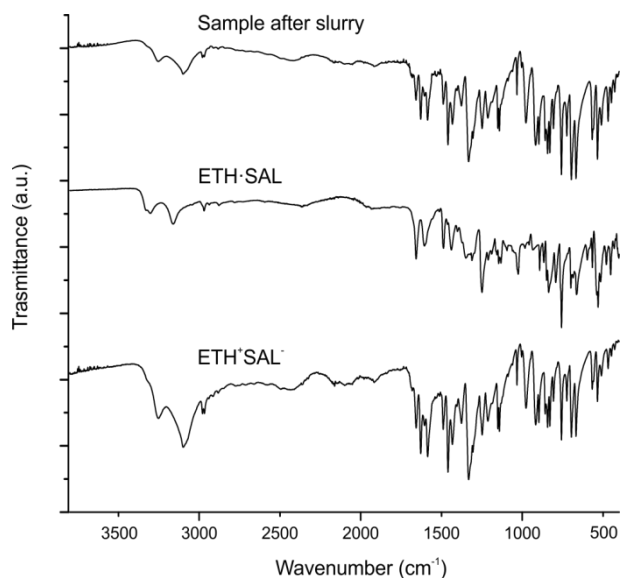
Figure A3.1 FTIR-ATR spectrum of the competitive slurry sample after 48 hours, compared to ETH·SAL and ETH⁺SAL⁻ spectra.
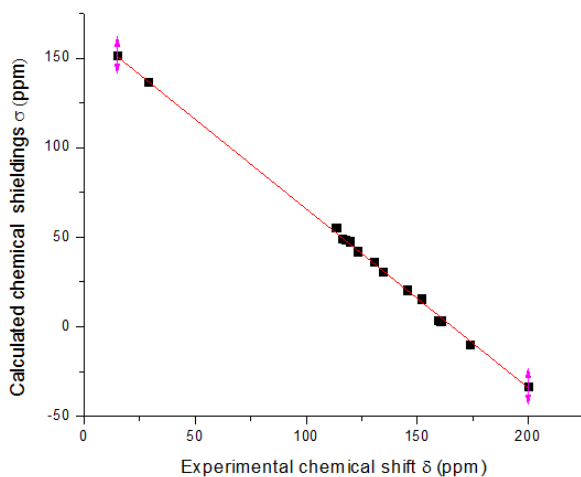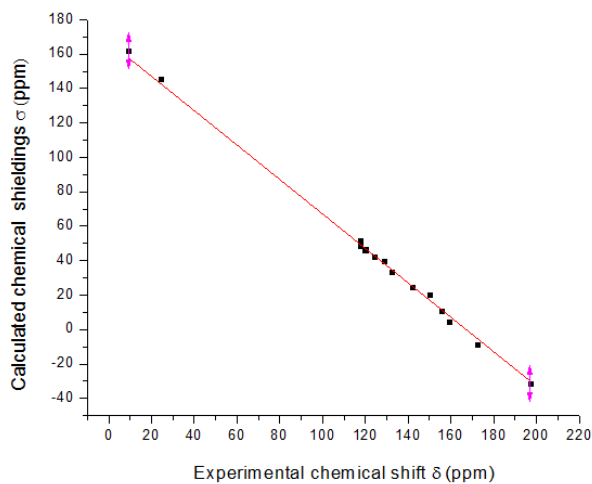
Figure A3.2 Plots of the experimental ^{13}C chemical shifts $\delta_{(exp)}$ against the GIPAW-calculated ^{13}C chemical shieldings (σ) for the salt (top) and cocrystal (bottom). The linear regression model with slope constrained to -1 was applied to find the best fit to the data. The value of σ_{ref} is determined by the intercepts with the y axis, which are 167.13 and 165.86 ppm for the salt and cocrystal, respectively.
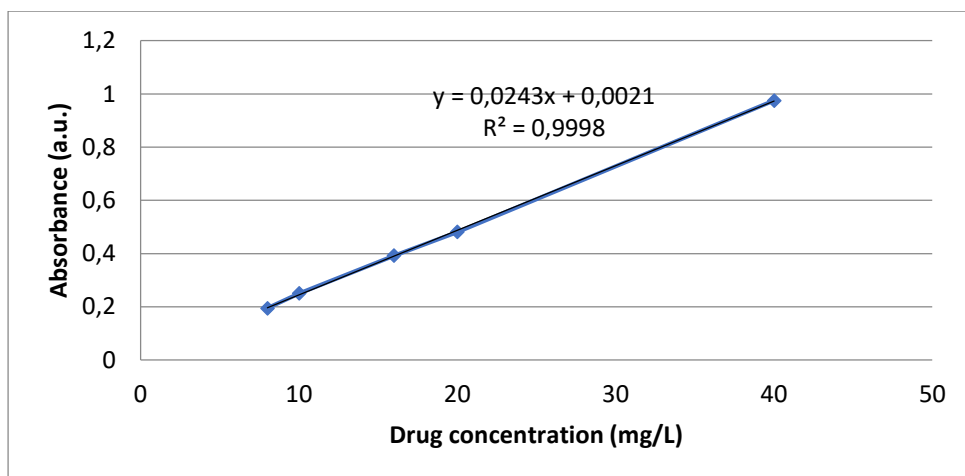
Figure A3.3 Calibration curve for ETH dissolution carried out in water (pH = 7.4 phosphate buffer) at 37 °C.
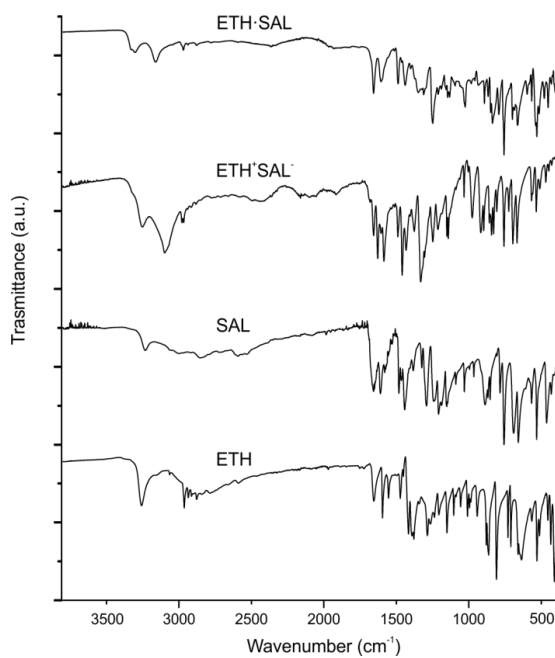
Figure A3.4 FTIR-ATR spectra of ETH·SAL and ETH$^+$SAL$^-$, compared to the starting materials.

206
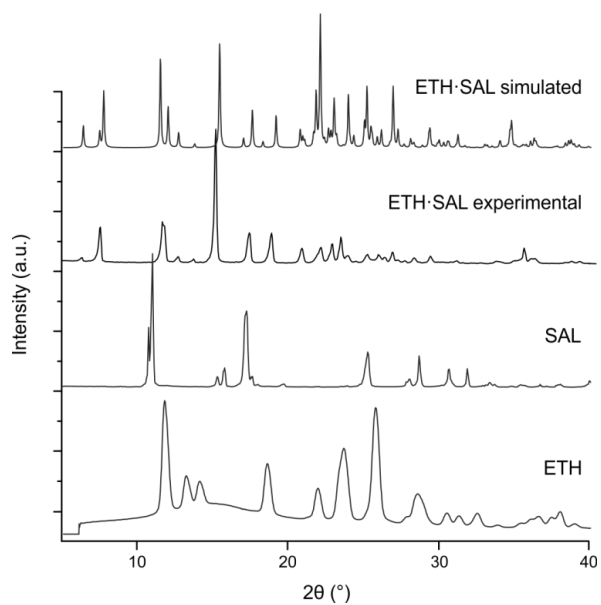
Figure A3.5 Experimental and simulated PXRD patterns of ETH·SAL, with respect to the starting materials.
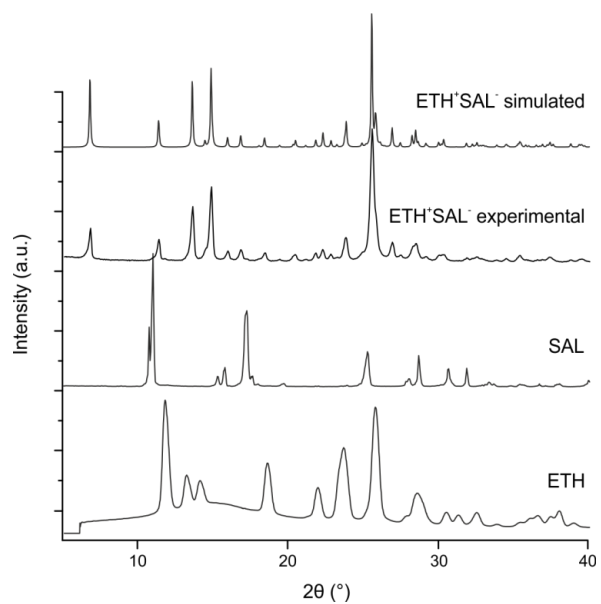
Figure A3.6 Experimental and simulated PXRD patterns of ETH⁺SAL⁻, with respect to the starting materials.
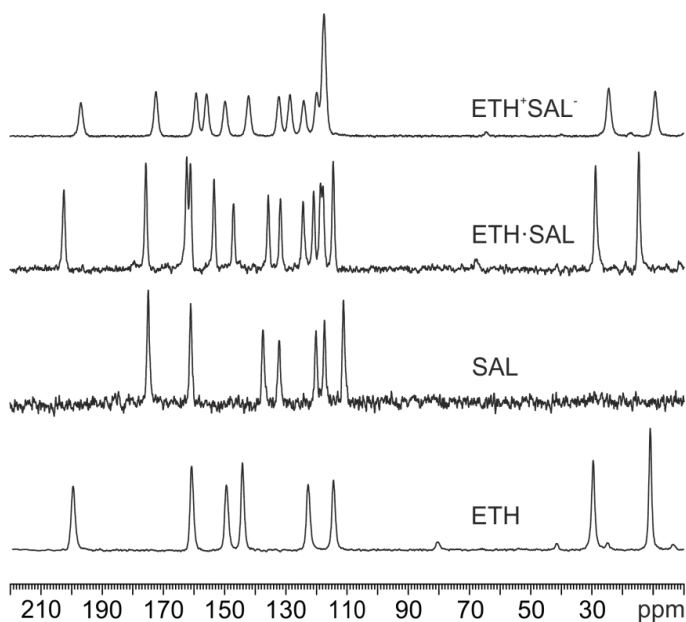
Figure A3.7 ^{13}C (150.9 MHz) CPMAS spectra of ETH·SAL and ETH$^+$SAL$^-$, compared to pure ETH and pure SAL, recorded at 20 kHz at room temperature.

Table A3.5 ^{13}C, ^{15}N and ^{1}H chemical shift assignments for both polymorphs and starting materials.

Atom	ETH	SAL	ETH$^+$SAL$^-$	ETH·SAL
	(ppm)	(ppm)	(ppm)	(ppm)
^{13}C				
2	161.0		155.8	159.4
3	122.9		124.1	123.0
4	149.6		149.9	151.8
5	114.6		117.5	113.5
6	144.4		142.2	145.5
7	199.7		197	200.1
10	29.7		24.4	28.9
11	11.1		9.2	14.9
1*		162.1	117.5	116.2
2*		138.5	159.4	160.6
3*		121.1	119.9	117.5
4*		111.8	132.3	134.4

208

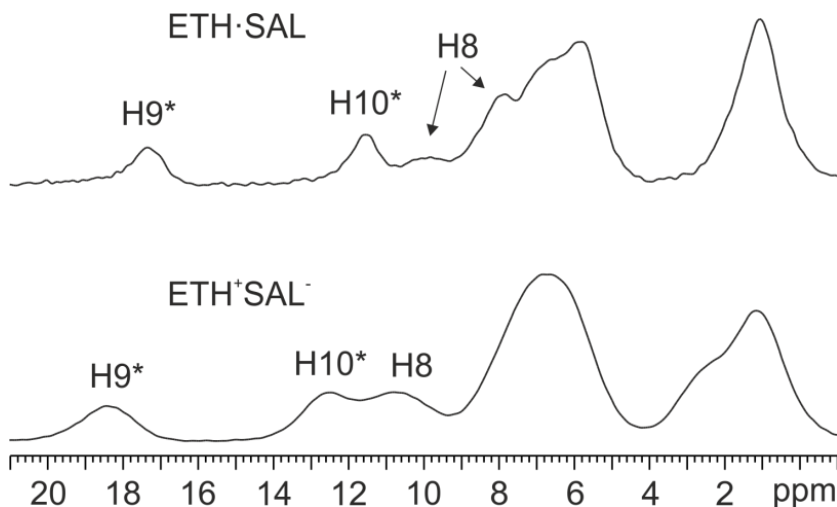|				
5*		133.2	119.9	119.6
6*		118.0	128.7	130.4
7*		176.0	172.4	173.8
15N				
8	154.0		147.4	148.7
1	309.0		211.9	273.4
1H				
8			10.8	10.3/8.7
9*			18.4	17.3
3/5/6/3*/4*/5*/6*			7.1/6.7	5.8/6.6/7.9
10/11			1.2/2.4	1.08
10*			12.6	11.6

Figure A3.8 ^{1}H (600.1 MHz) MAS spectra of ETH·SAL and ETH$^+$SAL$^-$, recorded at 70 kHz at room temperature.

Analysis of the 2D ^{1}H-{^{14}N} D-HMQC spectra

Figure 4.4 shows the 2D ^{1}H-{^{14}N} D-HMQC spectra of ETH$^+$SAL$^-$ and ETH·SAL, respectively, in which the N-H correlations for N1 and N8 atoms of ETH are observed. These spectra allow the ^{1}H assignment of the thioamidic N-H (H8) and pyridinic N$^+$-H or N···H (H9*) resonances as follows: at 10.8 (H8) and 18.4 (H9*) ppm for ETH$^+$SAL$^-$ and at 10.3/8.7 (H8) and 17.3 (H9*)

209

ppm for ETH·SAL. Concerning ^{14}N, it suffers from a strong quadrupolar interaction, stemming from the interaction between an intrinsic quadrupolar moment (because of spin-1 nucleus) and the electric field gradient (because of the surrounding environment). While the ^{14}N line shape is dominated by the first-order quadrupolar broadening at the static conditions, MAS gets rid of the broadening and results in a set of spikelet spinning sidebands. These sidebands are folded in the indirect (^{14}N) dimension of D-HMQC spectra, giving a sharp peak at the isotropic peak positions. In the end, the ^{14}N resonance positions depend on both the isotropic chemical shift (σ_{iso}) and an additional second-order isotropic quadrupolar shift. Since the quadrupolar coupling strongly depends on the surrounding environment of the quadrupolar nucleus, the additional shift is more significant for asymmetric nitrogen sites and *vice versa*. This perfectly agrees with the experimental ^{14}N shifts found in the 2D ^{1}H-{^{14}N} D-HMQC spectra of ETH^{+}SAL^{-} and ETH·SAL, confirming the ionic/neutral character of the samples:

- in the case of ETH^{+}SAL^{-}, the ^{14}N shifts of N1 and N8 slightly differ from each other implying that the environments surrounding the two nitrogen sites are similar in terms of symmetry and thereby suggesting a protonation of N1 (NH^{+} group);

- the ^{14}N shift of N1 in ETH·SAL is much larger than that of N8 (nearly 400 ppm), indicating a less symmetric surrounding environment which agrees with a farther hydrogen position from the nitrogen (N···H-O).

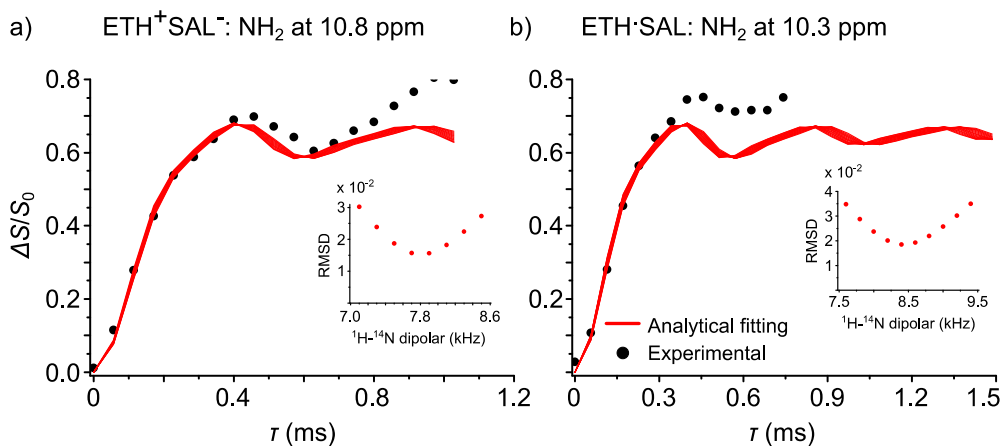a) ETH$^+$SAL$^-$: NH$_2$ at 10.8 ppm   b) ETH·SAL: NH$_2$ at 10.3 ppm

Figure A3.9 Experimental ^{14}N-^{1}H fraction curves (dots) achieved by PM-S-RESPDOR of (a) ETH$^+$SAL$^-$ and (b) ETH·SAL at ^{1}H chemical shifts of 10.8 and 10.3 ppm, respectively and analytical fitting curves (solid red lines). The fitting was up to 0.40 ms for ETH$^+$SAL$^-$ and 0.34 ms for ETH·SAL. The insets show the best fitting ^{1}H-^{14}N dipolar coupling based on root mean square deviation analysis. The experimental $\Delta S/S_0$ data larger than 0.8 are not shown in the figures. The obtained values of N-H distance for these NH$_2$ sites are 1.04 and 1.01 Å for ETH$^+$SAL$^-$ and ETH·SAL, respectively.
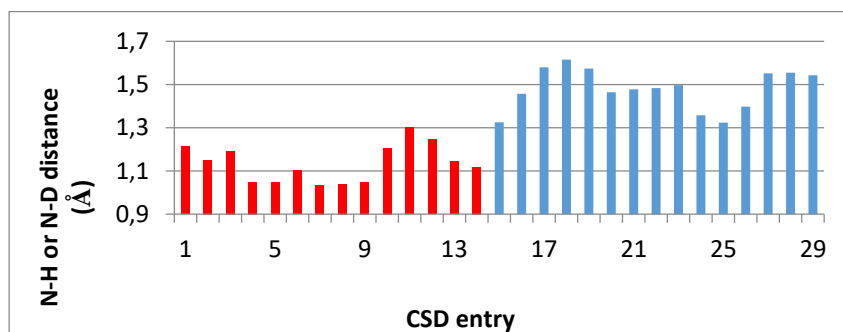
Figure A3.10 N-H or N-D distances of the 29 CSD structures, obtained by neutron diffraction, containing pyridine-carboxylic acid interaction (14 salt structures are indicated in red, while 15 cocrystal structures are indicated in blue).
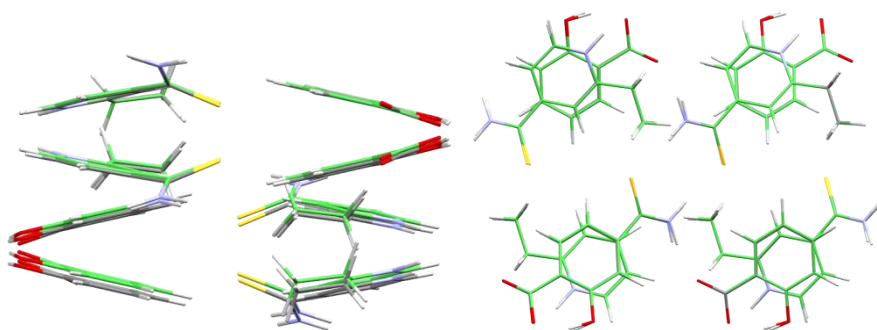
Figure A3.11 Superposition of experimental and DFT-optimized (green) ETH⁺SAL⁻ structures.
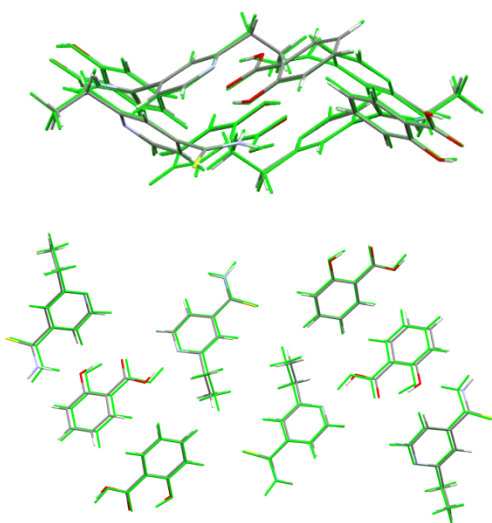

Figure A3.12 Superposition of experimental and DFT-optimized (green) ETH·SAL structures.
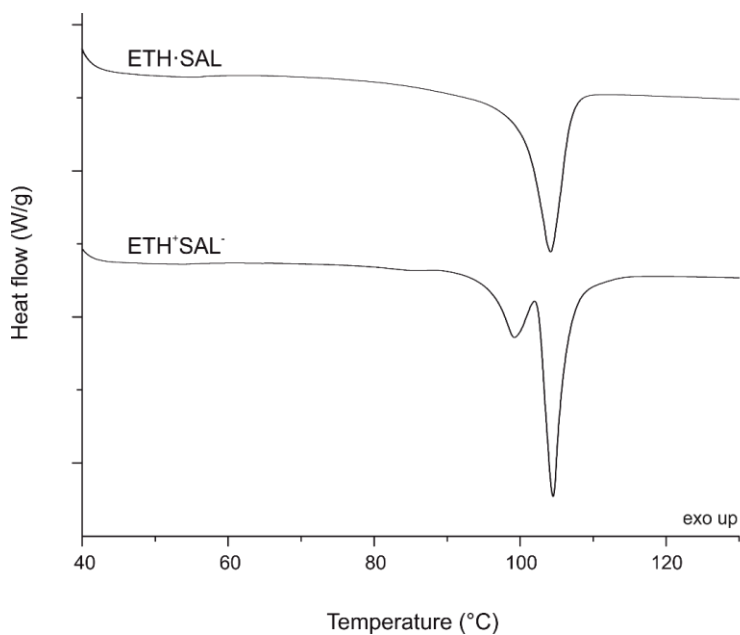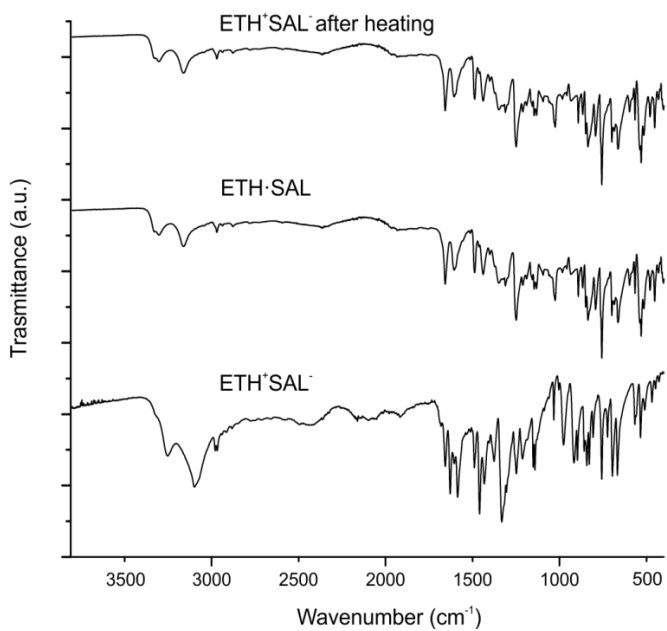
Figure A3.13 DSC curves of ETH$^+$SAL$^-$ and ETH·SAL.

Figure A3.14 FTIR-ATR spectrum of ETH$^+$SAL$^-$ sample after heating to 100 °C, compared to the spectra of ETH·SAL and ETH$^+$SAL$^-$.
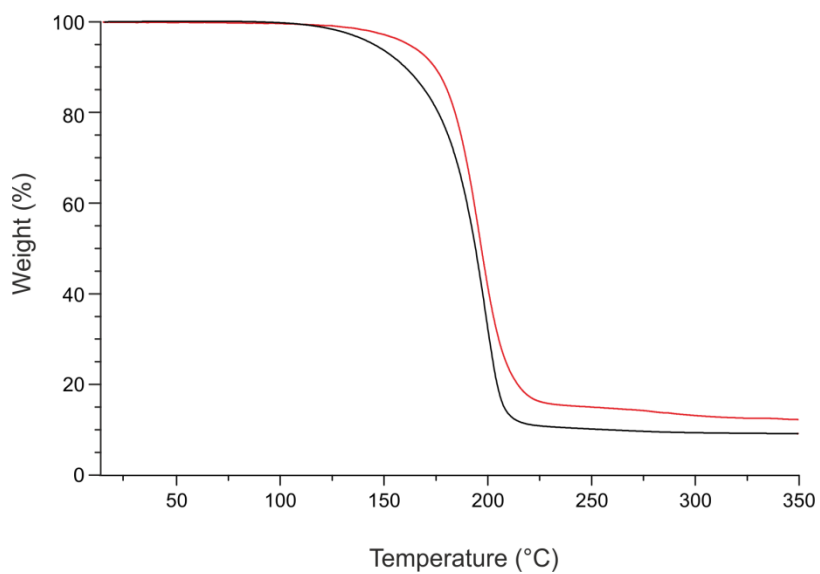
Figure A3.15 TGA curves of ETH$^+$SAL$^-$ (black) and ETH·SAL (red).

Appendix IV: Additional data for Chapter 5

Table A4.1 Representative examples of all the crystallization techniques.

Entry	Stochiometric ratio (KET:LYS)	Experiment type	Solvent	XRPD	Notes
1	1:1	GR	-	KET + LYS	amorphous
2	1:2	GR	-	KET + LYS	amorphous
3	2:1	GR	-	KET + LYS	amorphous
4	1:1	KN	ethanol	KET + LYS	low crystallinity degree
5	1:1	KN	methanol	KET + LYS	low crystallinity degree
6	1:1	KN	2-propanol	KET + LYS	amorphous
7	1:1	KN	acetonitrile	KET + LYS	amorphous
8	1:1	EvRT	acetonitrile	-	LYS not soluble
9	1:1	EvHT	anisole	sticky solid	
10	1:1	EvHT	N,N-dimethylformamide	KET	
11	1:1	EvHT	dimethylsulfoxide	KET	
12	1:1	EvRT	dichloromethane	sticky solid	
13	1:1	EvRT	chloroform	-	LYS not soluble
14	1:1	EvRT	1,2-dimethoxy ethane	-	LYS not soluble
15	1:1	EvRT	diethyl carbonate	-	LYS not soluble
16	1:1	EvRT	isopropyl acetate	-	LYS not soluble
17	1:1	EvRT	methyl ethyl ketone	-	LYS not soluble
18	1:1	SLRT	acetonitrile	sticky solid	
19	1:1	SLRT	ethanol	sticky solid	
20	1:1	SLRT	methanol	amorphous	
21	1:1	SLRT	N,N-dimethylformamide	amorphous	
22	1:1	SLRT	dimethylsulfoxide	amorphous	
23	1:1	SLRT	dichloromethane	KET + LYS	

24	1:1	PAD	1-butanol	KET + LYS	
25	1:1	PAD	1-pentanol	KET + LYS	
26	1:1	PAD	1-propanol	sticky solid	
27	1:1	PAD	2-butanol	sticky solid	
28	1:1	PAD	2-methoxy ethanol	KET + LYS	
29	1:1	PAD	2-propanol	sticky solid	
30	1:1	PAD	acetonitrile	KET-LYS P1	low crystallinity degree
31	1:1	PAD	acetone	KET-LYS P1	low yield
32	1:1	PAD	1,4-dioxane	KET-LYS P1 + LYS	
33	1:1	PAD	N,N-dimethylacetamide	no precipitation	
34	1:1	PAD	N,N-dimethylformamide	no precipitation	
35	1:1	PAD	dimethylsulfoxide	no precipitation	
36	1:1	PAD	ethanol	KET-LYS P1	**selected procedure for P1**
37	1:1	PAD	methanol	KET-LYS P1	
38	1:1	PAD	tetrahydrofuran	no precipitation	
40	1:1	CRY	1-pentanol	KET-LYS P1 + LYS	
41	1:1	CRY	1-propanol	KET-LYS P1 + LYS	
42	1:1	CRY	2-butanol	KET-LYS P1 + LYS	
43	1:1	CRY	2-methoxy ethanol	sticky solid	
44	1:1	CRY	2-propanol	amorphous	
45	1:1	CRY	acetonitrile	sticky solid	
46	2:1	CRY	acetone	sticky solid	
47	2:1	CRY	1,4-dioxane	amorphous	
48	2:1	CRY	N,N-dimethylacetamide	no precipitation	
49	2:1	CRY	N,N-dimethylformamide	no precipitation	
50	2:1	CRY	dimethylsulfoxide	no precipitation	
51	1:1	CRY	ethanol	KET-LYS P1	

52	1:1	CRY	methanol	KET-LYS P1	
53	1:1	CRY	tetrahydrofuran	no precipitation	
54	1:1	PAI	1. methanol 2. tetrahydrofuran	no precipitation	
55	1:1	PAI	1. ethanol 2. tetrahydrofuran	no precipitation	
56	1:1	PAI	1. acetonitrile 2. tetrahydrofuran	no precipitation	
57	1:1	PAI	1. methanol 2. ethyl acetate	KET-LYS P2	**selected procedure for P2**
58	1:1	PAI	1. 2-propanol 2. acetonitrile	amorphous	
59	1:1	PAI	1. ethanol 2. acetonitrile	KET-LYS P2 + KET	
60	1:1	PAI	1. ethanol 2. ethyl acetate	KET-LYS P2	low yield

GR: grinding; KN: kneading; Ev: evaporation; SL: slurry; PAD: precipitation by antisolvent addition to a supersaturated solution. A solution of KET in selected solvent was added dropwise to aqueous solution of LYS, the solvent becomes antisolvent for the species KET-LYS P1.

PAI: Precipitation by supersatured solution addition to the antisolvent. A solution of KET and LYS in solvent 1 was added to the antisolvent 2.

CRY: The experiments were performed by adding a saturated solution of ketoprofen to solid lysine.

LT: low temperature (5-8 °C); RT: room temperature (20-25 °C); HT: high temperature (60 °C).

Table A4.2 Tested samples and model taste solutions for E-tongue analysis.

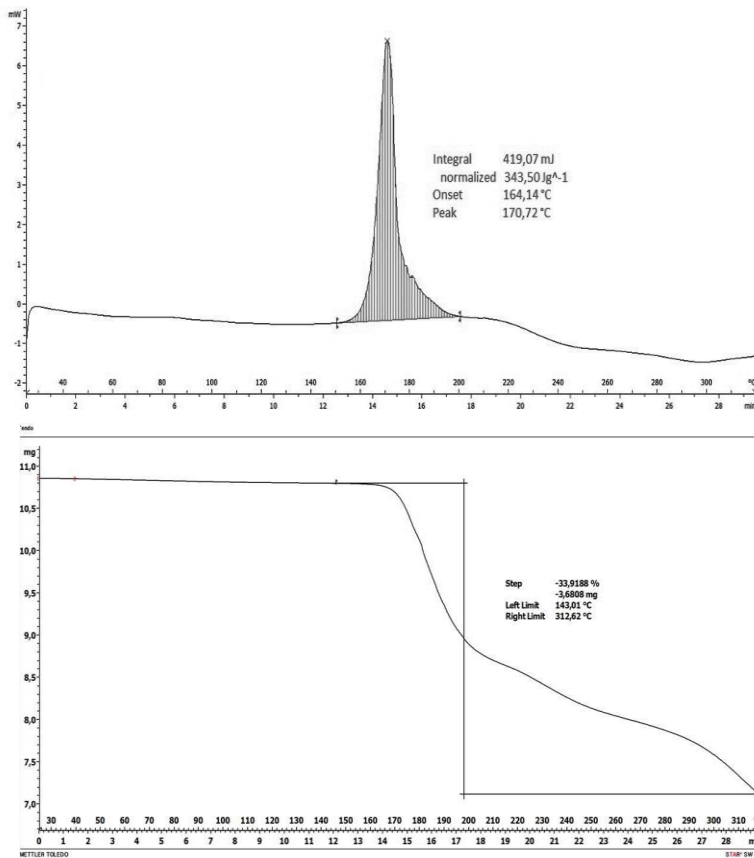| Compound	Composition	Concentration
KET-LYS P1	ketoprofen:lysine 1:1	40 mg/20 mL
KET-LYS P2	ketoprofen:lysine 1:1	40 mg/20 mL
Sweet	fructose	33 mg/30 mL (0.006 mol/L)
Bitter	MgCl2	2.7 mg/30 mL (0.001 mol/L)
Salty	NaCl	1.66 mg/30 mL (0.001 mol/L)

Figure A4.1 DSC and TGA of KET-LYS P1. KET-LYS P1 DSC profile (upper panel) showed an endothermic event occurring at 170.7 °C (onset 164.1 °C), whileTGA analysis (lower panel) showed compound degradation.
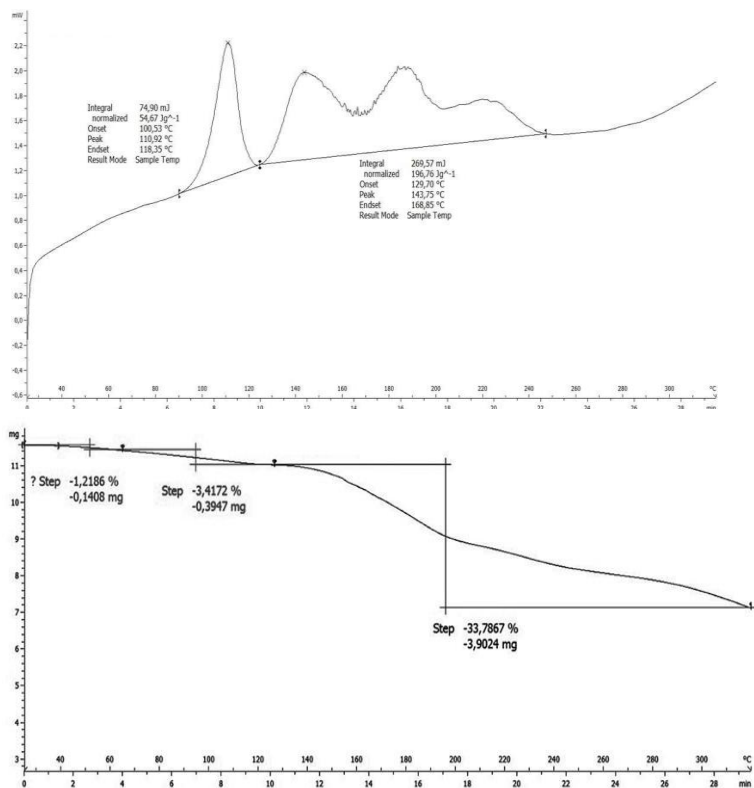
Figure A4.2 DSC and TGA of KET-LYS P2. Multiple endothermic peaks are detectable in KET-LYS P2 DSC profile (upper panel), the first one occurring at 110.9 °C (onset 100.5 °C), while the other multiple partially overlapped endothermic peaks at above 120 °C. Progressive degradation of the compound is visible in TGA analysis (lower panel).
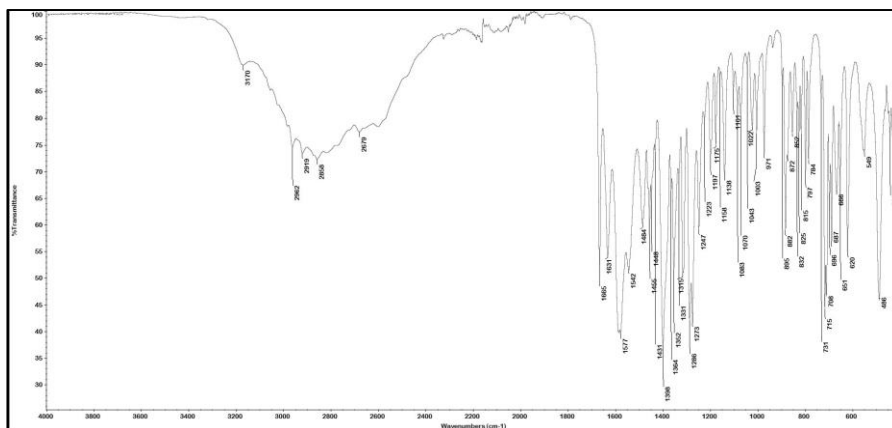
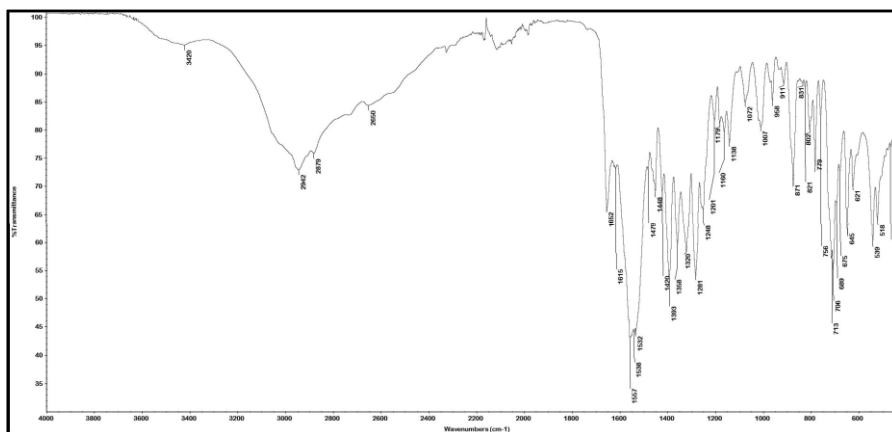**Figure A4.3** FT-IR of KET-LYS P1. The IR band was centered around 3160 cm⁻¹.

Figure A4.4 FT-IR of KET-LYS P2. A very broad band is detectable at 3400-3660 cm⁻¹.
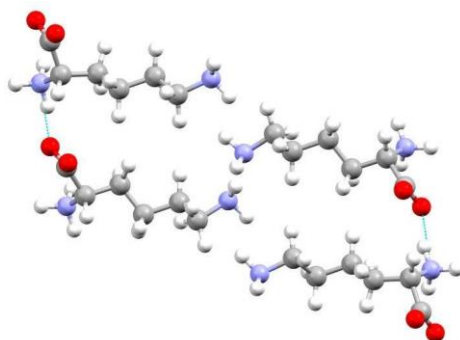
Figure A4.5 Crystal structure of L-lysine. C = grey; O = red; N = azure; H = white; hydrogen bonds are indicated through cyan dotted lines.
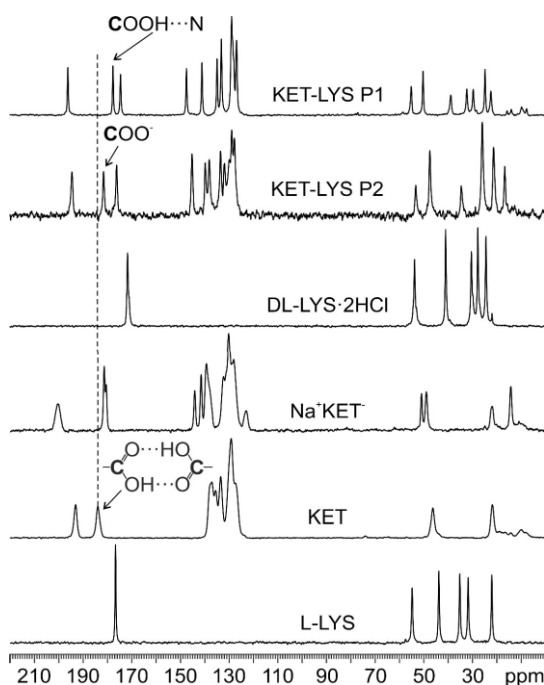

Figure A4.6 ^{13}C CPMAS spectra of samples KET, L-LYS, Na^+KET^-, DL-LYS·2HCl, KET-LYS P1 and KET-LYS P2. Depending on the employed instrument, the resonance frequency for ^{13}C equals 100 or 150 MHz, while the spinning speed is 12 or 20 kHz, respectively (see Material and Methods in Chapter 5 for details). All the spectra were acquired at room temperature, except for KET-LYS P2, which was acquired at 273 K. The labels are referred to the carboxylic group of KET.
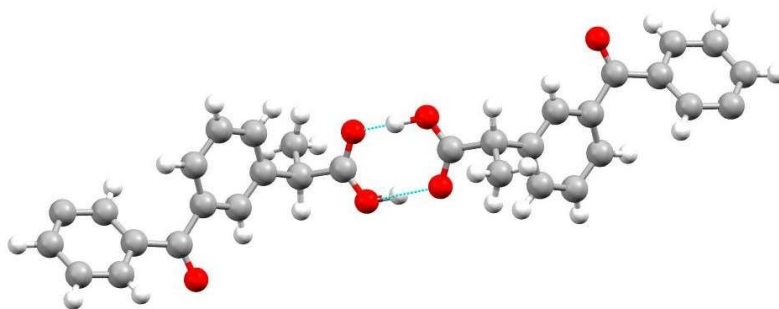
Figure A4.7 Crystal structure of (*RS*)-KET displaying the typical carboxylic homodimeric synthon. C = grey; O = red; H = white; hydrogen bonds are indicated through cyan dotted lines.
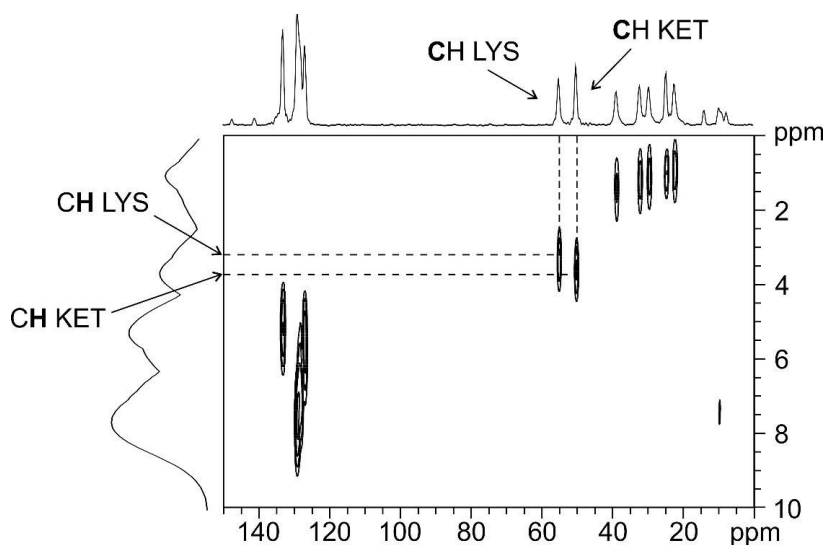
Figure A4.8 On-resonance ^{1}H-^{13}C FSLG HETCOR spectrum (contact time = 0.1 ms) of KET-LYS P1. Above, ^{13}C spectrum; on the left, ^{1}H spectrum. Dashed lines represent significant correlations among covalently bonded protons and C atoms in the crystal structure (see Chapter 5). Spinning speed = 12 kHz, room temperature.

Figure A4.9 XRPD comparison between KET-LYS P1 and commercial KLS samples. The diffraction patterns of KET-LYS P1 and commercial KLS are superposable.

Appendix V: Additional data for Chapter 6

Figure A5.1 Plot of C-O distance vs. nominal composition measured from single crystal XRD data.
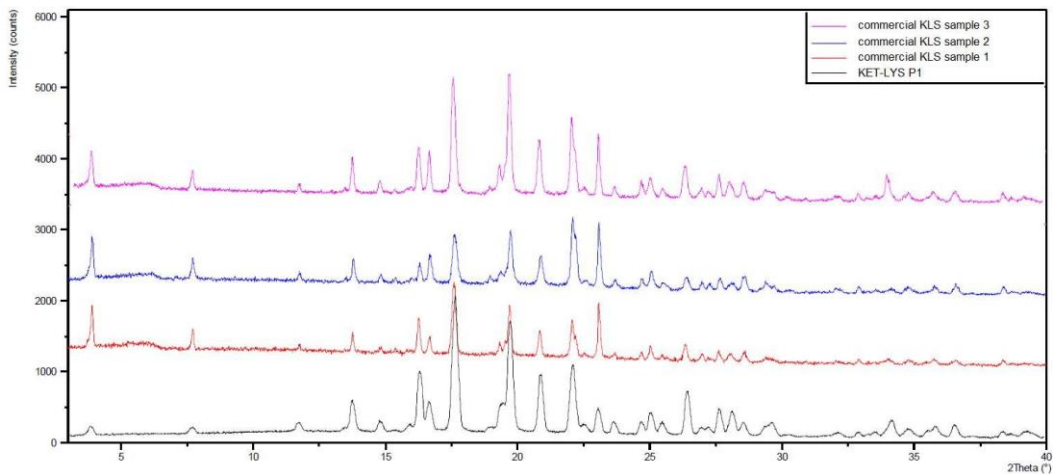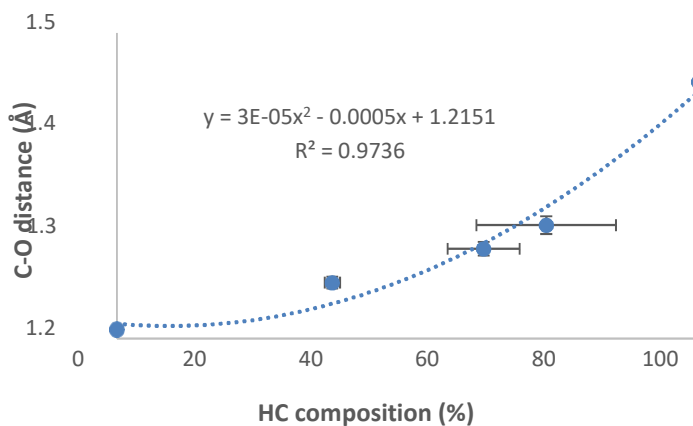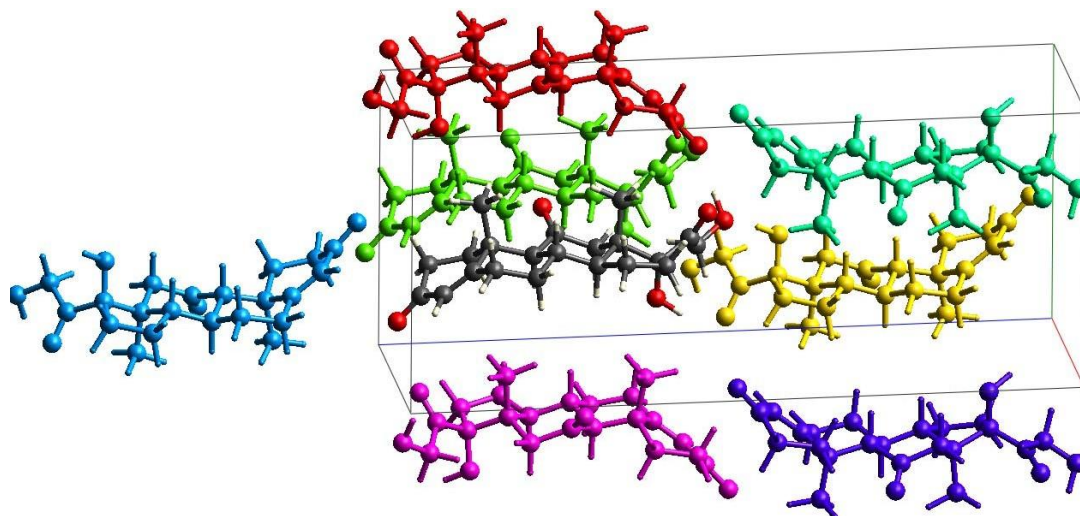

Figure A5.2 Cortisone crystal packing; the molecular colour matches the one in Tables A5.1a and A5.1b.

Table A5.1a Interaction energies for cortisone in the solid solutions.

	Symop	R	E_ele	E_pol	E_dis	E_rep	E_tot
C in pure C	-x, y+1/2, -z+1/2	6.46	-43.9	-12.4	-40.1	44	-53.3
	x+1/2, -y+1/2, -z	11.9	-51.4	-16.8	-17.3	37.7	-48.3
	x, y, z	7.78	-2.4	-2.8	-25.2	10.1	-18.8
	-x+1/2, -y, z+1/2	12.11	-6.4	-4.1	-17	5.3	-20.2
	x+1/2, -y+1/2, -z	13.4	-5.4	-3.4	-11.7	3.9	-15.1
	-x+1/2, -y, z+1/2	13.96	-9.9	-1.1	-1.7	0	-12.3
	-x, y+1/2, -z+1/2	6.35	-5.4	-5	-53.1	21	-39.6
C in C:HC = 2:1	-x, y+1/2, -z+1/2	6.48	-34	-10.1	-39.9	34.3	-49.3
	x+1/2, -y+1/2, -z	12	-53.7	-17.4	-17	37.1	-51.2
	x, y, z	7.73	-1.3	-2.1	-26.2	9.2	-18.9
	-x+1/2, -y, z+1/2	12.1	-8.1	-3.2	-17.5	5.9	-21.4
	x+1/2, -y+1/2, -z	13.4	-6.1	-3.5	-12.1	4.2	-16.1
	-x+1/2, -y, z+1/2	14	-9.9	-1.1	-1.6	0	-12.2
	-x, y+1/2, -z+1/2	6.36	-5.6	-5.1	-51.6	19.7	-39.5
C in C:HC = 1:2	-x, y+1/2, -z+1/2	6.47	-36.9	-10.7	-40.3	37.2	-50.6
	x+1/2, -y+1/2, -z	11.9	-53.6	-17.4	-17.4	37.3	-51.3
	x, y, z	7.7	-1	-2.1	-27.2	9.8	-19
	-x+1/2, -y, z+1/2	12.1	-8	-3.5	-17.5	5.9	-21.4
	x+1/2, -y+1/2, -z	13.4	-5.8	-3.4	-12.4	4.4	-15.8
	-x+1/2, -y, z+1/2	14	-9.7	-1	-1.6	0	-12
	-x, y+1/2, -z+1/2	6.34	-5.5	-5	-52.1	21.5	-38.4
C in C:HC = 1:3	-x, y+1/2, -z+1/2	6.47	-36.8	-10.7	-40	37	-50.5
	x+1/2, -y+1/2, -z	12	-53.4	-17.3	-17.1	37.4	-50.8
	x, y, z	7.74	-1.5	-2.2	-25.8	9.1	-18.9
	-x+1/2, -y, z+1/2	12.1	-7.5	-3.4	-17.2	5.5	-21
	x+1/2, -y+1/2, -z	13.4	-5.8	-3.4	-11.9	4	-15.6
	-x+1/2, -y, z+1/2	14	-9.8	-1.1	-1.6	0	-12.1
	-x, y+1/2, -z+1/2	6.36	-5.4	-5	-52.1	20.2	-39.3

Table A5.1b Interaction energies for hydrocortisone in the solid solutions.

	Symop	R	E_ele	E_pol	E_dis	E_rep	E_tot
HC in pure C	-x, y+1/2, -z+1/2	6.44	-42	-13.3	-43.2	43.9	-54.3
	x+1/2, -y+1/2, -z	11.93	-52	-16.3	-17.3	37.5	-48.4
	x, y, z	7.78	2.6	-7.1	-30.8	27.4	-7.5
	-x+1/2, -y, z+1/2	12.11	-4.5	-4.3	-17	5.2	-18.5
	x+1/2, -y+1/2, -z	13.42	-5.3	-3.5	-11.8	3.9	-15.1
	-x+1/2, -y, z+1/2	13.96	-9	-1.1	-1.7	0	-11.3
	-x, y+1/2, -z+1/2	6.37	-6.8	-3.7	-53.2	20.4	-40.7
HC in C:HC = 2:1	-x, y+1/2, -z+1/2	6.46	-37	-12.2	-43.3	40.3	-52.1
	x+1/2, -y+1/2, -z	11.95	-52	-16.4	-17	36.2	-49.9
	x, y, z	7.74	3.8	-5.5	-31.2	17.5	-13.7
	-x+1/2, -y, z+1/2	12.13	-5.6	-3.9	-17.2	5.5	-19.3
	x+1/2, -y+1/2, -z	13.43	-5.6	-3.6	-11.9	4	-15.5
	-x+1/2, -y, z+1/2	14	-8.8	-1	-1.6	0	-11.1
	-x, y+1/2, -z+1/2	6.37	-6.7	-3.7	-52.4	19.9	-40.3
HC in C:HC = 1:2	-x, y+1/2, -z+1/2	6.47	-35	-11.7	-43.4	38.3	-51.2
	x+1/2, -y+1/2, -z	11.96	-53	-16.5	-16.9	36	-50.7
	x, y, z	7.73	4.1	-5.1	-31.8	15.8	-15.1
	-x+1/2, -y, z+1/2	12.14	-6.2	-3.9	-17.4	5.9	-19.8
	x+1/2, -y+1/2, -z	13.44	-5.9	-3.7	-12	4.1	-15.9
	-x+1/2, -y, z+1/2	14.02	-8.9	-1.1	-1.6	0	-11.2
	-x, y+1/2, -z+1/2	6.37	-6.6	-3.8	-52.1	20	-40
HC in C:HC = 1:3	-x, y+1/2, -z+1/2	6.46	-36	-11.9	-44.4	41	-50.9
	x+1/2, -y+1/2, -z	11.93	-54	-17	-17.3	37.2	-51.7
	x, y, z	7.7	3.9	-4.8	-33	14.5	-17.2
	-x+1/2, -y, z+1/2	12.1	-5.6	-4	-17.3	5.7	-19.4
	x+1/2, -y+1/2, -z	13.39	-5.8	-3.6	-12.5	4.5	-15.8
	-x+1/2, -y, z+1/2	13.98	-8.7	-1	-1.7	0	-11
	-x, y+1/2, -z+1/2	6.36	-6.6	-3.7	-52.4	21.2	-39.2
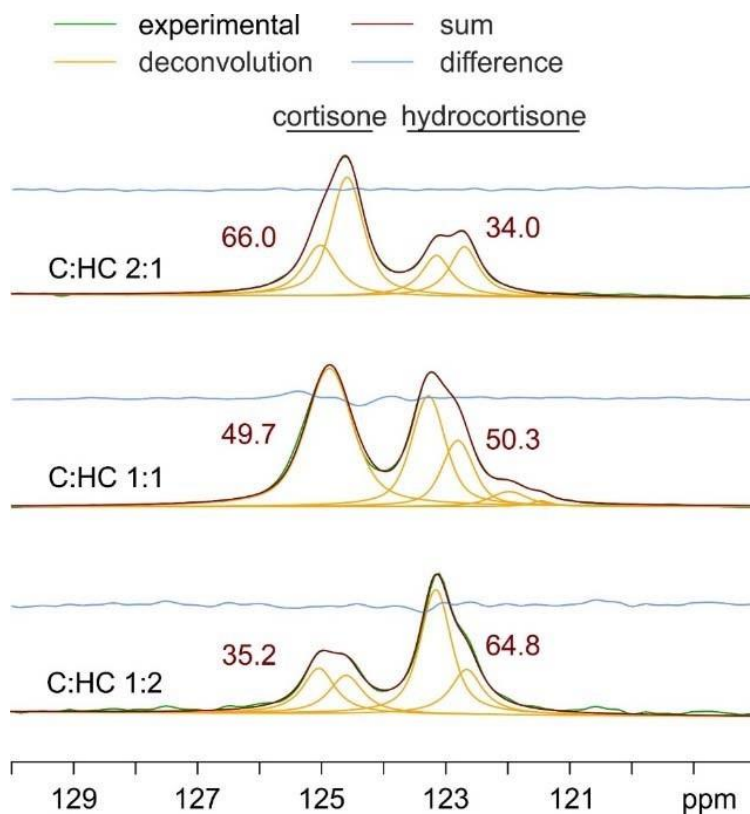
Figure A5.3 Detail of the ^{13}C CPMAS spectra of the three mixtures (in green), with deconvolved peaks (in yellow). The red line corresponds to the sum of the deconvolved resonances, while the blue line represents the difference between the experimental and the sum spectra. Red labels represent relative amounts (expressed as percent values) of C and HC in the three samples, as calculated through the integral areas of the deconvolved peaks.

Figure A5.4 Thermograms measured for pure cortisone (C), pure hydrocortisone (HC) and three C:HC mixed phases generate by SADS (stoichiometric ratios = 2:1; 1:1; 1:2).
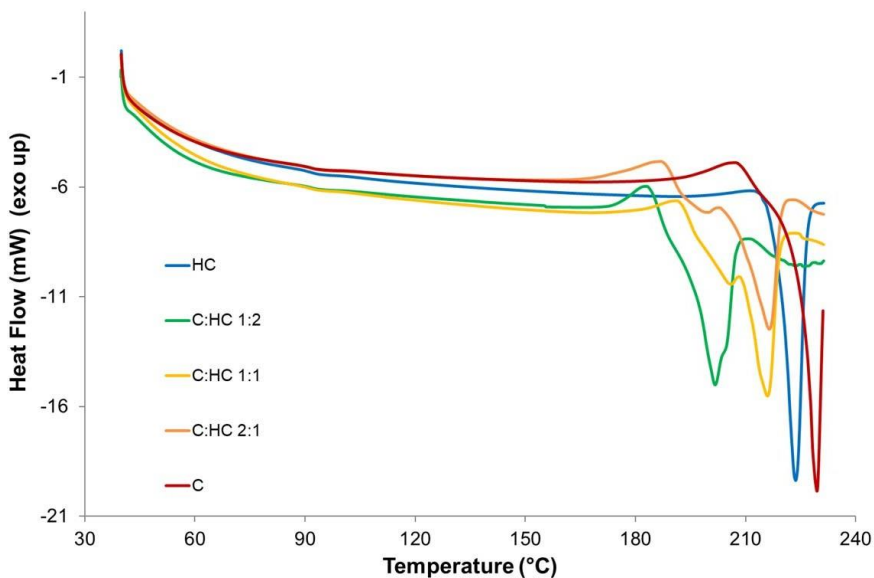
Figure A5.5 Calorimetric measurements for pure cortisone (C), pure hydrocortisone (HC) and three C:HC mixed phases generate by SADS (stoichiometric ratios = 2:1; 1:1; 1:2).

228

Table A5.2 Summary of phase quantification by Rietveld refinement for the products of mechanochemical (MC) and SADS synthesis.
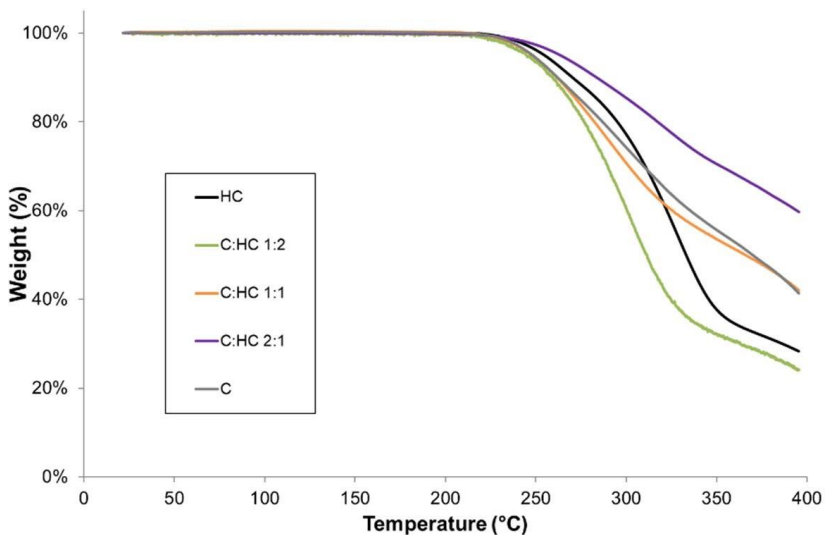
Sample Ratio		Crystal Form Calculated Weight %		Crystal Form Found (MC synthesis) Weight fraction %		Crystal Form Found (SADS synthesis) Weight fraction %	
C	HC	C	HC	DHPRTO (C)	ZZZPNG01 (HC)	DHPRTO (C)	ZZZPNG01 (HC)
1	0	100	0	100	0	100	0
1	2	33.18	66.82	32.2(5)	67.8(3)	100	0
1	1	49.86	50.14	48.7(4)	51.3(3)	100	0
2	1	66.58	33.42	65.4(3)	34.6(2)	100	0
0	1	0	100	0	100	0	100

Summary of publications and activities

Phd courses	
2019	An insight into epistemological and didactic issues related with science teaching, **2 CFU**
2019	Introduction to Crystallography (Crystallography School), **1.5 CFU**
2019	Instrumentation for X-Ray Diffraction (Crystallography School), **1 CFU**
2019	Electron Diffraction (Crystallography School), **1 CFU**
2019	X-Ray Diffraction (Crystallography School), **1 CFU**
2019	X-Ray Diffraction Methods: Polycrystalline (Crystallography School), **2.5 CFU**
2019	X-Ray Diffraction Methods: Single Crystal (Crystallography School), **2.5 CFU**
2019	In situ/operando X-Ray Powder Diffraction (Crystallography School), **1 CFU**
2019	Inorganic Crystallochemistry (Crystallography School), **1 CFU**
2019	Causes of Colour in Minerals (Crystallography School), **2 CFU**
2020	English for scientific academic purpose, **7.5 CFU**
2020	Introduction to Scientific Programming (in Python), **5 CFU**
Congresses | Workshops | Schools | Seminars	
2019	Giornate del CrisDi: X-ray Powder Diffraction: a useful tool for Chemistry and Material Science, Department of Chemistry, University of Torino, 28 February 2019, **1 CFU**
2019	Young Researchers meet Molecular Spectroscopy (YRMS) – Pisa (Italy), 4-5 April 2019, **2 CFU** | Oral presentation, **2 CFU**
2019	Bioorthogonal Photocatalysis for the Activation of Metal-based Prodrugs, Prof. Luca Salassa, Department of Chemistry, University of Torino, 12 April 2019, **0.5 CFU**
2019	Immobilization of multi-enzyme systems; an avenue to fabricate self-sufficient heterogeneous biocatalysts, Prof. Fernando Lopez-Gallego, Department of Chemistry, University of Torino, 3 May 2019, **0.5 CFU**
2019	10th Crystal Forms – Bologna (Italy), 9-11 June 2019, **3 CFU** | Poster presentation, **1 CFU**
2019	GIDRM XLVIII National Congress on Magnetic Resonance – L'Aquila (Italy), 11-13 September 2019, **3 CFU** | Poster presentation, **0.5 CFU**
2021	GIDRM XLIX National Congress on Magnetic Resonance – Online – 8-10 September 2021, **3 CFU** | Oral presentation, **2 CFU**
2021	11th Crystal Forms – Online – 10-11 September 2021, **3 CFU**
Publications	
2019	C. Anelli, M. R. Chierotti, **S. Bordignon**, P. Quadrelli, D. Marongiu, G. Bongiovanni, L. Malavasi, Investigation of Dimethylammonium Solubility in MAPbBr$_3$ Hybrid Perovskite: Synthesis, Crystal Structure, and Optical Properties, *Inorg. Chem.* **2019**, *58*, 944–949, **2 CFU**

2019	R. Vismara, G. Tuci, A. Tombesi, K. V. Domasevitch, C. Di Nicola, G. Giambastiani, M. R. Chierotti, **S. Bordignon**, R. Gobetto, C. Pettinari, A. Rossin, S. Galli, Tuning Carbon Dioxide Adsorption Affinity of Zinc(II) MOFs by Mixing Bis(pyrazolate) Ligands with N-Containing Tags, *ACS Appl. Mater. Interfaces* **2019**, *11*, 26956–26969, **2 CFU**
2020	D. Bernasconi, **S. Bordignon**, F. Rossi, E. Priola, C. Nervi, R. Gobetto, D. Voinovich, D. Hasa, N. T. Duong, Y. Nishiyama, M. R. Chierotti, Selective Synthesis of a Salt and a Cocrystal of the Ethionamide–Salicylic Acid System, *Cryst. Growth Des.* **2020**, *20*, 906–915, **2 CFU**
2020	**S. Bordignon**, P. Cerreia Vioglio, E. Amadio, F. Rossi, E. Priola, D. Voinovich, R. Gobetto, M. R. Chierotti, Molecular Crystal Forms of Antitubercular Ethionamide with Dicarboxylic Acids: Solid-State Properties and a Combined Structural and Spectroscopic Study, *Pharmaceutics* **2020**, 12, 818–835, **4 CFU**
2020	V. Verma, **S. Bordignon**, M. R. Chierotti, M. Lestari, K. Lyons, L. Padrela, K. Ryan, M. Lusi, Cortisone and cortisol break hydrogen-bonding rules to make a drug–prodrug solid solution, *IUCrJ*, **2020**, *7*, 1124–1130, **2 CFU**
2021	A. Crosino, E. Moscato, M. Blangetti, G. Carotenuto, F. Spina, **S. Bordignon**, V. Puech-Pagès, L. Anfossi, V. Volpe, C. Prandi, R. Gobetto, G. C. Varese, A. Genre, Extraction of short chain chitooligosaccharides from fungal biomass and their use as promoters of arbuscular mycorrhizal symbiosis, *Sci. Rep.* **2021**, *11*, 3798–3809, **2 CFU**
2021	M. Arhangelskis, D. Bučar, **S. Bordignon**, M. R. Chierotti, S. A. Stratford, D. Voinovich, W. Jones, D. Hasa, Mechanochemical reactivity inhibited, prohibited and reversed by liquid additives: examples from crystal-form screens, *Chem. Sci.*, **2021**, *12*, 3264–3269, **2 CFU**
2021	A. Kumar, K. A. Ramishetty, **S. Bordignon**, B. K. Hodnett, P. Davern, S. Hudson, Preparation, stabilisation, isolation and tableting of valsartan nanoparticles using a semi-continuous carrier particle mediated process, *Int. J. Pharm.*, **2021**, *597*, 120199, **2 CFU**
2021	C. Pistidda, A. Santhosh, P. Jerabek, Y. Shang, A. Girella, C. Milanese, M. Dore, S. Garroni, **S. Bordignon**, M. R. Chierotti, T. Klassen, M. Dornheim, Hydrogenation via a low energy mechanochemical approach: the MgB_2 case, *J. Phys. Energy*, **2021**, *3*, 044001, **2 CFU**
2021	A. Aramini, G. Bianchini, S. Lillini, **S. Bordignon**, M. Tomassetti, R. Novelli, S. Mattioli, L. Lvova, R. Paolesse, M. R. Chierotti, M. Allegretti, Unexpected salt/cocrystal polymorphism of the ketoprofen–lysine system: discovery of a new ketoprofen–L-lysine salt polymorph with different physicochemical and pharmacokinetic properties, *Pharmaceuticals*, **2021**, *14*, 555–572, **2 CFU**
2021	A. Daolio, A. Pizzi, M. Calabrese, G. Terraneo, **S. Bordignon**, A. Frontera, G. Resnati, Molecular electrostatic potential and noncovalent interactions in derivatives of group 8 elements, *Angew. Chem. Int. Ed.*, **2021**, *60*, 1–6, **2 CFU**

2021	**S. Bordignon**, P. Cerreia Vioglio, C. Bertoncini, E. Priola, R. Gobetto, M. R. Chierotti, Pseudopolymorphism driven by stoichiometry and hydrated/anhydrous reagents: the riveting case of methyl gallate·L-proline, *Cryst. Growth Des.* **2021**, *21*, 6776–6785, **4 CFU**
Auxiliary teaching	
2019	Tutoring for "Chimica Generale e Inorganica" (Corso di Laurea Triennale in Chimica e Tecnologie Chimiche), A and B courses: 40 hours, **4 CFU**
2020	Tutoring for "Chimica Generale e Inorganica" (Corso di Laurea Triennale in Chimica e Tecnologie Chimiche), A and B courses: 40 hours, **4 CFU**
2021	Tutoring for "Chimica Generale e Inorganica" (Corso di Laurea Triennale in Chimica e Tecnologie Chimiche), B course: 20 hours, **2 CFU**
2021	NMR Laboratory for "Risonanza magnetica e diffrazione di raggi X in chimica clinica e forense" (Corso di Laurea Magistrale in Chimica Clinica, Forense e dello Sport), Prof. Chierotti: 20 hours, **2 CFU**
Periods abroad	
2020	Bernal Insistute – Limerick, Ireland. Supervisor: Dr. Matteo Lusi, 16/01/2020 – 01/05/2020 (**9 CFU**)

CFU	
PhD courses	28
Congresses | Workshops | Schools | Seminars	16
Presentations	5.5
Publications	26
Auxiliary teaching	12
Periods abroad	9
2nd year presentation	3
TOTAL	**99.5**

Acknowledgments

Eccoci qui, un'altra tesi, un'altro catartico momento che serve a dire grazie a chi è stato importante in questo percorso, un percorso molto più lungo dei 3 anni (più proroga) di dottorato, un percorso che è nato dall'inizio della mia tesi magistrale, e per certi versi anche prima, un percorso che in un senso è finito, ma in altri è appena incominciato.

Sono innanzitutto riconoscente a tutti coloro che mi hanno aiutato nel mio percorso di ricerca, sia qui a Torino (tesisti, borsisti, dottorandi e collaboratori vari), sia in altri Dipartimenti e centri di ricerca, per aver contribuito alla produzione di stimolanti lavori scientifici che hanno portato a questo sudato e lieto epilogo professionale.

Il primo personale grazie va a mio Papà, perché nonostante tutto quello che la vita ti ha riservato, nonostante il mio carattere a volte scostante, nonostante a 30 anni ti sia ancora rimasto sulle croste, mi sei sempre stato dietro, cercando di trasmettermi tutto l'amore che hai per me, e quello di Mamma. Per questo ti vorrò sempre due mondi di bene.

Ad Andre, il mio fratellone, dico grazie per tutto il sostegno negli anni. Come ci siamo detti, il nostro rapporto purtroppo non riflette quanto ci vogliamo bene, ma ti prometto che ci lavorerò al massimo. Intanto, grazie perché con me non ti sei arreso.

Grazie a Nala, che mi ha accompagnato per metà della mia vita, nel bene e nel male. Mi mancherai Cucciolina.

Grazie a Ginny e Gabry, due fonti di luce propria che rischiarano i momenti difficili. Grazie ai miei cugini, Carlotta e Francesco, per i momenti divertenti che passiamo insieme, che cancellano lo stress e il disagio cosmico che ogni tanto mi invadono. Grazie ai miei zii, Gloria, Beppe, Mary. Grazie a Zio Fiorenzo. Mai avrei pensato che non saresti stato qui a chiamarmi Dottore quando davvero me lo sarei guadagnato. Chissà, magari da qualche parte lo stai facendo, orgoglioso. Mi piace pensarla così.

Un grosso ringraziamento a Michele, a Roberto, a Claudio, a Giorgio. Difficile seguire il discorso di Michele, che mi ha già fatto piangere a sufficienza il giorno della discussione. Non dico nulla di nuovo quando

ribadisco che, insieme a tutto il gruppo, mi avete sempre fatto sentire in una seconda famiglia. Credetemi quando vi dico che, aldilà di tutto il supporto scientifico e professionale, aldilà di tutta la stima che avete sempre dimostrato nei miei confronti e che mi ha portato dove sono oggi, tutte cose per cui ovviamente vi ringrazio profondamente, l'accoglienza che mi avete riservato (nonostante le freddure e le derive autistiche) è ciò per cui vi sono più riconoscente.

Grazie a Matteo e Chiara: per una persona patologicamente radicata nella routine come me, sono stati fondamentali perché durante il periodo all'estero mi sentissi a casa. Certo, neanche nei miei peggiori incubi trovava spazio l'idea che scoppiasse una pandemia a peggiorare il mio dramma interiore da sradicamento, ma ce l'hanno fatta ugualmente.

Grazie a Laura, Lele, Rebecca, Angelo e a tutti coloro che in Dipartimento si sono sorbiti le mie ansie, i miei scazzi, i miei consigli psicologici (anche non richiesti), e in cambio mi hanno dimostrato amicizia e mi sono stati a fianco nei momenti di giubilo in tutto il regno e in quelli di sconforto, professionali e non.

Grazie a Davide: attraverso gli alti e i bassi, sei comunque stato un motore che mi ha spinto ad arrivare qui.

Grazie ai miei amici, da quelli più datati, come Riky, Silvia e Yle, che mi reggono dal lontanisssssssimo liceo, a quelli più recenti: il gruppo da me soprannominato "di Capodanno", con cui ho condiviso gioie e dolori sì a Capodanno, ma anche in altre innumerevoli occasioni; a Eli e Riky, per le risate che ci facciamo in compagnia di uno (o due, o tre, ecc…) aperitivi insieme alle 3 fanciulle che seguono.

Grazie a FedeB, "la donna delle mouffe", per i suoi dolci, il suo sconfinato altruismo, la premura verso le persone a cui tiene e le sue risate incontrollabili alcol-correlate, che mi fanno scassare.

Grazie a FeRossi, "mi mariposa", mia collega tennnica e infinita viaggiatrice del mondo, che se si ferma per un attimo, la trovi qui, pronta ad esserci.

Grazie a Ele, "my sister from another mister". Portiamo le stesse cicatrici, ma abbiamo imparato a volerci bene in una maniera più unica

che rara soprattutto per i tantissimi momenti felici insieme. Ti voglio bene! Ma adesso smettila di piangere che mi rovini la Tesi. E ora smettila di ridere.

Sono tante, tantissime, onestamente inelencabili, le persone a cui dovrei rivolgere un ringraziamento, perché, magari anche solo in piccola parte, hanno contribuito a farmi arrivare fin qui. Non amo ripetermi (non è vero, lo adoroh!), ma se siete stati presenti, in un modo o nell'altro, in questo mio percorso, rappresentate una parte di me, e di questo, vi sono grato.

E poi oh, un ringraziamento a me stesso (in particolare alle mie personalità numero 8 e 23) per aver accettato la sfida, per aver resistito, per essere caduto e per essermi rialzato.

E un ringraziamento da parte vostra a me perché mi sono violentato a tradurre quello che nasce come monologo interiore in inglese in un testo scritto in italiano. Prego!